INVESTIGATION OF METAL-ORGANIC FRAMEWORKS AS ADSORBENTS FOR CO_2 CAPTURE FROM FLUE GAS

Juergen Kahr

A Thesis Submitted for the Degree of PhD
at the
University of St Andrews

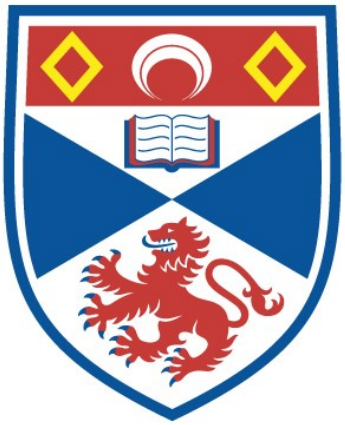

2014

Investigation of Metal-Organic Frameworks as Adsorbents for CO_2 Capture from Flue Gas

This thesis is submitted in partial fulfilment for the degree of

Doctor of Philosophy

in the Faculty of Science of the University of St Andrews by

Juergen Kahr, MSc

February 2014

Supervisors: Prof. Paul A. Wright and Prof. Russell E. Morris

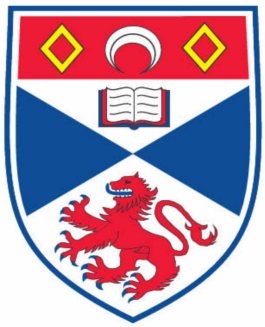

University of
St Andrews

Declarations

1. I, Juergen Kahr, hereby certify that this thesis, which is approximately 40000 words in length, has been written by me, that it is the record of work carried out by me and that it has not been submitted in any previous application for a higher degree.
   I was admitted as a research student in January, 2010 and as a candidate for the degree of *Doctor of Philosophy* in May, 2011 the higher study for which this is a record was carried out in the University of St Andrews between 2010 and 2014.
   Date ……. Signature of Candidate ……..
2. I hereby certify that the candidate has fulfilled the conditions of the Resolution and Regulations appropriate for the degree of PhD in the University of St Andrews and that the candidate is qualified to submit this thesis in application for that degree.
   Date ……. Signature of Supervisor …….
3. In submitting this thesis to the University of St Andrews I understand that I am giving permission for it to be made available for use in accordance with the regulations of the University Library for the time being in force, subject to any copyright vested in the work not being affected thereby. I also understand that the title and the abstract will be published, and that a copy of the work may be made and supplied to any bona fide library or research worker, that my thesis will be electronically accessible for personal or research use unless exempt by award of an embargo as requested below, and that the library has the right to migrate my thesis into new electronic forms as required to ensure continued access to the thesis. I have obtained any third-party copyright permissions that may be required in order to allow such access and migration, or have requested the appropriate embargo below.
   Embargo on all of printed copy and electronic copy for the same fixed period of one year on the following ground: Publication would preclude future publication.
   Date……Signature of Candidate ……
   Signature of Supervisor ……..

Acknowledgements

I owe a great and many thanks to a great many people who helped and supported me during my PhD study.

I would like to thank my supervisor Prof. Paul A. Wright whose knowledge, support and guidance were invaluable throughout my thesis. I am also indebted to my other supervisor Prof. Russell E. Morris, for his never failing enthusiasm and for the many useful discussions.

Further to this I would like to thank John Mowat for the numerous stimulating discussions and general advice on structure solution methods.

My thanks and appreciations go to present and past PAW group members: Magdalena Lozinska, David Price, Berenice Gonzalez, Laura Mitchell, Lorena Picone, Alessandro Turrina, Michael Wharmby, Eike Eschenroeder and Alex Greenaway for their help, useful suggestions and wishes for the successful completion of this work.

I am grateful to many of the technical and scientific staff of the University of St Andrews, particularly Mrs. Sylvia Williamson for training in the use of equipment and collecting adsorption data.

Many thanks go to Stephen Francis for many inspiring discussions and his advice in XPS analysis.

I am grateful to Scott Sneddon and Prof. Sharon Ashbrook for their prompt and thorough collection and analysis of solid-state NMR data. I thank Dr. David Cordes and Prof. Alex Slawin for their help and support with crystallography.

I would like to thank the following people from outside the University of St Andrews for their help and assistance with the collection of my data: Dr. Enzo Mangano and Prof. Stefano Brandani (ZLC method), Dr. David Fairen-Jimenez (computer simulation of adsorption), Dr. Anders Barlow and Prof. Peter Cumpson (XPS measurements) and the EPSRC for financial support.

Last but not least, I wish to express my love and gratitude to my beloved family, my mother, father and sisters, for their understanding, support and endless love when it was most required.

This thesis is dedicated to my parents,
Wolfgang and Sieglinde

Abstract

The post-synthetic modification of CPO-27(Mg) by introducing nickel cations into the framework is described. A combination of surface sensitive XPS analysis, synchrotron powder X-ray diffraction and selected area and bulk EDX measurements revealed the distribution of Ni^{2+} throughout the crystal with the highest concentration towards the external surface forming a nickel-rich rim. By adding nickel acetate and chloride salts in combination with a weak acid, Ni^{2+} contents of up to 67% for the bulk material were achieved via a one-pot preparative procedure. A combined mechanism of overgrowth and isomorphous cation exchange is proposed. The study led to an improvement of porosity to N_2 (77 K) up to 17 mmol g^{-1}, close to values achieved elsewhere via complex activation procedures. High values for the adsorption of carbon dioxide of up to 6.7 mmol g^{-1} at temperatures and partial pressure relevant for carbon capture from post-combustion power plants were accomplished (298 K, 0.1 bar) and were shown to be repeatable over cycles under dry conditions.

The synthesis, structure and adsorption properties of a series of zinc imidazolate zeolitic imidazolate framework, ZIF, materials was also investigated. Structural details of the zinc nitroimidazolate ZIF-65(Zn) were determined by Rietveld refinement. Heating experiments of as prepared ZIF-65(Zn) revealed a partial transformation from a cubic framework to an unknown structure, shown to be reversible. The new phase possess high porosity to nitrogen and showed stepped, hysteretic adsorption and desorption isotherms for at 77 K and CO_2 at 298 K. Using methanol instead of DMF in synthesis yielded a novel dense non-porous zinc nitro imidazolate structure.

A series of novel structures was prepared via synthesis including a mixture of 2-nitroimidazole (NIm) and purine with different zinc metal sources. Two MOF structures were found to consist of purine linkers only, but could not be rendered porous. By changing the metal source or solvent an isoreticular structure of the ZIF-68 (GME) family was obtained, composed of purine and NIm, as well as a novel form of a mixed linker ZIF with the RHO topology with *Im-3m* symmetry that exhibits large pores and *exo*-Zn and *exo*-NIm moieties decorating the cavity walls. The nitrogen uptake (77 K) of 6.5 mmol g^{-1} could be increased to 12.5 mmol g^{-1} by removing *exo*-moieties through water washing.

The use of a diamino functionalised purine linker (DAP) together with NIm gave a new ZIF material, STA-17, with a novel topology. The structure was found to exhibit porosity to nitrogen (77 K) of 6.5 mmol g^{-1} and carbon dioxide at (198 K) of 5 mmol g^{-1}, but shows weak interaction with CO_2 at 298 K. Indexing from synchrotron powder XRD data gave a hexagonal unit cell with $a = b = 29.725$ Å and $c = 18.606$ Å. Subsequent analysis of the composition using NMR, TGA and IR techniques revealed the presence of both linkers in the structure and a linker ratio of 2:1 (NIm : DAP). Although crystals of suitable quality for single crystal X-ray diffraction were not obtained, a partial model for the structure is proposed via analogy with a hypothetical zeolite structure and analysis of powder X-ray diffraction data.

Publications arising from this work

1. J. Kahr, J. P. S. Mowat, A. M. Z. Slawin, R. E. Morris, D. Fairen-Jimenez and P. A. Wright,

   Synthetic control of framework zinc purinate crystallisation and properties of a large pore, decorated, mixed-linker RHO-type ZIF,

   Chem. Commun., 2012, 48, 6690-6692, DOI: 10.1039/C2CC32927A

Information presented in this thesis has been published and has been adapted with permission from above authors. Copyright 2012, Royal Society of Chemistry.

2. *J. Kahr*, R. E. Morris and P. A. Wright,

   Post-synthetic incorporation of nickel into CPO-27(Mg) to give materials with enhanced permanent porosity,

   CrystEngComm, 2013, 15, 9779-9786, DOI: 10.1039/C3CE41228H

Information presented in this thesis has been published and has been adapted with permission from above authors. Copyright 2013, Royal Society of Chemistry.

3. E. Mangano, S. Brandani, M. C. Ferrari, H. Ahn, D. Friedrich, M. L. Lozinska, P. A. Wright, J. Kahr, R. Morris, M. Croad, N. McKeown, H. Shamsipour and P. Budd,

   Efficient and Rapid Screening of Novel Adsorbents for Carbon Capture in the UK IGSCC Project,

   Ener. Proc., 2013, 37, 40-47, DOI: 10.1016/j.egypro.2013.05.083

Abbreviations

Abbreviation	Explanation
4mr	four membered ring
6mr	six membered ring
a	unitcell parameter
b	unitcell parameter
bbmp	N,N′-bipiperidine(bismethylenephosphonic acid)
BET	Brunauer-Emmet-Teller
c	unitcell parameter
cbIm	5-carboxybenzimidazole
CCD	charge-coupled device
CCS	carbon capture and storage
CdIF	Cadmium imidazolate framework
CHN	carbon, hydrogen and nitrogen analysis
cpmp	4-carboxypiperidyl-N-methylenephosphonic acid
CPO	coordination polymer from Oslo
d6r	double six membered ring
d8r	double eight membered ring
DAP	2,6-diaminopurine
DEF	diethylformamide
dhtp	dihydroxyterephthalic acid
DMF	dimethylformamide
EDX	energie dispersive X-ray spectrocopy
et al	and others (latin: et alii)
EXPGUI	graphical user interface for GSAS experiment (.EXP) files
FT	Fourier transform
GCMC	grand canonical monte carlo methods
GIS	Gismondine
GME	Gmelinite
GSAS	generalized crystal structure analysis software
HKUST-1	Hong Kong University of Science and Technology - Structure 1
IGA	intelligent gravimetric analyser
IGSCC	innovative gas separations for carbon capture

IM	imidazole
IR	infra-red spectroscopy
IRMOF	isoreticular metal-organic framework
LTA	Linde type A
MAS	magic angle spinning
MeOH	methanol
MIL	materials of Institut Lavoisier
MOF	metal-organic framework
NMR	nuclear magnetic resonance
pbmp	N,N′-piperazinebis(methylenephosphonic acid)
PIM	polymers of intrinsic microporosity membranes
PSA	pressure swing adsorption
PTFE	polytetrafluoroethylene
SBU	secondary building units
SOD	sodalite
PXRD	powder X-ray diffraction
SEM	scanning electron microscopy
SIR	semivariants representation
STA	St. Andrews microporous materials
SXRD	single-crystal X-ray diffraction
TGA	thermogravimetric analysis
XPS	X-ray photoelectron spectroscopy
ZABU	zinc-adeninate secondary building unit
ZIF	zeolitic imidazolate framework
ZLC	zero-length-columns chromatographs

Contents

1. Introduction

1.1 Background

In many developed and developing countries carbon dioxide (CO_2) and other gases from fossil fuel use are expected to be the major source of anthropogenic greenhouse gas emissions in the future. As a result, the applicability of CO_2 capture and storage (CCS) for reduction of CO_2 emissions from the use of coal and other fossil fuels at large point sources could become very important in determining the feasibility of climate change mitigation.[1]

The composition of flue gases varies greatly depending on the fuel source. Flue gases have oxidizing properties and generally consist of N_2, O_2, H_2O, CO_2, SO_2, NO_x and HCl. The typical non-nitrogen components of untreated flue gases from eastern low-sulfur bituminous coal[2] are CO_2 (15 - 16 %), H_2O (5 - 7 %) and O_2 (3 - 4 %).[3] Some industrial processes, such as the production of steel, result in flue gases with a considerably higher CO_2 concentration. Untreated flue gas streams also contain considerable particulate matter.[3]

There are three different approaches for CO_2 capture at power plants and other large point sources of CO_2, which are illustrated in Figure 1.1.[1]

(i) In pre-combustion processes, a solid fuel such as coal represents a source for gaseous fuel which is produced through a high-temperature conversion process known as gasification. The fuel gas produced from gasification contains: hydrogen (H_2), carbon monoxide (CO), CO_2, hydrocarbons, such as methane, and a number of other compounds. This fuel gas then undergoes a

reaction known as a water-gas shift that converts the CO and water to CO_2 and H_2. CO_2 created during gasification and from the water gas-shift reaction is removed from the fuel gas through adsorption processes. In adsorption the fuel gas is flowed through or over a liquid or solid material which adsorbs only the CO_2 and leaves the other parts of the fuel gas behind. The CO_2 is then prepared for transport, while the fuel gas is burnt in a gas turbine to generate electricity.[4]

(ii) In post-combustion processes, a solid or gaseous fuel is burnt in the traditional ways like a boiler or gas turbine producing electricity. The exhaust from the turbine or boiler contains a very low concentration (%) of CO_2. Using an adsorption process, similar to that used in pre-combustion processes, the CO_2 in the exhaust is removed and prepared for transport.[4]

(iii) The oxyfuel process burns a solid fuel such as coal in a mixture of CO_2 and in the presence of just the right amount of oxygen to allow combustion to be completed. Usually coal is burnt in air that contains a large amount of nitrogen and leads to a relatively low concentration of CO_2 in the exhaust. Thus, the resulting exhaust is nearly pure carbon dioxide using a CO_2/air mixture. Some of this CO_2 is recycled and used for combustion in the boiler, while the majority is ready for sequestration.[4]

One important difference between these approaches is that post-combustion capture could be applied to industry-standard pulverised coal combustion plants[5] with minimal modifications to the base power plant. By contrast, changes to base combustion power plant designs are required for oxyfiring and a complete change in base plant technology is required for pre-combustion capture in integrated gasification combined cycle (IGCC) plants.[1]

To avoid the re-emission of separated CO_2 into the atmosphere, "gas tight" long term storage media are required. One possible solution is the storage of CO_2 underground (Figure 1.2).[6] One established technique is the compression of CO_2 into active or former

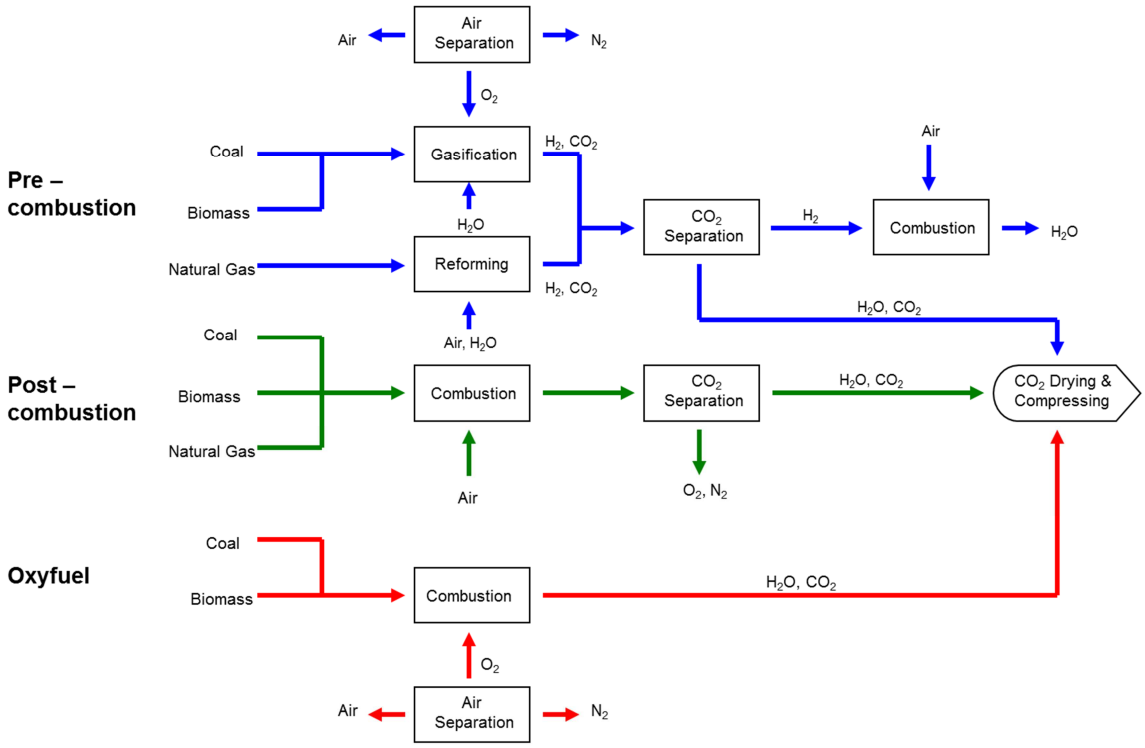

Figure 1.1: *Options for CO_2 capture in power plants.*

gas and oil deposits. In tertiary gas and oil recovery, gas or water vapour is already pumped into nearly depleted deposits in order to recover the last residues of fossil raw material. The CO_2 is converted into its supercritical state and injected into these deposits where it remains.[6]

Another option is the use of deep saline aquifers and groundwater reservoirs. Deep saline aquifers are geological formations frequently found near to large marine and terrestrial sediment basins. Carbon dioxide is pressed into deep water-bearing strata, where it dissolves in the water. This leads to the formation of hot, aggressive carbonic

acid solutions, which put great strain on the corrosion stability of the pumping technology.[6]

Further unmineable coal seams at depths of over 1,500 m can be used to store CO_2 because of the CO_2-adsorbing surface of coal.[6]

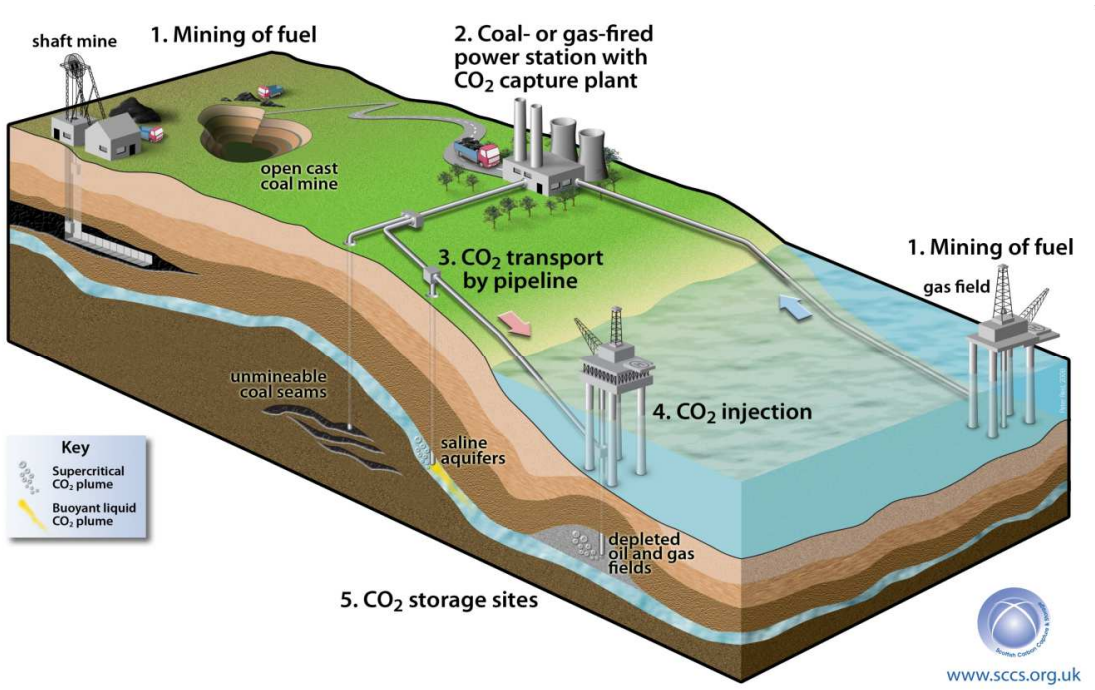

Figure 1.2: *Schematic of CO_2 capture and sequestration in geological formations.*[6]

The CO_2 separation step is the most costly step in carbon capture and sequestration (CCS) schemes.[7] Established technologies available for separation at low partial pressure of CO_2 are scrubbing processes based on chemical solvents. These processes are related to amines or K_2CO_3 in aqueous solution.[8-10] By using a pressure swing adsorption (PSA) based system these problems can be avoided. This process is known to be one of the most economic to recover CO_2 in flue streams from power plants.[11,12] This conventional process mainly involves zeolite materials, but this family of adsorbents are difficult to regenerate without significant heating. Metal-organic framework materials (MOFs) are a new form of porous materials that have been proven

to be promising new candidates for these applications owing to their high capacities in carbon capture and the possibility of tuning functionalities.[13, 14] A continuous search for more efficient and environmentally friendly ways to capture CO_2 from various gas streams is necessary. Processes based on adsorption of porous MOF solids might be an attractive option.[15, 16]

1.2 Metal Organic Frameworks (MOFs)

Metal Organic Frameworks (MOFs), also known as coordination polymers, are a subgroup of porous solids and form 1D, 2D or 3D porous structures. They are built up from inorganic metal nodes arranged as clusters, chains or layers interconnected by organic linkers (phosphonates, carboxylates, sulfonates, imidazolates). Often these hybrid materials contain divalent (Zn^{2+}, Cu^{2+}…) or trivalent (Cr^{3+}, Al^{3+}…) cations connected to each other via organic moieties. The structures consist of tunnels or cavities with pore sizes between 3 and 35 Å.[17] It is possible to tune the pore size, shape and connectivity by subtle modifications of the inorganic moiety and the organic linker molecules[18,19, 20] during synthesis or after, via post-synthetic modification (Figure 1.3).[21-24]

Yaghi et al demonstrated the effect of varying ligand functionalities on tuning surface area and pore volume by developing isoreticular chemistry.[25] By introducing derivatives of dicarboxylate linkers to the synthesis of MOF-5, which is constructed from Zn_4-O tetrahedral clusters and benzene dicarboxylate or related links, it was possible to create a series of topologically identical structures (IRMOFs - isoreticular metal organic frameworks) with different pore sizes varying between 3.8 Å and 28.8 Å, and with different functionalities projecting into the cavities (Figure 1.4).[26]

The preparation of MOFs with the same topology but different functional groups not only influences the structures' pore size, but also can change the interaction with chemically active gases as shown by Mowat et al where the introduction of amine functionalities increase the CO_2 uptake at 273 K (Figure 1.5).[27]

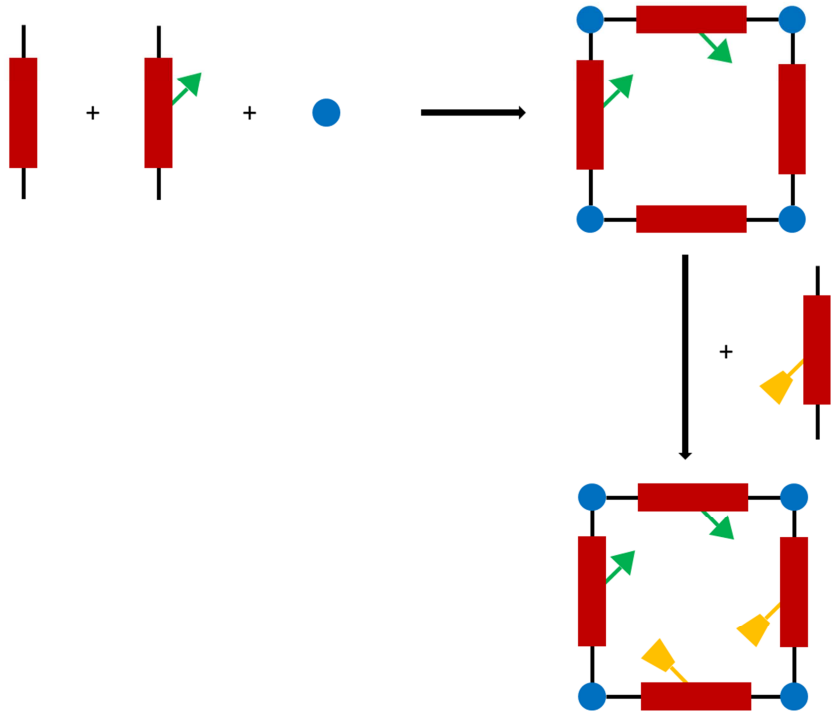

***Figure 1.3**: Schematic of MOF synthesis where the self-assembly of linker anions and cationic metals creates 3 dimensional coordination polymers. The introduction of different linker species or various functionalities during or through a post synthetic method forms the basis of MOFs' tuneability.*

Metal-organic framework materials that exhibit permanent porosity are promising in a wide range of applications, i.e gas storage, separation and purification.[28-31] Additionally, they have attracted attention over the last few years in other applications including magnetism, catalysis or drug delivery.[32-37] Metal-organic frameworks with high surface area and pore volumes appear as candidates to incorporate coordinatively unsaturated metal sites into porous frameworks.[38] In structures where the coordination sphere of metal nodes is completed with solvent molecules, desolvation can lead to unsaturated

metal sites. In order to compensate for the solvent removal the framework can collapse and become amorphous or a rearrangement of the coordination environment of the metal can occur resulting in changing the coordination number and/or geometry.[39-41] In cases where the framework is sufficiently rigid to avoid structure change, an empty coordination site forms and gives an open metal site. Examples of framework compounds that contain such coordinatively unsaturated metal atoms have increased over the duration of this thesis.[28, 42]

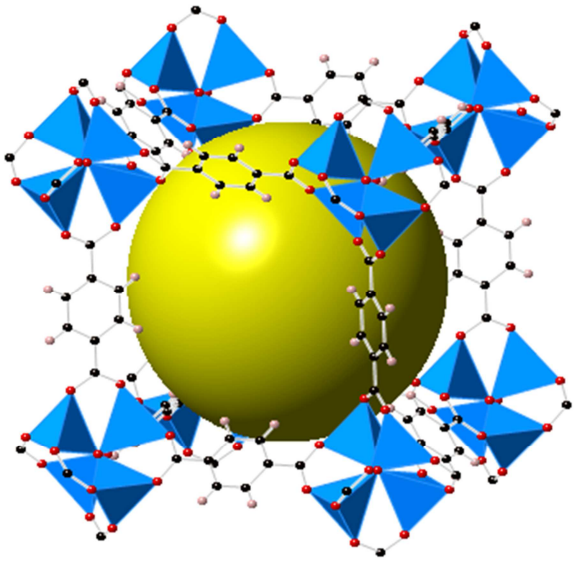

Figure 1.4: *Structure of MOF-5 (IRMOF-1) showing Zn_4-O tetrahedral aggregates connected via benzenedicarboxylate linkers.*[26]

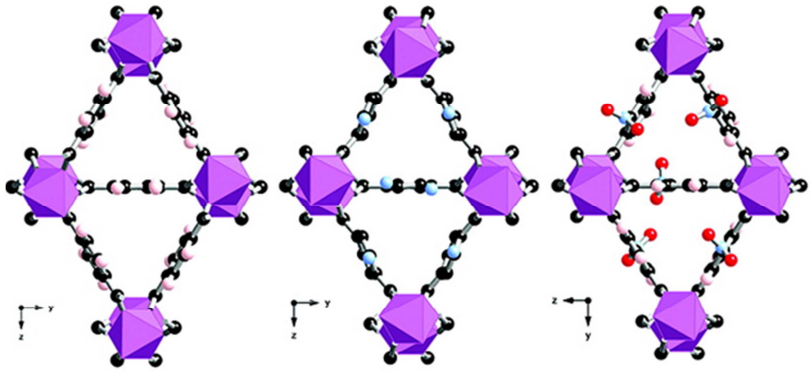

Figure 1.5: *Structures of ScBDC synthesised with (left) benzenedicarboxylate (bdc) compared with (middle) amine and (right) nitro functionalised bdc linker.*[27]

Apart from being potentially active in catalysis, accessible metal sites enhance the interaction of adsorbed gases with the framework and thus can improve its performance in gas separation as well as its ability to retain adsorbed molecules.[43, 44] The properties of a material upon desolvation are crucial to its suitability for application.[45, 46] Sufficiently rigid frameworks will remain stable and show permanent porosity upon solvent removal.[28]

A group of isostructural metal-organic frameworks has been discovered, that contain a high density of open metal sites [M-CPO-27 (M = Mg, Mn, Co, Ni, Zn)].[16, 47, 48] These hybrid materials were prepared by the reaction of metal nitrates or acetates and dihydroxyterephthalic acid under solvothermal conditions. The framework is built up from MO chains separated by the organic linkers forming 1D channels along the *c* axis. It has a honeycomb structure with channels of ~11 Å diameter (Figure 1.6). The large

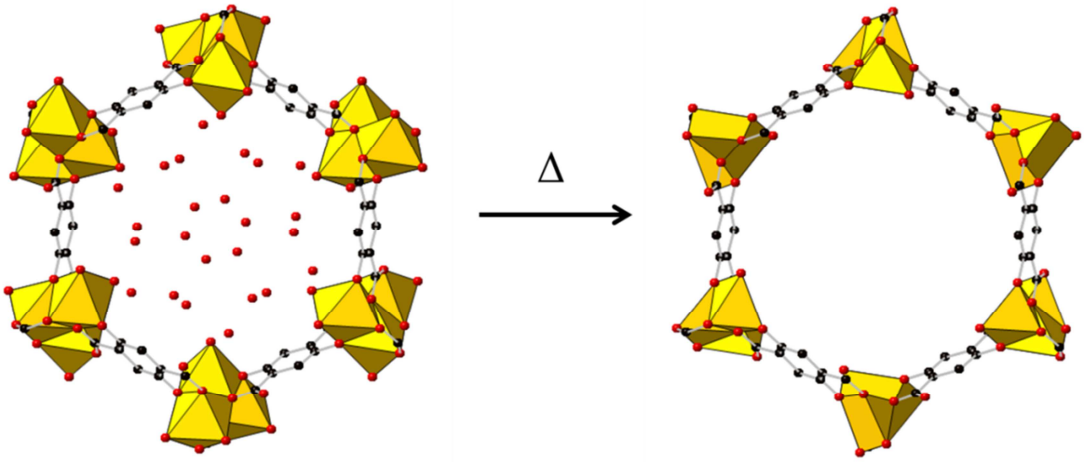

Figure 1.6: *Hydrated (left) and dehydrated (right) CPO-27(Mg) or Mg-MOF-74.*

pores and especially the high adsorption heats of 47 kJ/mol for CO_2 (compared to 17 kJ/mol for N_2) makes it suitable for CO_2 / N_2 gas separation at low carbon dioxide partial pressure, which is typical for flue gas of coal-fired power plants.[49, 50] CO_2 uptakes of up to 6.7 mmol g^{-1} at 0.1 bar and 298 K are reported.[51] A variety of activating procedures are known for the Mg species, which lead to different surface

areas,[16, 52, 53] whereas simple heating to remove metal-bound water and achieve open metal sites tends to result in low porosity. Further work on gaining permanent porosity via framework cation exchange is discussed later in this thesis.[51] During this thesis studies of the water stability of CPO-27 materials revealed the deleterious effect on CO_2 uptake when the solid is exposed to humidity.[54] One way to overcome this problem was demonstrated by Das et al. and Choi et al. with diamine derivatives as carbon dioxide adsorbents grafted on the open metal sites.[55, 56]

Another example of isostructural materials with open metal sites is exemplified with St. Andrews porous materials STA-12(Ni)[57] and STA-16(Co)[58] hosting a honeycomb like topology (Figure 1.7). STA-12(Ni) shows a reversible change from cylindrical to elliptical channels after removal of solvent, as the resulting open metal sides are partially blocked by rotated phosphonate groups. This property is reflected by the CO_2

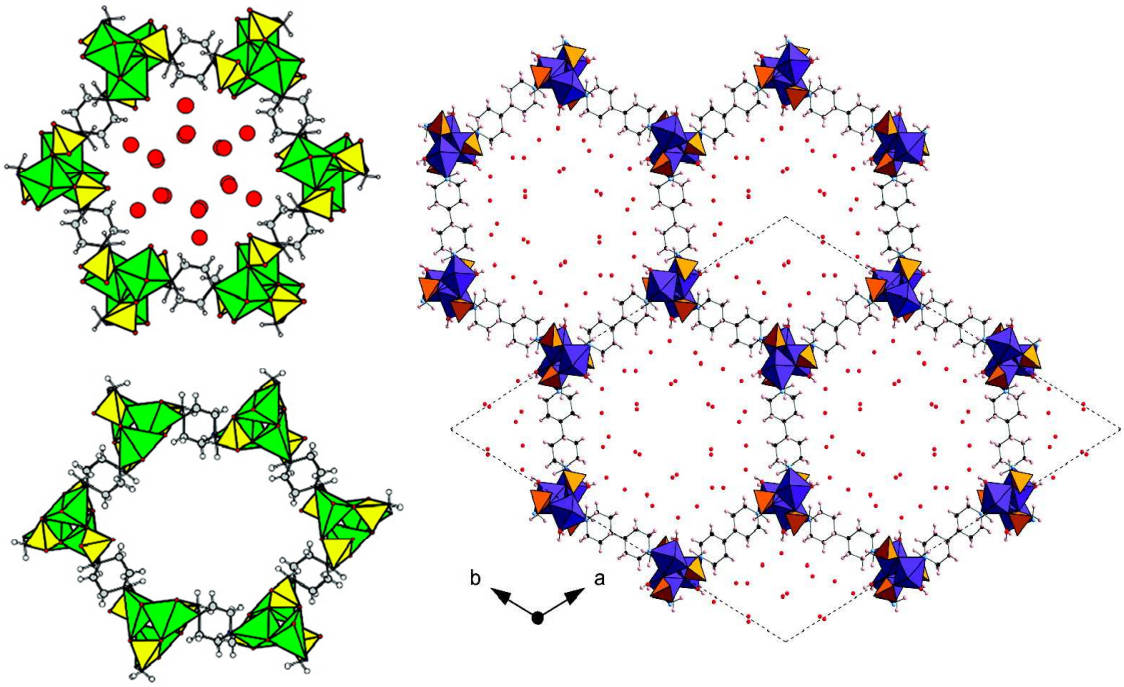

Figure 1.7: *Hydrated (top left) and dehydrated (bottom left) Ni-STA-12 compared to hydrated Co-STA-16 (right).*[57,58]

uptake of 6 mmol/g at higher pressure, but relatively low uptake under flue gas conditions (< 0.5 mmol g^{-1}, 304 K, 0.1 bar). The material consists of bisphosphonate linkers that show a high thermal stability and makes phosphonates competitive with metal carboxylate hybrid materials in applications.[59]

Extended investigations on MOFs with open metal sites have been carried out on the copper 'paddlewheel' MOF, HKUST-1, that exhibits isolated $[Cu_2C_4O_8]•2H_2O$ cages interconnected via tricarboxylate linkers (btc) (Figure 1.8).[42] The framework was rendered crystalline and open metal sites remained accessible after desolvation and so it has attracted interest in catalysis[60] and gas separation, making the material a promising candidate for carbon capture from flue gas.[61, 62]

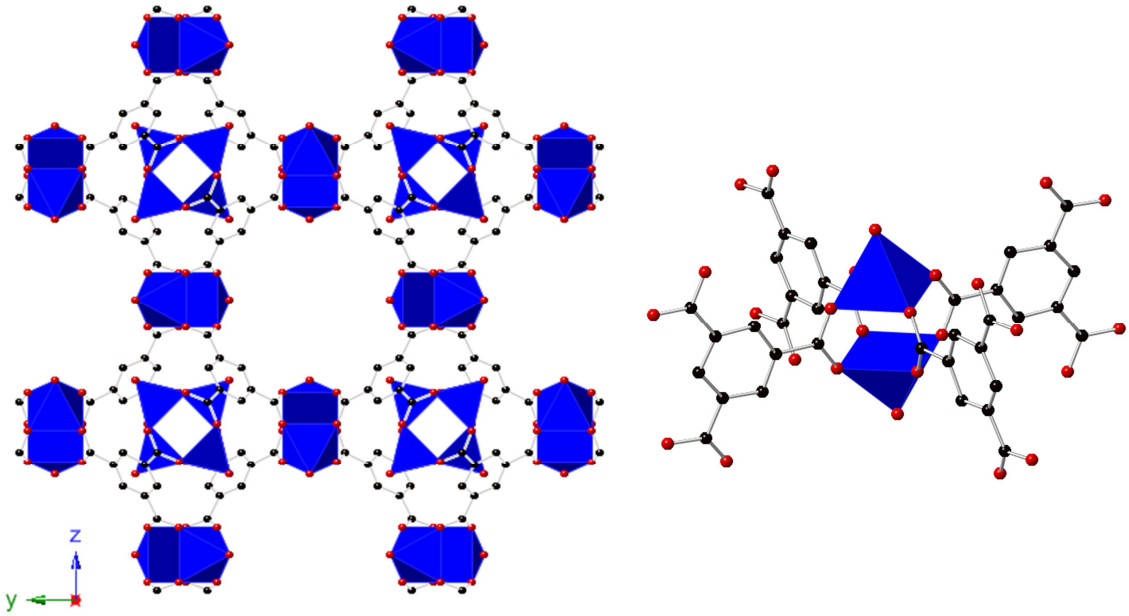

Figure 1.8: *HKUST-1, showing (left) clusters interconnected by btc linkers and (right) the coordination environment of a single cluster. Cu (blue), C (black), O (red), H not shown.*[60]

Examples of rigid porous materials with mesoporous cavities and microporous windows are given by MIL-100[63] and MIL-101.[64] These materials consist of Cr_3O (also Fe_3O, Sc_3O) trimer nodes interconnected by trimesates (MIL-100) or terephthalate ligands (MIL-101), to form supertetrahedra, which leads to the assembly of cages with different sized pores and pore windows. In contrast to CPO and STA materials these structures show spherical cavities connected in three dimensions to other spherical cavities (Figure 1.9). The activation of the MIL-101 cages requires an unusual procedure to remove trapped terephthalic acid molecules from its pores. To make the open space accessible for adsorption application the material must be treated in hot ethanol for several hours

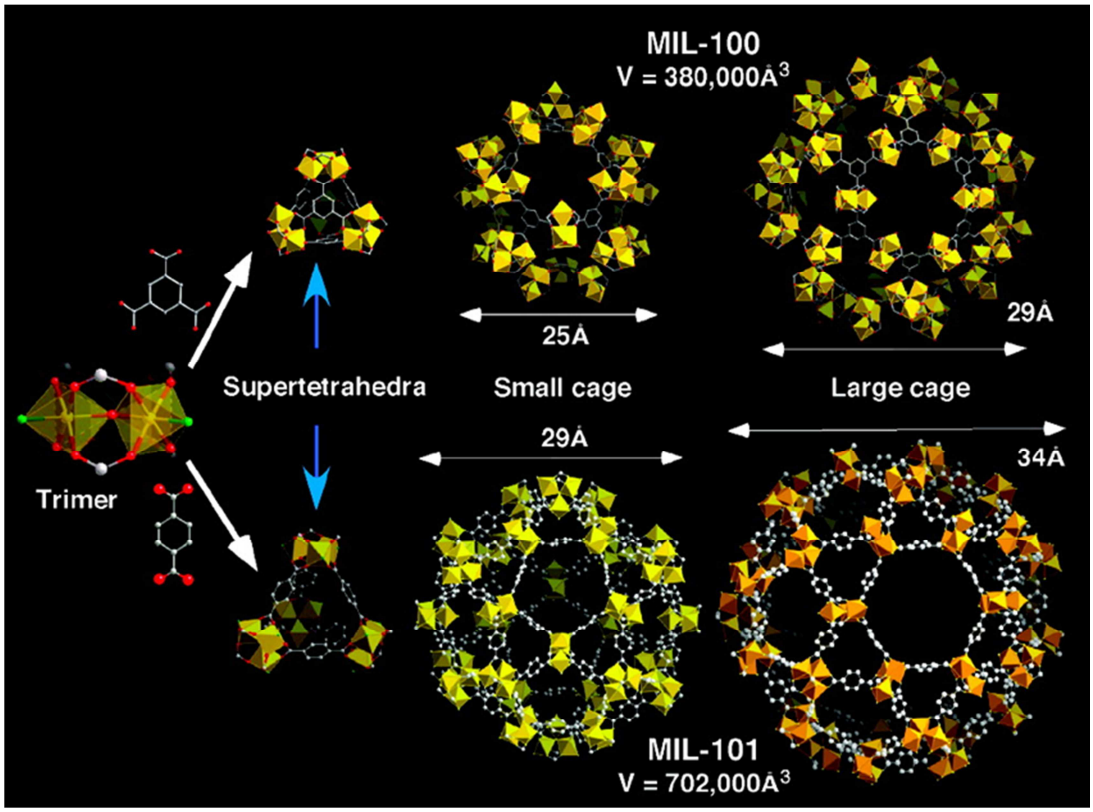

Figure 1.9: *Crystal structure of MIL-100 and MIL-101. (Left) Trimer of Cr octahedra and linkers (1,3,5-BTC for MIL-100 and 1,4BDC for MIL-101). (Middle) Hybrid supertetrahedra. (Right) Cages of MIL materials.*[64,65]

followed by aqueous ammonium fluoride treatment and washing in hot water. For the MIL-100 material no significant activation is required. Despite open metal sites, both materials show a high CO_2 uptake at high pressure, but a low adsorption at low

pressure, making them attractive for high pressure applications, rather than for CO_2 adsorption from flue gas.[64]

Next to rigid frameworks, structures of other materials with different behaviour on solvent removal have been studied, for example, exceptionally large breathing[65, 66] or more complex single-crystal-to-single-crystal transformations.[67, 68]

Serre et al presented MIL-53, a porous material with very significant breathing behaviour. The hybrid solid consists of $MO_4(OH)_2$ SBU ($M = Cr^{3+}$) (Secondary Building Units) connected by dicarboxylate groups.[65] Heating of the as-prepared MIL-53as(Cr) yields the *large pore* MIL-53lp(Cr) or MIL-53ht(Cr) (high temperature). Due to hydration, this latter gives at room temperature the *narrow pore* structure MIL-53np(Cr) or MIL-53lt(Cr) (low temperature), as shown in Figure 1.10. MIL-53(Cr) shows an unusual behaviour for the adsorption of CO_2 and CH_4. Compared to other nanoporous materials a step at 6 bar in the adsorption isotherm can be seen, which is

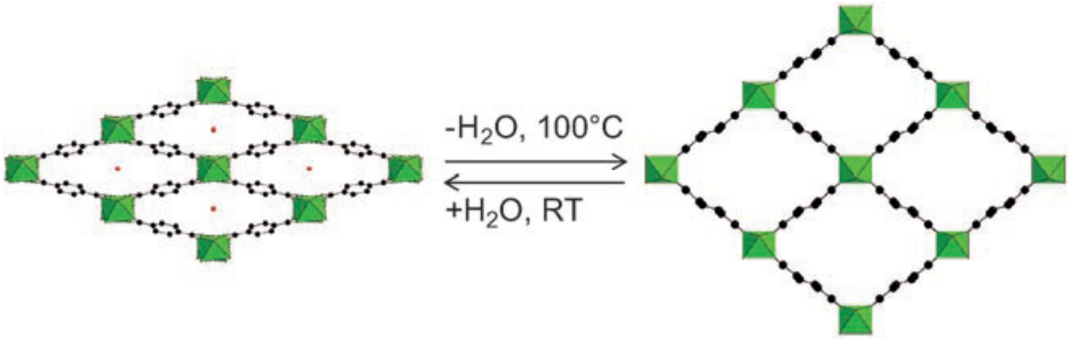

Figure 1.10: *Hydrated MIL-53lt (left) and Dehydrated MIL-53ht (right).*[65]

probably related to a structural change or different adsorption mechanism.[69] The breathing phenomenon is associated with a structural transition between two states separated by energy barriers higher than the thermal vibration energy.[18] More complex breathing behaviour was shown for the iron analogue describing a *very narrow pore*

(vnp) and *intermediate* (int) structure.[70, 71] The scandium species can also be obtained in a nonporous *closed pore* (cp) form.[72, 73] A comparison of various MIL-53 structures is presented in Figure 1.11. Investigations on the structural response of MIL-53(Sc) to CO_2 and temperature variations were elucidated by Chen el al in a combined computational and in situ gas adsorption PXRD study resulting in the accurate prediction of these structures.[74]

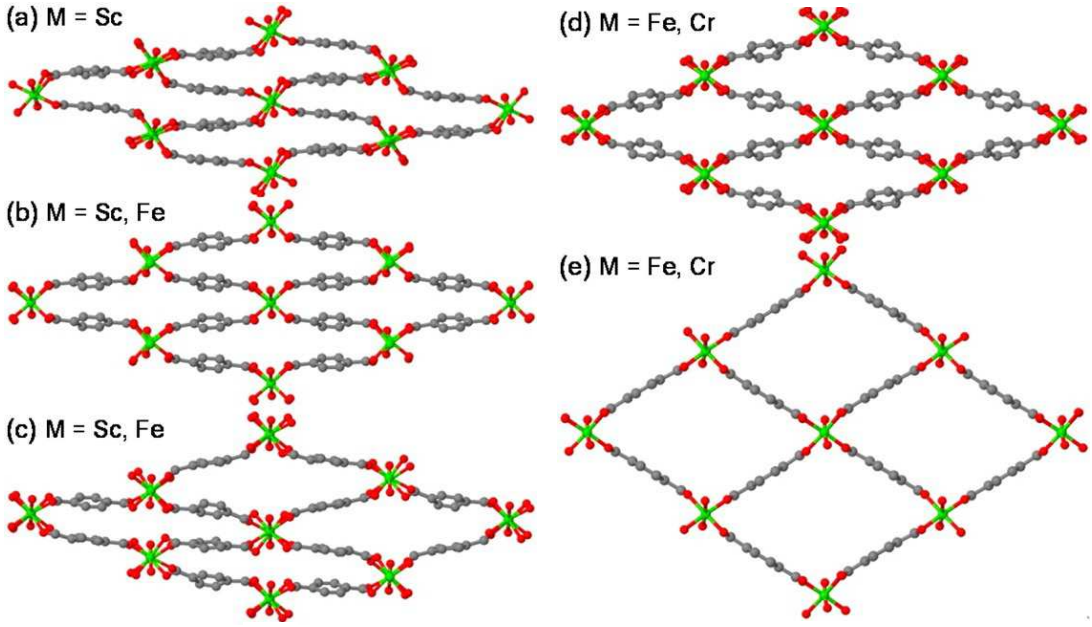

Figure 1.11: *Illustrates the structural complexity of MIL-53 structures. (a) cp; (b) vnp; (c) int; (d) np; and (e) lp. Color code: grey, carbon; red, oxygen; green, metal. Reprinted with the permission of the American chemical society.* [74]

A comparison of MOFs tested for low pressure carbon capture from flue gas is presented in Figure 1.12 where materials with a high concentration of open metal sites show the most promising performance.[62]

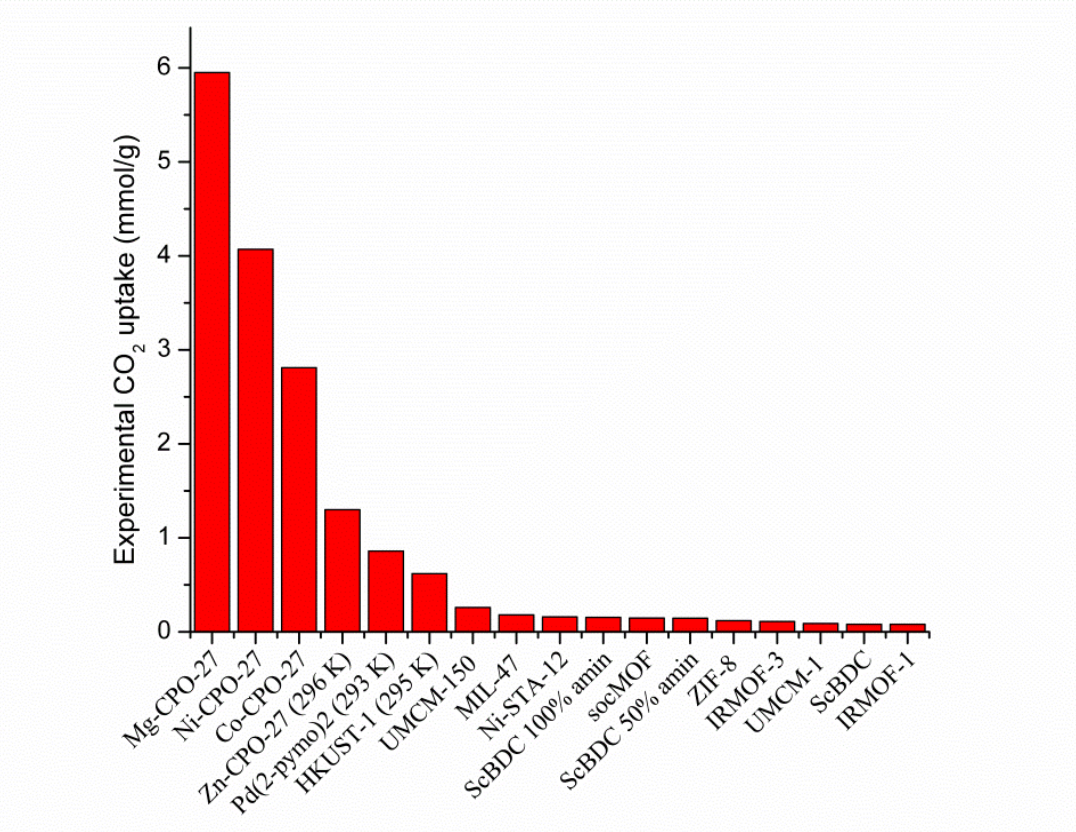

Figure 1.12: *Comparison of MOFs tested for carbon capture under flue gas conditions (0.1 bar CO_2 pressure at 298 K).[62] Ni-STA-12 and ScBDC materials were produced by co-workers in this group.[27,57]*

During this thesis the number of publications referring to metal organic frameworks as adsorbents with respect to the carbon dioxide uptake constantly increased. It is noteworthy that not all studies focused on measurements that meet the standards required in carbon capture from flue gas streams with usually low partial CO_2 pressure (0.1 bar) at gas stream temperatures of around 298 K (Figure 1.13).

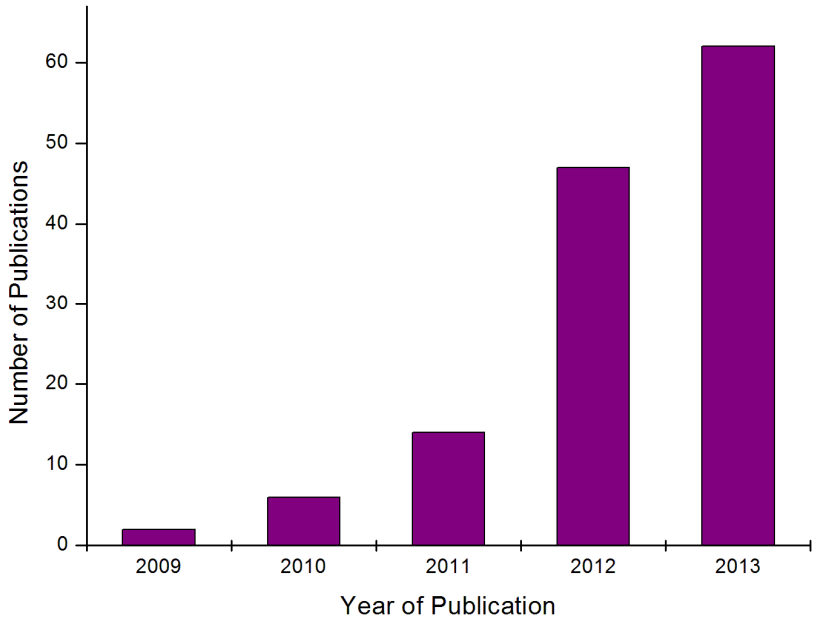

Figure 1.13: *Number of publication referring to studies on MOFs for carbon dioxide adsorptions.[Scifinder®]*

1.2.1 Mixed linker MOFs

In order to introduce functionality into MOFs, one route follows a mixed linker approach during synthesis with the aim to create catalytically active sites or functionalities that provide promising materials for gas purification or separation applications.[75]

MOFs isoreticular with MOF-5 (IRMOFs) attracted great attention in mixed linker synthesis and describe an early example of a mixed-component MOFs. They are composed of the octahedral SBU structure type of $ZnO(CO_2)_6$ clusters interconnected via both bdc and NH_2-bdc linkers. The material was shown to exhibit enhanced catalytic

activity and carbon dioxide uptake (room temperature, 35 bar) compared to the single linker bdc framework, MOF-5 (Figure 1.14).[76, 77]

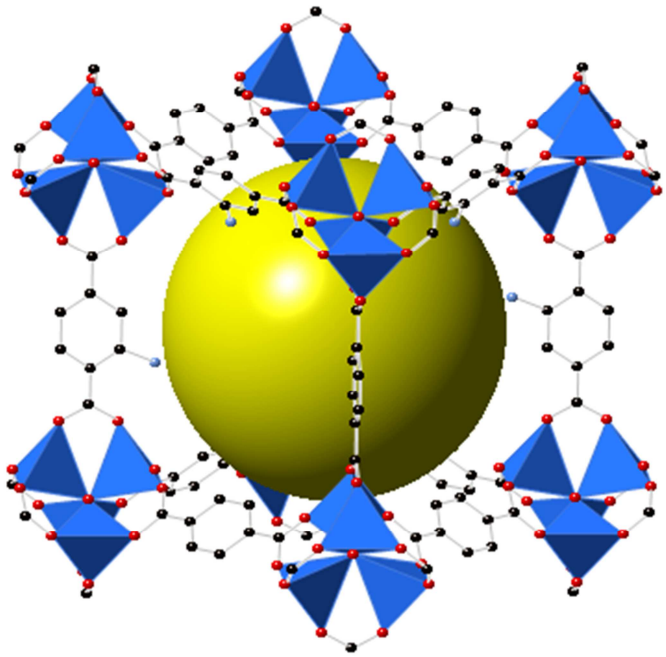

Figure 1.14: *Isoreticular example of IRMOF-3 with partially amine substituted bdc linkers.*

In a combined NMR and computational study Yaghi et al discusses the distribution of functional groups on a series of MTV-MOFs (multivariate MOFs isoreticular with MOF-5) comprising a mixture of bdc linkers with functional groups that differ in size. The investigation revealed that the isoreticular structures exhibit different void spaces and spacial distribution of linkers.[78]

The elongation in an aldehyde and methoxy-functionalised bpdc linker led to an interpenetrated version of MOF-5 with greater linker distance as found in a framework composed of bpdc only. It was also shown that the aldehyde group could be modified into a bulky hydrazone functionalized linker through post-modification despite the interpenetrated framework.[79]

The post-synthetic modification of linkers appears as another method to prepare mixed functionalised porous materials and has been found to be successful in creating MOFs which were not accessible through common solvothermal synthesis.[80]

Wang et al. demonstrated the post-synthetic acylation of amine groups in an IRMOF-3 structure, originally composed only from NH_2-bdc. NMR analysis of the digested material showed a conversion of >80%.[81] Modification of MIL-101-NH_2 with photoswitchable azo-dyes gave materials where reversible switching gave recognizable changes in methane adsorption.[82]

1.3 Zeolitic Imidazolate Frameworks (ZIFs)

ZIFs are a subgroup of microporous Metal Organic Framework MOFs where self-assembly processes of metal cations (Zn^{2+}, Co^{2+}, Cd^{2+}) and imidazolate (Im) linkers with different functionalities form a large diversity of structures with the same types of tetrahedrally-connected topologies that are found in zeolites. Many cases are known where these materials exhibit large pores and high surface areas.[83-85] Their good thermal and chemical stability makes them promising materials for catalysis[86-88], drug delivery[89], sensing, gas purification and separation processes.[90, 91] Their close structural relation to zeolites is based on the similar angle of M-Im-M to the Si-O-Si of about 145° (Figure 1.15).

Structural features in zeolites have therefore also been found in ZIFs, comprising of four membered rings (4mrs), six membered rings (6mrs), double four membered rings (d4mrs), double six membered rings (d6mrs), sodalite or β-cage and α-cage. These secondary building units (SBU) (Figure 1.16) form the basis in constructing almost 30 different net structures with a large number of topologies (SOD, RHO, GME, LTA etc.) that have been published so far (Table 1).[92, 93]

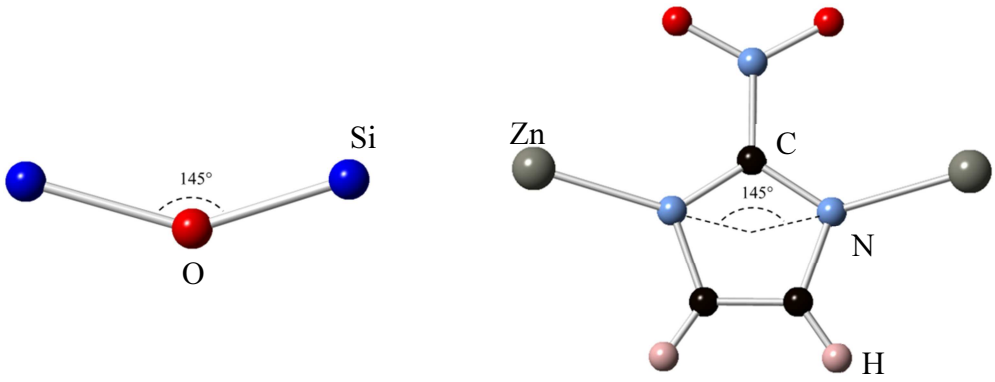

Figure 1.15: *This model illustrates the close structural relation of Zeolites (left) and Zeolitic Imidazolate Frameworks (ZIFs) (right). The angle between Si-O-Si and Zn-Im-Zn is ~145°.*

These distinct topologies are accessible through the careful choice of functionalities available on the imidazolate linkers' C2 and C4/C5 atoms that act to direct the strutures' crystallisation (Figure 1.17). It is noteworthy that bulky substituents utilized on C4/C5 in direct synthesis result in large cages.[92, 94] To give a few examples, the 2-methylimidazole and 2-nitroimidazole linker give ZIF-8 and ZIF-65, respectively. Both ZIFs are built up from β-cages (SOD topology). Adding groups at the C4 and C5 position, for example by using benzimidazole, can either yield a distorted SOD topology as found in ZIF-7 or, by changing the experimental conditions, ZIF-11, which that is built up of α-cages (RHO topology). The purinate linker with pyrimidine

substitution on C4/C5 results in ZIF-20 with the LTA topology consisting of α- and β-cages interconnected by d4mrs.

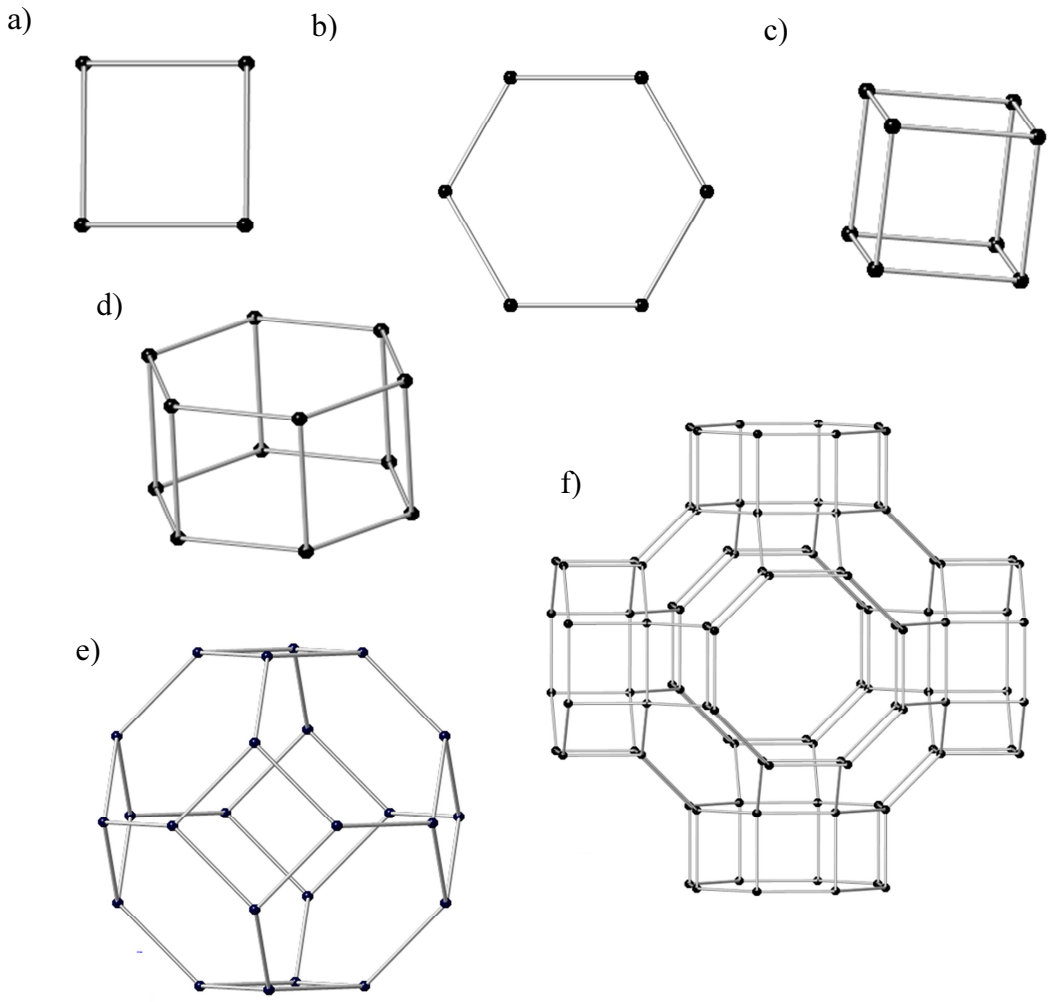

Figure 1.16: *SBU topologies found in ZIFs: a) four membered ring (4mr), b) six membered ring (6mr), c) double four membered ring (d4mr), d) double six membered ring (d6mr), e) sodalite or β-cage and f) the RHO topology (with LTA cage and d8r).*

The large cage RHO topology is also found in a series of structures obtained via isoreticular synthesis (ZIF-25, -71, -93, -96, and -97) built from C4/C5 substituted 4,5-dimethylimidazole, 4,5-dichloroimidazo, 4-methylimidazole-5-carbaldehyde, 4-aminoimidazole-5-carbonitrile and 4-hydroxymethyl-5-methylimidazole, respectively. These materials are synthesized under similar synthetic conditions (Figure 1.18).[94]

Table 1: *Topologies and composition of different zinc imidazolate framework (ZIFs).*[91,92]

ZIF	Topologies	Composition
7	SOD	Zn(benzimidazole)$_2$
8	SOD	Zn(2-methylimidazole)$_2$
11	RHO	Zn(benzimidazole)$_2$
14	ANA	Zn(2-ethylimidazole)$_2$
20	LTA	Zn(purine)$_2$
68	GME	Zn(2-nitroimidazole)(benzimidazole)
74	GIS	Zn(2-nitroimidazole)(5-methylbenzimidazole)
76	LTA	Zn(imidazole)(5-chlorobenzimidazole)
95	POZ	Zn(5-chlorobenzimidazole)$_2$
100	MOZ	Zn(5-chlorobenzimidazole)$_2$

The term isoreticular synthesis describes the preparation of topologically identical materials with different linker functionalities and was introduced by Yaghi in MOF synthesis.[26]

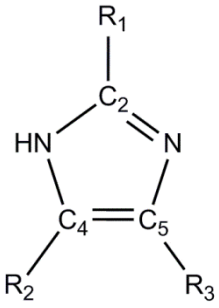

Figure 1.17: *Imidazole linker with substituted carbon atoms in position C2, C4 and C5.*

This approach was also found to be valuable in the mixed linker synthesis of ZIF materials to yield a series of isoreticular structures with hexagonal GME topology that exhibit precisely controlled pore size and functionalities. Subsequent testing for the application as materials for carbon capture showed the greatest uptake of 0.8 mmol g^{-1} for ZIF-78 (which contains 2-nitroimidazole and 6-nitrobenzimidazole linkers). The increased uptake is in agreement with the greater attraction of the polar functional group and the significant quadrupole moment of CO_2. A relation between uptake and pore size could not be found.[90] A typical synthesis is carried by mixing a C2 (NIm) and a C4/C5 functionalised linker together where the former linker is kept the same for each synthesis (Figure 1.19).

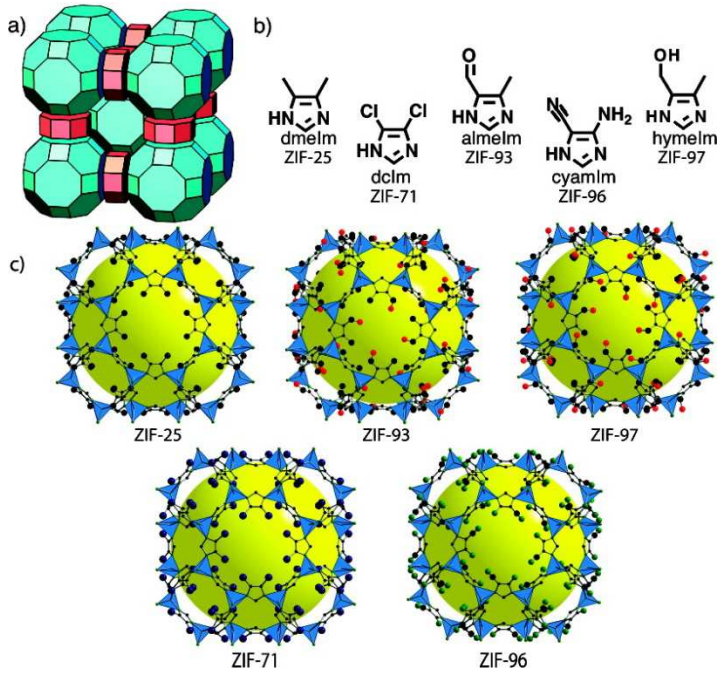

Figure 1.18: *Showing the structures of ZIF-25, -71, -93, -96, and -97 in RHO topology. Reprinted with the permission of the American Chemical Society.*[95]

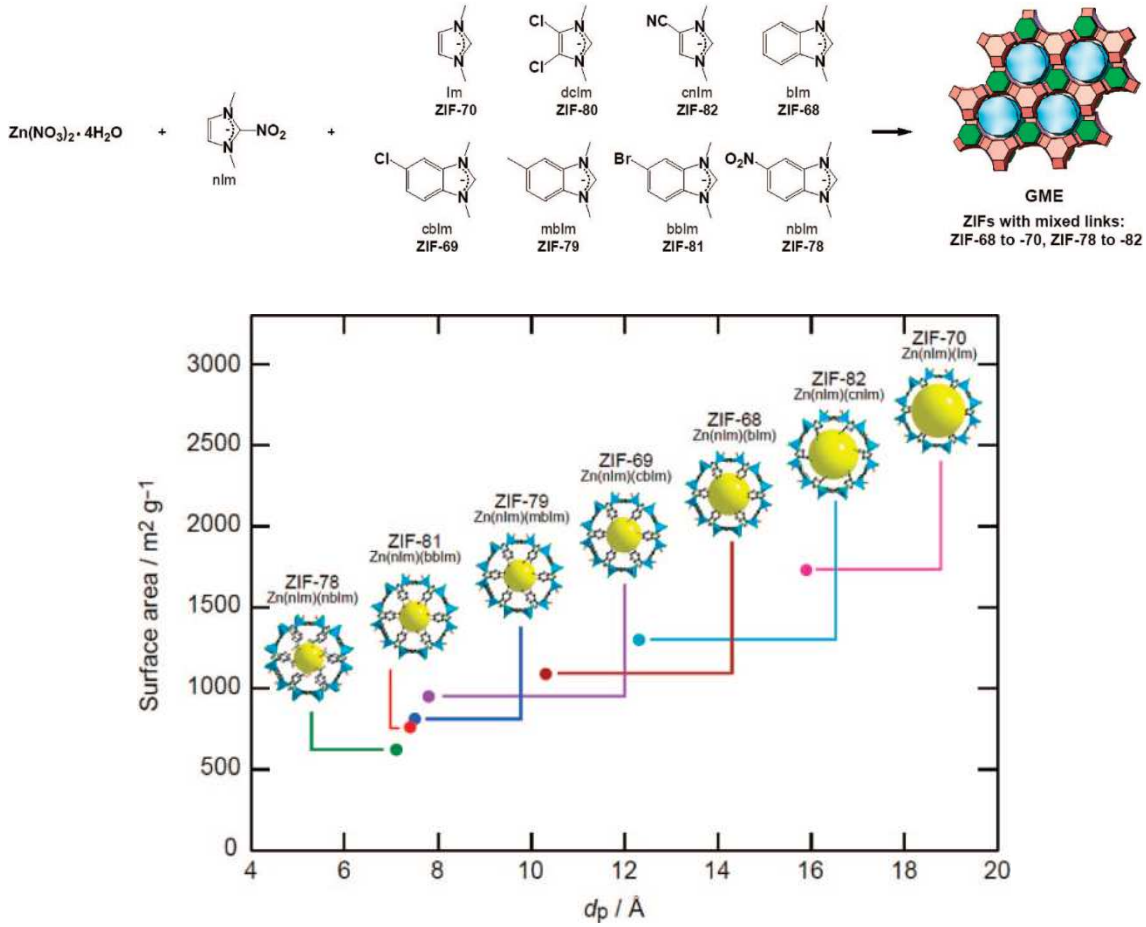

Figure 1.19: *Illustrates the isoreticular synthesis approach with the aim to create a series of topologically identical structures with different functionalised imidazolate linkers. Reprinted with the permission of the American Chemical Society.*[91]

The series was extended in this thesis to include a GME ZIF comprising a mixture of NIm and purine linker by following the same method, and similar studies, using different metal sources were found to give a mixed linker RHO structure with, previously unreported *exo*-zinc and *exo*-NIm moieties and two further materials with framework zinc atoms coordinating to purine N lone pairs (these structures are discussed in chapter 5). Mixed linker species of the LTA topology have been studied with unfunctionalised imidazole linker kept as constant ingredient.[93, 95] A prominent example is ZIF-76, $Zn(Im)_{1.5}(5\text{-ClbIm})_{0.5}$, which was also subject of CO_2 adsorption

studies and was found to take up 0.3 mmol g^{-1} at 0.1 bar and 6 mmol g^{-1} at 10 bar (both at 303 K)[96] which would suggest application in pre-combustion rather than post-combustion carbon capture.

Many ZIFs are discovered with frameworks containing zinc metal nodes with some of them giving the same topology with cobalt, for example ZIF-11 and -12 (RHO), ZIF-20 and -21 (LTA) or the mixed linker framework ZIF-74 and -75 (GIS).[93] These findings were extended by the research of Tian et al who discovered a range of cadmium imidazolate frameworks (CdIFs).[97, 98]

Computational work was carried out on ZIFs that have been successfully synthesized and compared with total energies of ZIFs with hypothetical zeolite topologies. The total energy of simplified structures composed of pure imidazole linkers was calculated with the result that ZIFs prepared with functionalised linkers giving higher energies and are therefore less stable compared with those that can be synthesised from the pure imidazole, suggesting a stabilizing effect of the functional groups. Further, it is expected to provide routes to unknown topologies through a templating effect of appropriately chosen substituted ligands (Figure 1.20).[85]

The impact of the position of substituents in imidazolate linkers on the energy landscape of LiB based ZIFs was investigated by Mellot-Drazniek et al. The findings agree with experimental data where 4-substituded imidazole linker form the RHO topology and substitution at position 2 and 2,4 leads to the SOD topology.[99]

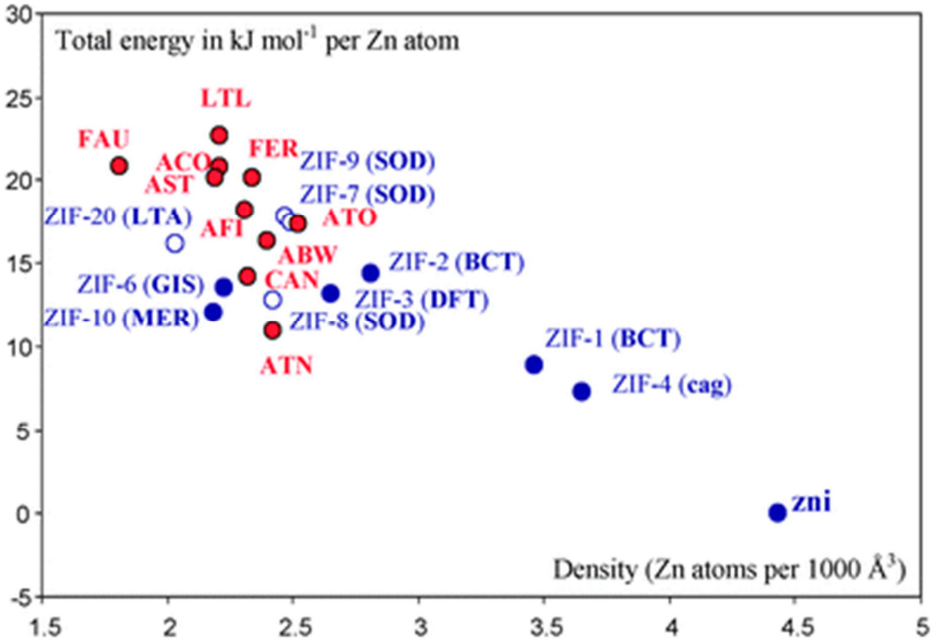

Figure 1.20: *Illustrates the total energy of hypothetical zeolite topologies, as ZIFs (red) compared to known ZIFs (blue). The density is expressed as zinc atoms per unit cell. Full symbols indicate ZIFs with unsubstituted imidazolates and empty symbols are used for structures that are obtained with functionalised linkers. Reprinted with permission of the Royal Society of Chemistry.*[86]

1.4 Aims

The principal aim of this thesis was to investigate porous metal organic frameworks (MOFs) as adsorbents for the use of CO_2 capture from post-combustion (low pressure adsorption) flue gases.

This work focused on the post-synthetic modification of magnesium, nickel and cobalt forms of CPO-27 (chapter 3) and the synthesis of new zeolitic imidazolate framework (ZIF) materials from mixed linker synthesis (chapter 4,5 and 6).

All materials were characterized using X-ray diffraction techniques, solution phase and solid state NMR techniques, SEM/EDX, XPS, CHN and TGA. The porosity was

examined by nitrogen adsorption at 77 K and carbon dioxide adsorption at 198 K and 298 K through gravimetric and volumetric adsorption techniques.

1.5 References

1. J. Gibbins and H. Chalmers, *Energy Policy*, 2008, **36**, 501-507.

2. E. J. Granite and H. W. Pennline, *Ind. Eng. Chem. Res.*, 2002, **41**, 5470-5476.

3. C. E. Powell and G. G. Qiao, *J. Membrane Sci.*, 2006 **279**, 1-49.

4. C. o. E. Engineering and Public Policy Department, Carnegie Mellon University 2008.

5. *Energy Policy Act*, 2005.

6. C. Ploetz, *Technology Guide*, 2009, 416-419.

7. R. Steeneveldt, B. Berger and T. A. Torp, *Chem. Eng. Res. Des.*, 2006, **84**, 739-763.

8. M. C. Duke, B. Ladewig, S. Smart, V. Rudolph and J. C. D. da Costa, *Front. Chem. Eng. China*, 2010, **4**, 184-195.

9. J. D. Figueroa, T. Fout, S. Plasynski, H. McIlvried and R. D. Srivastava, *Int. J. Greenh. Gas Con.*, 2008, **2**, 9-20.

10. H. Yang, Z. Xu, M. Fan, R. Gupta, R. B. Slimane, A. E. Bland and I. Wright, *J. Environ. Sci.*, 2008, **20**, 14-27.

11. N. A. Ramsahye, G. Maurin, P. L. Llewellyn, T. Loiseau and G. Férey, *Phys. Chem. Chem. Phys.*, 2007, 1059-1063.

12. D. M. Ruthven, F. Shamasuzzaman and K. S. Knaebel, *VCH Publishers, New York*, 1994.

13. K. Sumida, D. L. Rogow, J. A. Mason, T. M. McDonald, E. D. Bloch, Z. R. Herm, T.-H. Bae and J. R. Long, *Chem. Rev.*, 2011, **112**, 724-781.

14. D. Britt, H. Furukawa, B. Wang, T. G. Glover and O. M. Yaghi, *Proc. Natl. Acad. Sci. U.S.A.*, 2009, **106**, 20637-20640.

15. J.-R. Li, R. J. Kuppler and H.-C. Zhou, *Chem. Soc. Rev.*, 2009, **38**, 1477-1504.

16. P. D. C. Dietzel, V. Besikiotis and R. Blom, *J. Mater. Chem.*, 2009, 7362-7370.

17. A. Vimont, A. Travert, P. Bazin, J.-C. Lavalley, M. Daturi, C. Serre, G. Férey, S. Bourrelly and P. L. Llewellyn, *Chem. Comm.*, 2007, 3291-3293.

18. F. Salles, A. Ghoufi, M. Guillaume, R. G. Bell, C. Mellot-Draznieks and G. Férey, *Angew. Chem. Int. Ed.*, 2008, **47**, 8487-8491.

19. G. Férey, *Chem. Soc. Rev.*, 2008, **37**, 191 - 214.

20. S. Kitagawa and K. Uemura, *Chem. Soc. Rev.* , 2005, 109 - 119.

21. Y.-S. Bae, O. K. Farha, J. T. Hupp and R. Q. Snurr, *J. Mater. Chem.*, 2009, **19**, 2131-2134.

22. Y.-F. Song and L. Cronin, *Angew. Chem. Int. Edit.*, 2008, **47**, 4635-4637.

23. A. M. Shultz, A. A. Sarjeant, O. K. Farha, J. T. Hupp and S. T. Nguyen, *J. Am. Chem. Soc.*, 2011, **133**, 13252-13255.

24. B. Li, Y. Zhang, D. Ma, L. Li, G. Li, G. Li, Z. Shi and S. Feng, *Chem. Commun.*, 2012, **48**, 6151-6153.

25. O. M. Yaghi, M. O'Keeffe, N. W. Ockwig, H. K. Chae, M. Eddaoudi and J. Kim, *Nature*, 2003, **423**, 705.

26. M. Eddaoudi, J. Kim, N. Rosi, D. Vodak, J. Wachter, M. O'Keeffe and O. M. Yaghi, *Science*, 2002, **295**, 469-472.

27. J. P. S. Mowat, S. R. Miller, J. M. Griffin, V. R. Seymour, S. E. Ashbrook, S. P. Thompson, D. Fairen-Jimenez, A.-M. Banu, T. Düren and P. A. Wright, *Inorg. Chem.*, 2011, **50**, 10844-10858.

28. P. D. C. Dietzel, R. E. Johnsen, R. Blom and H. Fjellvag, *Chem. Eur. J.*, 2008, **8**, 2389-2397.

29. S. L. James, *Chem. Soc. Rev.* , 2003, **32**, 276 -288.

30. C. Janiak, *Dalton Trans.*, 2003, 2781 - 2804.

31. S. Kitagawa, R. Kitaura and S. Noro, *Angew. Chem. Int. Ed.*, 2004, **43**, 2388.

32. X. Feng, J. Zhao, B. Liu, L. Wang, S. Ng, G. Zhang, J. Wang, X. Shi and Y. Liu, *Cryst. Grow. & Des.*, 2010, **10**, 1399-1408.

33. E. Coronado and G. Minguez Espallargas, *Chem. Soc. Rev.*, 2013, **42**, 1525-1539.

34. A. Corma, H. García and F. X. Llabrés i Xamena, *Chem. Rev.*, 2010, **110**, 4606-4655.

35. D. Farrusseng, S. Aguado and C. Pinel, *Angew. Chem. Int. Edit.*, 2009, **48**, 7502-7513.

36. J. Lee, O. K. Farha, J. Roberts, K. A. Scheidt, S. T. Nguyen and J. T. Hupp, *Chem. Soc. Rev.*, 2009, **38**, 1450-1459.

37. F. Ke, Y.-P. Yuan, L.-G. Qiu, Y.-H. Shen, A.-J. Xie, J.-F. Zhu, X.-Y. Tian and L.-D. Zhang, *J. Mater. Chem.*, 2011, **21**, 3843-3848.

38. S. Kitagawa, S. Noro and T. Nakamura, *Chem. Commun.*, 2006, 701 - 707

39. C.-L. Chen, A. M. Goforth, M. D. Smith, C.-Y. Su and H.-C. zur Loye, *Angew. Chem. Int Ed.*, 2005, **117**, 6831-6835.

40. M. P. Suh, Y. E. Cheon and E. Y. Lee, *Wiley-Vch Verlag*, 2007, 4208-4215.

41. J. Jia, X. Lin, A. J. Blake, N. R. Champness, P. Hubberstey, L. Shao, G. Walker, C. Wilson and M. Schroeder, *Inorg. Chem.*, 2006, **45**, 8838-8840.

42. S. S.-Y. Chui, S. M.-F. Lo, J. P. H. Charmant, A. G. Orpen and I. D. Williams, *Science*, 1999, **283**, 1148-1150.

43. J. L. C. Rowsell and O. M. Yaghi, *Wiley-Vch Verlag*, 2005, 4748-4758.

44. P. D. C. Dietzel, B. Panella, M. Hirscher, R. Blom and H. Fjellvag, *Chem. Commun.*, 2006, 959-961.

45. K. Uemura, R. Matsuda and S. Kitagawa, *J. Solid State Chem.*, 2005, **178**, 2420-2429.

46. S. Kitagawa and K. Uemura, *Chem. Soc. Rev.*, 2005, **34**, 109-119.

47. W. Zhou, H. Wu and T. Yildirim, *J. Am. Chem. Soc.*, 2008, **130**, 15268-15269.

48. P. D. C. Dietzel, Y. Morita, R. Blom and H. Fjellvag, *Angew. Chem. Int. Ed.* , 2005, **117**, 6354 -6358.

49. S. R. Caskey, A. G. Wong-Foy and A. J. Matzger, *J. Am. Chem. Soc.*, 2008, **130**, 10870-10871.

50. D. Yu, A. O. Yazaydin, J. R. Lane, P. D. C. Dietzel and R. Q. Snurr, *Chem. Sci.*, 2013, **4**, 3544-3556.

51. J. Kahr, R. E. Morris and P. A. Wright, *CrystEngComm*, 2013, **15**, 9779-9786.

52. S. R. Caskey, A. G. Wong-Foy and A. J. Matzger, *J. Am. Chem. Soc.*, 2008, 10870-10871.

53. A. R. Millward and O. M. Yaghi, *J. Am. Chem. Soc.*, 2005, **127**, 17998-17999.

54. A. C. Kizzie, A. G. Wong-Foy and A. J. Matzger, *Langmuir*, 2011, **27**, 6368-6373.

55. A. Das, P. D. Southon, M. Zhao, C. J. Kepert, A. T. Harris and D. M. D'Alessandro, *Dalton Trans.*, 2012, **41**, 11739-11744.

56. S. Choi, T. Watanabe, T.-H. Bae, D. S. Sholl and C. W. Jones, *J. Phys. Chem. C*, 2012, **3**, 1136-1141.

57. J. A. Groves, S. R. Miller, S. J. Warrender, C. Mellot-Draznieks, P. Lightfoot and P. A. Wright, *Chem. Commun.*, 2006, 3305-3307.

58. M. T. Wharmby, J. P. S. Mowat, S. P. Thompson and P. A. Wright, *J. Am. Chem. Soc.*, 2011, **133**, 1266.

59. S. R. Miller, G. M. Pearce, P. A. Wright, F. Bonino, S. Chavan, S. Bordiga, I. Margiolak, N. Guillou, G. Frey, S. Bourrelly and P. L. Llewellyn, *J. Am. Chem. Soc.*, 2008, **130**, 15967-15981.

60. S. Marx, W. Kleist and A. Baiker, *J. Catal.*, 2011, **281**, 76-87.

61. S. Ye, X. Jiang, L.-W. Ruan, B. Liu, Y.-M. Wang, J.-F. Zhu and L.-G. Qiu, *Micropor. Mesopor. Mat.*, 2013, **179**, 191-197.

62. A. O. Yazaydın, R. Q. Snurr, T.-H. Park, K. Koh, J. Liu, M. D. LeVan, A. I. Benin, P. Jakubczak, M. Lanuza, D. B. Galloway, J. J. Low and R. R. Willis, *J. Am. Chem. Soc.*, 2009, **131**, 18198-18199.

63. G. Férey, C. Serre, C. Mellot-Draznieks, F. Millange, S. Surblé, J. Dutour and I. Margiolaki, *Angew. Chem. Int. Edit.*, 2004, **43**, 6296-6301.

64. P. L. Llewellyn, S. Bourrelly, C. Serre, A. Vimont, M. Daturi, L. Hamon, G. De Weireld, J.-S. Chang, D.-Y. Hong, Y. Kyu Hwang, S. Hwa Jhung and G. Férey, *Langmuir*, 2008, **24**, 7245-7250.

65. C. Serre, F. Millange, C. Thouvenot, M. Nogues, G. Marsolier, D. Louer and G. Férey, *J. Am. Chem. Soc.*, 2002, **124**, 13519-13526.

66. C. Serre, C. Mellot-Draznieks, S. Surble, N. Audebrand, Y. Filinchuk and G. Férey, *Science*, 2007, **315**, 1828-1831.

67. K. Biradha and M. Fujita, *Angew. Chem. Int. Edit.*, 2002, **41**, 3392-3395.

68. K. Biradha, Y. Hongo and M. Fujita, *Angew. Chem. Int. Edit.*, 2002, **41**, 3395-3398.

69. S. Bourrelly, P. L. Llewellyn, C. Serre, F. Millange, T. Loiseau and G. Férey, *J. Am. Chem. Soc.*, 2005, **39**, 13519-13521.

70. F. Millange, N. Guillou, R. I. Walton, J.-M. Greneche, I. Margiolaki and G. Férey, *Chem. Commun.*, 2008, 4732-4734.

71. T. Devic, F. Salles, S. Bourrelly, B. Moulin, G. Maurin, P. Horcajada, C. Serre, A. Vimont, J.-C. Lavalley, H. Leclerc, G. Clet, M. Daturi, P. L. Llewellyn, Y. Filinchuk and G. Férey, *J. Mater. Chem.*, 2012, **22**, 10266-10273.

72. J. P. S. Mowat, V. R. Seymour, J. M. Griffin, S. P. Thompson, A. M. Z. Slawin, D. Fairen-Jimenez, T. Duren, S. E. Ashbrook and P. A. Wright, *Dalton Trans.*, 2012, **41**, 3937-3941.

73. J. P. S. Mowat, S. R. Miller, A. M. Z. Slawin, V. R. Seymour, S. E. Ashbrook and P. A. Wright, *Micropor. Mesopor. Mat.*, 2011, **142**, 322-333.

74. L. Chen, J. P. S. Mowat, D. Fairen-Jimenez, C. A. Morrison, S. P. Thompson, P. A. Wright and T. Düren, *J. Am. Chem. Soc.*, 2013, **135**, 15763-15773.

75. A. D. Burrows, *CrystEngComm*, 2011, **13**, 3623-3642.

76. W. Kleist, F. Jutz, M. Maciejewski and A. Baiker, *Eur. J. Inorg. Chem.*, 2009, **2009**, 3552-3561.

77. K. Koh, A. G. Wong-Foy and A. J. Matzger, *Chem. Commun.*, 2009, 6162-6164.

78. X. Kong, H. Deng, F. Yan, J. Kim, J. A. Swisher, B. Smit, O. M. Yaghi and J. A. Reimer, *Science*, 2013, **341**, 882-885.

79. A. D. Burrows, C. G. Frost, M. F. Mahon and C. Richardson, *Angew. Chem. Int. Edit.*, 2008, **47**, 8482-8486.

80. H. Deng, C. J. Doonan, H. Furukawa, R. B. Ferreira, J. Towne, C. B. Knobler, B. Wang and O. M. Yaghi, *Science*, 2010, **327**, 846-850.

81. Z. Wang and S. M. Cohen, *J. Am. Chem. Soc.*, 2007, **129**, 12368-12369.

82. A. Modrow, D. Zargarani, R. Herges and N. Stock, *Dalton Trans.*, 2012, **41**, 8690-8696.

83. X.-C. Huang, Y.-Y. Lin, J.-P. Zhang and X.-M. Chen, *Angew. Chem. Int. Edit.*, 2006, **45**, 1557-1559.

84. K. S. Park, Z. Ni, A. P. Co, J. Y. Choi, R. Huang, F. J. Uribe-Romo, H. K. Chae, M. O'Keeffe and O. M. Yaghi, *Proc. Natl. Acad. Sci. U.S.A.,* 2006 **103**, 10186-10191.

85. D. W. Lewis, A. R. Ruiz-Salvador, A. Gomez, L. M. Rodriguez-Albelo, F.-X. Coudert, B. Slater, A. K. Cheetham and C. Mellot-Draznieks, *CrystEngComm*, 2009, **11**, 2272-2276.

86. T. T. Dang, Y. Zhu, J. S. Y. Ngiam, S. C. Ghosh, A. Chen and A. M. Seayad, *ACS Catalysis*, 2013, **3**, 1406-1410.

87. O. Karagiaridi, M. B. Lalonde, W. Bury, A. A. Sarjeant, O. K. Farha and J. T. Hupp, *J. Am. Chem. Soc.*, 2012, **134**, 18790-18796.

88. M. Zhu, D. Srinivas, S. Bhogeswararao, P. Ratnasamy and M. A. Carreon, *Catal. Commun.*, 2013, **32**, 36-40.

89. C.-Y. Sun, C. Qin, X.-L. Wang, G.-S. Yang, K.-Z. Shao, Y.-Q. Lan, Z.-M. Su, P. Huang, C.-G. Wang and E.-B. Wang, *Dalton Trans.*, 2012, **41**, 6906-6909.

90. R. Banerjee, H. Furukawa, D. Britt, C. Knobler, M. O'Keeffe and O. M. Yaghi, *J. Am. Chem. Soc.*, 2009, **131**, 3875-3877.

91. Z. Hu and Y. Chen, *Mol. Simulat.*, 2012, **38**, 830-837.

92. B. Wang, A. P. Côté, H. Furukawa, M. O'Keeffe and O. M. Yaghi, *Nature*, 2008, **453**, 207-211.

93. R. Banerjee, A. Phan, B. Wang, C. Knobler, H. Furukawa, M. O'Keeffe and O. M. Yaghi, *Science*, 2008, **319**, 939-943.

94. W. Morris, B. Leung, H. Furukawa, O. K. Yaghi, N. He, H. Hayashi, Y. Houndonougbo, M. Asta, B. B. Laird and O. M. Yaghi, *J. Am. Chem. Soc.*, 2010, **132**, 11006-11008.

95. D. Peralta, G. Chaplais, A. Simon-Masseron, K. Barthelet and G. D. Pirngruber, *Micropor. Mesopor. Mat.*, 2012, **153**, 1-7.

96. J. Pérez-Pellitero, H. Amrouche, F. R. Siperstein, G. Pirngruber, C. Nieto-Draghi, G. Chaplais, A. Simon-Masseron, D. Bazer-Bachi, D. Peralta and N. Bats, *Chem. Eur. J.*, 2010, **16**, 1560-1571.

97. Y.-Q. Tian, S.-Y. Yao, D. Gu, K.-H. Cui, D.-W. Guo, G. Zhang, Z.-X. Chen and D.-Y. Zhao, *Chem. Eur. J.*, 2010, **16**, 1137-1141.

98. Y.-T. Li, S.-Y. Yao, Y. Wang, K.-H. Cui, H.-Q. Li, X. Wang, J.-Q. Zhu, J. Li and Y.-Q. Tian, *CrystEngComm*, 2011, **13**, 3470-3473.

99. R. Galvelis, B. Slater, R. Chaudret, B. Creton, C. Nieto-Draghi and C. Mellot-Draznieks, *CrystEngComm*, 2013, **15**, 9603-9612.

2. Experimental Methods

2.1 Hydrothermal and Solvothermal Synthesis

All materials were produced using hydrothermal or solvothermal synthesis routes. These are methods to grow crystalline material under high temperature and high pressure. Usually in solvothermal synthesis the metal source (oxide or salt) together with the ligand are dissolved or suspended in a non-aqueous solvent placed in a Teflon-lined steel autoclave (Figure 2.1), stirred thoroughly, sealed and heated in an oven. Under hydrothermal conditions water is the solvent. After the reaction the products were filtered, washed (typically with the solvent used in synthesis) and dried at room temperature.

Figure 2.1: *Examples of Teflon-lined steel autoclaves (40 ml) used in solvothermal synthesis experiments in this thesis.*

2.2 Characterisation of Materials

Materials synthesized in this thesis were initially characterised using powder X-ray diffraction techniques. Selected samples were further analysed using TGA, adsorption techniques, SEM/EDX, XPS, IR, CHN and NMR techniques.

2.3 X-ray Crystallography[1-3]

2.3.1 Basic Crystallography

X-ray diffraction is the principal technique for the determination of the atomic structure of crystalline materials. A crystal is a solid consisting of a three dimensional array of atoms, which are arranged in an ordered repeated pattern. The geometrical array of lattice points (identical points in space, see Figure 2.2) of the crystalline material and its translational symmetry can be represented by choosing a repeating unit, the unit cell (see Figure 2.3), which is described by its lattice parameters.

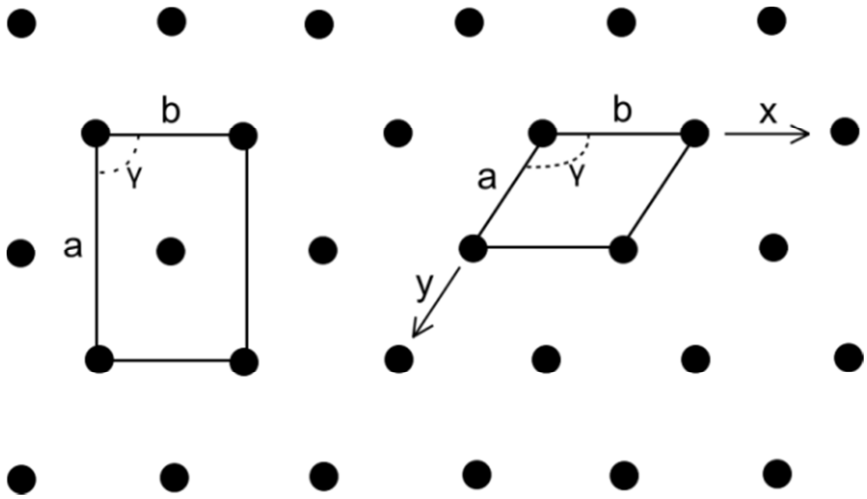

Figure 2.2: *Two dimensional array of lattice points showing different ways to describe the unit cell.*

The unit cell is usually chosen as the smallest repeating unit within a crystal which displays the maximum symmetry, and whose repetition creates the entire crystal. It can be described through the unit cell parameters composed of three edge vectors *a, b* and *c* and the angles between them *α, β* and *γ*. The asymmetric unit is the smallest set of

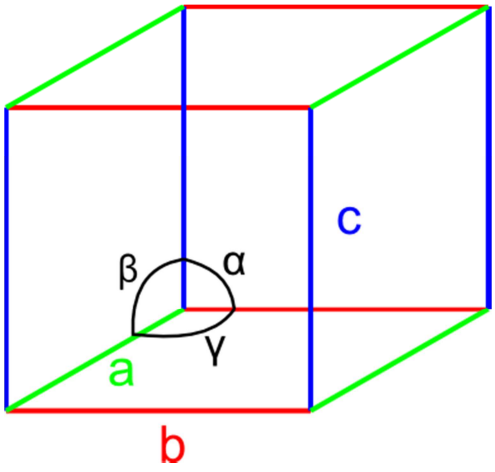

Figure 2.3: *Unit cell with its axes a, b, c and angles α, β, γ.*

atoms necessary to produce the crystal structure operated upon by all its symmetry elements. The atom positions are described as fractional x, y and z coordinates. In three dimensional space there are 7 crystal systems relating to the unit cell dimensions and symmetry: triclinic, monoclinic, orthorhombic, tetragonal, trigonal, hexagonal and cubic, and four lattice centring types: P (primitive) describes lattice points only at the corners of the unit cell, A,B,C (end-centred or base-centred) denotes lattice points at the corners and in the centre of one face of a pair of opposite faces; I (body-centred) describes lattice points at the corners and at the centre of the cell; F (face-centred) is related to lattice points at the corners and the centre of each face. The combination of crystal systems and lattice point centring gives 14 distinguishable Bravais lattices within the crystal systems and was introduced by August Bravais in 1850 (Table 2.1). Other possibilities can be shown to be equivalent to the 14 Bravais lattices.

Table 2.1: *Crystal system with unit cell dimensions and Bravais lattice*

Crystal system	Unit cell dimension	Bravais lattice
Triclinic	$a \neq b \neq c$ / $\alpha \neq \beta \neq \gamma$	P
Monoclinic	$a \neq b \neq c$ / $\alpha = \beta = 90° \neq \gamma$	P,C
Orthorhombic	$a \neq b \neq c$ / $\alpha = \beta = \gamma = 90°$	P, C, I, F
Tetragonal	$a = b \neq c$ / $\alpha = \beta = \gamma = 90°$	P, I
Cubic	$a = b = c$ / $\alpha = \beta = \gamma = 90°$	P, I, F
Trigonal	$a = b = c$ / $\alpha = \beta = \gamma \neq 90°$ $a = b \neq c$ / $\alpha = \beta = 90°$ $\gamma = 120°$	R (rhombohedral) P
Hexagonal	$a = b \neq c$ / $\alpha = \beta = 90°$ $\gamma = 120°$	P

The complete symmetry of a structure is not only described by its lattice, for example the atoms around a lattice point can also be arranged symmetrically. There are 32 point groups defined by the arrangement of mirror planes, rotation axes and inversion axes. The combination of the 32 point groups with the 14 Bravais lattices gives the three dimensional space groups. There are 230 space groups that describe the complete symmetry of all crystalline materials. The space group symmetry elements and their related symbols are summarized in Table 2.2. For example the space group symbol *Im-3m* describes a body-centred (I) cubic unit cell where the entire cell of atoms is generated by applying a mirror plane (*m*) perpendicular to [001], a 3 fold rotary inversion axis (*-3*) along [111] and another mirror plane (*m*) perpendicular to [1-10].

Miller indices are used to characterise planes in lattices and crystals. They describe how the crystal planes intersect with the crystallographic principal axes and are quoted as a set of integers *hkl*, giving the direction but not the position of a plane. For example, when the nearest plane to the origin cuts the x-axis at *a*/2, the y-axis at *b*/3 and the z-axis at *c*/3 then the Miller indices for this plane are (233). Zero indicates the plane is parallel to axis and a negative value represents a plane cutting the axis in the negative direction.

Table 2.2: *Space group symmetry elements and symbols.*

Symmetry elements	Symbols
Inversion (or centre of symmetry)	-1
Mirror plane (or plane of symmetry)	m (= -2)
Glide planes	a, b, c, d, n
Rotation axis (or n-fold rotation)	2, 3, 4, 6
Screw axis	2_1, 3_1, 3_2, 4_1, 4_2, 4_3, 6_1, 6_2, 6_3, 6_4, 6_5
Rotary inversion axis	-3, -4, -6

2.3.2 Introduction to X-ray diffraction

The knowledge of structural information of porous solids forms the basis of gaining insight on materials' properties. Porous solids often exhibit a complex structure with large unit cells, which can make structure determination a complicated task, in particular when dealing with powder diffraction data. Single crystal diffraction is a common technique to identify structures of zeolites and MOFs, but routinely requires single crystals typically > 50 μm in size. Single crystal data gives a complex 3 dimensional output of reflections which, via computational methods gives a powerful tool to directly access the three dimensional arrangement of atoms in a crystal and so is the primary technique in structure determination. In this thesis, single crystal diffraction was used wherever single crystals of sufficient quality were obtained.

For all materials prepared powder X-ray diffraction has been employed as the primary technique to analyse and characterise the produced solid. It was also applied as a

technique for phase identification and to establish the crystallinity of microcrystalline materials. Powder data was used for structural refinement and where possible collected as high resolution data at a synchrotron source

2.3.3 Scattering of X-rays

The concept of X-ray diffraction was first proposed by Max von Laue and developed further by William and Lawrence Bragg. In X-ray diffraction a crystal can be considered as a regular array of lattice planes that acts as a diffraction grating via which X-rays are scattered constructively when the path difference between two incident beams is equal to an integral number of wavelengths, described by the Bragg equation.

$$n\lambda = 2d \sin\theta \quad (1)$$

Constructive interference occurs when the path difference is an integral number of wavelengths.

$$AB + BC = 2d \sin\theta \quad (2)$$

and is further shown in Figure 2.4.

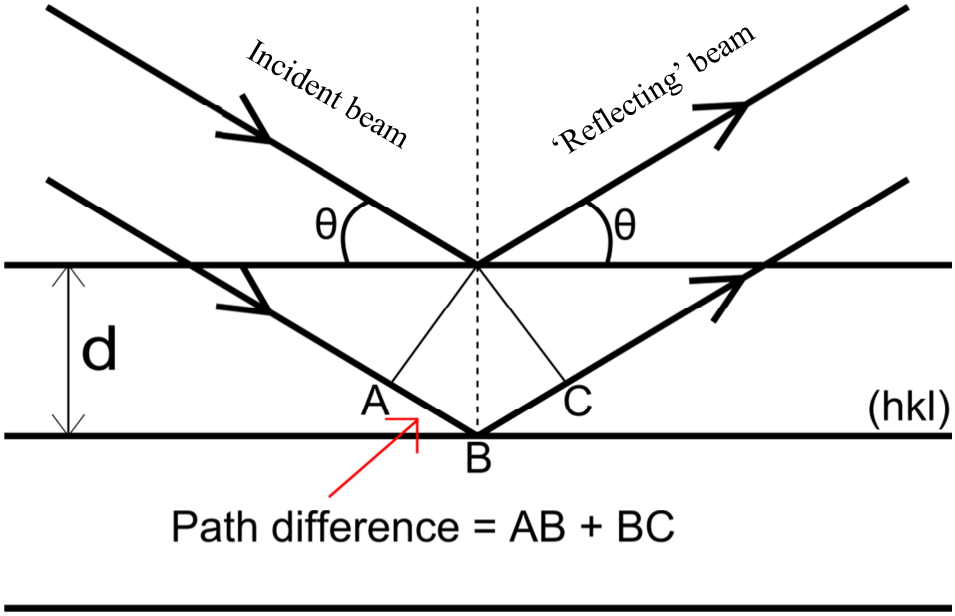

Figure 2.4: *Conditions for Bragg reflection from hkl planes and spacing dhkl.*

X-rays are electromagnetic waves with a wavelength in the range of 0.01 to 10 nanometers. The oscillating nature of the X-ray induces an oscillation in the electron cloud, which then re-emits secondary X-rays with same (or lower) frequency. In general, heavier atoms scatter more strongly than lighter atoms since they have more

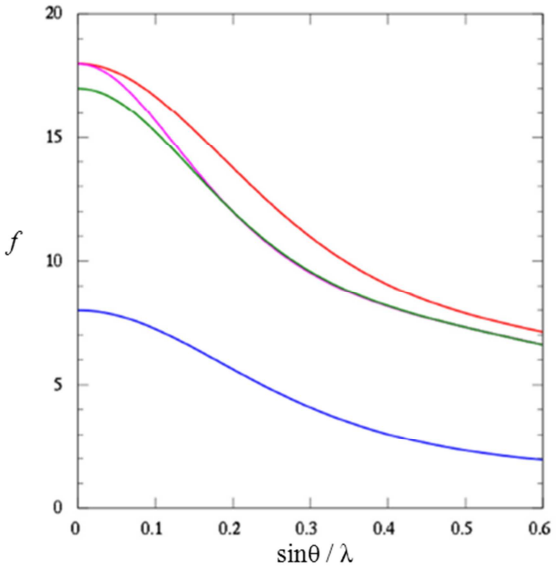

Figure 2.5: *Relationship between the scattering factor f and the term sinθ/λ. 2θ is the scattering angle and λ is the wavelength of the incident X-ray radiation. O (blue), Cl (green), Cl^- (magenta), and K^+ (red).*

electrons. The atomic scattering factor *f* also depends on the scattering angle of the X-rays (Figure 2.5). This derives from the distribution of the electron clouds in space (the displacement factor U).

In single crystal diffraction the sample is mounted on a goniometer, which enables the single crystal to be oriented accurately into the X-ray beam. Rotation of the crystal around 2 different axes enables the positions and intensities of thousands of reflections to be measured on a stationary area detector. Series of two dimensional diffraction patterns are collected using a CCD (charge-coupled device) detector. A schematic diagram is presented in Figure 2.6. The data analysis includes indexing of the collected spots to determine the space group of the crystal.

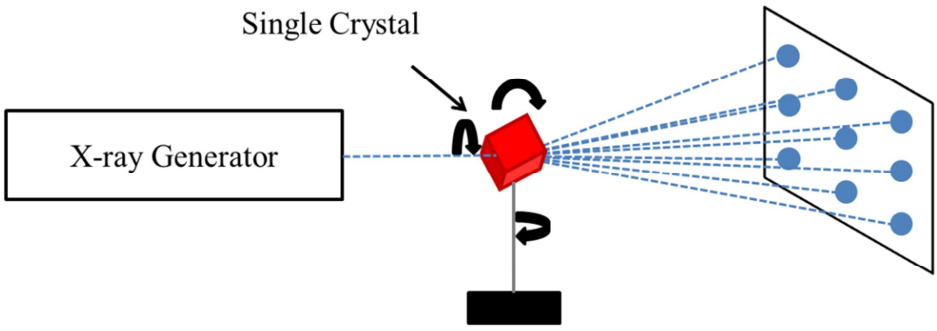

Figure 2.6: *Schematic of single crystal diffraction, showing the rotation of the crystal and the resulting reflections.*

After assigning symmetry to the diffraction pattern the intensity of each spot (I) is reduced to give the structure factor (F) of each reflection.

$$I_{hkl} \alpha |F_{hkl}|^2 \quad (3)$$

The phase of each reflection cannot be calculated directly from diffraction data, because the intensity is proportional to the square of the structure factor, which results in the well known phase problem. Experimental diffraction patterns derive from the scattering of parallel planes (*hkl*) and are dependent on the type and position of atoms in the unit cell (*xyz*).

$$F_{hkl} = \sum f_n \, e^{2\pi i(hx+ky+lz)} \tag{4}$$

where f_n corresponds to the atomic scattering factor for each atom (n).

The scattering is further influenced by thermal vibration, also expressed as a positional disorder of atoms.

$$F_{hkl} = \sum f_n \, e^{2\pi i(hx+ky+lz)} \times e^{\frac{-8\pi^2 U_n sin^2\theta}{\lambda^2}} \tag{5}$$

where U_n is the temperature factor of an atom, a measure of the displacement around a point (*xyz*), and can be isotropic (spherical) or anisotropic (elliptical).

To obtain the structure, the structure factor (F) can be used in a Fourier transformation to obtain the electron density ρ_{xyz} of each point, once the phase of the reflection is known.

$$\rho_{xyz} = \frac{1}{V} \sum |F_{hkl}| e^{-2\pi i(\mathrm{h}x+\mathrm{k}y+\mathrm{l}z)} \tag{6}$$

There are various mathematical methods to overcome the phase problem. The most common technique is known as 'Direct Methods' and was developed by Karle and Hauptman[4]. Direct Methods is a mathematical approach to determine phase data from

diffraction intensities and is based on two assumptions: (i) The structure is composed of discrete atoms and (ii) the electron density must be zero or an integer positive number, but cannot be negative. The method uses the normalized structure factor E_{hkl} and is given by

$$|E_{hkl}|^2 = \frac{|F_{hkl}|^2}{\varepsilon \sum f^2} \tag{7}$$

These assumptions together with the amplitude of the structure factor are the mathematical requirements that may determine the phase. Atomic positions from SXRD data were determined in the SHELX[5] and SIR[6] software suites, both implementing Direct Methods.

The structure solution derived from Direct Methods is then refined, which involves the comparison of observed data with a calculated pattern from the model via a least squares method. The aim is to determine any electron density remaining that is not in the model. The difference between observed (F_{obs}) and calculated (F_{calc}) structural model is expressed by:

$$\Delta\rho(xyz) = \frac{1}{V}\sum(\mathrm{F_{obs}} - \mathrm{F_{calc}}) \cos 2\pi(\mathrm{hx} + \mathrm{ky} + \mathrm{lz}) \tag{8}$$

$$\mathrm{D} = \sum \omega(|\mathrm{F_{obs}}| - |\mathrm{F_{calc}}|)^2 \tag{9}$$

In this thesis the data sets in single crystal diffraction have been collected on a Rigaku Mo MM-007 Saturn 92 diffractometer with Mo K_α radiation (λ = 0.71073 Å) or a Rigaku Cu MM007 HF with a Cu K_α radiation (λ = 1.54051 Å). To determine and refine the atomic positions the SHELX and SIR software has been applied.[5,6]

2.3.4 Powder X-ray diffraction

Where single crystals are not available for a compound, powder X-ray diffraction was used to obtain structural information. Before using powder diffraction the sample was ground to reduce the size of the crystallites. A powder diffraction sample is rotated during collecting data. The result can be assumed as an average of all possible crystal orientations with respect to the incident X-ray beam with all possible orientations of the planes and with some in the correct orientation to fulfil Bragg's law leading to a diffraction pattern that therefore represents an average of reflection points that would be seen for a single crystal producing a series of diffraction cones (Figure 2.7). Grinding

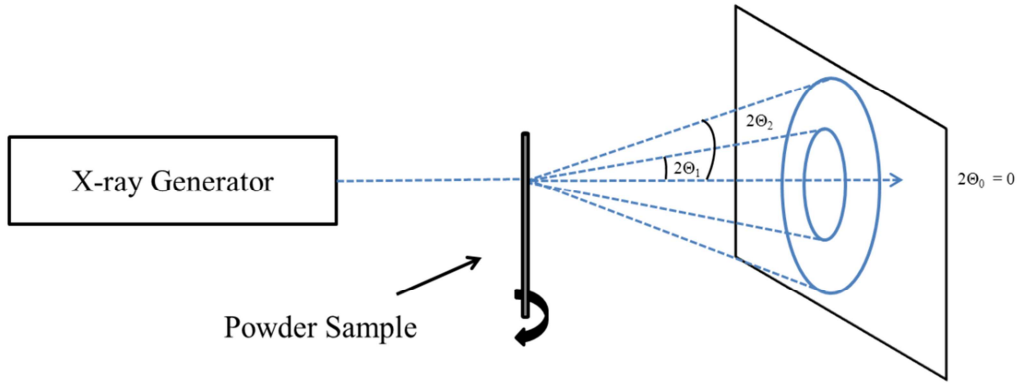

Figure 2.7: *Schematic diagram of a powder diffraction experiment.*

(before measurement) and spinning (during measurement) the sample avoids preferred orientation effects and increases the number of planes (hkl) that fulfil the Bragg conditions. Powder XRD patterns are usually obtained by scanning cones in the radial directions and are presented by plotting the observed intensity (y-axis) versus the angle 2Θ (x-axis) (Figure 2.8).

Powder XRD is an effective technique for initial sample screening or phase identification of MOF materials. The diffraction patterns of crystalline materials can be compared with those of other experimentally-observed patterns or with those of a

computerized database, for example that of the International Centre for Diffraction Data (ICDD). For materials where single crystals have yielded a structural solution, PXRD is used to ensure the bulk structure is that observed by SXRD. As a result of overlap of the diffraction data in the one, 2 Θ dimension, structure determination is difficult, making structure solution from powder data a challenging task.[7]

By indexing the peaks of the observed diffraction pattern, information about the unit cell parameters and lattice system can be gained. The peak position and intensity of each reflection form the input for search algorithms for the indexing process, for

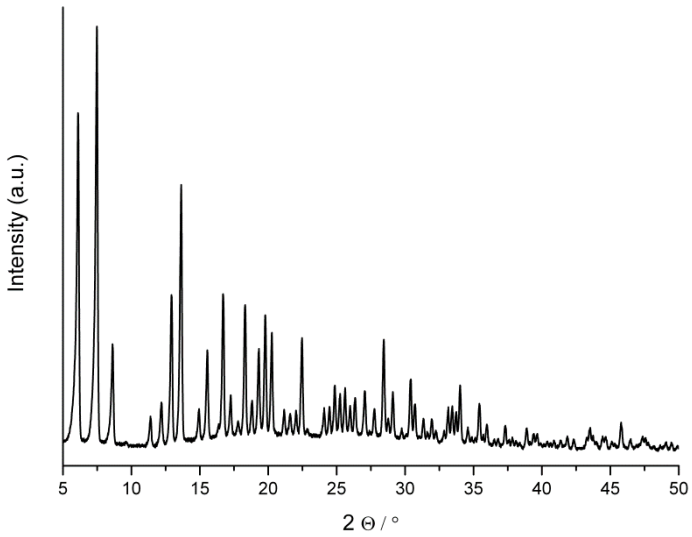

Figure 2.8: *X-ray powder diffraction pattern of as prepared zinc imidazolate with a novel structure collected in St. Andrews with Cu $K_{\alpha 1}$ radiation (λ = 1.54051 Å).*

example DICVOL,[8] TREOR,[9] or ITO.[10] Furthermore, it is possible to determine potential space groups by investigating the systematic absences. There is also software available, such as EXPO[11] or JANA2006,[12] that combine the indexing algorithm with methods for structure determination via direct methods or simulated annealing to suggest a model or partial structure model directly from powder diffraction data.

Synchrotron X-rays may also be used for X-ray diffraction experiments, especially where its high intensity and brilliance is required to give high resolution, high signal-to-

noise powder diffraction patterns or to examine small crystals via single crystal diffraction methods. Synchrotron radiation is generated by accelerating electrons almost to the speed of light and redirecting them by magnets on a circular path, the storage ring. For experiments requiring monochromatic radiation, the wavelength is selected by a monochromator and guided into the experimental station where the light is focused and used for diffraction experiments. Beamline I11 at the Diamond Light Source, located at the Harwell Science and Innovation Campus in Oxfordshire is optimized for high resolution X-ray radiation for powder diffraction experiments.[13] High resolution powder data from dehydrated samples of the CPO-27 materials and novel porous zinc imidazolate structures was collected with short scan times. Furthermore, a gas handling line at the facility enabled the *in situ* dehydration of samples (using hot air up to 550 K) and CO_2 adsorption of up to 30 bar and variable temperatures.

Powder X-ray diffraction data was collected in house on a Stoe STAD i/P diffractometer in capillary mode using Debye-Scherrer geometry with primary monochromation and Cu $K_{\alpha 1}$ (λ = 1.54051 Å) radiation. For samples containing cobalt a Fe $K_{\alpha 1}$ (λ = 1.93604 Å) radiation source was employed to avoid fluorescence. High resolution synchrotron X-ray diffraction data was collected at I11 at the Diamond Light Source (λ = 0.827055 Å) assembled with a Mythen microstrip X-ray detector.

2.3.5 Le Bail and Rietveld method

Screening samples as an initial investigation is not the only information that can be generated from PXRD data. It is also used to refine structural models, taking advantage of the Rietveld refinement technique.[14] This requires a structural starting model that, ideally, is in close agreement with the real structure since it is a refinement technique

rather than a structure solution method. The structural models used for Rietveld refinements in this thesis are based on structures derived from SXRD or altered versions of those found in the literature. In one case a structure was obtained by accessing a computational database and using a modified version of a hypothetical zeolite structure to generate the starting point for the refinement.

Before conducting a structural refinement it is often advisable to apply the Le Bail method[15] first. The Le Bail method is structureless whole-pattern fitting independent of the unit cell content. It is used to determine unit cell and instrumental parameters and to determine the possible fit of the proposed symmetry for the model.

The Rietveld method is a least squares whole-pattern structure refinement technique able to characterize and quantify crystal structures. It minimizes the difference between the experimental diffraction pattern and a calculated pattern and takes overlapping peaks into account.

$$M = \sum w(I_O - I_C)^2 \tag{10}$$

where I_O and I_C are the observed and calculated intensities. The weighting is composed of errors associated with peaks and background. The sum (10) is over the full data set.

The main statistics quantify how well the calculated pattern fits the experimental data and this is expressed by the reduced χ^2, R_p and R_{wp} values.

$$\chi^2 = \frac{M}{(N_{obs} - N_{var})} \tag{11}$$

where N_{obs} is the number of observations in the pattern and N_{var} the number of variables in the least squares refinement with χ^2 is 1 as the optimum value. Other measures of the

difference between observed and calculated pattern are expressed through the calculated residuals, R_p and R_{wp}.

$$R_p = \frac{\Sigma | I_O - I_C |}{\Sigma I_O} \quad (12)$$

and

$$R_{wp} = \sqrt{\frac{M}{\Sigma w I_O^2}} \quad (13)$$

The Le Bail and Rietveld method are combined in the GSAS / EXPGUI software suit.[16, 17] An example of the outcome of a structural Rietveld refinement is presented in Figure 2.9.

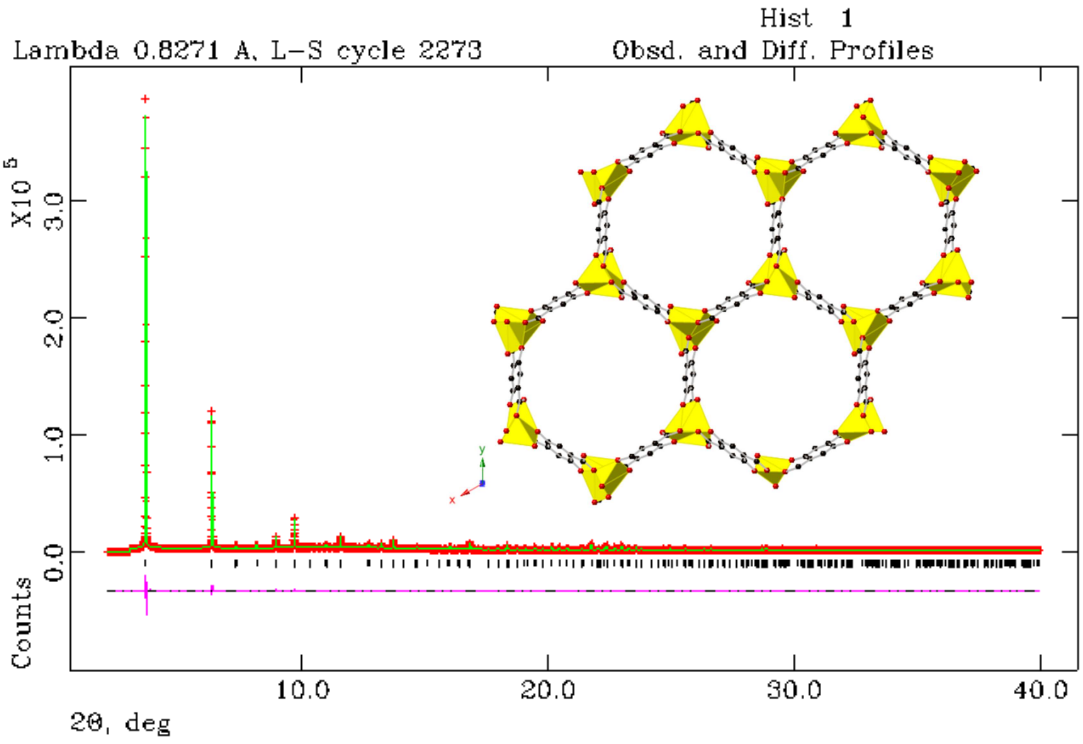

Figure 2.9: *Rietveld plot of the refinement of the structure of 70 mol% Ni-modified CPO-27(Mg), refined composition $Mg_{0.7}Ni_{1.3}$(dotp) against synchrotron X-ray powder diffraction data (λ = 0.827055 Å, Rwp = 0.0326) Observed pattern, red crosses, fitted profile in green, difference curve between observed and calculated pattern in pink.*

2.4 Nuclear Magnetic Resonance Spectroscopy (NMR)[18]

In this thesis solution phase NMR has been used to quantify ligand ratios in mixed linker frameworks via analysis of solution obtained by dissolution of solid samples in acid. Solid state magic angle spinning (MAS) NMR was used as an approach to gather additional structural information in MOF materials. Whereas X-ray diffraction gives insight into the long-range order of crystalline solids, NMR techniques give information on the local environment. Consequently, the combination of XRD techniques and solid state NMR can be valuable in structural investigations.

The NMR 'chemical shift' describes the frequency of absorption of radiation of the nucleus of interest relative to the frequency of absorption of an internal standard and so depends on the local chemical environment of the nucleus.

Solution phase NMR is the predominant characterisation technique in organic synthesis. It also can be of great use when analysing metal organic frameworks comprising of organic linkers. Since solution phase NMR requires liquids, ^{1}H NMR was conducted on digested materials that were treated with acidic solution. It was possible in this way to determine the presence and ratios of different linkers based on the chemical shift of their functional groups and, via the peak intensities, to determine relative abundance (Figure 2.10).

In solid state MAS NMR the sample is spun around the magic angle Θ_m (54.74 °) relative to the direction of the magnetic field. The spinning experiment modifies the shift anisotropy by the factor of $1\text{-}3\cos^2 \Theta_m$ which becomes for the given angle zero and results in isotropic chemical shifts (as in solution phase NMR) and the removal of small residuals of dipolar interactions. At this angle the line broadening is reduced which increases the spectrum resolution. Solid state NMR was measured for ^{13}C and ^{15}N

nuclei at natural abundance in mixed linker ZIFs and gave a qualitative analysis of the presence of certain linkers through their function at groups. Further, peak broadening was used as an indicator for local disorder. This study was performed on the ZIF frameworks prepared for the first time in this thesis as well as for a number of literature-reported ZIFs, in order to assess the structural information available from solid state NMR. The results are given both in the individual chapters and in a final solid state NMR note.

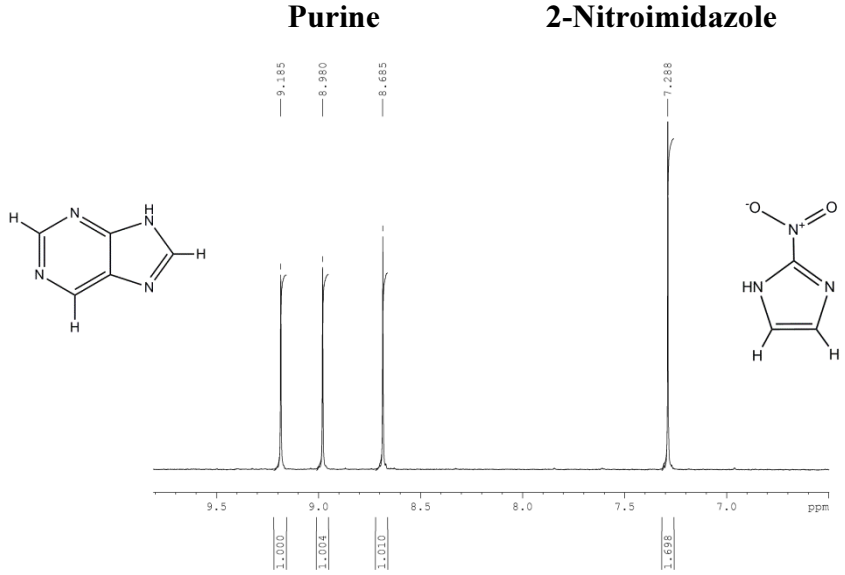

Figure 2.10: *^{1}H NMR of a mixed linker zinc imidazolate after dissolving in acid showing resonances of the linker purine (9.185 – 8.685 ppm) and 2-nitroimidazole (7.288 ppm) present in the original metal organic framework. The structures of purine (left) and 2-nitroimidazole (right) are presented next to their resonances.*

All ^{13}C and ^{15}N CP MAS spectra were acquired using a Bruker ADVANCE III 600 MHz and Bruker ADVANCE III 400 MHz spectrometers equipped with 14.1 T and 9.4 T wide bore magnets, respectively. The operating Larmor frequency was 150.9 MHz for ^{13}C and 600 MHz for ^{1}H. ^{15}N spectra were measured at a Larmor frequency of 40.6 MHz and 400 MHz for ^{1}H. Spectra for both nuclei were acquired using a commercial 4

mm HX probe. Samples were packed into conventional 4 mm ZrO_2 rotors and rotated at a MAS frequency of 12.5 kHz for ^{13}C and 5.0 kHz for ^{15}N nuclei. Chemicals shifts are shown in ppm relative to the primary reference of TMS(l) for ^{13}C spectra, measured using a secondary solid reference of L-alanine methyl with a chemical shift at 20.5 ppm.

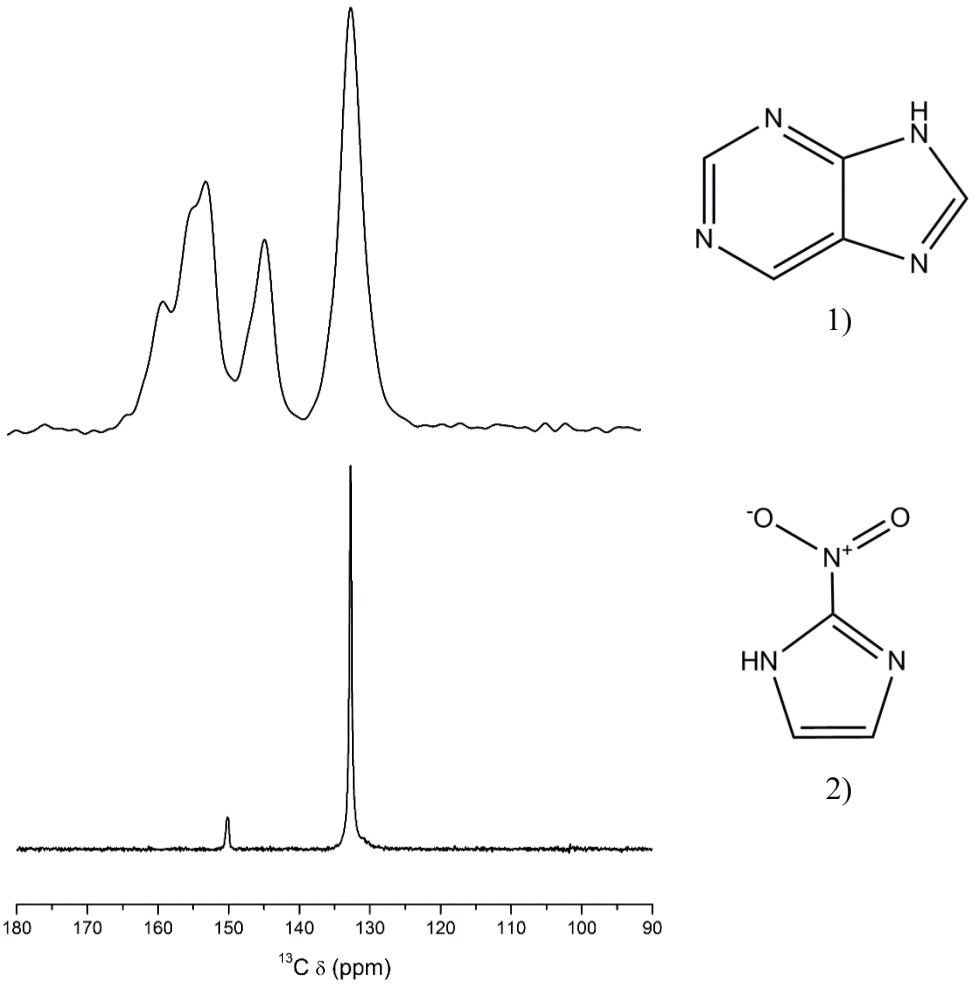

Figure 2.11: *^{13}C solid state MAS NMR spectra of (top) a mixed linker zinc imidazolate comprising of purine (1) and nitroimidazole (2) compared to (bottom) ZIF-65(Zn) that contains only the nitroimidazole linker. Resonances of nitroimidazole for C4 / C5 at 132 ppm and C2 at 150 ppm compared to those of purine (140 -165 ppm) indicate the presence of nitroimidazole in the top spectrum of the top material.*

Chemical shifts in ^{15}N spectra are shown in ppm relative to nitromethane(l) as a primary reference and ^{15}N-enriched glycine as a secondary solid reference with a peak at −347.4 ppm.

2.5 Fourier Transform Infrared Spectroscopy (FTIR)

Fourier Transform Infrared Spectroscopy is a common technique for sample analysis in organic and inorganic chemistry to determine the presence of chemical functional groups. IR spectra may be in MOF characterisation to determine not only organic linker, but also trapped water or hydroxyl groups. An IR spectrometer usually operates in the 400 – 4000 cm^{-1} region (Figure 2.12).

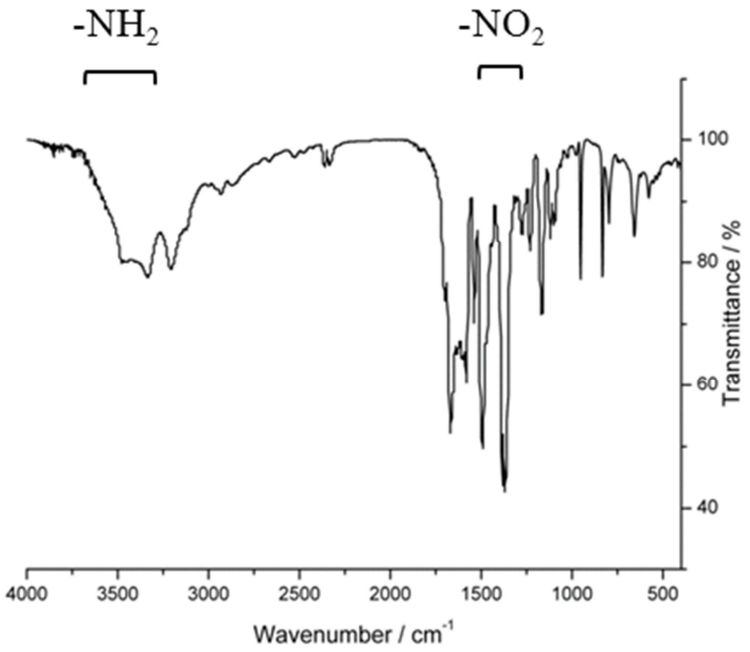

Figure 2.12: *Transmission Fourier Transform Infra-Red spectrum of a mixed linker zinc imidazolate indicating the presence of -NO_2 and -NH_2 functional groups.*

Bonds within molecules vibrate at characteristic energies which are defined by interatomic forces, in much the same as a spring between two vibrating masses.

Typically, frequencies of the IR spectrum match vibration frequencies in molecules. These vibrations are divided in two main categories of motions: Stretching (change of inter atomic bond distances along a bond axis) which can be further divided in to rocking, scissoring, wagging and twisting, and bending (changing the angle between two bonds). Only vibration modes that change the dipole moment of a molecule interact with the incident beam. As a result only these vibrations are IR active.

In a usual IR experiment (Figure 2.13) the beam splitter divides the incoming IR beam in two separate beams where half of the beam penetrates through to the fixed mirror and the rest is reflected to the moving mirror. Both beams reflect back to the beam splitter where they recombine. As one beam traveling on a constant path length is reflected from the fixed mirror and the other is constantly changing, the combined light is the result of two interfering beams, forming an 'interferogram' which is then measured and collected. It contains information about the IR frequencies originating from the infra-red

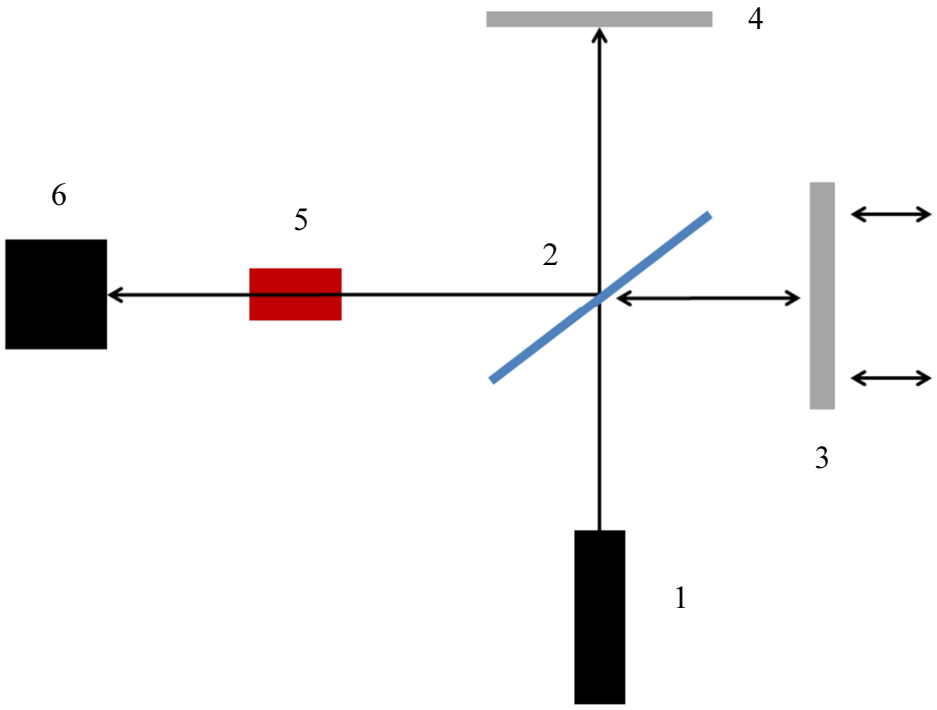

Figure 2.13: *Schematic diagram of basic FTIR system assembled of 1) IR source, 2) beam splitter, 3) moving mirror, 4) fixed mirror, 5) sample and 6) detector.*

sources. The recombined beam is passed to the sample, where frequencies according to IR active vibrations get absorbed and the residual radiation is collected at the detector resulting in an interferogram that contains information about absorption and transmission behaviour of the sample. Since the interferogram contains a length domain, but the analysis requires a frequency domain, a mathematical technique called the Fourier Transformation (FT) is applied.

Usually, a background scan is collected and automatically subtracted. The results are plotted as transmittance (%) versus wave number (cm^{-1}) between 400 and 4000 cm^{-1} creating a transmission FT-IR spectrum. The spectra were collected on a Nicolet Magna 860 esp using KBr pellets.

2.6 Thermogravimetric Analysis (TGA)

Thermogravimetric Analysis is an analytical method to determine weight change related to increased temperature. The analysis is carried out by increasing temperature gradually and heating the sample in inert or oxidizing atmospheres under a constant gas flow. The sample's weight is measured employing a high precision balance, usually a quartz crystal microbalance, in order to weigh samples in milligram range. The powder sample is placed in a crucible made of platinum or alumina. The results are analysed by plotting the weight loss (mg or %) against time or temperature (Figure 2.14).

Thermogravimetric analysis was performed in a constant flow of air at a heating rate of 5 K min^{-1} up to 1073 K, unless otherwise stated, and was collected by using a Netzsch TGA 760 or TGA 1000 using a constant flow of air.

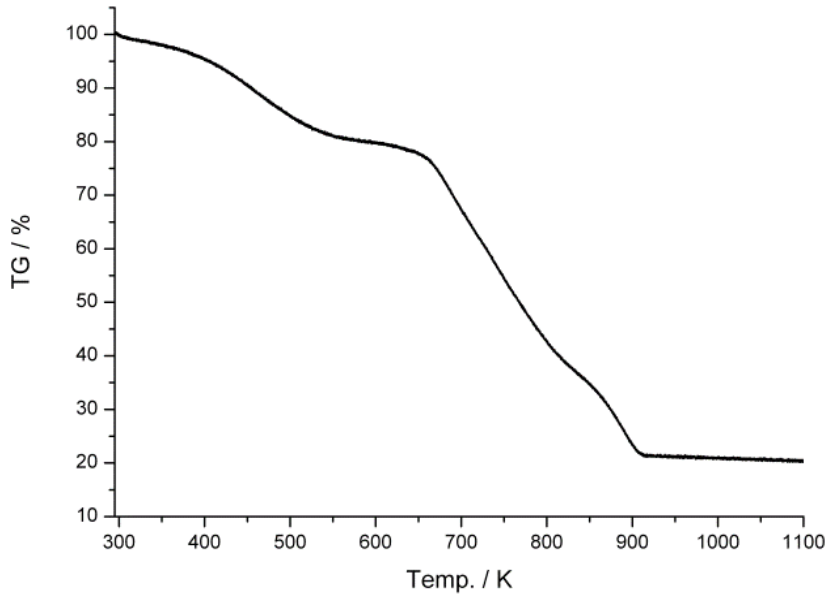

Figure 2.14: *Thermogravimetric analysis plot of an as-prepared mixed linker zinc imidazolate.*

2.7 CHN analysis

Elemental Analysis was carried out to determine chemical composition of the organic component of the prepared materials. For Elemental Analysis (CHN) a CE instruments EA 1110 CHN analyser was consulted to obtain the relative composition of carbon, hydrogen and nitrogen.

2.8 Energy dispersive X-ray spectroscopy (EDX or EDS) and Scanning Electron Microscopy (SEM)[19]

Energy dispersive X-ray spectroscopy (EDX or EDS) uses X-ray emission, where a high energy beam of electrons (0.5-40 keV) interacts with the sample producing

elemental specific X-ray emission (Figure 2.15). To stimulate characteristic X-ray emission, incident electrons (produced in an electron gun) collide with the sample and excite electrons from inner shells to create electron holes. This is filled by another electron from a higher-energy shell, at the same time emitting an X-ray with the energy that corresponds to the energy difference between the two shells. The radiation is measured by an energy dispersive X-ray spectrometer (Figure 2.16). As the energy difference is characteristic for each element this technique enables the elemental composition of the material to be determined.

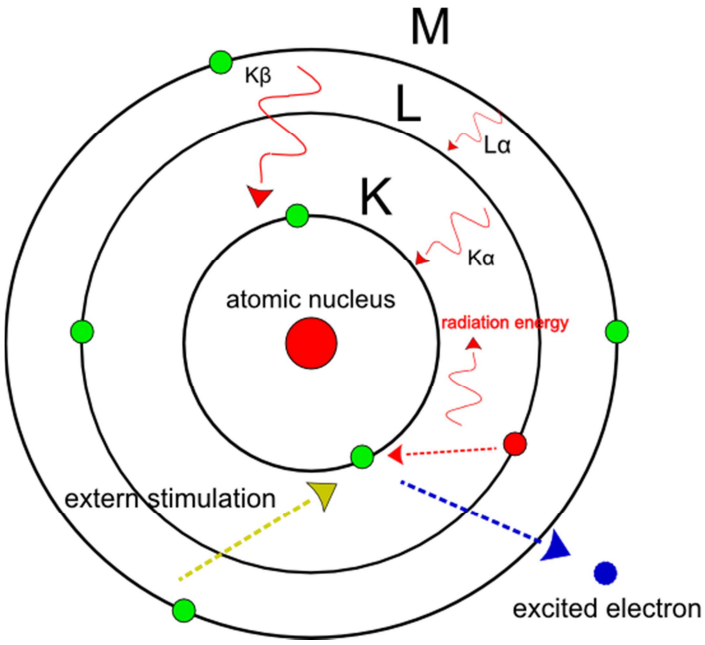

Figure 2.15: *Principle of X-ray source in EDX experiments.*

A typical EDX spectrum is composed of peaks referring to the X-ray emission lines of certain elements. The energy is usually given in keV (kilo electronvolt)) and plotted against the relative intensity. Figure 2.17 shows a spectrum of Ni modified Mg-CPO-27 and its emission lines of Mg, C, O, P and Ni. The emission energies (keV) for magnesium and nickel are given in Table 2.3. Semi-quantitative analysis is possible by calculating the peak area of specific elements and applying appropriate sensitivity factors to give the atomic %.

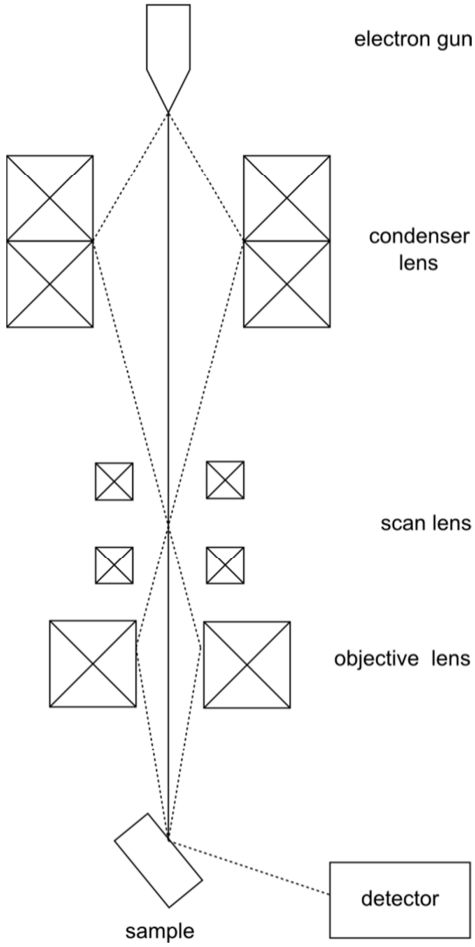

Figure 2.16: *Schematic setup for EDX and SEM.*

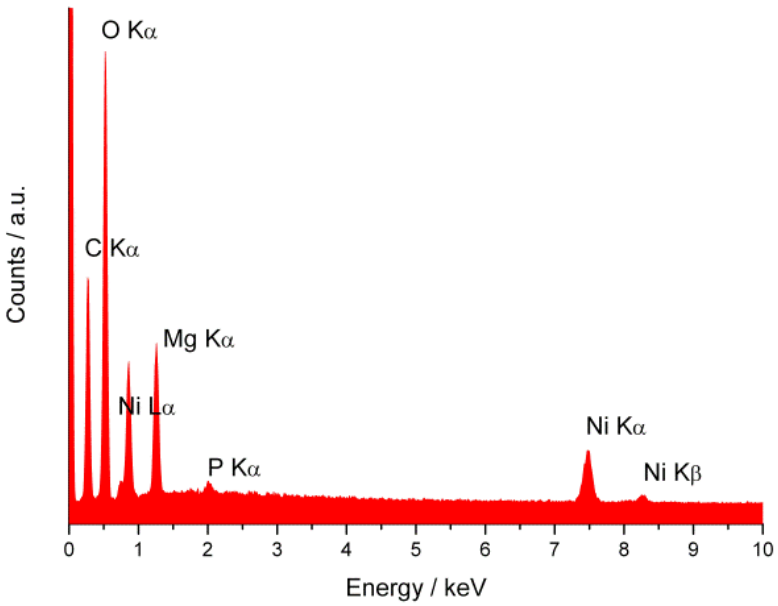

Figure 2.17: *Area selected EDX analysis of CPO-27(Mg) treated with 70% nickel acetate and 10% cpmp showing emission energies of C, O, Ni, Mg and P in keV.*

Table 2.3: *Chosen X-ray emission energies of Mg and Ni given in keV.*[20]

No.	Element	$K\alpha_1$	$K\alpha_2$	$K\beta_1$	$L\alpha_1$	$L\alpha_2$
12	Magnesium	1.25360	1.25360	1.3022		
15	Phosphorus	2.0137	2.0127	2.1391		
28	Nickel	7.47815	7.46089	8.26466	0.8515	0.8515

Selected area analysis by EDX on the same instrument with an Oxford INCA Energy 200 EDX analyser was used to estimate Ni, Mg and, where appropriate, P concentrations, and reported as molar Ni/(Mg+Ni) and P/(Ni+Mg) ratios in the case of CPO-27(Mg) modified by Ni^{2+}. The EDX sampling depth is a few microns under these conditions, so for the small sizes of most of the crystals, this technique will give the approximate bulk composition. The element distribution of Ni, Mg and P in single crystals was visualized via EDX mapping where the electron beam was focused on a single crystal (Figure 2.18).

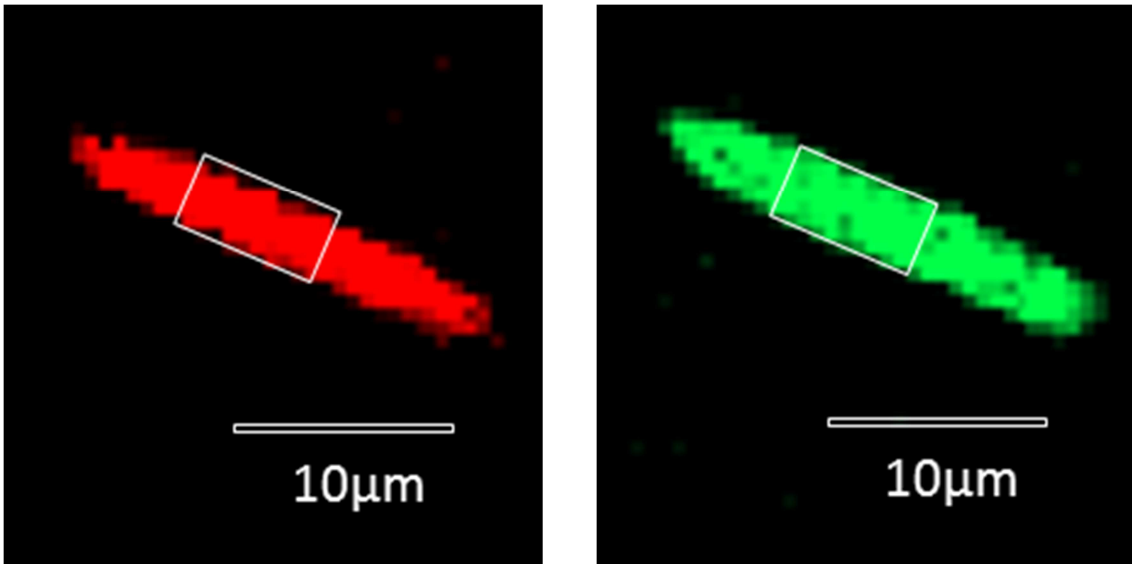

Figure 2.18: *Images obtained from EDX mapping presenting X-ray emissions corresponding to Mg (left) and Ni (right) of nickel modified CPO-27(Mg) indicating the formation of a Ni-rich layer on the crystal surface.*

SEM is a microscopy technique widely used to determine crystal or particle morphologies. High energy electrons (5 - 15 keV) produced by an electron gun interact with the specimen creating electrons in the same fashion as described for EDX. In SEM an electron beam is scanned over the sample, and secondary electrons are detected. Secondary electrons are produced by a primary source (electron beam) exciting electrons from inner shells (Figure 2.15). Imaging in the Electron Microscope is often combined with EDX analysis to permit selected area analysis (see above Figure 2.16). The electrons are detected by a scintillator-photomultiplier. SEM imaging is a powerful tool to obtain information about crystal size and shape as well as impurities or multiple phases (Figure 2.19).

Scanning electron micrographs in this thesis were taken on a JEOL 5600 SEM electron microscope using electrons with energies between 5 and 15 keV.

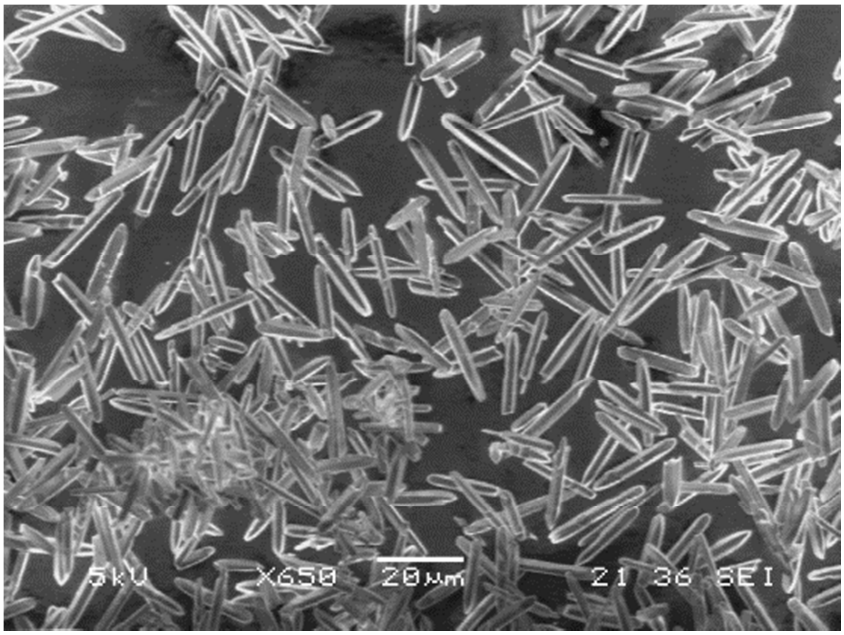

Figure 2.19: *SEM image of unmodified CPO-27(Mg).*

2.9 X-ray photoelectron spectroscopy (XPS)[18, 21]

X-ray photoelectron spectroscopy (XPS) is a surface-sensitive quantitative analytical technique that measures the elemental composition down to the ppm range. It also gives information of the chemical environment and electronic state. An XPS spectrum is collected by irradiating a material with an X-ray beam and measuring the kinetic energy and number of electrons escaping from the surface. The penetration depth is dependent on the irradiation energy and the samples composition and varies between 0 an 10 nm. The measurement requires high vacuum ($P \sim 10^{-8}$ millibar) or ultra-high vacuum (UHV; $P < 10^{-9}$ millibar) conditions because electrons interact strongly with atoms.

To measure the surface composition of selected samples (and so to determine how the surface composition differs from that of the bulk), XPS analysis was performed by an external, EPSRC-funded facility operated by Prof. Peter Cumpson and Dr. Anders Barlow (at NEXUS in Newcastle) on an AXIS Nova spectrometer (Kratos Analytical, Manchester) using incident X-rays of energy 1.4866 keV.[22] Crystals of as-prepared samples were gently pressed onto a double-faced adhesive copper tape prior to analysis. Analysis of the resulting spectra was performed using the CasaXPS software.[23] Element quantification was performed applying fitting parameters to the characteristic spectral lines. In the case of nickel, the spectra are complex, as seen previously for Ni XPS spectra.[24] The Ni $2p_{3/2}$ peak at 853.3eV has associated with it a broad satellite at higher binding energy (~860 eV) that can be associated with energy losses (~6eV) due to surface and bulk plasmon excitations. The $2p_{3/2}$ peak and the associated broad feature at around 858eV were fitted to calculate the area and so the nickel content (Figure 2.20).

Table 2.4: *Selected electron binding energies, in electron volts, for the elements Mg, P and Ni in their natural forms.*[25, 26]

No	Element	K 1s	L_1 2s	L_2 $2p_{1/2}$	L_3 $2p_{3/2}$	M_1 3s	M_2 $3p_{1/2}$	M_3 $3p_{3/2}$
12	Mg	1303.0	88.7	49.78	49.5			
15	P	2145.5	189	136	135			
28	Ni	8333	1008.6	870.0	852.7	110.8	68.0	66.2

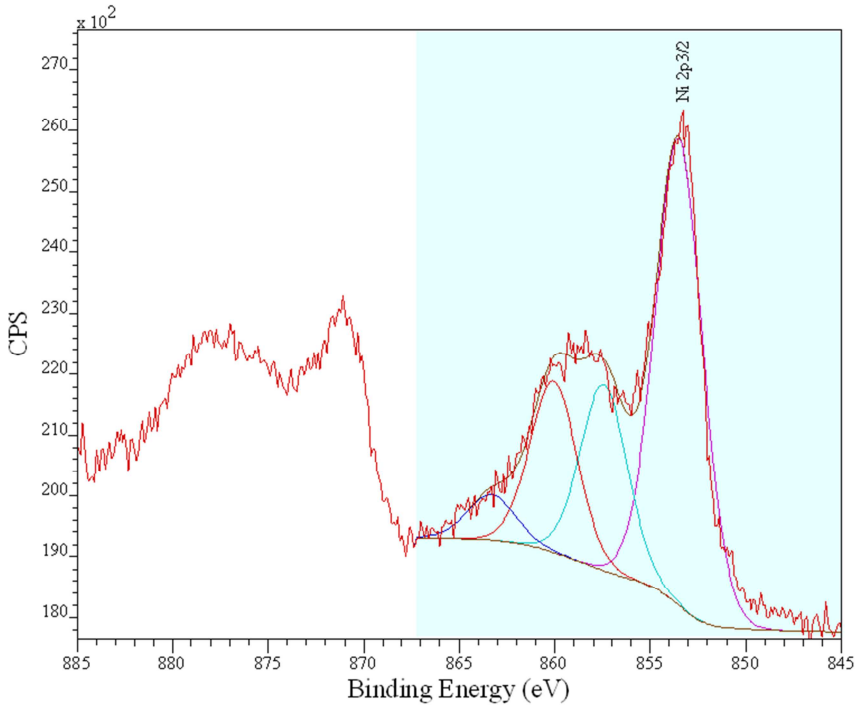

Figure 2.20: *XPS graph of a Ni modified CPO-27 with fitting parameters applied to the nickel $2p_{3/2}$ peak.*

2.10 Gas adsorption

To determine porosity, surface area and gas uptake gas adsorption measurements have been carried out. Adsorption isotherms are obtained by measuring the gas uptake while pressure changes at a constant temperature. Different shapes of isotherms are classified by Brunauer-Emmett-Teller into six categories (Figure 2.21).[27] Two techniques can be applied to yield information about the quantity of adsorption, normally gravimetric and volumetric adsorption measurement. Adsorption is a process of adhesion which creates

a film of atoms, ions or molecule (adsorbate) on the surface of a porous material (adsorbent).

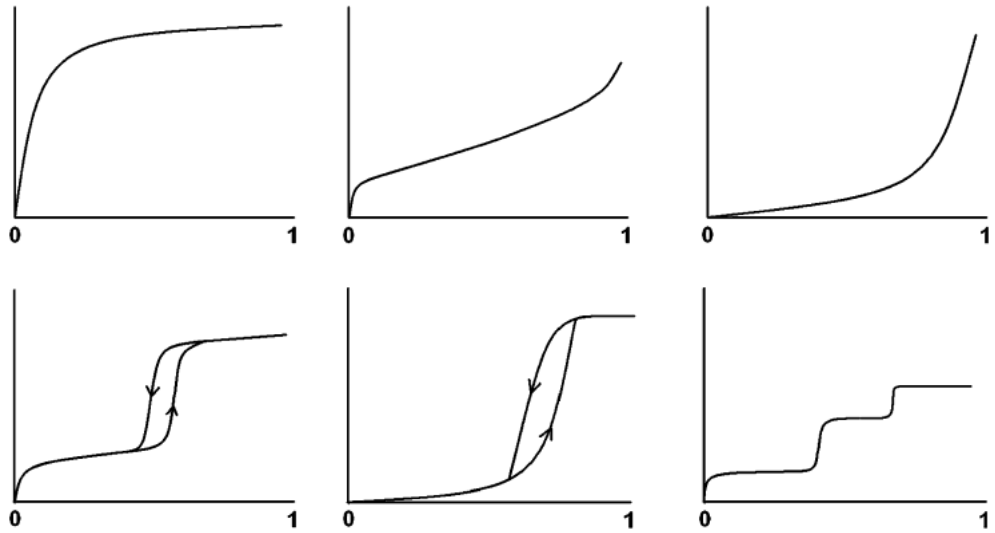

Figure 2.21: *BET classification of isotherms type I to VI (from top left to bottom right). All charts are plotted in quantity adsorbed against p/p_0, where p refers to the absolute pressure and p_0 to the saturated pressure of the liquid adsorbate at constant temperature.*

There are several methods to calculate the surface area depending on how many layers are formed during the adsorption process. The fractional coverage of adsorbate is given by

$$\theta = \frac{Number\ of\ surface\ sites\ occupied\ by\ adsorbate\ (Ns)}{Total\ number\ of\ substrate\ adsorption\ sites\ (N)} \qquad (14)$$

The Langmuir surface area calculations assume:[28]

(i) The solid surface is uniform and contains a number of equivalent sites each of which may be occupied by only one molecule of adsorbate.

(ii) A dynamic equilibrium exists between the gas (at pressure, P) and the adsorbed layer at constant temperature.

(iii) Adsorbate molecules from the gas phase are continually colliding with the surface. If they strike a filled site, they are reflected back into the gas phase.

(iv) Once adsorbed, the molecules are localized and the enthalpy of adsorption per site remains constant irrespective of coverage.

The Langmuir adsorption isotherm is calculated through equation (15) and predicts how the fractional coverage θ changes with P.

$$\theta = \frac{Ns}{N} = \frac{KP}{1+KP} \qquad \left(K = \frac{ka}{kd}\right) \tag{15}$$

To obtain the form of a straight line equation (16) can be rearranged:

$$\left(\frac{P}{Ns}\right) = \frac{1}{NK} + \mathrm{P}\left(\frac{1}{N}\right) \tag{16}$$

The plot of $\left(\frac{\mathrm{P}}{\mathrm{Ns}}\right)$ against P gives a straight line with the intercept $\frac{1}{\mathrm{NK}}$ and the gradient $\left(\frac{1}{\mathrm{N}}\right)$.

The Langmuir adsorption isotherm assumes surface monolayer coverage and the total surface area (S_A) is

$$S_A = N \times A_m \tag{17}$$

where A_m describes the area of one molecule.

When surface areas are determined employing the Langmuir adsorption calculation one should notice that only monolayer coverage and equivalent energy of all adsorption sites are applied with. Metal organic frameworks consist of channels and/or cavities

created by metals sites and organic moieties showing a variety of adsorption sites with different energy. Additionally MOFs exhibit pores with multilayer adsorption and therefore the surface area calculated by the Langmuir surface area calculations are not strictly valid.

Another method that can be applied to determine the surface area of porous materials is denoted as Brunauer-Emmett-Teller (BET) isotherm. It describes an extension of the Langmuir surface area calculation to multilayer adsorption and assumes as follows:[28]

(i) Adsorption of the first adsorbate layer is assumed to take place on an array of surface sites of uniform energy.

(ii) Second layer adsorption can only take place on top first, third on top of second etc. When P = P_0 an infinite number of layer will form.

(iii) At equilibrium, the rates of condensation and evaporation are the same for each individual layer.

(iv) When the number of adsorbed layers is greater or equal to two, the equilibrium constants are equal and the value ΔH^0_{AD} = - ΔH^0_{VAP}. For the first layer the enthalpy of adsorption is as in the Langmuir case. Summation of amount adsorbed in all layers leads to BET equation, which expressed in linear form is

$$\frac{P}{Ns(P0-P)} = \frac{1}{NC} + \frac{(C-1)}{NC} \times \frac{P}{P0} \qquad (18)$$

with C $\approx e^{\frac{(H^0_D - H^0_{VAP})}{RT}}$ and H^0_D = enthalpy of desorption = $-H^0_{AD}$.

It is important to note that no simple isotherm model can describe all behaviour over all ranges of θ and P. However, over restricted sections each of the isotherms can be used to obtain data about the surface area.

In this project gravimetric as well as volumetric adsorption measurements have been applied to determine surface area and gas uptake. Adsorption isotherms for N_2 at 77 K and CO_2 at 196 K and 298 K were measured on Tristar II and Micromeritics 2020 volumetric analysers. CO_2 adsorption isotherms at 298 K were measured gravimetrically on a Hiden Isochema IGA gravimetric porosimeter. In each case, the sample was dehydrated prior to measurement of the isotherm. In selected cases the sample was reheated a second time under these conditions (after exposure to air) and the permanent porosity remeasured. One advantage of the volumetric technique is the permanent contact of the sample with the refrigerant (liquid N_2 / 77 K) through the glass sample wall. Gravimetric adsorption analyser on the other hand can deal with much lower amounts of sample and can allow the measurement of vapour adsorption.

Further, to obtain data about the performance of MOFs as possible materials in gas separation of CO_2/N_2 gas mixtures, the method of Zero-Length-Column chromatography has been used to screen samples at the University of Edinburgh.[29] A schematic diagram of this apparatus is presented in Figure 2.22.

Zero Length Column (ZLC) chromatography is a useful technique to measure adsorption equilibria. A small amount of sample (0.5 – 2mg) is pre-equilibrated with sorbate and followed by desorption (Figure 2.23). Information about adsorption kinetics and equilibria can be obtained. Under low flow rate conditions it provides a simple tool to get equilibrium data (Henry's law constant, isotherm).

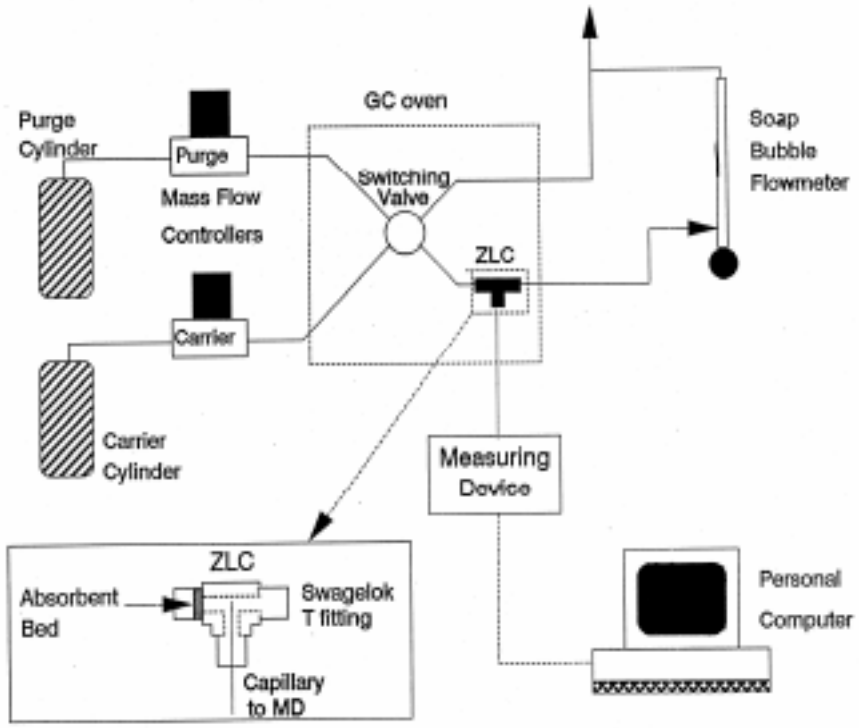

Figure 2.22: *Schematic setup for ZLC57.*

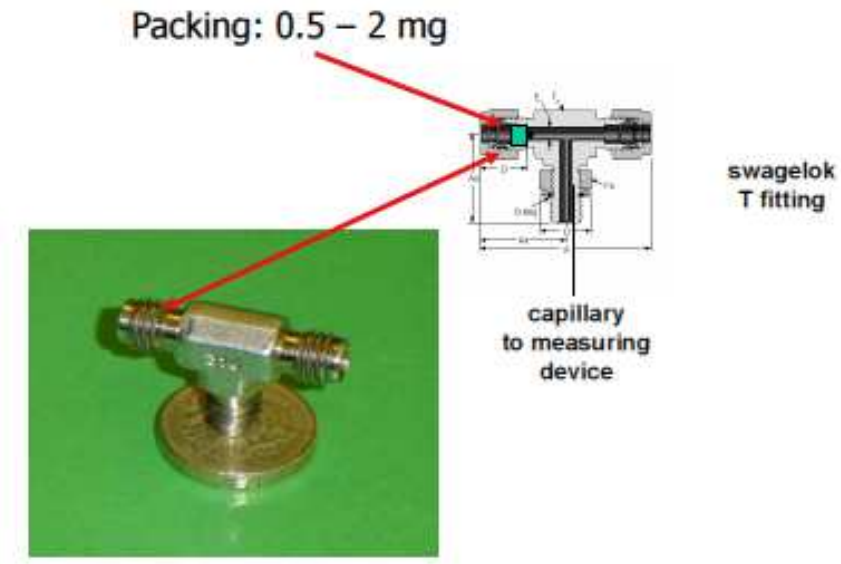

Figure 2.23: *Scheme and picture of the Zero-Length-Column (ZLC).*[26]

2.11 References

1. C. Hammond, *The Basics of Crystallography and Diffraction*, 2006, Oxford University Press, USA.

2. A. R. West, *Basic Solid State Chemistry*, 1999, John Wiley & Sons Ltd, UK.

3. A. K. Cheetham and P. Day, *Solid State Chemistry Techniques*, 1987, Oxford University Press, USA, 1987.

4. J. Karle and H. Hauptman, *Acta Cryst.*, 1956, **9**, 635-651.

5. G. M. Sheldrick, *Acta Cryst.*, 2008, **A64**, 112-122.

6. M. C. Burla, R. Caliandro, M. Camalli, B. Carrozzini, G. L. Cascarano, C. Giacovazzo, M. Mallamo, A. Mazzone, G. Polidori and R. Spagna, *J. Appl. Crystallogr.*, 2012, **45**, 357-361.

7. S. Brenner, L. B. McCusker and C. Baerlocher, *J. Appl. Crystallogr.*, 1997, **30**, 1167-1172.

8. A. Boultif and D. Louer, *J. Appl. Crystallogr.*, 1991, **24**, 987-993.

9. P.-E. Werner, L. Eriksson and M. Westdahl, *J. Appl. Crystallogr.*, 1985, **18**, 367-370.

10. J. Visser, *J. Appl. Crystallogr.*, 1969, **2**, 89-95.

11. A. Altomare, C. Cuocci, C. Giacovazzo, A. Moliterni, R. Rizzi, N. Corriero and A. Falcicchio, *J. Appl. Crystallogr.*, 2013, **46**, 1231-1235.

12. V. Petricek, M. Dusek and L. Palatinus, *Jana2006. The crystallographic computing system. Institute of Physics, Praha, Czech Republic*, 2006.

13. S. P. Thompson, J. E. Parker, J. Potter, T. P. Hill, A. Birt, T. M. Cobb, F. Yuan and C. C. Tang, *Rev. Sci. Instr.*, 2009, **80**.

14. H. Rietveld, *J. Appl. Crystallogr.*, 1969, **2**, 65.

15. A. Le Bail, H. Duroy and J. L. Fourquet, *Mater. Res. Bull.*, 1988, **23**, 447.

16. C. Larson and R. B. von Dreele, *Los Alamos National Labaratory: Los Alamos, NM*, 2001.

17. B. H. Toby, *J. Appl. Crystallogr.*, 2001, 210-213.

18. A. K. Cheetham, *'Solid State Chemistry Techniques'*, 1987, Oxford University Press, USA.

19. A. Putnis, *Introduction to Mineral Science*, Cambridge University Press, UK, 1992.

20. J. A. Bearden, *Reviews of Modern Physics*, 1967, **39**, 78.

21. J. W. Niemantsverdriet, *Spectroscopy in Catalysis*, VCH Verlagsgesellschaft mbH, Germany, 1993.

22. P. Cumpson and A. Barlow, *X-ray photoelectron spectra were obtained at the National EPSRC XPS User's Service (NEXUS) at Newcastle University, an EPSRC Mid-Range Facility.*

23. *CasaXPS version 2.3.15, Casa Software*.

24. A. P. Grosvenor, M. C. Biesinger, R. S. C. Smart and N. S. McIntyre, *Surf. Sci.*, 2006, **600**, 1771-1779.

25. M. Cardona and L. Ley, *Photoemission in Solids I: General Principles* Springer-Verlag, Berlin, 1978.

26. J. C. Fuggle and N. Mårtensson, *J. Electron Spectrosc. Relat. Phenom.*, 1980, **21**, 275.

27. P. A. Wright, *Microporous Framework Solids*, RSC Publishing, 2008.

28. G. Attard and C. Barnes, *Surfaces*, OCP, 2004.

29. J. C. L. Cavalcante, S. Brandani and D. M. Ruthven, *Zeolites*, 1997, **18**, 282-285.

3. Improvement of Permanent Porosity in CPO-27

3.1 Introduction

The magnesium 2,5-dioxoterephthalate, $Mg_2(H_2O)_2(O_2CC_6H_2O_2CO_2)xH_2O$, known variously as Mgdotp, CPO-27(Mg) or MOF-74(Mg) (CPO-27(Mg) elsewhere in this thesis) is one of the most widely studied MOFs, primarily as a consequence of its ability to bind adsorbates strongly at coordinatively unsaturated five-fold coordinated Mg^{2+} cations generated by removal of chemisorbed solvent (Figure 3.1). [1-4] In particular, its uptake of CO_2 at low partial pressures is high, with values measured in this work reaching 6.71 mmol g^{-1} at pressures and temperatures (e.g. 0.1 bar and 298 K) relevant to adsorption from flue gases from stationary power sources.[5, 6] Therefore, CPO-27(Mg) was chosen as a potential model adsorbent for the separation of CO_2 from flue gas

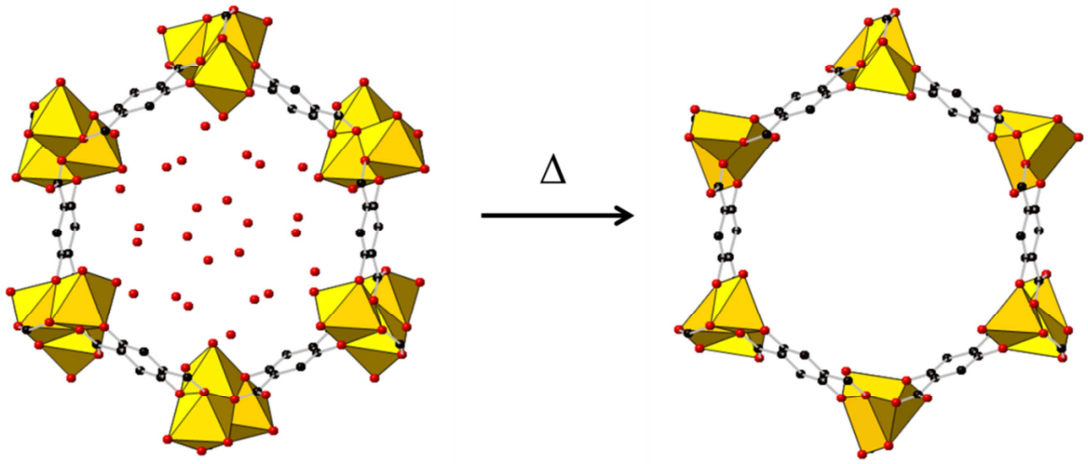

Figure 3.1: *Representation of a single channel of the metal organic framework CPO-27, viewed down the c axis, in the hydrated (left) and dehydrated (right) form. In the hydrated form, water molecules are bound to octahedrally-coordinated metal cations (yellow octahedra). Removal of water leaves the cation in square pyramidal geometry. Hydrated structure taken from [6], dehydrated form obtained from Rietveld refinement and H atoms omitted for clarity.*

within the UK IGSCC carbon capture program. Ni-, Co- and Zn-forms also show high uptakes when in the activated form, although these are lower than those of the Mg-form (Table 3.1).[7-14] However, in order to achieve these high CO_2 uptakes on CPO-27(Mg), considerable care must be taken to activate the material (Table 3.1).

The internal pore volume of MOFs, as measured by the adsorption of nitrogen at 77 K, is found to depend strongly on the method by which the solid is activated. Pore space can be filled or blocked by the occlusion of species during synthesis, such as solvent molecules, that cannot easily be removed by simple heating.[15, 16] A range of methods, including repeated solvent extraction and extraction via supercritical solvents [17-19] have been devised to remove guest molecules and improve the materials' porosity. Lower adsorption capacities than expected on the basis of the crystalline structure cannot always be explained in terms of included guests, however. Among metal phosphonate MOFs of the STA-12 family, for example, whereas the nickel form gives highly reproducible N_2 surface areas upon thermal dehydration, the manganese form is not porous to N_2 even though the guest water molecules can be completely removed with complete retention of crystallinity (and 'crystallographic' porosity).[20] A salient observation in this example is that the as-prepared STA-12 materials can all adsorb diamine molecules from solution, so the loss of porosity must result from the dehydration. One way to explain this lack of permanent porosity is to invoke the formation of non-crystallographic defects which have a particularly negative effect in solids with one-dimensional channel pore systems. In particular, reduced porosity due to loss of crystallinity at the surface might be a consequence of incomplete coordination of metal cations by ligands or of ligands by metal cations.[21] At the surface, metal cations might include solvent molecules rather than ligands in their coordination shells, so that solvent removal by heating would lower their coordination number and change their

coordination geometry. The ability of cations to tolerate reduced coordination numbers might vary from one metal to another, so that whereas some metal forms of a MOF would retain surface crystallinity and permeability, others would lose them so that the internal pore space would become inaccessible.

Simple thermal activation of the as-prepared form of CPO-27(Mg) does not give high pore volumes, as measured by N_2 adsorption at 77 K, but our preliminary experiments indicated that simple thermal activation of the Ni-form was more successful. We therefore reasoned that a CPO-27(Ni)@CPO-27(Mg) core-shell structure where the CPO-27(Mg) was coated by the Ni-form should have better properties.[22-24] Here a successful one-pot preparative procedure to modify the chemistry of CPO-27(Mg) by inclusion of Ni^{2+} cations is reported as well as the improvement of its adsorption properties when subjected to subsequent thermal activation. A mechanism is suggested by which this may occur. By applying these techniques to CPO-27(Ni) and CPO-27(Co), similar improvements in porosity were achieved.

Such modification processes typically result in intensive synthetic efforts and produce a large number of samples. The Zero Length Column (ZLC) method of porosity measurements represented a suitable available technique within the IGSCC program (operated by Enzo Mangano, a member of Stefano Brandani's group in the School of Engineering, University of Edinburgh) to screen samples, with the focus on CO_2 uptake and the study of materials' stability under post combustion flue gas conditions from power plants. The key advantage of this technique arises from the fact that the adsorption carried out on small amounts of adsorbent (10 mg) and as a result in shortened experiment time compared to conventional adsorption measurements.[25]

Table 3.1: *Various activation procedures reported in the literature for CPO-27 materials, and the measured uptakes on resulted materials.*

Material	Adsorption		Synthesis	Pre-adsorption treatment	Activation	Ref.
	CO_2 (mmol g^{-1}) 298K/0.1 bar	N_2 (m^2 / mmol g^{-1}) 77K				
Mg	5.68	1542 / 18.2	THF/water	MeOH exchange (7x7 days)	513 K/48 h, 393 K/1 h	7
Mg	5.9	1495 / --	DMF/EtOH/ water	MeOH exchange (4x2 days), stored under vac or inert gas	523 K/5 h	8
Mg	5.68	--	DMF/EtOH/ water	MeOH exchange (4x2 days)	523 K/6 h	9
Mg	5.5	-- / 0.57	DMF/EtOH/ water	Soaking DMF, MeOH, soak DMF(heating), MeOH exchange (6x36 h), 353 K/24 h under vac		10
Mg	4.59	--	DMF/EtOH/ water	hot DMF decanted, immediate MeOH exchange (2x), MeOH exchange (4x2 days), dried 303-313 K, 523 K vac 10 h, stored under N_2 atmosphere		11
Ni	4.09	1218 / 13.6	THF/water	--	473 K/19 h, 383 K/1 h	7
Ni	--	1083	THF/water	--	373 K/20 h	26
Ni	--	1242 / 13.6	THF/water	?	?	27
Ni mod	1.1	46.7 / --	THF/water	--	353 K/12 h	28
Ni	3.1	921 / --	THF/water	EtOH exchange (6x8 days)	323 K/vac in N_2-flow	12
Ni	3.1	1147 / --	THF/water	--	523 K/15 h vac or He	13
Ni	4.09	1070 / --	DMF/EtOH/ Water	MeOH exchange (4x/2 days), Stored under vac or inert gas	523 K/5 h	8
Ni	2.72	--	THF/water	hot mother liquor decanted, MeOH exchanged (4x2 days), dried RT, 523 K vac 5 h, stored in N_2 atmosphere	.	11
Co	2.95	1080 / --	DMF/EtOH/ water	MeOH exchange (4x2 days), Stored under vac. or inert gas	523 K/5 h	8
Co	2.59	--	DMF/EtOH/ water	hot mother liquor decanted, MeOH exchanged (4x2 days), dried RT, 523 K vac 5 h, stored under N_2 atmosphere		11
Zn	1.31	816 / --	DMF/water	hot mother liquor decanted, rinsed DMF, MeOH exchanged (3x6 days)	543 K	1

3.2 Experimental

CPO-27(Mg), CPO-27(Ni) and CPO-27(Co) were prepared via the literature syntheses [2, 26, 29] with yields based on dihydroxyterephthalic acid of around 69 %, 82 % and 83 % respectively, after heating at 383 K for 3 days, and their phase purity was confirmed by PXRD (Figure 3.2). In the 'one-pot' modification procedure reported in this thesis, the product at the end of the first heating period was left in the mother liquor and inorganic and/or organic additives added to this, and this suspension was resealed and reheated at the original synthesis temperature (Scheme 3.1).

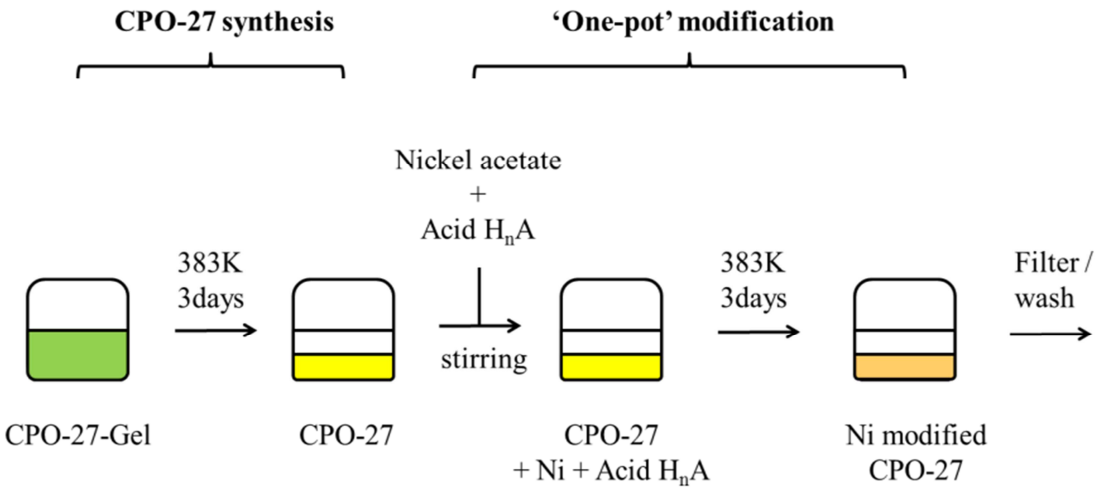

Scheme 3.1: *Reaction scheme of the one-pot synthesis and modification procedure of the metal dioxiterephthalate CPO-27(Mg) with Ni salt. A typical synthesis is performed in THF/water.*

At the end of the second period of heating the product was filtered and dried. As well as nickel salts (and in some cases magnesium salts), weak acids were also added as modifying agents. These included phosphonic and carboxylic acids and phosphorous acid: 4-carboxypiperidyl-N-methylenephosphonic acid, cpmp, N,N′-piperazinebis (methylenephosphonic acid), pbmp, N,N′-bipiperidine(bismethylenephosphonic acid),

bbmp (prepared according to the literature[30, 31]), 5-carboxybenzimidazole, cbIm, 96 %, Sigma-Aldrich; trimesic acid, 95 %, Sigma-Aldrich; phosphorous acid, 99.999 %, Sigma-Aldrich. The pH values of the modifying solutions were similar to those of the original synthesis. Details of the experiments are given in Table 3.2. In a typical experiment to prepare modified CPO-27(Mg), dihydroxyterephthalic acid, dhtp, (0.703 mmol / 139.3 mg) was placed in a PTFE liner and dissolved in 9.4 ml THF and mixed with 2.8 ml of an aqueous solution of $Mg(NO_3)_2 \bullet 6H_2O$ (1.406 mmol / 359.9 mg in 0.16 mmol H_2O). 2.8 ml of a 1 M NaOH solution was added while stirring. The PTFE liner was then sealed in a steel autoclave and heated at 383 K for 3 days, before being allowed to cool to room temperature. After cooling, the autoclave was opened and the required amount of $Ni^{2+}(aq)$ (as nickel acetate $Ni(OAc)_2 \bullet 4H_2O$, 98%, Sigma Aldrich, or a mixture of nickel acetate and nickel chloride ($NiCl_2 \bullet 6H_2O$, 98%, BDH Chemicals) and selected acid was added and the resulting suspension stirred until homogeneous (Table 3.2). For a '10%' modification, this corresponded to nickel acetate amounting to 10 mol% of the Mg content (0.141 mmol / 35.1 mg) and a molar equivalent of acid (for cpmp, 0.141 mmol / 31.4 mg). The autoclave was then resealed and heated for another 3 days at 383 K. After cooling, the resulting solid was filtered, washed with water and dried at room temperature. In one set of experiments where 70 mol % of $Ni^{2+}(aq)$ was added in the modification step, the second heating step at 383 K was stopped after times from 1 to 96 h.

In separate experiments, the nickel form was first prepared by a similar procedure where nickel acetate (6 mmol / 1488 mg) in 10 ml of water and dhtp (3 mmol / 594 mg) in 10 ml of THF were combined and sealed in a steel autoclave with Teflon inlet and heated as described above. After this first stage, 10 mol % magnesium acetate ($Mg(OAc)_2 \bullet H_2O$, 98%, Alfa Aesar) and 10 mol % phosphorous acid (H_3PO_3, 99.999 %,

Sigma-Aldrich) were added and the resulting suspension stirred until homogeneous before being heated again for 3 days at 383 K. The synthesis of CPO-27(Ni) was altered to give the cobalt species by mixing cobalt acetate (4.2 mmol / 1041 mg) in 10 ml of water and *dhtp* (2.1 mmol / 416 mg) in 10 ml of THF and completing the first step by the above described heating. One-pot modification took place by adding 10 mol % nickel or magnesium acetate salts ($Mg(OAc)_2 \bullet H_2O$, 98%, Alfa Aesar, $Ni(OAc)_2 \bullet H_2O$, 98%, Alfa Aesar) combined with 10 mol % phosphorous acid (H_3PO_3, 99.999 %, Sigma-Aldrich) to the resultant CPO-27(Co) gel followed by stirring and additional heating to 383 K for 3 days. Final workup included filtering and washing with water and drying the red powder at room temperature.

Table 3.2: *Summary of amounts of metal salts and acids used for modification of CPO-27(Mg), related to magnesium nitrate used in the first step, showing mixture of nickel acetate and nickel chloride.*

Amounts and Species used in post-modification			
% $Ni(OAc)_2$	% $NiCl_2$	% Acid	Acid
10	0	10	Trimesic acid
10	0	10	H_3PO_3
10	0	10	*cbIm*
10	0	10	*cpmp*
10	20	10	*cpmp*
10	40	10	*cpmp*
10	60	10	*cpmp*
30	60	30	*cpmp*
10	0	10	*pbmp*
10	0	10	*bbmp*

3.3 Modification of CPO-27(Mg) with 4-carboxypiperidyl-N-methylene-phosphonic acid, cpmp.

Initial modification was conducted on CPO-27(Mg) in the presence of the 4-carboxypiperidyl-N-methylenephosphonic acid *cpmp*, with addition of aqueous nickel acetate at a concentration corresponding to 10 mol % of the original Mg^{2+} in the synthesis, and an equivalent amount of the *cpmp* acid. The *cpmp* acid was chosen because it possessed two different coordinating groups and its presence could be quantified by P analysis using EDX. In the product, CPO-27 was the only crystalline phase although there was some fine-grained amorphous material that could not be separated. Selected area EDX analysis of CPO-27 crystals (Table 3.3) indicated 8.7 mol% of the Mg had been replaced by Ni and a little of the *cpmp* ligand was present, probably coating the surface (P/(Mg+Ni) = 0.01).

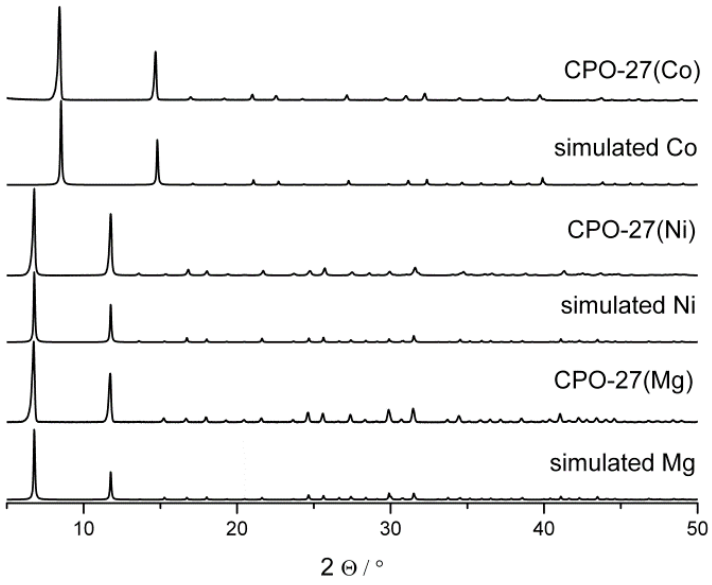

Figure 3.2: *Simulated and measured PXRD of unmodified magnesium, nickel and cobalt CPO-27. Magnesium and nickel samples were measured applying Cu $K_{\alpha 1}$- (λ = 1.540599 Å) and XRD pattern for the cobalt species was collected using Fe $K_{\alpha 1}$-radiation (λ = 1.936042 Å).*

3.4 Characterisation

The uptake of N_2 at 77 K was measured on as-prepared and 10 mol % Ni-modified CPO-27(Mg), following evacuation at 383 K and 523 K at 10^{-4} mbar as described in the experimental chapter. Table 3.3 gives the N_2 uptakes at $p/p_o = 0.5$, given in mmol g^{-1}. CPO-27(Mg) that had been filtered and dried without any special precautions gave very low uptakes of 0.1 – 0.5 mmol g^{-1}.

Table 3.3: *Aqueous Ni^{2+} and 4-carboxypiperidyl-N-methylenephosphonic acid quantities used in the one-pot modification of CPO-27 (Mg) with two 3 d, 383 K heating periods, and compositional ratios determined by EDX and XPS analysis: N_2 and CO_2 uptake for modified CPO-27(Mg).*

Ni^{2+} (% original Mg)[*1]	Added cpmp acid (% Mg)	Ni / Ni+Mg	P / Mg +Ni	Ni / Ni+Mg	P / Mg +Ni	Adsorption / mmol g^{-1}	
		EDX	EDX	XPS	XPS	N_2 at 77K[*2] ($p/p_0 = 0.5$)	CO_2 at 298K ($p = 0.1$bar)
CPO-27 (Mg) synthesis[11]		0	0	0	0	0.1 - 0.5	2.9
0	0	0	0	0	0	0	4.6
0	10	-	0.5	-	22.5	0.5	
10	0	7.4	-	45.7	-	2.4	
10	10	8.7	0.8	76.7	24.0	9.5 / 15.0[*3]	5.5
30	10	29.7	1.4	82.0	17.0	12.5 / 15.3[*3]	
50	10	47.9	2.0	86.0	0.0	13.3	
70	10	54.9	2.2	96.9	28.6	13.3	4.03
90	30	66.5	2.7	100.0	43.0	5.6	
CPO-27 (Ni) synthesis[6]		100.0	-	100.0	-	7	3.3

*[1] as nickel acetate or mixtures of nickel acetate and chloride (see experimental section)

*[2] several values taken

*[3] samples measured after one / two heating and evacuation periods (see text for details)

For this reason, complex protocols have been developed by a number of other research groups by which the full porosity expected on the basis of the crystal structure can be achieved. PXRD of the sample after the adsorption experiment (Figure 3.3) showed that

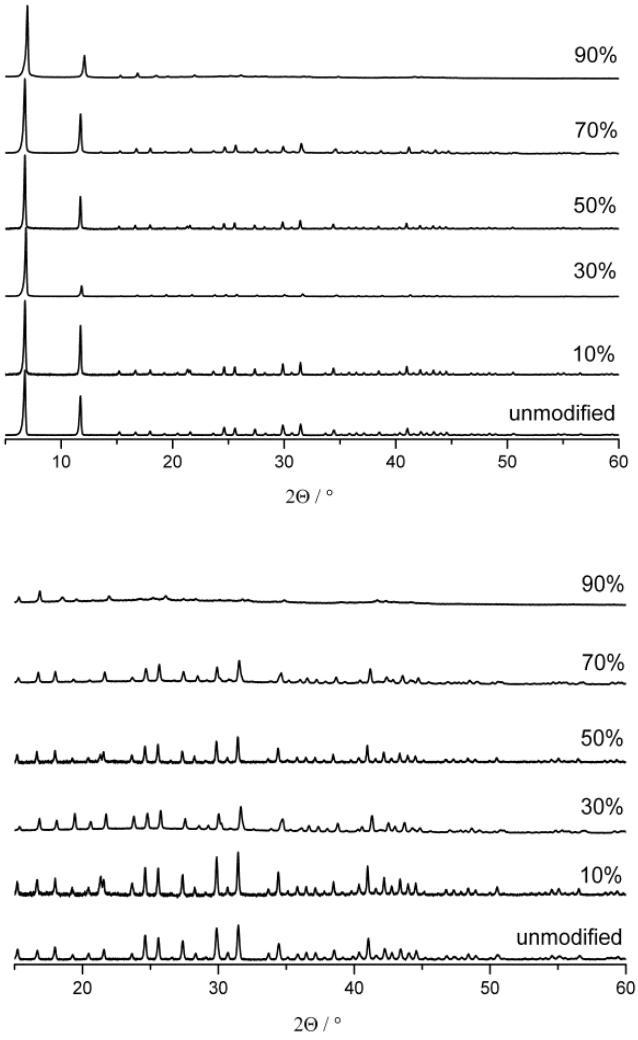

Figure 3.3: *PXRD of CPO-27 (Mg) unmodified and modified with various amounts of cpmp and nickel acetate. Powder patterns were collected after activation at 373 K followed by 523 K for all except the sample modified with 90% Ni, which was activated at 373 K and 473 K.*

the material was still crystalline, so that the low porosity of the evacuated and heated material was not due to a loss of long range order. By contrast, as-prepared CPO-27(Ni) showed appreciable, if less than maximum, porosity when dehydrated under vacuum, with an uptake of 7.3 mmol g^{-1}. Indeed, literature reports state that it is possible to achieve uptakes of N_2 of >13 mmol g^{-1} for CPO-27(Ni) via activation by simple heating

under vacuum.[7, 26] These data suggest that non-crystallographic defects that block the large pore channels, possibly at the surface, are readily formed in CPO-27(Mg) upon dehydration under vacuum, whereas CPO-27(Ni) is more stable under these conditions.

CPO-27(Mg) modified by the 'one-pot' method using Ni^{2+}(aq) at 10 mol % of the original added Mg^{2+} and with the equivalent amount of *cpmp* acid, gave much improved porosity to N_2, with uptakes of 9.5 mmol g^{-1} after a single heating and evacuation step and 15.0 mmol g^{-1} after a second heating and evacuation step (Figure 3.4), the latter value being close to the adsorption capacities measured on more carefully treated materials (literature value,[7] 18 mmol g^{-1}). With increasing amounts of additives deposited on the crystal surface (for details see p18, XPS) the gas porosity decreases which indicates that the grown Ni/P-rich layer begins to close pore apertures.

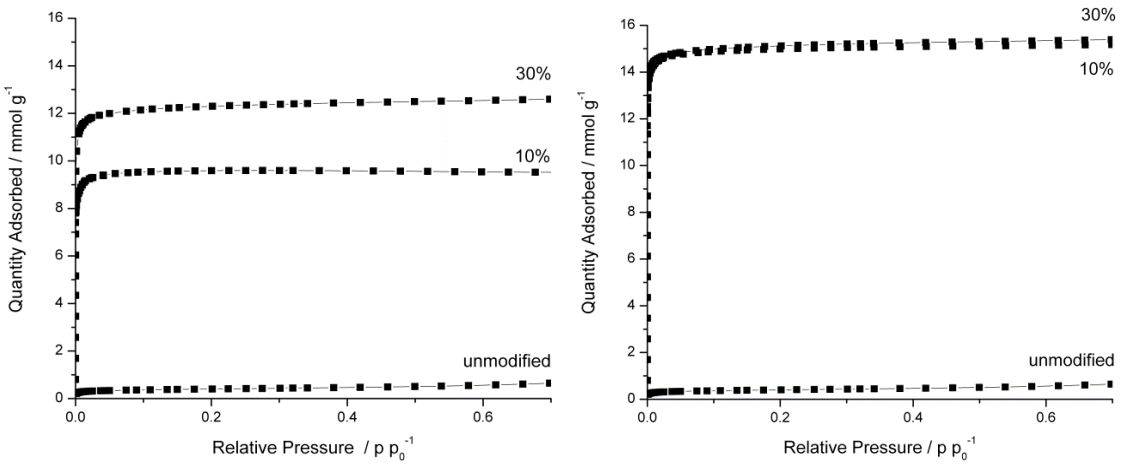

Figure 3.4: *(Left) N_2 adsorption (77K) of CPO-27(Mg) and material modified with 10% and 30% of Ni^{2+}(aq) solution and 10% cpmp after samples were activated at 373 K followed by 523 K. (Right) N_2 adsorption (77 K) of CPO-27(Mg) and material modified with 10% and 30% of Ni^{2+}(aq) solution and 10% cpmp where samples have been activated for a second time at 373 K followed by 523 K.*

The product CPO-27(Mg) obtained by simply reheating the crystallised gel for a second period of 3 days at 383 K gave no increased uptake upon thermal activation. Treatment of CPO-27(Mg) with 10 mol% *cpmp* acid (compared to initial Mg) but no nickel acetate in the second step gave very little improvement in N_2 uptake. Similar results are achieved by adding nickel acetate already in the first step. When nickel acetate was added in the absence of any additional acid in the second step of the treatment, the product CPO-27 gave a small but significant increase on the N_2 uptake (Figure 3.5). The greatest improvement was therefore achieved when both a nickel salt and a weak acid were added together in the second step.

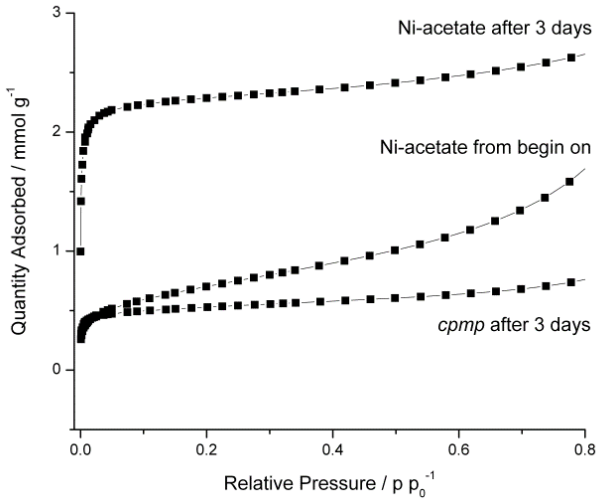

Figure 3.5: *N_2 adsorption (77 K) of CPO-27 (Mg) modified with 10% nickel acetate only added after 3 days, 10% nickel acetate only and 10% cpmp only after samples were activated at 373 K followed by 523 K.*

Adsorption isotherms were also measured at 298 K for CO_2 on the as-prepared and modified material. As-prepared, heated CPO-27(Mg) took up 2.9 - 4.6 mmol g^{-1} at 0.1 bar, conditions relevant to carbon capture from post-combustion flue gas. Uptakes of 5.9 mmol g^{-1} at these conditions have been reported previously for this material, [8] when activated with great care, values that are well in excess of those measured for most other MOFs, even other metal forms (Fe, Co, Ni) of the same framework. CPO-27(Mg)

treated with a 10 mol% equivalent of Ni^{2+}(aq) and 10 mol% *cpmp* acid gave a similar uptake of CO_2 (5.5 mmol g^{-1}) under the selected conditions to the unmodified material after the same evacuation and heating procedure (Figure 3.6).

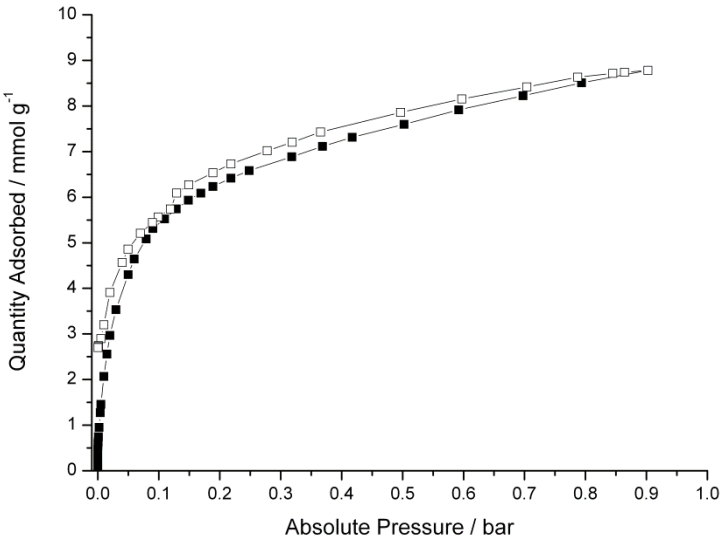

Figure 3.6: *CO_2 adsorption (filled) and desorption (open) at 298 K of CPO-27(Mg) modified with 10% nickel acetate and 10% cpmp.*

These adsorption results show that the modification procedure stabilises the CPO-27(Mg) structure to dehydration under vacuum, so that its permanent porosity may be accessed by N_2 without complex activation. One possible explanation of this behaviour is that the surface of CPO-27(Mg) is unstable to dehydration, and the surface of CPO-27(Ni) is more stable possibly because Ni^{2+} at the surface can better tolerate lower coordination numbers during removal of coordinated solvent. Subsequent replacement of Mg^{2+} by Ni^{2+} at the surface of CPO-27(Mg) during the modification would therefore increase stability of the Mg-rich materials to dehydration. The CO_2 adsorption data indicate that the non-crystallographic defects blocking the pores of heated CPO-27(Mg) to N_2 at 77 K are permeable to CO_2 at 298 K. This suggests that it is the interaction strength of the adsorbate rather than its molecular size that is important (the minimum kinetic diameter of CO_2 is less than that of N_2).

3.5 Understanding the Mechanism of Modification

To determine the origin of the enhancement in permanent porosity of these modified materials, and in particular the mechanism of incorporation of nickel into the CPO-27(Mg) structure, a series of experiments was performed in which the amount of added Ni^{2+} was increased from 10 to 90 mol % of the original Mg^{2+} in the synthesis (Table 3.3). PXRD indicated CPO-27 to be the main crystalline phase in all products (Figure 3.3). Scanning electron microscopy and selected area EDX, TGA, N_2 adsorption at 77 K and, for selected samples, XPS analyses, were performed. In each case the uptake of N_2 at 77 K after a thermal activation at 523 K under vacuum was much higher than for the unmodified CPO-27(Mg).

SEM indicated that the CPO-27 samples were made up of acicular crystals (Figure 3.7), with similar lengths in each batch but with mean lengths varying between 4 and 20 μm between batches, sensitive to small changes in preparative conditions like cooling temperature or different batches of starting materials.

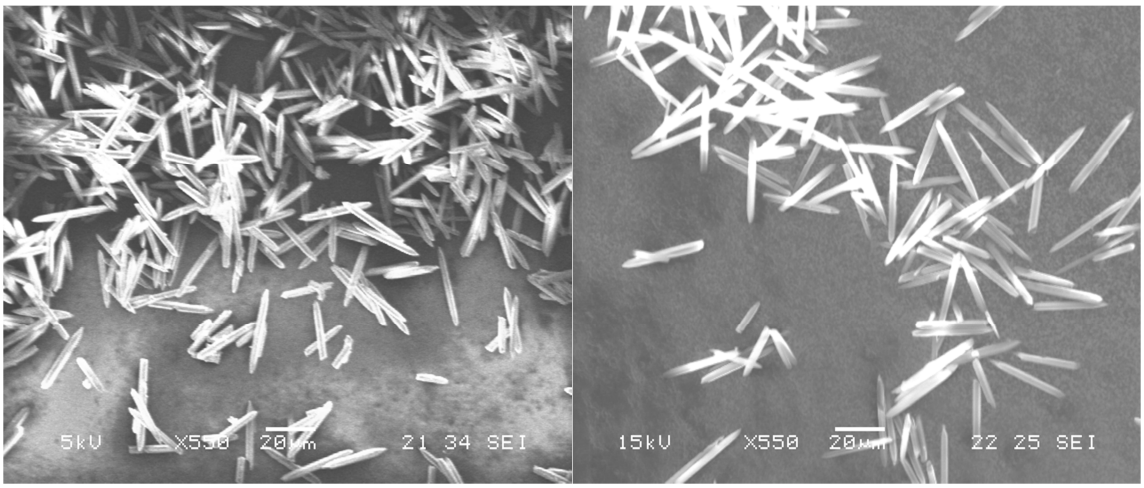

Figure 3.7: *SEM images of (left) as-prepared CPO-27(Mg) and (right) CPO-27(Mg) modified by the addition of 10 mol% Ni^{2+}(aq), compared with the original Mg^{2+}.*

EDX analysis at the voltages used here (15 keV) is expected to have a sampling depth of a few microns and so for these needle-shaped crystals of CPO-27 the measured elemental ratios will approximate to bulk compositional values. These selected area EDX analyses indicate that Ni^{2+} is strongly taken up in all these modifications (Table 3.3, Figure 3.8).

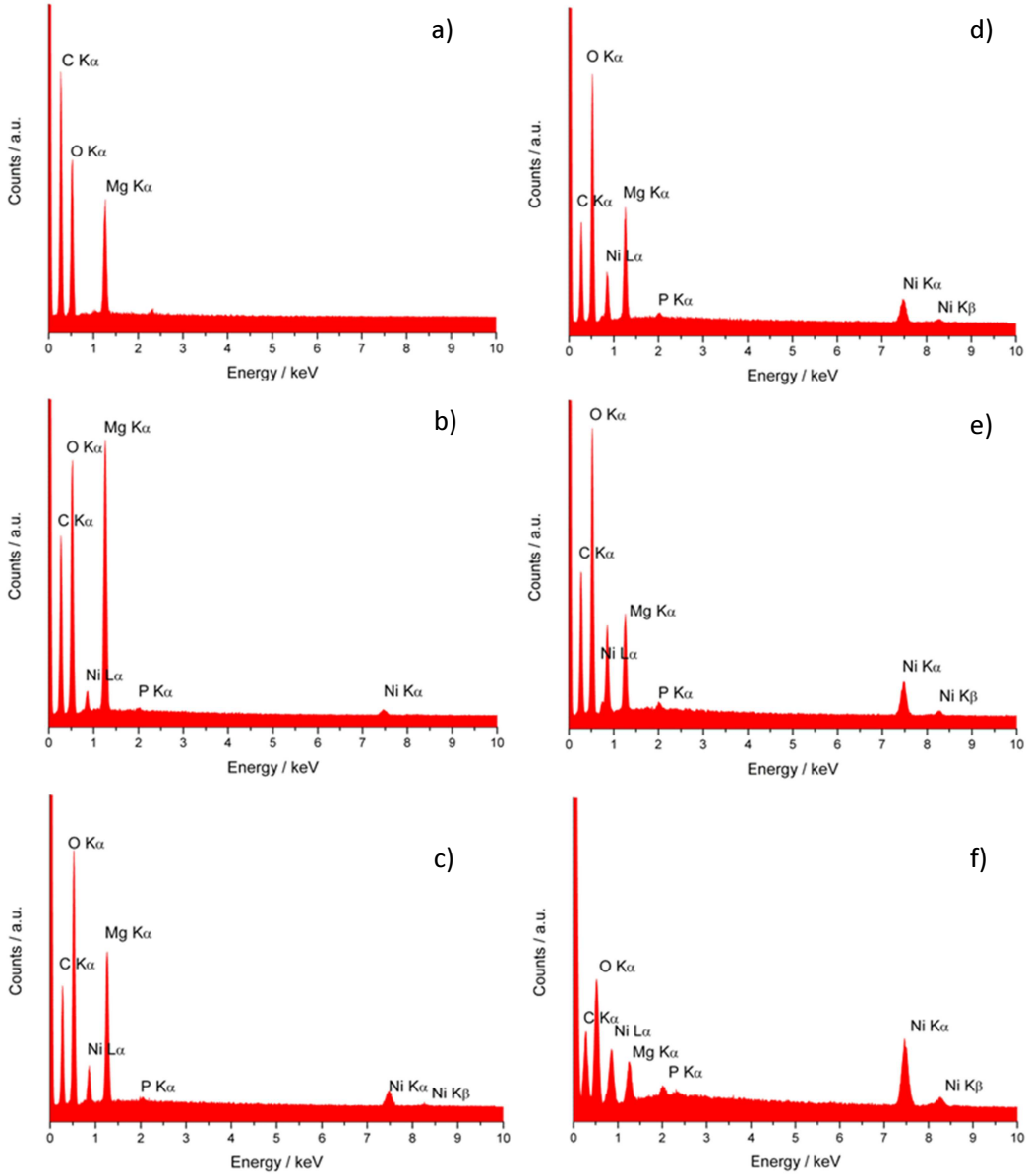

Figure 3.8: *Area selected EDX analysis of unmodified and with various amounts of nickel acetate and 10% cpmp treated CPO-27(Mg). a) Unmodified b) 10% c) 30% d) 50% e) 70% and f) 90% (later treated with 30% cpmp).*

The final yields increase after modification with Ni compared to samples where no Ni is added (Figure 3.9) so that, for example, adding 70 % Ni results in a final Ni/(Ni+Mg) molar ratio of 0.55 and an increase of yield of about 35 %. This is greater than expected (should be 8 %) if only isomorphous replacement of Mg^{2+} by Ni^{2+} had occurred but cannot be explained by simple overgrowth of pure CPO-27(Ni).

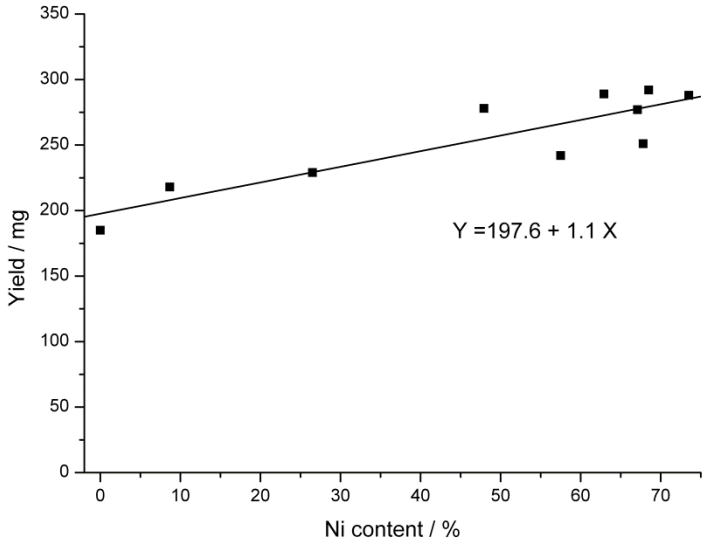

Figure 3.9: *Yield (mg) vs. Ni content (%) observed by EDX analysis of nickel and cpmp modified CPO-27(Mg).*

The surface composition measured by XPS is 97 % Ni for adding 70 % Ni, indicating there is some zonation in the crystals, with the Ni^{2+} concentration increasing and Mg^{2+} decreasing towards the surface of the crystals (Table 3.3, Figure 3.10). Further, XPS graphs exhibit broad peak shapes in Mg 1s and P 2p that can be fitted with an additional peak indicating more than one distinct magnesium and phosphorus environments (see chapter 2 section XPS).

Also, in parallel syntheses in which CPO-27(Mg) was prepared by the usual 3 days heating at 383 K followed by cooling and either (i) reheating at 383 K for 3 d or (ii) adding 70 mol % Ni^{2+} and *cpmp* acid (the latter at 10 % of the Mg^{2+} content) before reheating at 383 K for 3 d, there was a small increase in mean crystal size (from 20 to

22 μm) in the experiment where the 70 mol % Ni^{2+} was added (Figure 3.11). Considering that CPO-27(Ni) consist of crystals of poorly defined morphology and CPO-27(Mg) material of acicular crystals, it is notable that the crystal morphology remains unchanged despite the fact that 54.9% of the magnesium in the bulk material was exchanged by nickel according to EDX. Selected area EDX indicated that Ni^{2+} was distributed throughout the samples and not just on the surface, but careful inspection of the elemental Mg and Ni maps (Figure 3.12) suggested that the rim of the crystals was

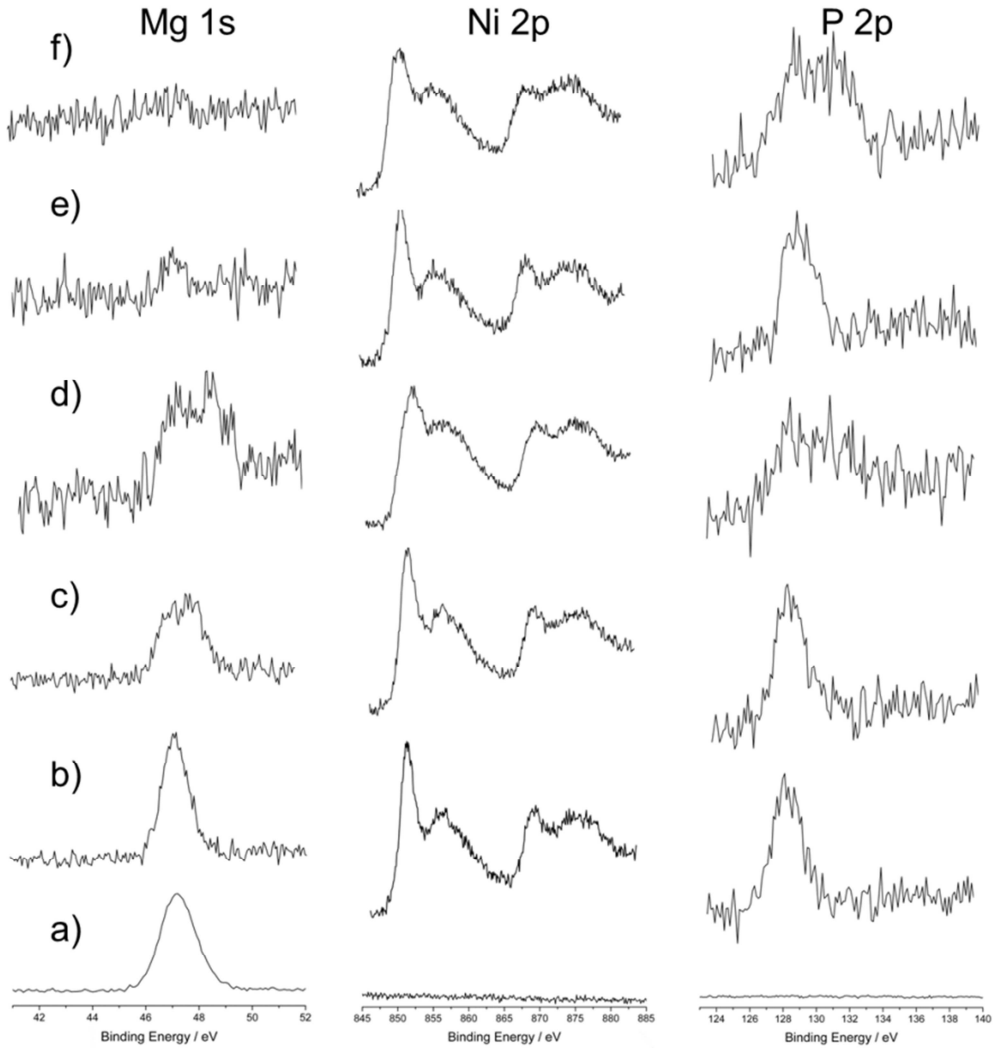

Figure 3.10: *XPS of Mg 1s, Ni 2p and P 2p on a) unmodified and with b) 10%, c) 30%, d) 50%, e) 70%, f) 90% Ni and 10% cpmp modified CPO-27(Mg) material (the latter was modified using 30% cpmp). In case of magnesium-a) Mg 2p lines were used.*

predominantly Ni-rich (The image of the crystal taken by Ni elemental mapping is slightly larger than that from Mg mapping).

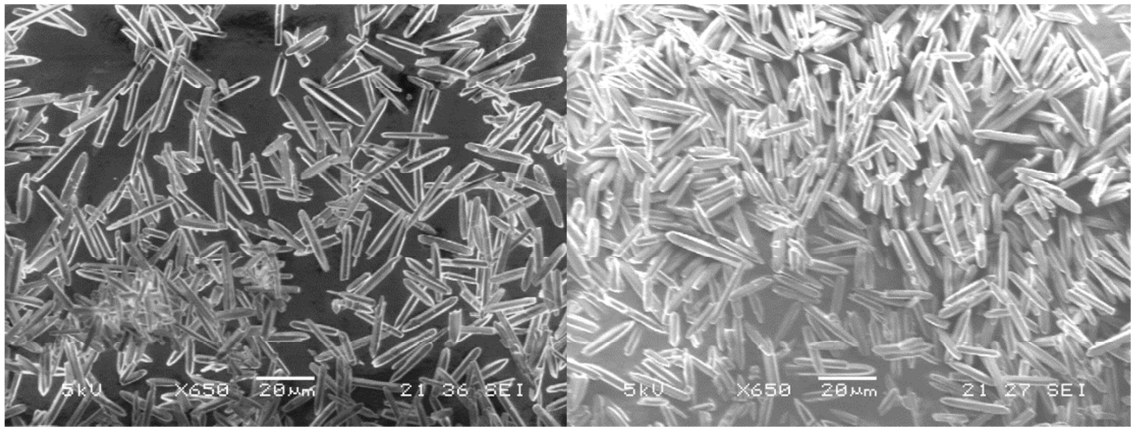

Figure 3.11: *SEM image of unmodified and with 70% Ni / 10% cpmp modified CPO-27(Mg).*

To determine how the Ni is distributed, the sample prepared by adding 70 % Ni and which had a Ni content of 54.9 % by EDX was examined further by synchrotron X-ray diffraction. The structure of this CPO-27(Mg, Ni) material was refined against data collected on station I11 at the Diamond Light Source (Table 3.4, Figure 3.13). No distance restraints were applied in the final refinements. The PXRD pattern showed only a single set of diffraction maxima indicating that there were not separate Mg and Ni forms of CPO-27 (they would be expected to show different peak positions due to the difference in size of their unit cells). The refined occupancy of the Mg^{2+} cation site was 64.6 % Ni and 35.4 % Mg, also consistent with Ni isomorphously replacing Mg and within experimental error of the value measured by EDX.

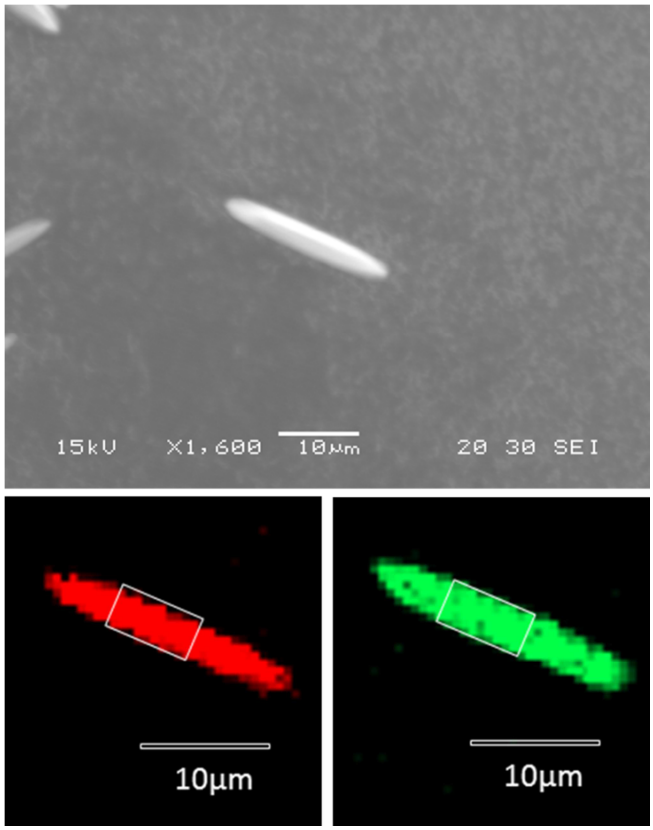

Figure 3.12: *(Above) SEM of a crystal of 70% Ni modified CPO-27(Mg) and (below) elemental mapping of the same crystal with Mg $K_{\alpha 1}$ (left) and Ni $K_{\alpha 1}$ (right).*

Table 3.4: *Crystallographic data for the Rietveld refinement of CPO-27(Mg, Ni). Prepared by the addition of 70 mol% of Ni^{2+}.*

Measured composition (EDX)	$C_4H_1Mg_{0.45}Ni_{0.55}O_3$
Refined composition	$C_4H_1Mg_{0.35}Ni_{0.65}O_3$
Formula mass [g / mol]	142.56
Space group	R-3
Z	18
a [Å]	25.87358(13)
b [Å]	25.87358(13)
c [Å]	6.79917(4)
β [°]	120
V [$Å^3$]	3941.845(33)
λ [Å]	0.827055
2Θ range [°]	2.1 - 40.0
No. of reflections	9249
Rp	0.0235
Rwp	0.0326
$R(F^2)$	0.1022

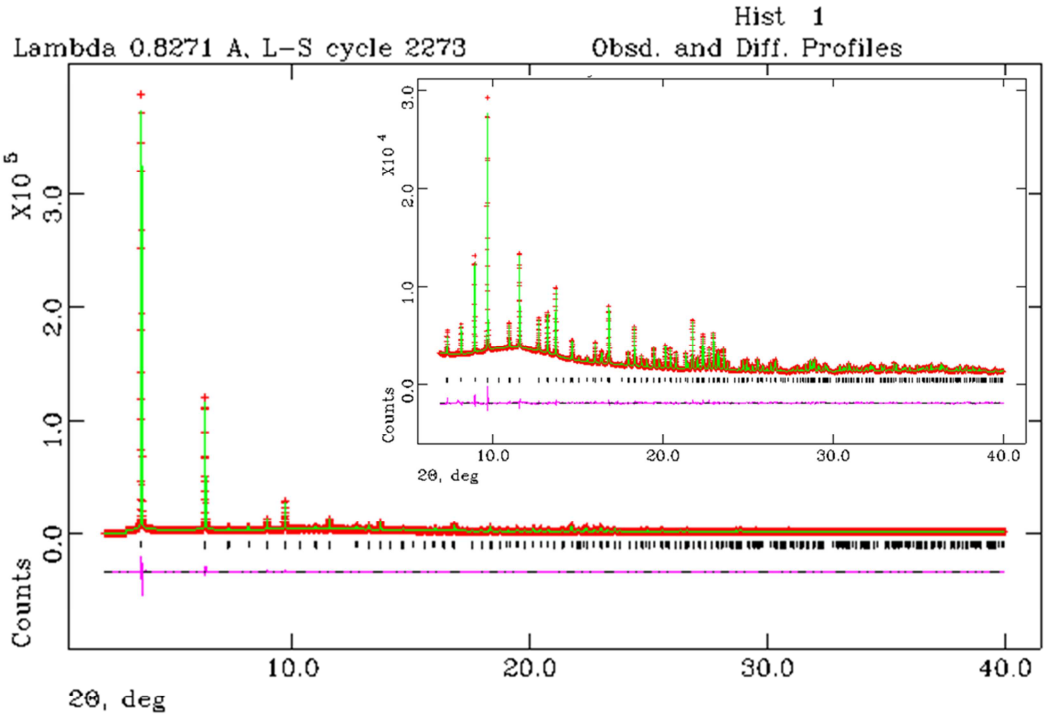

Figure 3.13: *Rietveld plot of the refinement of the structure of 70 mol% Ni-modified CPO-27(Mg), refined composition $Mg_{0.7}Ni_{1.3}$(dotp) against synchrotron X-ray powder diffraction data (λ = 0.827055 Å, Rwp = 0.0326) Observed pattern, red crosses, fitted profile in green, difference curve between observed and calculated pattern in pink.*

Table 3.5: *Atomic positions and occupancies obtained from Rietveld refined $Mg_{0.7}Ni_{1.3}$(dotp) prepared by adding 70 mol% Ni^{2+}.*

Atom	x	y	z	Occ	Uiso	Multiplicity
C1	0.2464(4)	0.3204(5)	0.0710(12)	1	0.0116(10)	18
C2	0.2017(5)	0.3254(4)	0.2097(15)	1	0.0116(10)	18
C3	0.1510(5)	0.3171(4)	0.1280(11)	1	0.0116(10)	18
C4	0.2211(4)	0.3432(4)	0.4029(17)	1	0.0116(10)	18
O1	0.22929(24)	0.30210(26)	-0.1032(8)	1	0.0116(10)	18
O2	0.29775(23)	0.33142(20)	0.1323(7)	1	0.0116(10)	18
O3	0.27419(22)	0.35698(20)	0.4964(8)	1	0.0116(10)	18
Mg1	0.28779(9)	0.30553(9)	0.30906(23)	0.355(6)	0.0138(7)	18
Ni1	0.28779(9)	0.30553(9)	0.30906(23)	0.645(6)	0.0138(7)	18

To confirm that the inclusion of nickel into CPO-27(Mg) occurs via a replacement mechanism rather than dissolution of CPO-27(Mg) and recrystallization as CPO 27(Mg,Ni), the modification step of the 70 mol% Ni modification in the presence of cpmp was stopped after reaction times of between 1 and 96 h and the products examined by SEM and EDX analysis (in both selected area and mapping modes). SEM shows (Figure 3.14) that the CPO-27 crystal morphology and size changes little over the

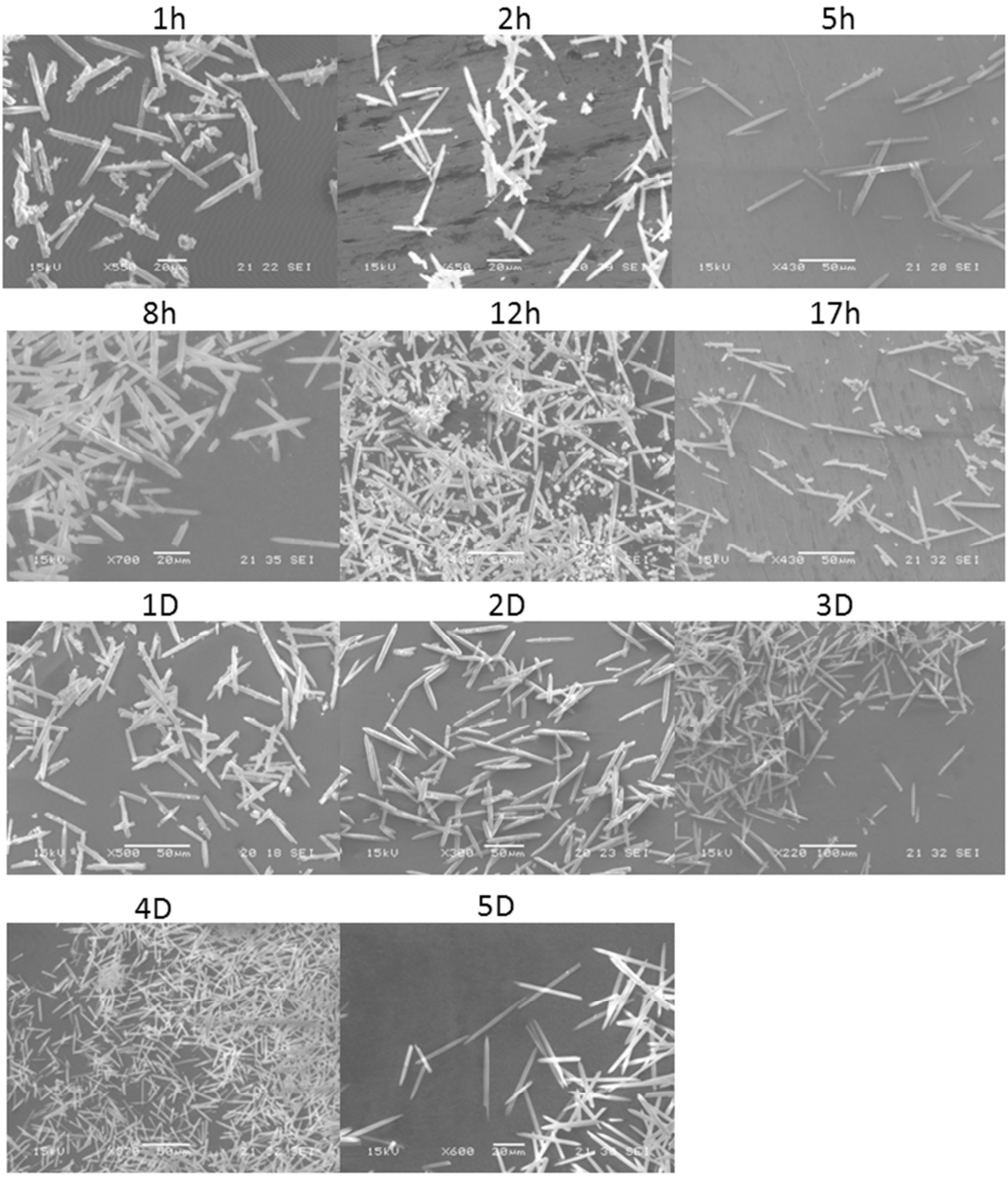

Figure 3.14: *SEM images of CPO-27(Mg) modified with 70% Ni^{2+} and 10% cpmp recorded after different second step reaction times.*

entire range, supporting a single crystal-single crystal mechanism. Images of samples after modification steps of short durations show the presence of a fine grained second phase. Selected area EDX suggests that it contains Ni, with some Mg and P, which is likely a product of rapid precipitation. Images obtained from EDX mapping visualize these small particles consisting mainly of nickel (circles in Figure 3.15). This disappears as heating times increase (and nickel is incorporated in the CPO-27). EDX analysis of the CPO-27 crystals shows that the nickel content increases gradually, levelling out at 55 - 60 mol% Ni after ca. 2 days (Figure 3.16). This is consistent with a solid state replacement of Mg by Ni in the CPO-27 crystals.

TGA analysis of CPO-27 (Mg), CPO-27(Ni) and CPO-27(Mg,Ni) samples where nickel acetate and *cpmp* have been added via the one pot modification procedure confirm the above findings and are shown in Figure 3.16. All samples show a loss of weakly physisorbed water below 373 K, with chemisorbed water gradually leaving up to around 523 K. Comparison of the pure Mg- and Ni-forms indicate that the former material is much more thermally stable, with the onset of framework decomposition decreasing from 673 to 573 K. Notably, the thermal stability of the modified samples decreases as the nickel content increases, which is consistent with inclusion of nickel in the CPO-27 framework.

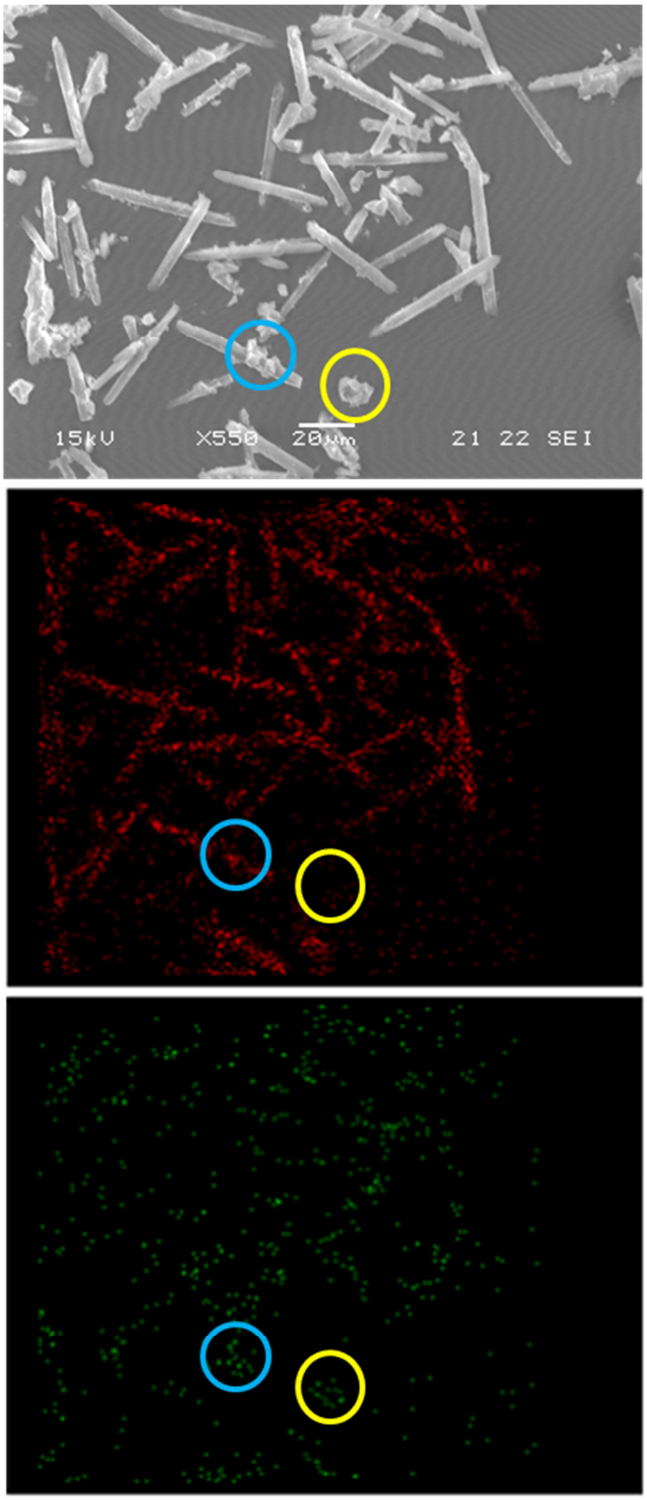

Figure 3.15: *(Top) SEM of CPO-27(Mg) crystals modified with 70% Ni^{2+} and 10% cpmp were heating in second step was stopped after 1h. (Below) Elemental mapping of the same crystal with Mg $K_{\alpha 1}$ (middle) and Ni $K_{\alpha 1}$ (bottom). Circles indicating nickel rich regions of second phase.*

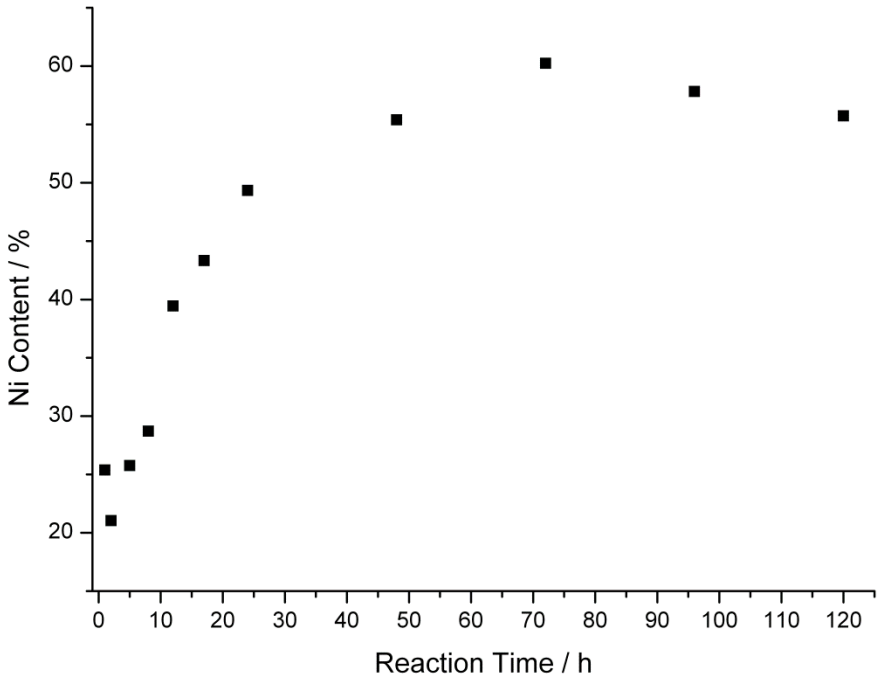

Figure 3.17: *Nickel content of CPO-27 crystals (measured by selected area EDX analysis) prepared by the modification of CPO-27(Mg) by treatment with 70 mol% Ni^{2+}(aq) in the presence of 10 mol% cpmp at 383 K for different durations.*

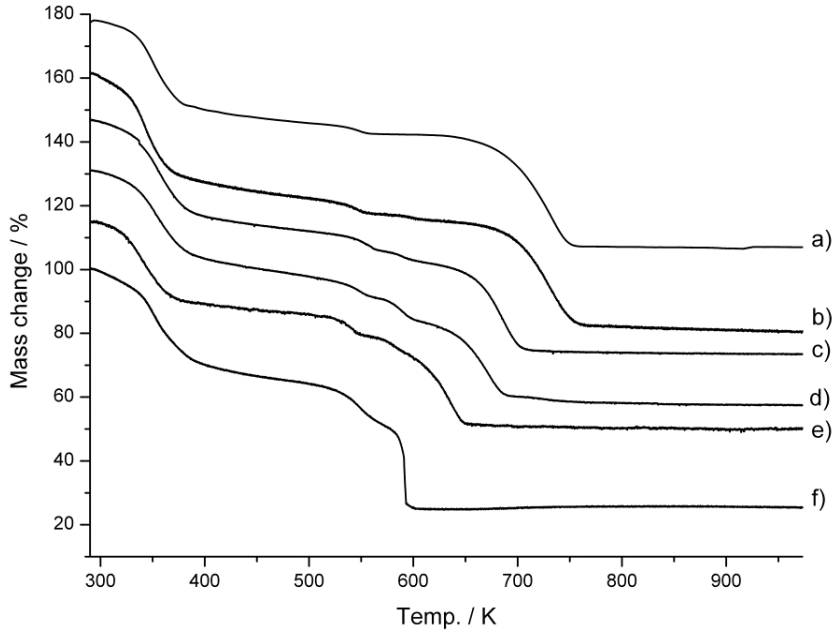

Figure 3.16: *TGA plots (in air at a heating rate of 5 K min^{-1}) of graphs of unmodified (a) Mg and (f) Ni CPO-27. Modified CPO-27(Mg) materials were treated with (b) 10 mol%, (c) 30 mol%, (d) 50 mol% and (e) 70 mol% Ni^{2+}(aq) and 10 mol% 4-carboxypiperidyl-N-methylenephosphonic acid.*

Taken together, the data indicate that there has both been additional CPO-27 crystallisation and also Ni^{2+} has replaced Mg^{2+} throughout the pre-formed crystals of CPO-27(Mg). Although some dissolution and recrystallization of the CPO-27 crystals cannot be ruled out, the similarity in morphology before and after modification suggests that isomorphous replacement is the major process. There is growing evidence that such processes are possible in MOF structures.[32-37] Studies suggest that post-synthetic exchange of ligands and metals are universal in MOF materials with metal to linker bonds being reversible (Figure 3.19).[35] The post-synthetic method appears as approach to introduce certain metals into MOFs that are not accessible through common one step solvothermal synthesis (Figure 3.18).[34] It is likely that hydrated cations can exchange into framework sites from solution and can diffuse along large channels in the structure, from which framework cation sites throughout the crystal can be accessed. The essential role of the acidic anions may be to facilitate removal of Mg^{2+} from the framework and its complexation.

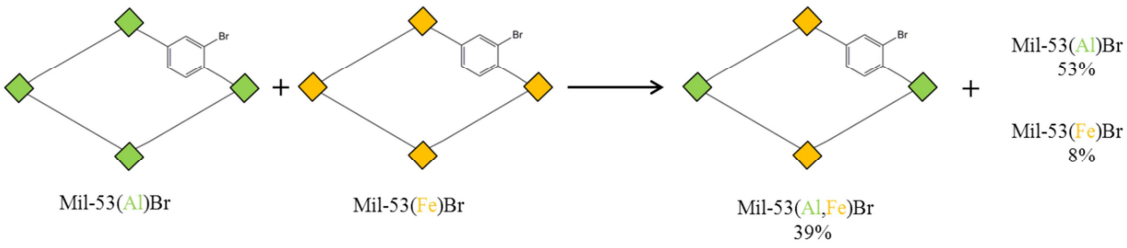

Figure 3.19: *The framework cation exchange reaction in MIL-53.*[35]

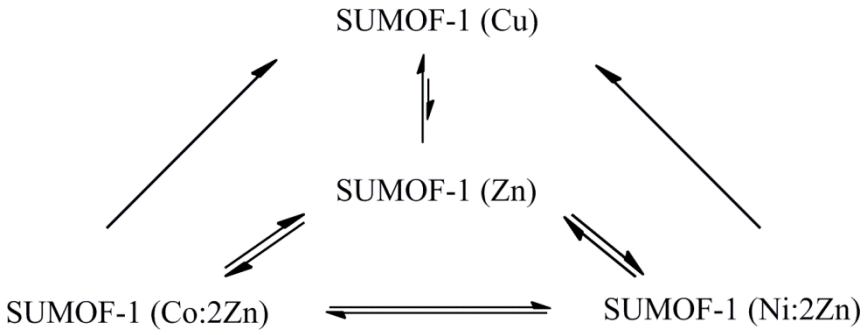

Figure 3.18: *Shows accessibility of different SUMOF-1 species through the post synthetic cation exchange reaction of SUMOF–1 (Zn).*[34]

3.6 Modification with different weak acids

To investigate the use of other acids that might be used in combination with nickel acetate to facilitate the incorporation of Ni^{2+} into the framework sites and to improve the permanent porosity of CPO-27(Mg), 5-carboxybenzimidazole (*cbIm*), trimesic acid N,N′-piperazinebis (methylenephosphonic acid) (*pbmp*) or N,N′-bipiperidine(bis-methylenephosphonic acid) (*bbmp*) and phosphorous acid were added in the second step, with nickel acetate and the acid concentrations both at a level of 10 mol % of the initial Mg^{2+}. In each case the products were crystalline CPO-27 materials (Figure 3.20). The analytical results and measured porosities after heating under vacuum are given in Table 3.6. In each case Ni^{2+} is found by selective area EDX analysis of the crystals (8.4 - 11.7 mol %) and XPS (23.6 - 79.4 mol %) indicates Ni enrichment at the surface, although this is variable (Figure 3.21). The materials give high permanent porosities to N_2, approaching maximum observed literature values in the case of modification by H_3PO_3 (Figure 3.22).

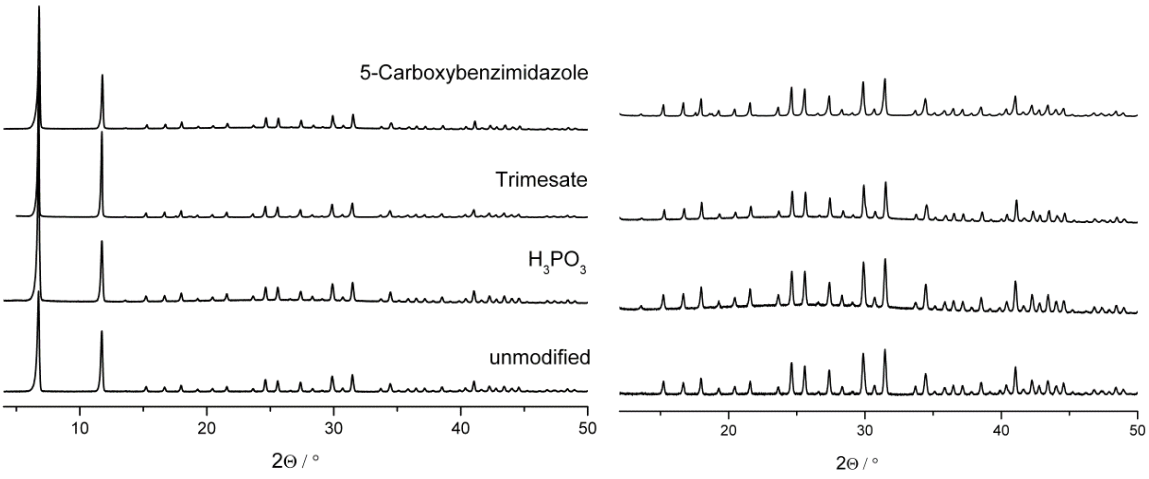

***Figure 3.20**: PXRD of unmodified CPO-27(Mg) and CPO-27(Mg) modified with 10% nickel acetate and different acids.*

These solids also show enhanced uptakes of CO_2 at 0.1 bar and 298 K, of up to 6.3 - 6.7 mmol g^{-1} which are to the best of our knowledge the highest values reported (Table 3.6). It may be that the modification results in a larger fraction of the pore volume (and the metal cations) being accessible. The uptakes measured here are close to these predicted to be the maximum uptakes of CO_2 on CPO-27(Mg) as simulated by Chen et al.[38]

Table 3.6: *Amounts of nickel acetate and different acids (related to the total Mg^{2+} present in the preparations) used for the modification of CPO-27(Mg). N_2 (77 K) and CO_2 (298 K) uptake.*

Amounts used in post-synthesis			Mol% Ni/(Mg+Ni)		Adsorption mmol g^{-1}	
% Ni^{2+}	% Acid	Acid	EDX	XPS	N_2 at 77K (p/p_0 = 0.5)	CO_2 at 298K (p/p_0 = 0.1bar)
10	10	*cbIm*	8.4	43.1	15.3	6.7
10	10	trimesic	11.5	79.4	12.0	6.4
10	10	H_3PO_3	11.7	23.6	17.0	5.6
0	10	H_3PO_3	0.0	0.0	0.3	
Unmodified CPO-27 (Mg)			--	--	0.0	4.8

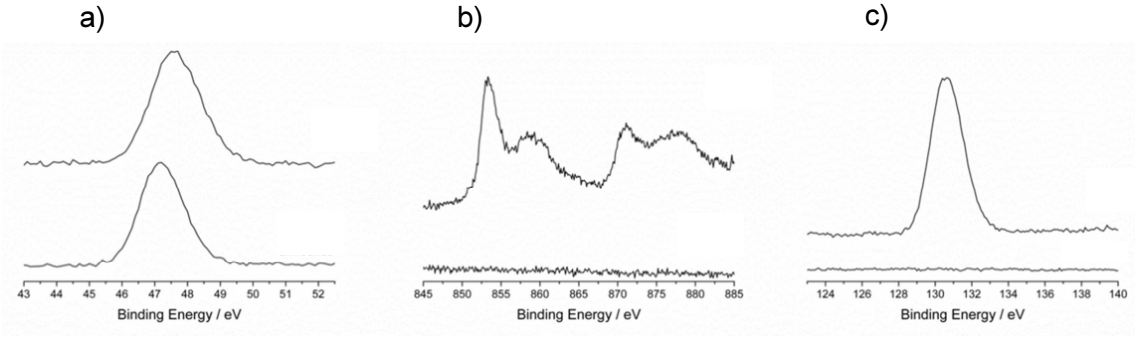

Figure 3.21: *XPS spectra of unmodified CPO-27(Mg) (bottom) and CPO-27(Mg) modified with 10 % nickel and H_3PO_3 modified CPO-27(Mg) (top). Spectra show lines for a) Mg2p, b) Ni2p and c) P2p.*

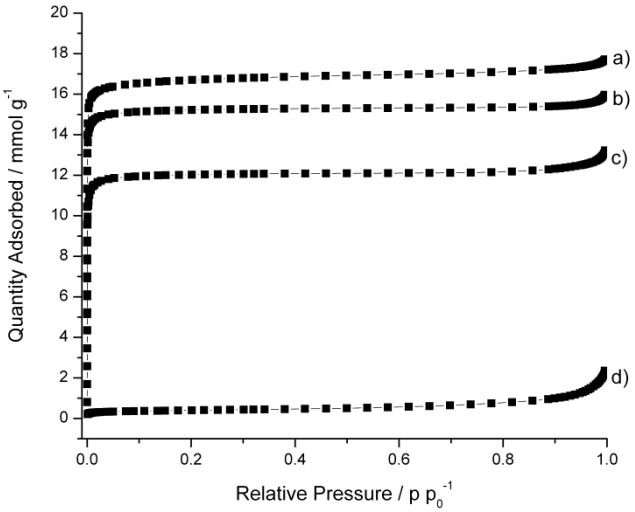

Figure 3.22: *N_2 adsorption (77 K) of CPO-27(Mg) modified with a) 10% phosphorous acid, b) cbIm and c) trimesic acid. d) Refers to unmodified material.*

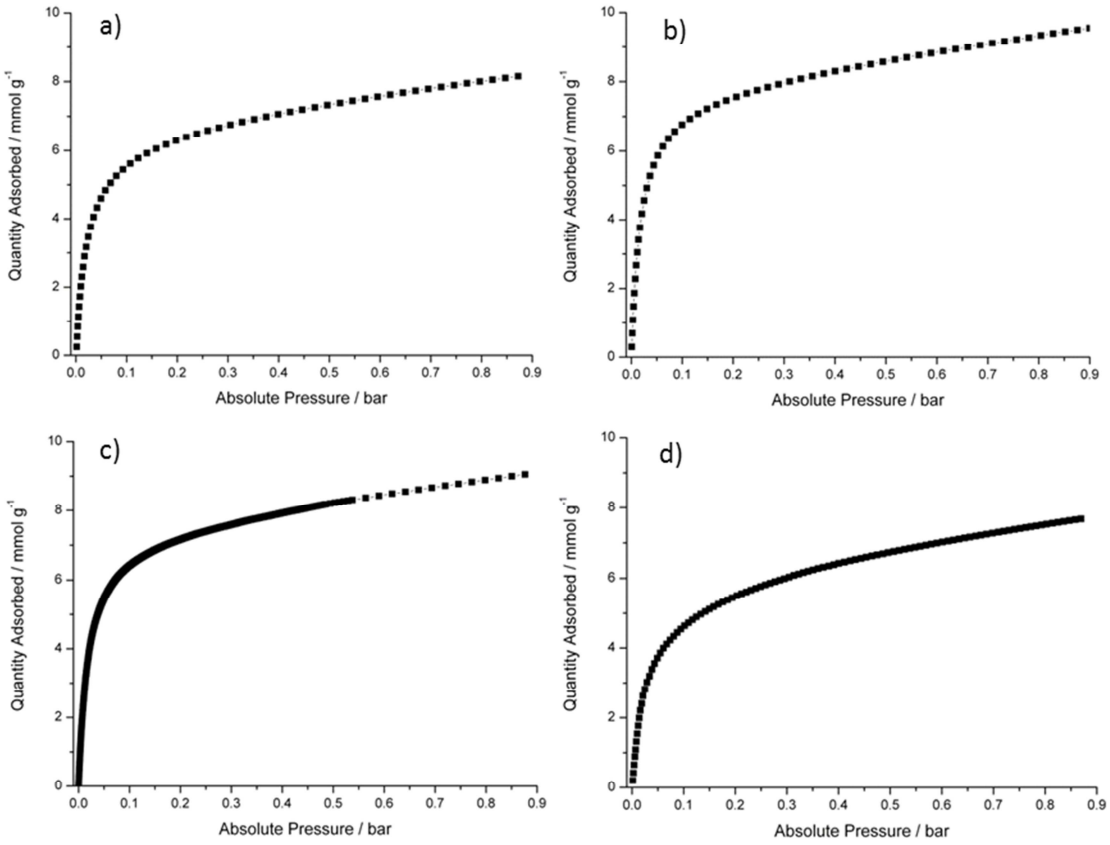

Figure 3.23: *CO_2 adsorption (298 K) of CPO-27(Mg) modified with a) 10% phosphorous acid, b) 10% cbIm, c) 10% trimesic acid and d) unmodified material.*

Repeated CO_2 adsorption experiments at 298 K of either a single or three different samples modified with 10% nickel acetate and 10% *cbIm* show high reproducibility and uptakes between 6.3 and 6.7 mmol g^{-1} at 0.1 bar (Figure 3.24).

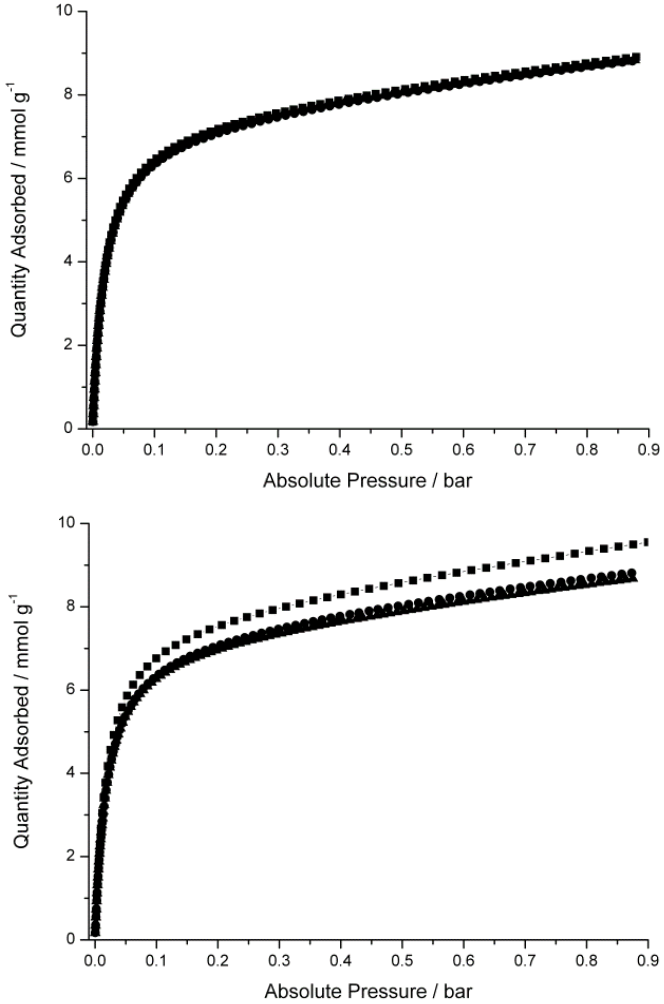

Figure 3.24: *Repeated CO_2 adsorption (298 K) of CPO-27(Mg) modified with 10% nickel acetate and 10% cbIm. Same sample has been activated at 373 K followed by 553 K and measured for 3 times (top), and of CPO-27(Mg) modified with 10% nickel acetate and 10% cbIm. Samples were obtained as described in experimental part from 3 separated synthesis an activated at 373 K followed by 553 K before measured (bottom).*

Further, a CPO-27(Mg) sample of the 10 % $Ni(OAc)_2/H_3PO_3$-modified solid that was repeatedly cycled in alternating flowing Ar at 493 K and CO_2 at 313 K was found to have a stable working capacity of 6.1 mmol g^{-1} under these conditions (Figure 3.25).

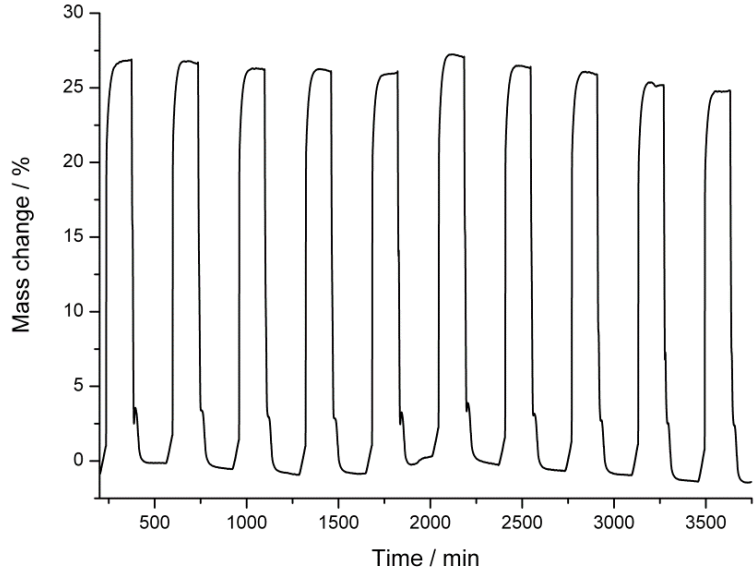

Figure 3.25: *Gravimetric measurement of CO_2 uptake at 1 bar of CPO-27(Mg) modified with 10 % $Ni(OAc)_2$ and H_3PO_3 and 313 K following cycles of desorption in flowing Ar at 433 K.*

Unlike the described experiments above, the addition of nickel and N,N′-piperazinebis (methylenephosphonic acid) [*pbmp*] or N,N′-bipiperidine(bismethylenephosphonic acid) [*bbmp*] as weak acids resulted in the insertion of nickel in CPO-27(Mg) and in crystalline second phases. The physical mixture of the conglomerated particles facilitated the phase separation and eased their separate characterisation. Powder XRD pattern identified the second phases as STA-12 and an unknown phase (Figure 3.26) indexed as a monoclinic unit cell with a = 20.4987 Å, b = 9.9579 Å, c = 14.5187 Å, β = 114.287° when modified with *pbmp* and *bbmp*, respectively. EDX analysis revealed the presence of nickel in both CPO-27 samples suggesting the same mechanism of isomorphous replacement and core-shell crystal growth as found for the materials described above. Further, the second phase obtained with *pbmp* was characterised as mixed metal STA-12(Mg,Ni) containing mainly phosphorous and magnesium next to traces of nickel. X-ray spectroscopy data of the second phase obtained from *bbmp* as additive does not show any nickel, but a 1 : 1 ratio of Mg to P (Table 3.7).

Table 3.7: *Content of additives found in EDX analysis after modifying CPO-27(Mg) with Ni^{2+} and pbmp or bbmp.*

Amounts used in post-synthesis			Products	Mol% Ni/(Mg+Ni)	Mol% P / Mg +Ni	Adsorption (mmol g-1)
% Ni^{2+}	% Acid	Acid	By-product	EDX		N_2 at 77K (p/p_0 = 0.5)
10	10	*pbmp*	CPO-27(Mg,Ni)	11	15	7
			STA-12(Mg,Ni	53	167	--
10	10	*bbmp*	CPO-27(Mg,Ni	10	9	10.5
			Unknown phase	-	100	--

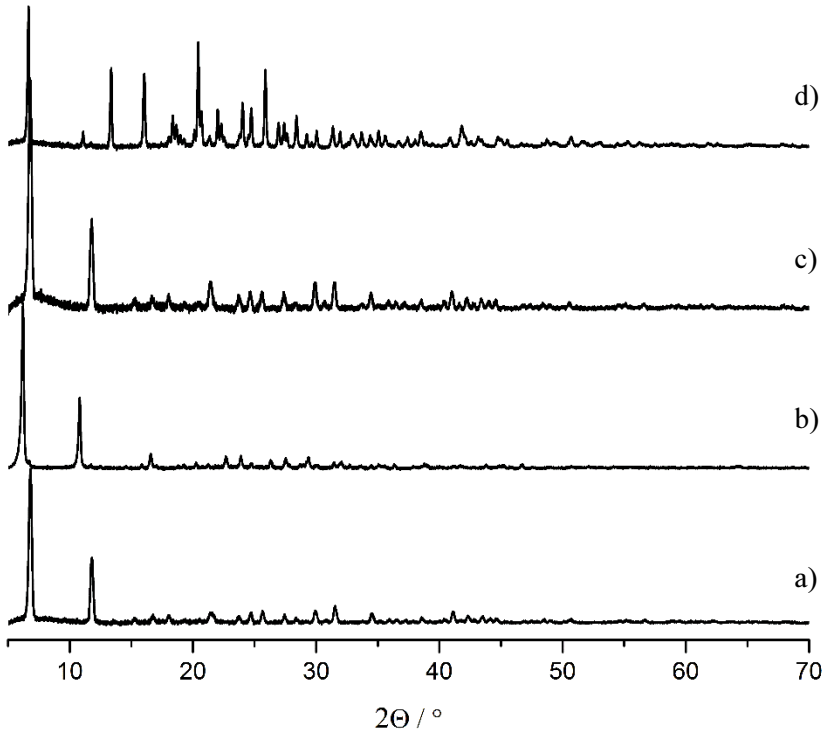

Figure 3.26: *Powder XRD pattern of a) 10 % Ni / pbmp modified CPO-27(Mg) compared to reflections of b) STA-12(Mg,Ni) obtained as minor by-product. Pattern c) resulted from modifying CPO-27(Mg) with 10 % Ni / bbmp and d) its second phase.*

3.7 CO_2 uptake and water stability measured on a Zero Length Column (ZLC)

As part of the IGSCC program carbon dioxide adsorption measurements on a Zero Length Column (ZLC) were carried out in the context of gas uptake and water stability measurements.

CO_2 uptake experiments were conducted on unmodified nickel and magnesium CPO-27. These values are compared with CPO materials modified with 10 - 50 % of nickel and 10 % of various ligands in Figure 3.27. The ZLC experiments reproduce trends found in volumetric and gravimetric measurements (Table 3.3 and Table 3.6), although

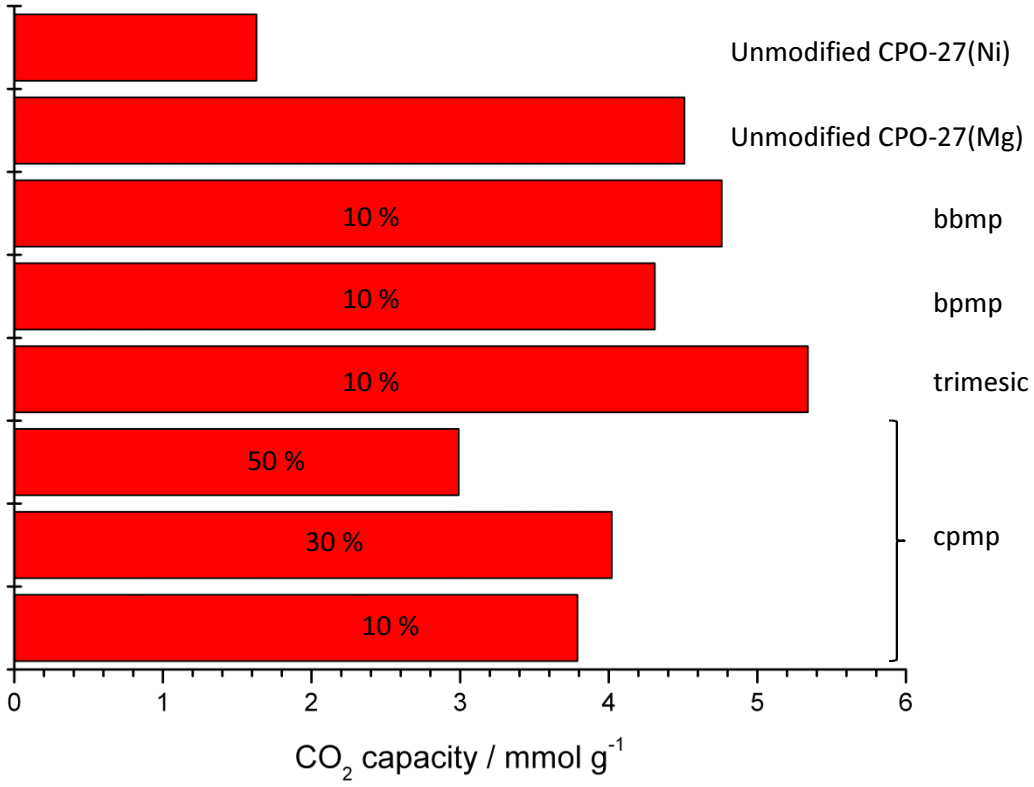

Figure 3.27: *Results of CO_2 uptake from ZLC experiments comparing as prepared nickel and magnesium CPO-27 with modified samples varying the amounts of nickel content and species of weak acids. The data was collected at 305 K and 0.1 bar partial pressure of CO_2. Values in % refer to the amounts of nickel used in the modification step relative to magnesium. With courtesy of Enzo Mangano.*

they give lower uptakes due to the experimental setup of observing desorption processes of CO_2. The highest value of 5.3 mmol g^{-1} was found for the magnesium species modified with 10 % nickel / trimesic acid.

Treated flue gas from coal fired power plants contain certain amounts of water next to nitrogen and carbon dioxide that causes stability, issues in adsorbents, particularly those with open metal sites. In order to investigate the impact of various water contents on as prepared nickel and magnesium CPO-27 and the 10 % nickel / cpmp modified magnesium form, water stability tests were conducted. The adsorbents are exposed to a wet CO_2 gas mixtures followed by activation and the ZLC CO_2 experiment. The results are presented in Figure 3.28 and show the unmodified nickel material has the highest stability over several cycles. Unmodified CPO-27(Mg) gives an increased uptake of 4.5 mmol g^{-1} after the first cycle before gradually losing its ability to adsorb CO_2. During this thesis similar findings were reported by Kizzie et al.[11] The initial increase is probably related to a surface effect rearranging blocking elements at the pore apertures by the exposure to water. Adsorption experiments conducted on the modified magnesium adsorbent show the immediate decrease of CO_2 capacity after the first water exposure ranking this material with the lowest stability. The low stability of the magnesium form compared to the observed performance of CPO-27 (Ni) (Figure 3.28) may be caused by hydrolysis effects at the metal centres caused by carbonic acid formed with CO_2 and water.

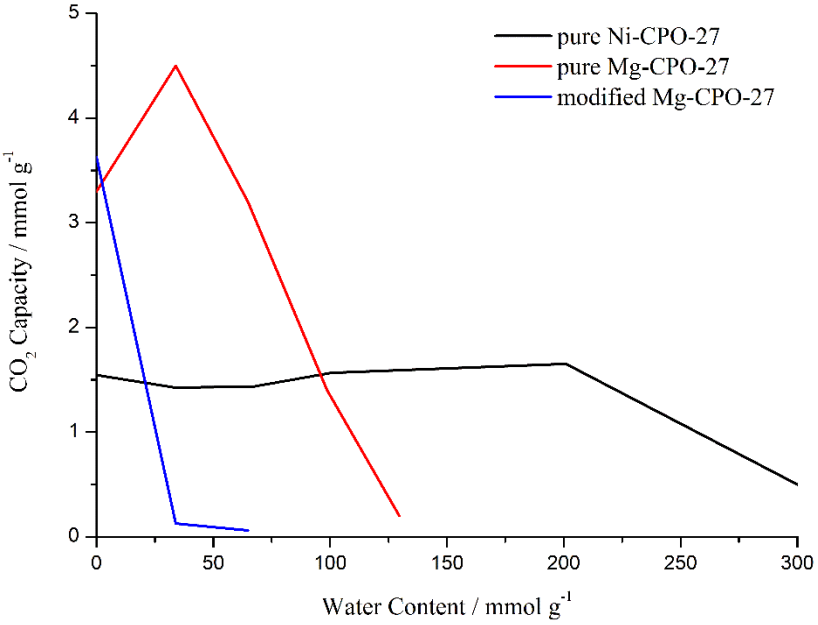

Figure 3.28: *Illustrates the results of the water stability tests obtained from ZLC experiments on unmodified nickel (black), unmodified magnesium (red) and CPO-27 modified with 10 % nickel / cpmp. Courtesy of Enzo Mangano, University of Edinburgh.*

3.8 Applying the Post-Synthesis Modification Method to Nickel and Cobalt CPO-27

The method of modifying CPO-27(Mg) with Ni^{2+} and H_3PO_3 has been extended to assess whether framework cations in CPO-27(Ni) can be replaced by Mg^{2+} or Co^{2+}, or whether the Co^{2+} in CPO-27(Co) could be replaced by Mg^{2+} or Ni^{2+} in a reverse of the observed reaction. However, addition of 50 mol % Mg to the Ni form, for example, only replaced 7.2 % of the Ni^{2+} in the crystals, and even at the surface only 21 mol %, indicating that while the exchange of Mg^{2+} for Ni^{2+} was possible, the replacement of Ni^{2+} by Mg^{2+} was not favoured (Table 3.8). Notably, applying phosphorous acid only to the procedure improves the performance, but with no P observed in bulk or on the surface. One explanation might be the acid acts as a leaching agent, cleaning the surface

and allows more pores to be accessible. Introducing 30 mol% Ni into CPO-27(Co) gave similar results with only 7.3% Ni^{2+} in the bulk material and 24.9 % on the crystal surface being replaced, but giving only small improvement of porosity which might be explained by blocked pores through high ligand concentration on the surface (XPS 85.3 % P) in combination with added nickel (Table 3.9). In fact adding 30 mol % Mg to CPO-27(Co) gives the lowest improvement, and XPS indicates magnesium accumulation on the surface that may cause similar surface effects which led to the low porosity of unmodified CPO-27(Mg) (Table 3.10). The facile replacement of Mg^{2+} by Ni^{2+} in the Mg form may be possible because of the higher solubility of Mg^{2+} over Ni^{2+} or Co^{2+} under these conditions.

Table 3.8: *Different amounts of magnesium acetate and phosphorous acid used in the CPO-27(Ni) modification and compositional ratios determined by EDX and XPS analysis. N_2 (77 K) and CO_2 (298 K) adsorption.*

Mg^{2+} (% original Ni)	Added H_3PO_3 acid (% Ni)	Mg / Mg+Ni	P / Mg+Ni	Mg / Mg+Ni	P / Mg+Ni	Adsorption / mmol g^{-1}	
		EDX	EDX	XPS	XPS	N_2 77K, p/p_0 = 0.5	CO_2 298K, p = 0.1bar
0	0					7	3.4
10	10	0.0	0.0	0	0	12.5	4.0
30	30	3.1	10.8	9.1	14.28	11	3.5
50	50	7.2	21.1	18.4	163.9	10.5	3.4
0	10	0	0	0	0	13.6	--

Table 3.9: *Different amounts of nickel acetate and phosphorous acid used in the CPO-27(Co) modification and compositional ratios obtained via EDX and XPS analysis: N_2 (77 K) and CO_2 (298 K) uptake.*

Ni^{2+} (% original Co)	Added H_3PO_3 acid (% Co)	Ni / Ni+Co	P / Ni+Co	Ni / Ni+Co	P / Ni+Co	Adsorption / mmol g^{-1}	
		EDX	EDX	XPS	XPS	N_2 77K, p/p_0 = 0.5	CO_2 298K, p = 0.1bar
0	0	--	--			0.7	1.7
10	10	0	0	12.5	11.5	12	2.2
30	30	7.3	4.8	24.9	85.3	3	--

Table 3.10: *Results of EDX and XPS analysis after modification of CPO-27(Co) with magnesium acetate and phosphorous acid: N_2 (77 K) and CO_2 (298 K) uptake.*

Mg^{2+} (% original Co)	Added H_3PO_3 acid (% Co)	Mg / Mg+Co	P / Mg+Co	Mg / Mg+Co	P / Mg+Co	Adsorption / mmol g^{-1}	
		EDX	EDX	XPS	XPS	N_2 77K, p/p_0 = 0.5	CO_2 298K, p = 0.1bar
0	0	--	--			0.7	1.7
30	30	2.7	15.5	5.2	1.27	4.5	1.7
0	10	0	13.7	0	1.15	2.7	--

Although enhanced porosity of nitrogen for the nickel and cobalt species can be achieved, the carbon dioxide uptake for both materials shows only little improvement (Figure 3.29 and 3.30).

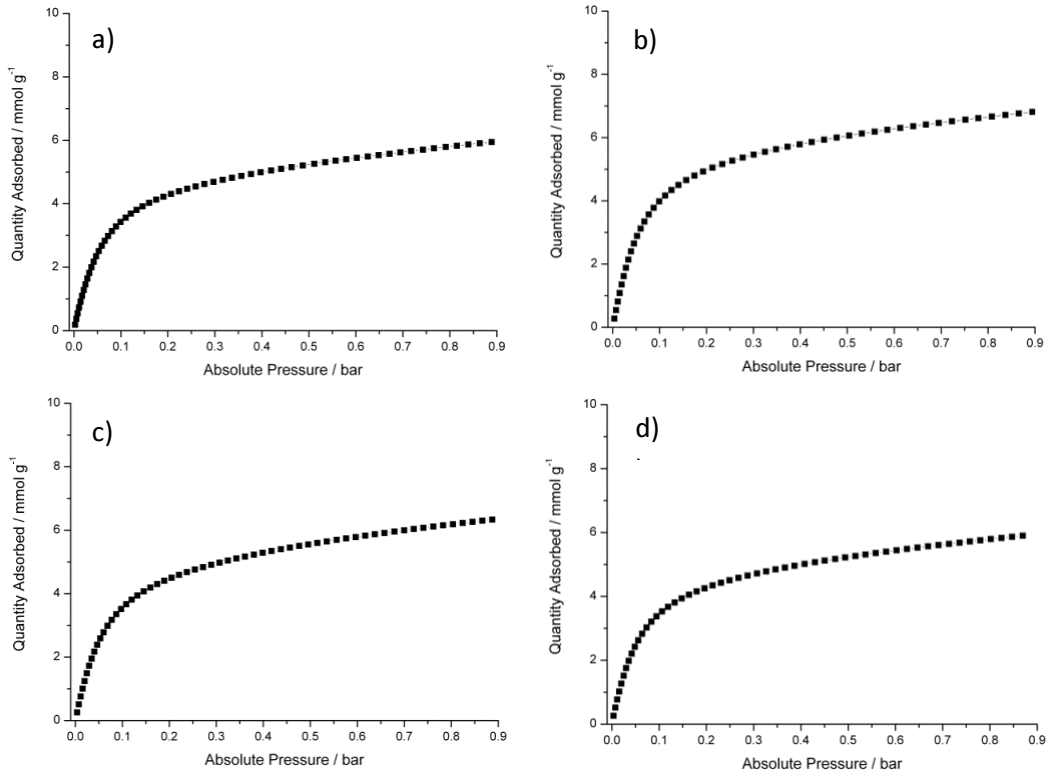

Figure 3.29: *CO_2 (298 K) isotherm of a) unmodified and with b) 10%, c) 30% and d) 50% magnesium and phosphorous acid modified CPO-27(Ni).*

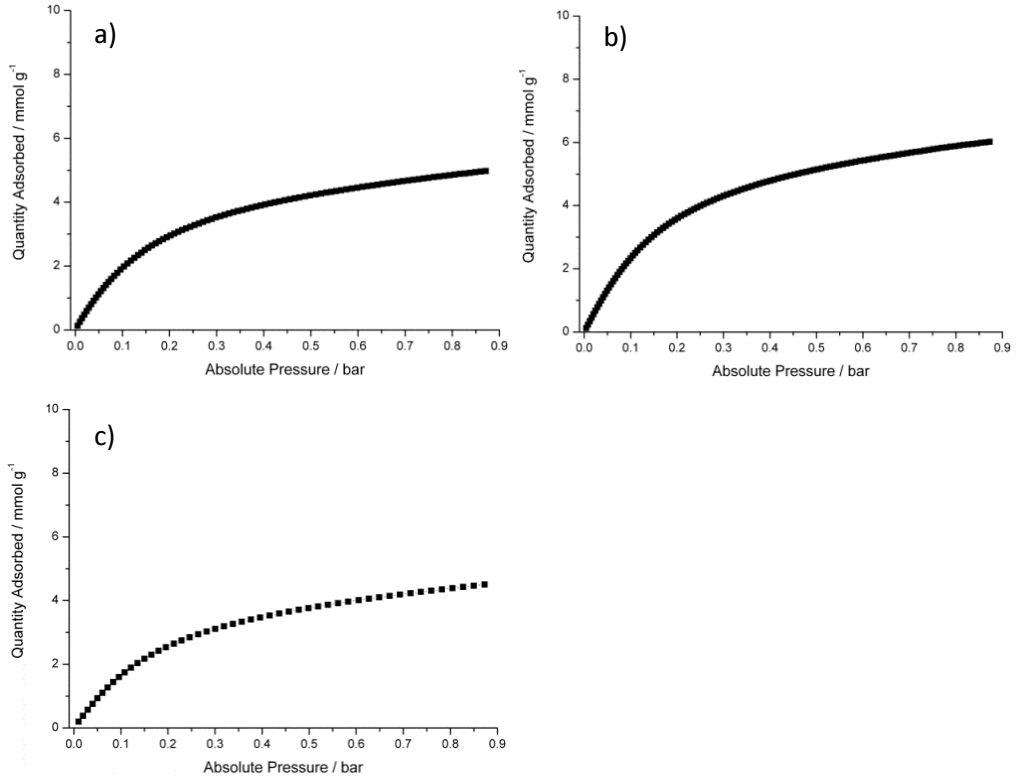

Figure 3.30: *CO_2 (298 K) isotherm of a) unmodified and with a mixture b) 10% nickel acetate / 10% phosphorous acid and c) 30% magnesium acetate / 30% phosphorous acid modified CPO-27(Co).*

Similarly to CPO-27(Mg), the nickel and cobalt analogue of unmodified and modified CPO-27 lose physisorbed water accumulated in the pores at the same temperature, below 373K. Water leaving the framework below 500 K is associated with molecules strongly interacting via chemisorption with unsaturated nickel or cobalt open metal sites. Addition of 10% magnesium acetate and 10 % phosphorous acid to the synthesis of CPO-27(Ni), where no additives were found by EDX or surface sensitive XPS spectroscopy, seems to slightly reduce the structures' thermal stability with a slightly lower decomposition temperature (Figure 3.31). Adding 50 % of magnesium and weak acid, where 7.2 % by EDX and 18.4 % found by XPS (Table 3.8), does not improve thermal stability. Experiments with adding each of magnesium or nickel to the one-pot

modification of CPO-27 (Co) led to the same results with lower thermal stability (Figure 3.32).

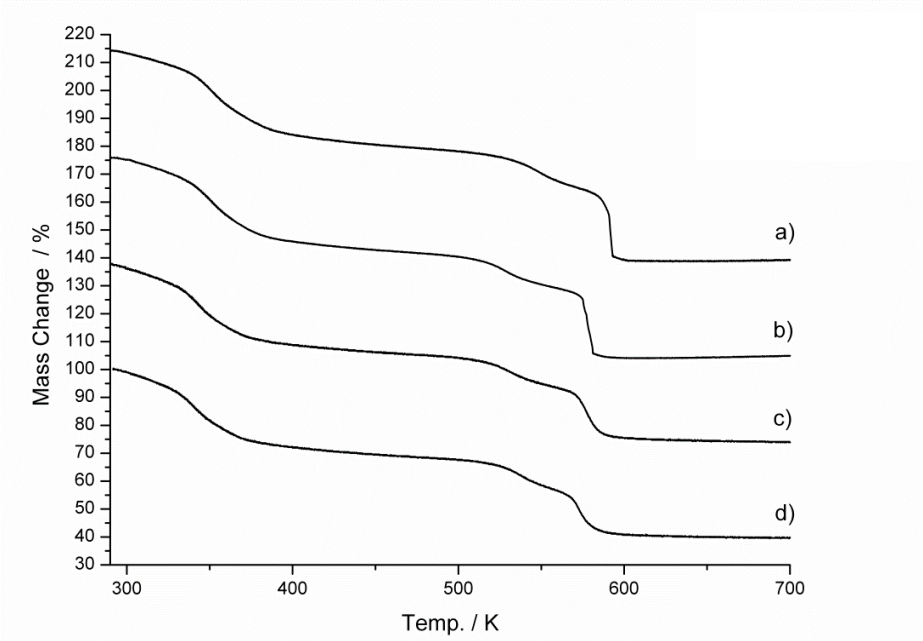

***Figure 3.31**: TGA plots on a) unmodified and with various amounts of nickel acetate and phosphorous acid modified CPO-27(Ni). b) 10%, c) 30%, d) 50% Mg.*

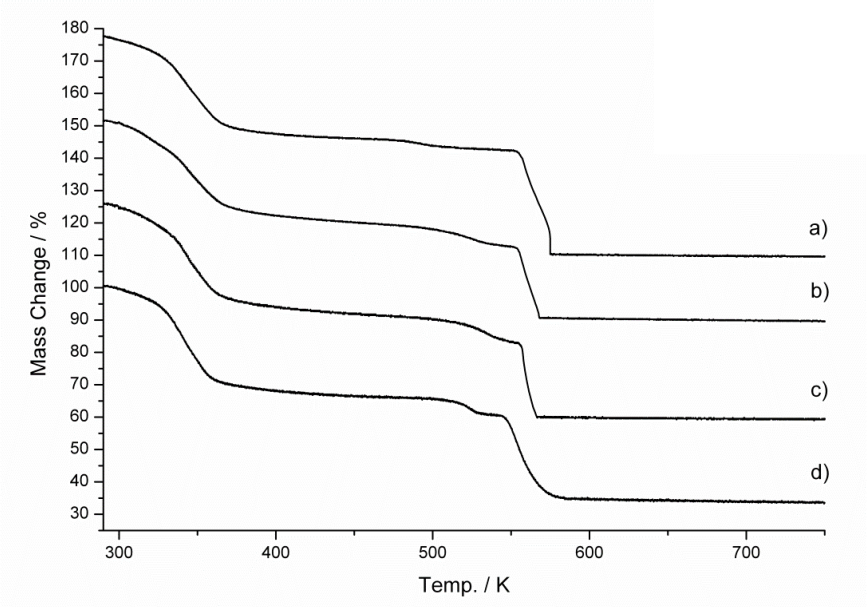

***Figure 3.32:** TGA plots on a) unmodified and with various amounts of metal acetate and phosphorous acid modified CPO-27(Co). b) 30% Mg, c) 30% Ni and d) 10% Ni.*

3.9 PIM1 / CPO-27(Mg) Composite Membrane

Great interest has been drawn by MOF composite membranes in gas separation processes with the aim to improve gas permebility and selectivity of membrane materials.[39-41] In an early stage of this thesis and in collaboration with Dr Christopher Mason, a sample of CPO-27(Mg) modified with 10 % nickel acetate and *cpmp* was sent to the University of Manchester to prepare and test a PIM1 composite membrane. The results are presented in figure 3.33. The Robeson plot[42] reveals that introducing CPO-27 into PIM1 reduces the permeability for membranes treated with ethanol and the composite material with 10 : 1 w / w CPO-27 with little change in selectivity. Increasing the amounts of MOF in the membrane reduces selectivity and at the same time increases the permeability. As a result the desired trespass over the Robeson line was not observed. One reason could be based on incomplete activation of the MOF where chloroform used for generating the membrane composite was removed via

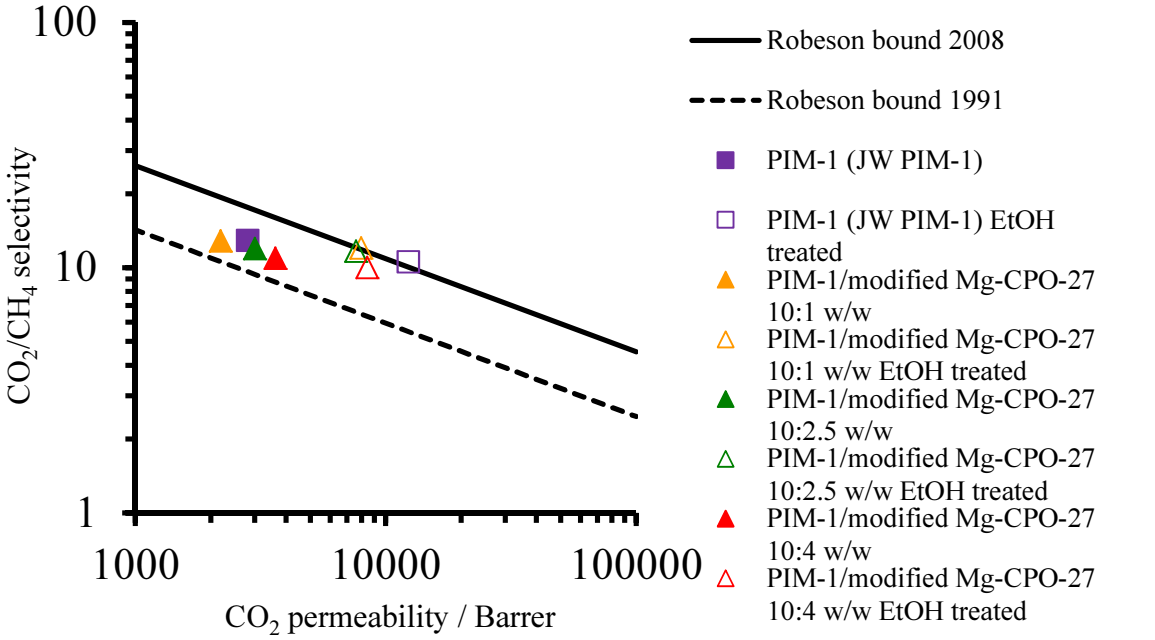

Figure 3.33: *Robeson plot of PIM1 compared with PIM1 / modified CPO-27(Mg composite material. Courtesy of Christopher Mason.*

evaporation in a desiccator leaving pores in CPO-27 filled with solvent: This will be examined in further studies.

3.10 Conclusion

CPO-27(Mg) can be modified by addition of aqueous nickel salts in a one-pot post-synthetic reaction to give Ni modified CPO-27(Mg) solids in which Ni^{2+} is enriched at the surface but also distributed throughout the crystals via isomorphous replacement of Mg^{2+} by Ni^{2+}. This replacement is facilitated by the addition of weak acids, including phosphonic and carboxylic acids and also phosphorous acid. Bulk Ni^{2+} contents up to 66.5 % have been achieved, but it is likely that higher values are possible. Mg modified CPO-27(Ni) and Ni or Mg modified CPO-27(Co) in a reverse replacement (of Ni^{2+} by Mg^{2+} or Co by Ni or Mg) are more challenging, which is likely to be due to the lower or similar solubility of added metal salts over the framework cation. The post-synthetic isomorphous replacement of less soluble by more soluble metal cations in metal organic frameworks reported previously for other MOFs therefore appears to be more generally applicable.

Replacement of just 10% of the Mg^{2+} by Ni^{2+} in CPO-27(Mg) is sufficient to greatly improve the permanent porosity of thermally activated materials, as measured by N_2 uptake at 77 K. This is attributed to improvement of the surface permeability to weakly interacting gases. In the case of CO_2, simple thermal activation gives materials that remain at least partially porous to CO_2 at 298 K, indicating that the more strongly interacting CO_2 can diffuse into the pore system at the higher temperatures. Nevertheless, some of the modification procedures do increase the observed porosity to

CO_2, achieving uptakes of up to 6.3 - 6.7 mmol g^{-1}. However, water stability tests found the unmodified nickel CPO-27 more stable compared to the magnesium forms. The adsorption of CO_2 on these modified materials under dry conditions is found to be repeatable over several cycles. Applying modification to CPO-27(Ni) and CPO-27(Co) yields increased porosity to nitrogen but little improvement in carbon dioxide uptakes.

The crystal morphology of CPO-27(Mg) is not affected by the modification process even at higher additive content. Increase of Ni^{2+} occurs not only via isomorphous replacement of Mg^{2+} but also through additional growth of a nickel-rich layer on the crystal surface. Throughout the modification step CPO-27(Mg) crystals remain unchanged over time and serve as rigid framework body for the thermodynamically driven process of replacement and growth.

3.11 References

1. A. R. Millward and O. M. Yaghi, *J. Am. Chem. Soc.*, 2005, **127**, 17998-17999.
2. P. D. C. Dietzel, R. Blom and H. Fjellvåg, *Eur. J. Inorg. Chem.*, 2008, **2008**, 3624-3632.
3. Z. R. Herm, R. Krishna and J. R. Long, *Micropor. Mesopor. Mat.*, 2012, **157**, 94-100.
4. A. Betard, D. Zacher and R. A. Fischer, *CrystEngComm*, 2010, **12**, 3768-3772.
5. E. J. Granite and H. W. Pennline, *Ind. Eng. Chem. Res.*, 2002, **41**, 5470-5476.
6. K. B. Lee and S. Sircar, *AIChE Journal*, 2008, **54**, 2293-2302.
7. P. D. C. Dietzel, V. Besikiotis and R. Blom, *J. Mater. Chem.*, 2009, **19**, 7362-7370.
8. S. R. Caskey, A. G. Wong-Foy and A. J. Matzger, *J. Am. Chem. Soc.*, 2008, **130**, 10870-10871.

9. D. Britt, H. Furukawa, B. Wang, T. G. Glover and O. M. Yaghi, *Proc. Natl. Acad. Sci. U.S.A.*, 2009, **106**, 20637.

10. J. A. Mason, K. Sumida, Z. R. Herm, R. Krishna and J. R. Long, *Energ. Environ. Sci.*, 2011, **4**, 3030-3040.

11. A. C. Kizzie, A. G. Wong-Foy and A. J. Matzger, *Langmuir*, 2011, **27**, 6368-6373.

12. J. Liu, Y. Wang, A. I. Benin, P. Jakubczak, R. R. Willis and M. D. LeVan, *Langmuir*, 2010, **26**, 14301-14307.

13. J. Liu, J. Tian, P. K. Thallapally and B. P. McGrail, *J. Phys. Chem. C*, 2012, **116**, 9575-9581.

14. J. L. C. Rowsell and O. M. Yaghi, *J. Am. Chem. Soc.*, 2006, **128**, 1304-1315.

15. L. Mitchell, B. Gonzalez-Santiago, J. P. S. Mowat, M. E. Gunn, P. Williamson, N. Acerbi, M. L. Clarke and P. A. Wright, *Cat. Sci. Tech.*, 2013, **3**, 606-617.

16. P. L. Llewellyn, S. Bourrelly, C. Serre, A. Vimont, M. Daturi, L. Hamon, G. De Weireld, J.-S. Chang, D.-Y. Hong, Y. Kyu Hwang, S. Hwa Jhung and G. Férey, *Langmuir*, 2008, **24**, 7245-7250.

17. J. T. Hupp and O. K. Farha, *U.S. Pat. Appl. Publ.*, 2011, **US 20110144367 A1 20110616**.

18. A. P. Nelson, O. K. Farha, K. L. Mulfort and J. T. Hupp, *J. Am. Chem. Soc.*, 2008, **131**, 458-460.

19. O. K. Farha, I. Eryazici, N. C. Jeong, B. G. Hauser, C. E. Wilmer, A. A. Sarjeant, R. Q. Snurr, S. T. Nguyen, A. Ö. Yazaydın and J. T. Hupp, *J. Am. Chem. Soc.*, 2012, **134**, 15016-15021.

20. M. T. Wharmby, G. M. Pearce, J. P. S. Mowat, J. M. Griffin, S. E. Ashbrook, P. A. Wright, L.-H. Schilling, A. Lieb, N. Stock, S. Chavan, S. Bordiga, E. Garcia, G.

D. Pirngruber, M. Vreeke and L. Gora, *Micropor. Mesopor. Mat.*, 2012, **157**, 3-17.

21. K. Szelagowska-Kunstman, P. Cyganik, M. Goryl, D. Zacher, Z. Puterova, R. A. Fischer and M. Szymonski, *J. Am. Chem. Soc.*, 2008, **130**, 14446-14447.
22. T. Li, J. E. Sullivan and N. L. Rosi, *J. Am. Chem. Soc.*, 2013, **135**, 9984-9987.
23. P. Cubillas, M. W. Anderson and M. P. Attfield, *Cryst. Growth Des.*, 2013, **13**, 4526-4532.
24. M. Faustini, J. Kim, G.-Y. Jeong, J. Y. Kim, H. R. Moon, W.-S. Ahn and D.-P. Kim, *J. Am. Chem. Soc.*, 2013, **135**, 14619-14626.
25. E. Mangano, S. Brandani, M. C. Ferrari, H. Ahn, D. Friedrich, M. L. Lozinska, P. A. Wright, J. Kahr, R. Morris, M. Croad, N. McKeown, H. Shamsipour and P. Budd, *Ener. Proc.*, 2013, **37**, 40-47.
26. P. D. C. Dietzel, B. Panella, M. Hirscher, R. Blom and H. Fjellvag, *Chem. Commun.*, 2006, 959-961.
27. S. Chavan, F. Bonino, J. G. Vitillo, E. Groppo, C. Lamberti, P. D. C. Dietzel, A. Zecchina and S. Bordiga, *Phys. Chem. Chem. Phys.*, 2009, **11**, 9811-9822.
28. A. Das, P. D. Southon, M. Zhao, C. J. Kepert, A. T. Harris and D. M. D'Alessandro, *Dalton Trans.*, 2012, **41**, 11739-11744.
29. P. D. C. Dietzel, R. E. Johnsen, R. Blom and H. Fjellvag, *Chem. Eur. J.*, 2008, **8**, 2389-2397.
30. N. Stock, K. Karaghiosoff and T. Bein, *Z. Anorg. Allg. Chem.* , 2004, **630**, 2535 - 2540.
31. C. Serre, N. Stock, T. Bein and G. Férey, *Inorg. Chem.*, 2004, **43**, 3159-3163.
32. O. Karagiaridi, M. B. Lalonde, W. Bury, A. A. Sarjeant, O. K. Farha and J. T. Hupp, *J. Am. Chem. Soc.*, 2012, **134**, 18790-18796.

33. Z. Wei, W. Lu, H.-L. Jiang and H.-C. Zhou, *Inorg. Chem.*, 2013, **52**, 1164-1166.

34. Q. Yao, J. Sun, K. Li, J. Su, M. V. Peskov and X. Zou, *Dalton Trans.*, 2012, **41**, 3953-3955.

35. M. Kim, J. F. Cahill, H. Fei, K. A. Prather and S. M. Cohen, *J. Am. Chem. Soc.*, 2012, **134**, 18082-18088.

36. M. Lalonde, W. Bury, O. Karagiaridi, Z. Brown, J. T. Hupp and O. K. Farha, *J. Mater. Chem. A*, 2013, **1**, 5453-5468.

37. H. Fei, J. F. Cahill, K. A. Prather and S. M. Cohen, *Inorg. Chem.*, 2013, **52**, 4011-4016.

38. L. Chen, C. A. Morrison and T. Düren, *J. Phys. Chem. C*, 2012, **116**, 18899-18909.

39. H. B. Tanh Jeazet, C. Staudt and C. Janiak, *Dalton Trans.*, 2012, **41**, 14003-14027.

40. F. Zhang, X. Zou, X. Gao, S. Fan, F. Sun, H. Ren and G. Zhu, *Adv. Funct. Mater.*, 2012, **22**, 3583-3590.

41. J. A. Thompson, K. W. Chapman, W. J. Koros, C. W. Jones and S. Nair, *Micropor. Mesopor. Mat.*, 2012, **158**, 292-299.

42. L. M. Robeson, *J. Membrane Sci.*, 1991, **62**, 165-185.

4. Structure and Adsorption of Zinc Nitroimidazolate ZIFs

4.1 Introduction

ZIF-8 is one of the most widely studied zeolitic imidazolate materials. Its framework has the SOD topology and was reported first in 2006 [1, 2] Investigations have revealed a broad range of potential applications in fields from gas adsorption and separation processes to catalysis.[2-7] Various isoreticular structures of ZIF-8 have been reported.[2, 8-10] One of these, ZIF-65, made up from nitroimidazole linkers was published with cobalt (Co^{2+}) nodes in 2008 by Yaghi et al.[11] The zinc analogue was synthesized recently by Banerjee et al.[12] and they have subsequently shown that the reaction of cobalt nitrate with NIm with a careful choice of solvent and reaction time yields initially a large pore cobalt analogue of ZIF-11 that then recrystallizes to give the thermodynamically more stable SOD product, ZIF-65.[13] Tian et al. report a cadmium nitroimidazole (CdIF-8) with the SOD topology and slightly longer M-N bond distances.[14]

The work of this thesis investigates further the single-linker synthesis including NIm in ZIFs and discusses the zinc analogue of ZIF-65, a $Zn(NIm)_2$ in SOD topology, with the aim of generating a more environmentally-acceptable (Zn rather than Co) material for gas separation processes. The structure directing action of the NIm linker is then developed in later chapters in this thesis, within the context of synthesising mixed ligand ZIFs.

Remarkably, simple removal of DMF in the resultant ZIF-65(Zn) via heating results in a phase change to a material that retains high porosity to nitrogen and carbon dioxide.

Solvent exchange reactions in MeOH combined with its removal show the direct phase transformation can be driven nearly to completion. The phase change was found to be reversible upon exposure to the removed solvent. Additional studies of zinc and NIm as precursors for ZIF synthesis in methanol as the solvent gave a $Zn(NIm)_2$ ZIF with a previously unreported topology.

4.2 Experimental

4.2.1 Synthesis of ZIF-65(Zn)

Zinc nitrate hexahydrate (1 mmol, 297.5 mg, Aldrich) and 2-nitroimidazole (2 mmol, 226.2 mg, Alfa Aesar) were placed in a 40 ml Teflon-lined steel autoclave and dissolved in 15 ml DMF or DEF (Aldrich). The solution was heated to 383 K for 1 day and then allowed to cool to room temperature. The red crystalline material was filtered and washed three times with DMF before drying at room temperature (198 mg, 54 %). Elemental analysis for as-prepared $Zn(NIm)_2$ •1DMF, $C_9\ H_{11}\ N_7\ O_4\ Zn_1$ found % (calc. %): C 29.7 (29.8), H 3.0 (3.1), N 26.8 (27.0), $Zn(NIm)_2$ •0.8DEF•0.5HCOOH, yield (178 mg, 43 %) $C_{52.5}\ H_{69}\ N_{34}\ O_{29}\ Zn_5$ found % (calc. %): C 31.8 (32.0), H 3.6 (3.5), N 23.8 (24.2). Methanol exchange was carried out on the as-prepared material obtained from DMF synthesis (170 mg) which was gently ground to accelerate the solvent exchange. The material was then placed in a beaker and immersed in 150 ml MeOH. After 7 days the solid was filtered, washed in MeOH and dried at room temperature (128 mg). Elemental analysis of ZIF-65(Zn) that was MeOH exchanged and heated to

393 K; $Zn(NIm)_2$, $C_6\ H_4\ N_6\ O_4\ Zn_1$ found % (calc. %): C 24.9 (24.9), H 1.3 (1.4), N 28.8 (29.0).

4.2.2 Synthesis of a Novel Zinc Nitroimidazolate

A novel zinc nitroimidazolate was obtained following a modified version of the synthesis of ZIF-65(Zn) described above. A solution of zinc nitrate hexahydrate and 2-nitroimidazole in 15 ml methanol was sealed in a Teflon-lined steel autoclave and heated to 383 K for 3 days. After cooling to room temperature bright green crystals were filtered and washed three times with methanol and dried in air (238 mg, 82%). Elemental analysis of as-prepared $Zn(NIm)_2$, $C_6\ H_4\ N_6\ Zn_1$ found % (calc. %): C 25.0 (24.9), H 1.4 (1.2), N 28.8 (29.0).

4.3 Results and Discussion

The published synthesis procedure for ZIF-65(Co)[11] was adopted using zinc instead of cobalt nitrate under solvothermal conditions in DMF giving a highly crystalline phase of ZIF-65(Zn) (Figure 4.1). Its purity was proven by PXRD (Figure 4.2) and indexing gave a cubic unit cell with a = 17.48 Å, but the micro crystalline material was not suitable for single crystal XRD. The chemical composition was obtained via elemental analysis and yielded $Zn(NIm)_2$•DMF. Further structural information was gained by Rietveld refinement of the structure against laboratory powder XRD (Figure 4.3, Table 4.1 and 4.2) and from solid state NMR.

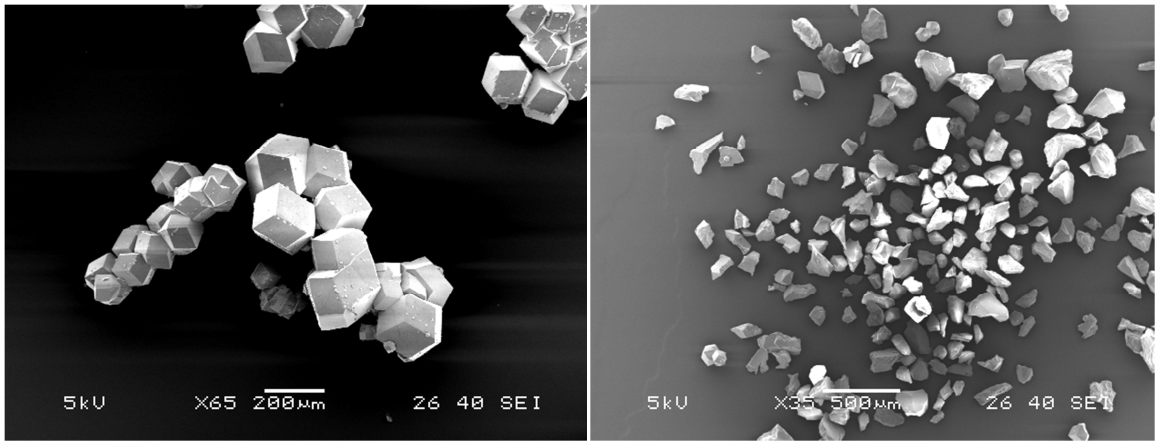

Figure 4.1: *SEM images of as-prepared ZIF-65(Zn) (left) and after methanol exchange followed by heating at 383 K for 16 h.*

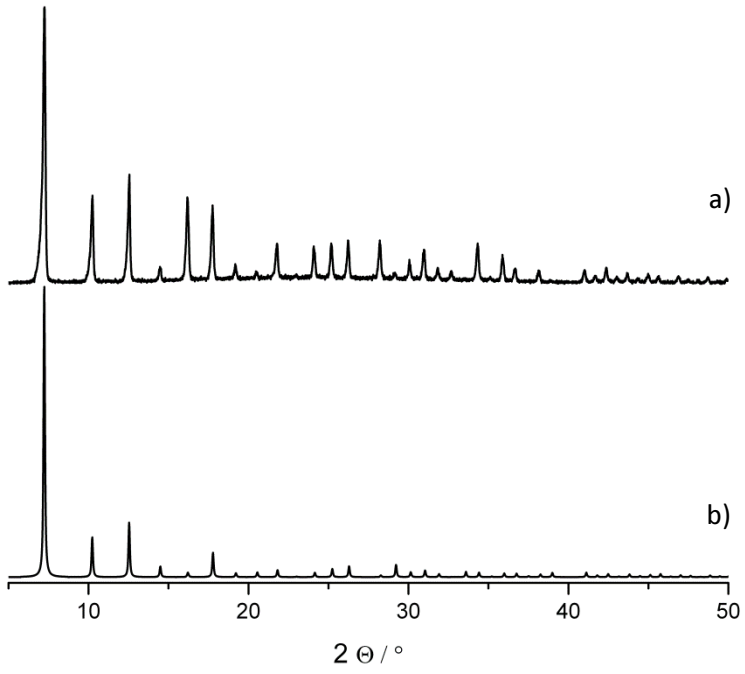

Figure 4.2: *Powder XRD pattern of a) as-prepared ZIF-65(Zn) compared with a simulated pattern of its b) cobalt analogue.*

Despite the high crystallinity of ZIF-65(Zn) synthesis failed to yield single crystals amenable for single crystal diffraction, but it was possible to derive structural information via Rietveld refinement from laboratory powder XRD data using ZIF-65(Co) as a starting model (Table 4.1, Figure 4.3).[11]

Table 4.1: *Crystallographic data of Rietveld refined SOD ZIF-65(Zn), $Zn(NIm)_2x4O$*

Refined composition	$C_6N_6O_6Zn$
Formula mass [g / mol]	317.4
Space group	*I -4 3 m*
Z	12
a [Å]	17.4785(4)
b [Å]	17.4785(4)
c [Å]	17.4785(4)
α [°]	90
β [°]	90
γ [°]	90
V [$Å^3$]	5339.67(33)
λ [Å]	1.54056
2Θ range [°]	3 - 70.0
No. of reflections	6700
Rp	0.0647
Rwp	0.0864
$R(F^2)$	0.13749

Bond restraints were applied to C-C, N-C, N-O, N-N and Zn-N bond lengths during the refinement process. The refined cubic unit cell dimension of 17.4784(5) Å was found to be slightly larger than that observed for ZIF-65(Co), due to larger Zn-N bond length of 2.114 Å compared to 2.022 Å for Co-N bonds. Residual electron density within the voids was determined using Fourier mapping implemented in the EXPGUI/GSAS software package and modelled as isolated solvent 'oxygen' atoms. The typical SOD type topology, as also seen in ZIF-65(Co), ZIF-8 and several other examples of single linker ZIFs with functional groups at position 2 of the imidazolate linker consists of *β*-

cages that are built up of 4mr and 6mr (Figure 4.4).[1, 8, 15] Each cage comprises 24 zinc atoms and is constructed of six 4mr where each of them is surrounded by four 6mrs.

Table 4.2: *Atomic positions and occupancies obtained from Rietveld refined of ZIF-65(Zn), $Zn(NIm)_2 \bullet 4O$.*

Atom	x	y	z	Occ	Uiso	Multiplicity
C1A	0.1292(5)	0.4749(8)	0.1292(5)	1	0.0383(22)	24
C2A	0.1662(4)	0.5764(5)	0.2214(5)	1	0.0383(22)	48
N1A	0.1083(4)	0.5124(6)	0.19761(31)	1	0.0383(22)	48
N2A	0.0814(6)	0.4234(8)	0.0814(6)	1	0.0383(22)	24
O1A	0.1153(4)	0.40338(33)	0.02490(33)	1	0.0383(22)	48
Zn1T	0.25	0.5	0	1	0.0354(10)	12
OS1	0.1734(9)	0	0	1	0.332(9)	12
OS2	0.2149(9)	0.2149(9)	0.2149(9)	1	0.332(9)	8
OS3	0.8403(11)	0.1597(11)	0.1597(11)	1	0.332(9)	8
OS4	0.1656(5)	0.1656(5)	-0.0272(11)	1	0.332(9)	24

As a result every NIm linker within a 4mr shows the same conformation (Figure 4.4, 4.5a,c). This structural feature can also be found in NIm-only 4mrs in mixed linker ZIFs as seen in later chapters (edge sharing 4mr in RHO structure 4 and structures with GME topology in chapter 5). In this case $-NO_2$ functional groups point towards 4mr centres and away from 6mr leaving 6mr windows, 3.1 Å in free diameter, unblocked and so enable solvent molecules to enter and leave the open cavity (Figure 4.4, Figure 4.5a, b).

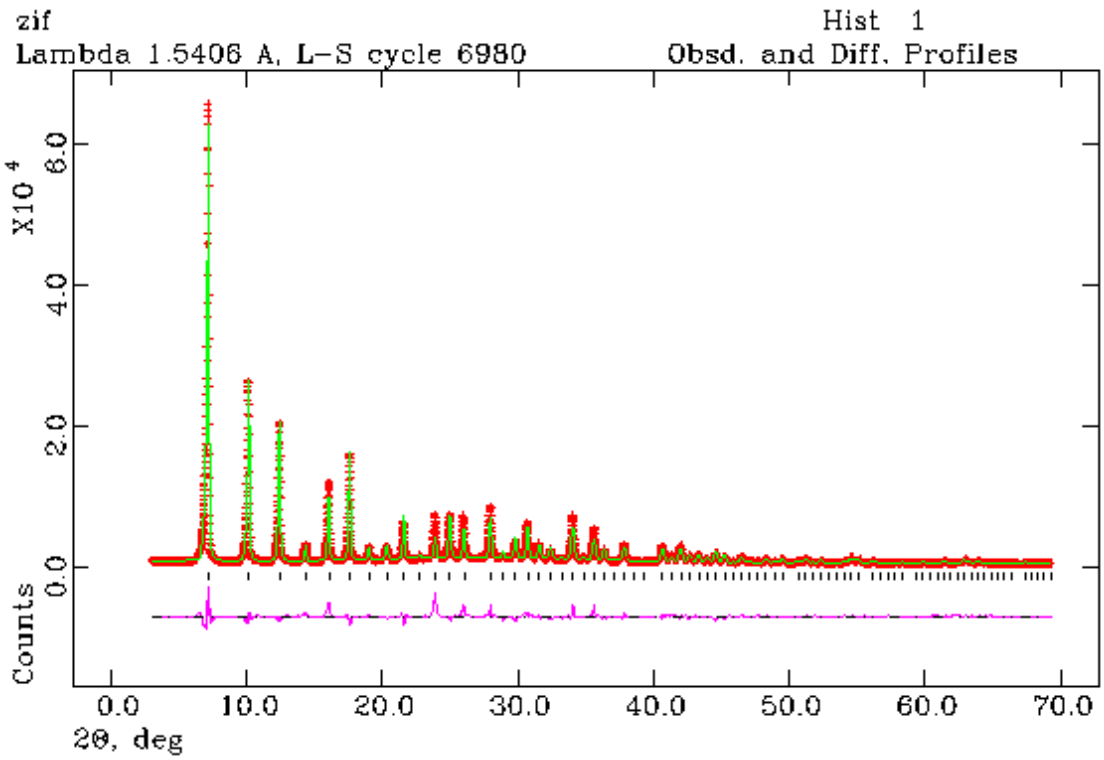

***Figure 4.3**: Rietveld plot of the structural refinement of ZIF-65(Zn) against lab X-ray $CuK_{\alpha 1}$ powder diffraction data (λ = 1.5406 Å, Rwp = 0.11210). Observed pattern, red crosses; fitted profile in green; difference curve between observed and calculated pattern in pink.*

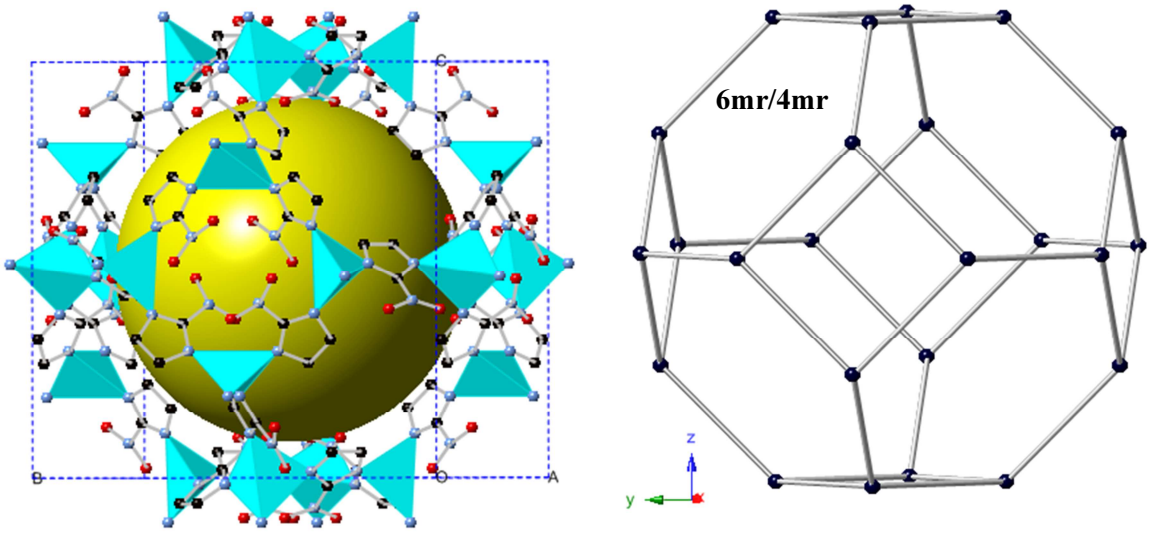

***Figure 4.4:** Illustration of (left) SOD topology built up of 4mr and 6mr rings. Black balls indicate zinc positions, (right) Ball and stick model with space filled cavity demonstrating open pore volume. Zn (turquoise), O (red), N (blue) and C (black), H omitted for clarity.*

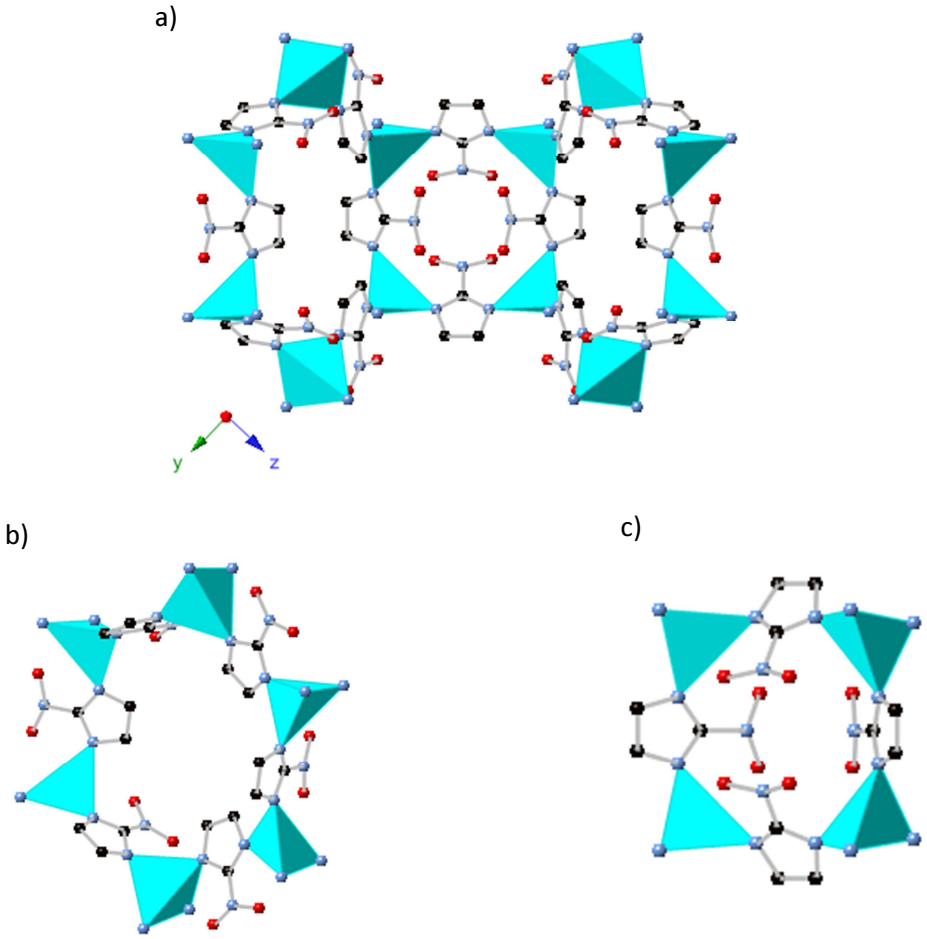

Figure 4.5: *Diagrams showing features of the SOD topology in ZIF-65(Zn) with a) 4mr connected to 6mr building β-cages. Windows are present due to b) nitro functionalities pointing away from 6mr window but the nitro groups c) block smaller 4mr windows. C black, N blue, O red, Zn turquoise, H not shown.*

Thermogravimetric analysis revealed DMF leaves the framework at 500 K and the framework decomposes at 550 K. The complete removal of solvent was proven by TGA collected after previously heating a sample to 493 K for 3h (Figure 4.6). In order to perform gas adsorption the material was heated to 493 K to remove solvent. Powder XRD patterns of partially desolvated samples revealed broad reflections next to those of ZIF-65(Zn), and indicate a partial phase change to an unknown phase (Figure 4.7).

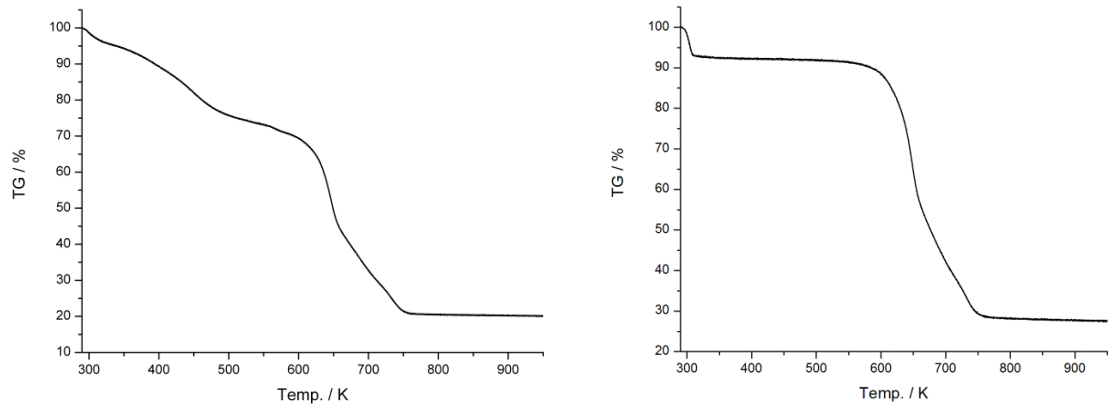

Figure 4.6: *Illustrating TGA of as prep sample before (left) and after heating (right) to 493 K for 3 h.*

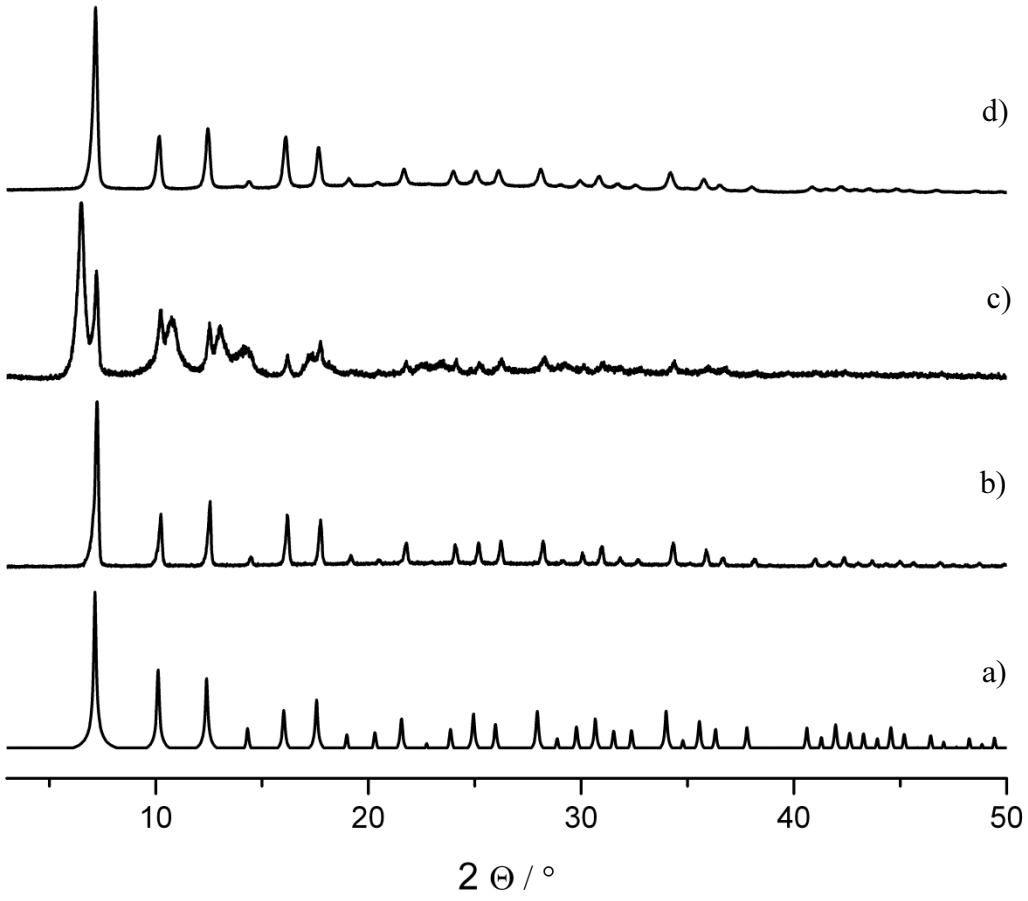

Figure 4.7*: PXRD patterns of ZIF-65(Zn) a) simulated from structure obtained by Rietveld refinement b) as-prepared ZIF-65(Zn), c) as-prepared ZIF-65(Zn) heated to 493 K and d) as-prepared ZIF-65(Zn) heated to 493 K followed by soaking in DMF.*

The process of phase transformation was found to be reversible by exposing the material again to DMF (Figure 4.7). PXRD of samples heated to different temperatures showed that the second phase appears at 363 K (Figure 4.8) which indicates the phase change is triggered by solvent removal at higher temperature. Heating to 563 K where complete removal of DMF is expected, shows significant amounts of residual ZIF-65(Zn) (Figure 4.8(h)). Notably, such additional reflections were also found in the reported powder XRD pattern of ZIF-65(Co) analogue, although with significantly lower intensities.[13] Attempts in preparing the transformed phase directly by using DEF as solvent in synthesis yielded $Zn(NIm)_2(SOD)$ (Figure 4.9).

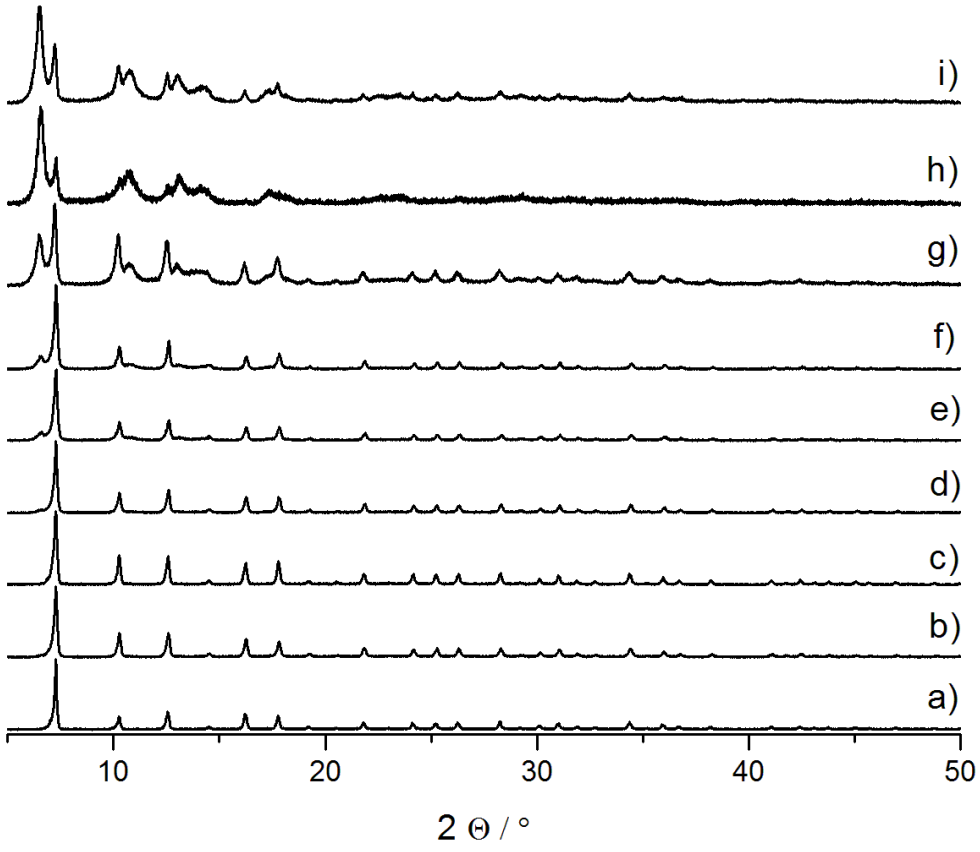

Figure 4.8: *Powder XRD patterns of ZIF-65(Zn) collected after heating at a) 333 K, b) 353 K, c) 363 K d) 373 K e) 383 K f) 393K g) 433 K h) 463 K and i) 493 K.*

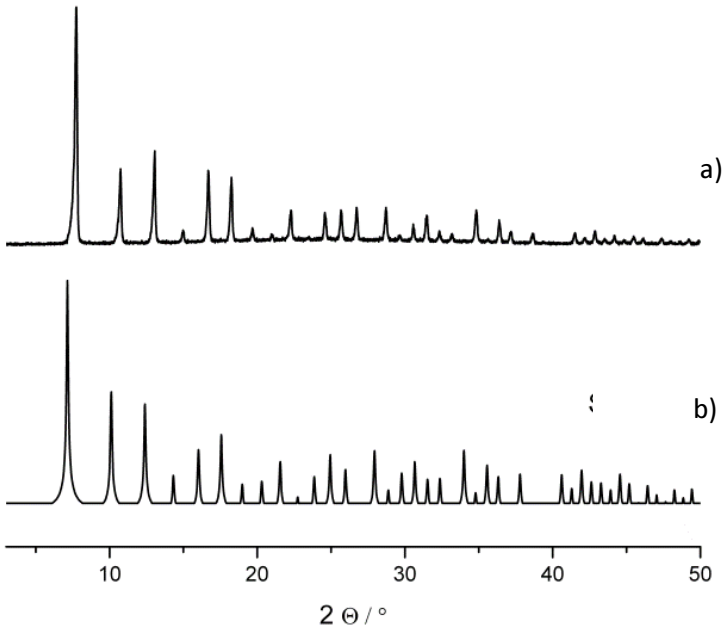

Figure 4.9: *Graph illustrating a) as prep ZIF-65(Zn) obtained from DEF synthesis approach compared to b) simulated pattern derived from Rietveld refined structure.*

4.4 MeOH Exchange Experiments on ZIF-65(Zn)

Investigation of whether the phase transformation is caused by increased temperature or the loss of solvent was carried out by treating as-prepared ZIF-65(Zn) with MeOH in order to exchange DMF for a solvent with a lower boiling point and therefore expose the material to lower thermal stress when desolvating. The powder XRD pattern of the freshly solvent-exchanged material shows the transformation over cycles of repeated solvent treatment and heating. MeOH treatment in a sonication bath results in a pure SOD phase and the complete exchange of DMF (Figure 4.10b and Figure 4.11 left). Heating to 338 K leads to an almost complete phase transformation that can be cycled

several times (Figure 4.10). This observation suggests that the chemical composition remains unaltered with the transformed phase as $Zn(NIm)_2$•DMF. Solvent hosted in open cavities leaves the framework above 300 K. No mass loss was observed till decomposition at 550 K suggesting that all DMF can be exchanged. Further, thermal treatment at 335 K for 2 h results in complete removal of MeOH (Figure 4.11) and leaves the desolvated framework amenable to gas adsorption.

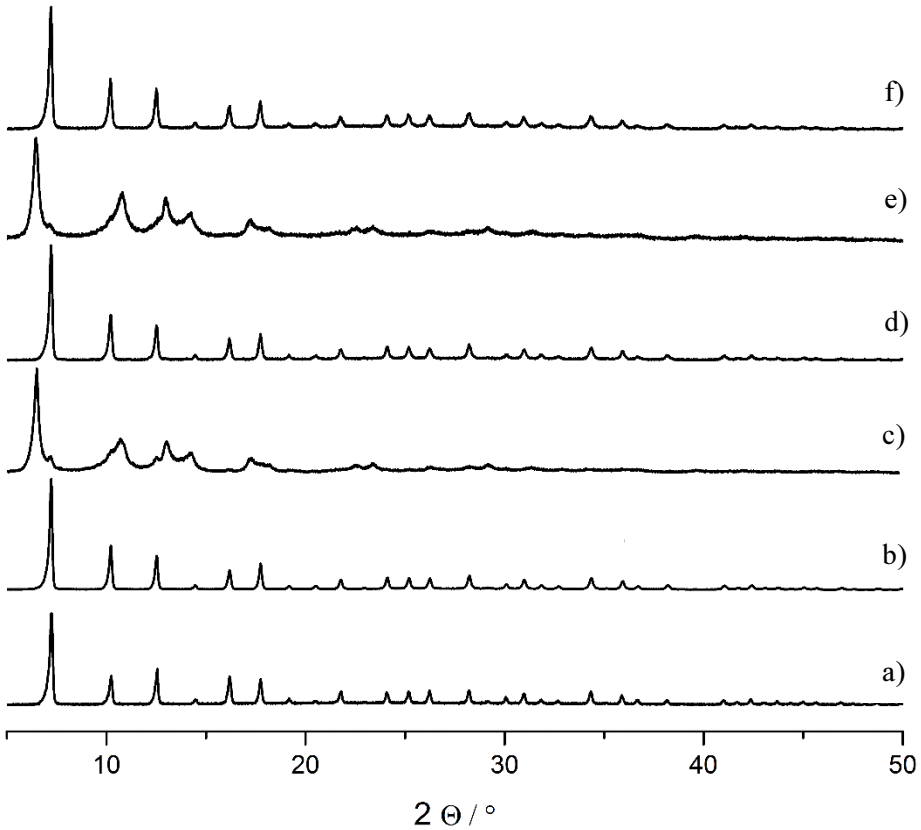

Figure 4.10: *Powder XRD pattern of repeated solvent exchanged and heating cycles of the same ZIF-65(Zn) sample. a) As-prepared ZIF-65(Zn), b) sonicated in MeOH, c) heated to 338 K, d) soaking in MeOH, e) heated to 393 K and f) additional MeOH treatment.*

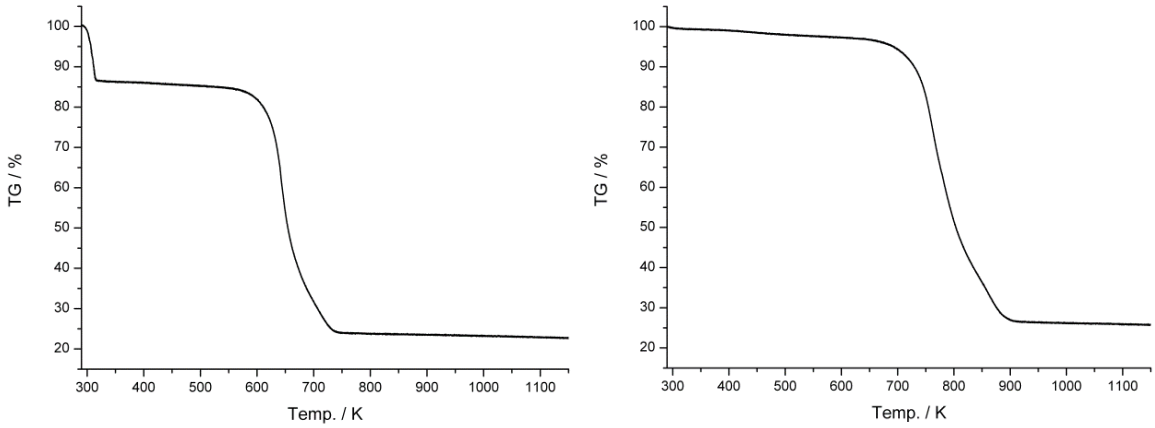

Figure 4.11: *TGA of MeOH treated (left) and heated to 333 K (right) ZIF-65(Zn).*

Adsorption measurements taken on a sample that was activated by sonication in MeOH followed by heating to 433 K showed high porosity to nitrogen (77 K) (664.3 m^2 g^{-1}) indicating ZIF-65(Zn) transforms into a framework with accessible open pores. The N_2 isotherm collected at 77 K is of type 6 and reveals several steps above 6.5 mmol g^{-1} and a total uptake of 13 mmol g^{-1} (Figure 4.12 top). Similar stepwise adsorption was observed for the CO_2 isotherm collected at 198 K (Figure 4.12 bottom left) with hysteretic stepwise desorption behaviour, indicating the framework's flexibility not only when exchanging solvents, but also to gas uptake. Carbon dioxide adsorption at 298 K shows values similar to those reported for ZIFs (Figure 4.12 bottom).[16] By comparison the SOD ZIF-65(Co), proven to be stable to the activation conditions, exhibits a Type I isotherm and takes up 8.65 mmol g^{-1} nitrogen at 77 K.[13]

Non-rigid framework behaviour in a ZIF with the SOD topology was previously demonstrated for ZIF-8, where linker tilting was observed upon nitrogen and carbon dioxide adsorption.[17, 18] Further, phase-to-phase transformation in a ZIF with SOD topology was described by Farrusseng in ZIF-7 for a reversible gate-opening effect when adsorbing and desorbing CO_2 at 303 K.[15] Experimental data presented in this chapter obtained from diffraction and adsorption experiments show a similar behaviour

of reversible structural change and add another example of the framework flexibility of ZIFs with SOD topology.

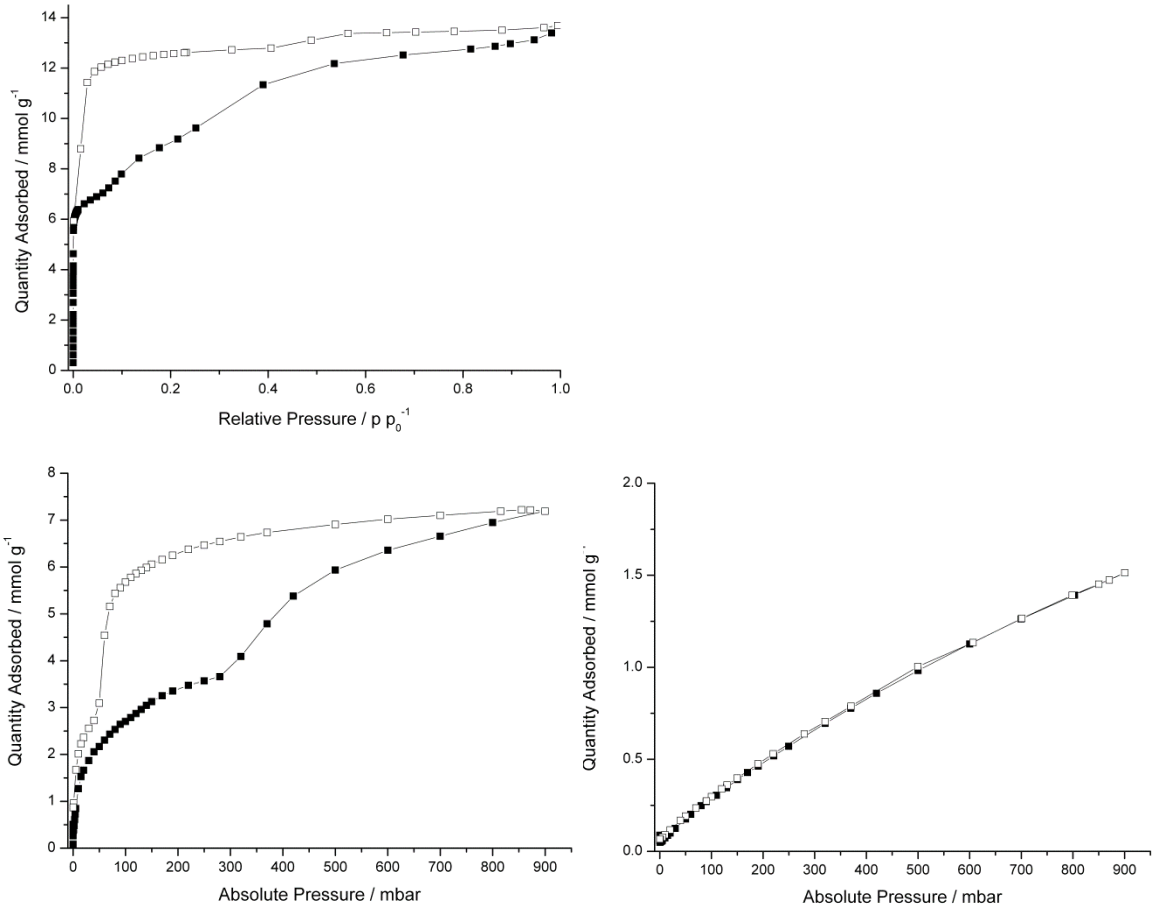

Figure 4.12: *N_2 (77 K) (top) and CO_2 isotherms collected at 198 K (bottom left) and 298 K (bottom right) of ZIF-65(Zn) after MeOH treatment and heating at* 433 K. Full symbols – Adsorption, Empty symbols – Desorption.

From the broad peak shape and low number of reflections in collected powder XRD pattern unit cell parameters can only be estimated as hexagonal. Reasoning that the SOD cage would remain intact during transformation, a possible structure was created based on the trigonal ZIF-7 (R-3) with SOD topology. Benzimidazole linkers were changed into NIm and unit cell parameters altered and simulated powder pattern

compared with experimental data, until unit cell parameters of $a = b = 27.00$ Å, $c = 9.00$Å gave a possible fit (Figure 4.13).

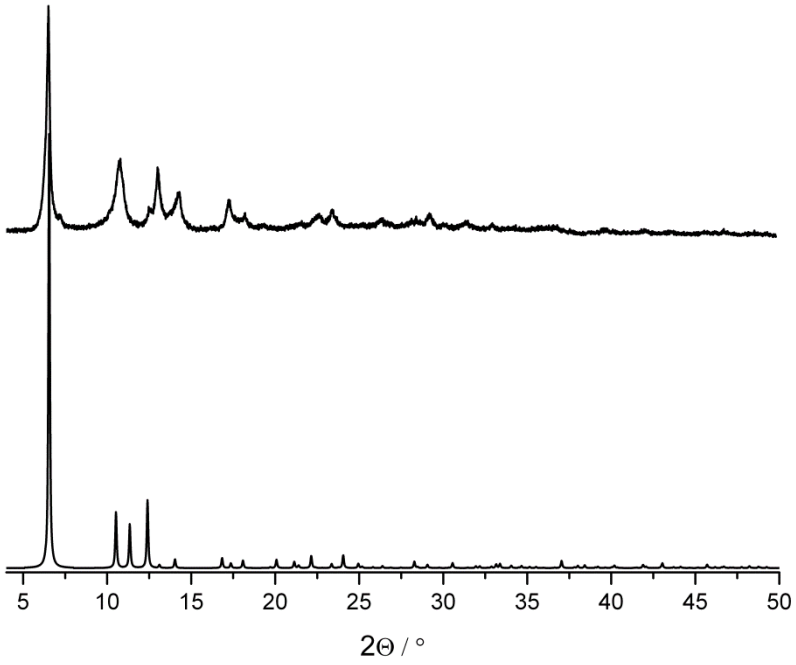

Figure 4.13: *Powder XRD pattern of MeOH exchanged and heated ZIF-65(Zn) (top) compared to the simulated pattern of a possible structure.*

The observed peak shape indicates the loss of long range order when transforming from the cubic phase. However, structural investigations using solid state NMR of the as-prepared and the heated material shows sharp peaks for C2 (150 ppm) and C4 / C5 (127-135 ppm) that suggest a high ordered local environment around ^{13}C nuclei (Figure 4.14). The increased number of peaks in the spectra of the MeOH solvent-exchanged / heated sample points toward a lower crystallographic symmetry with different nuclear environments (whereas the single peak in the as-prepared spectrum is consistent with spacegroup I-43m).

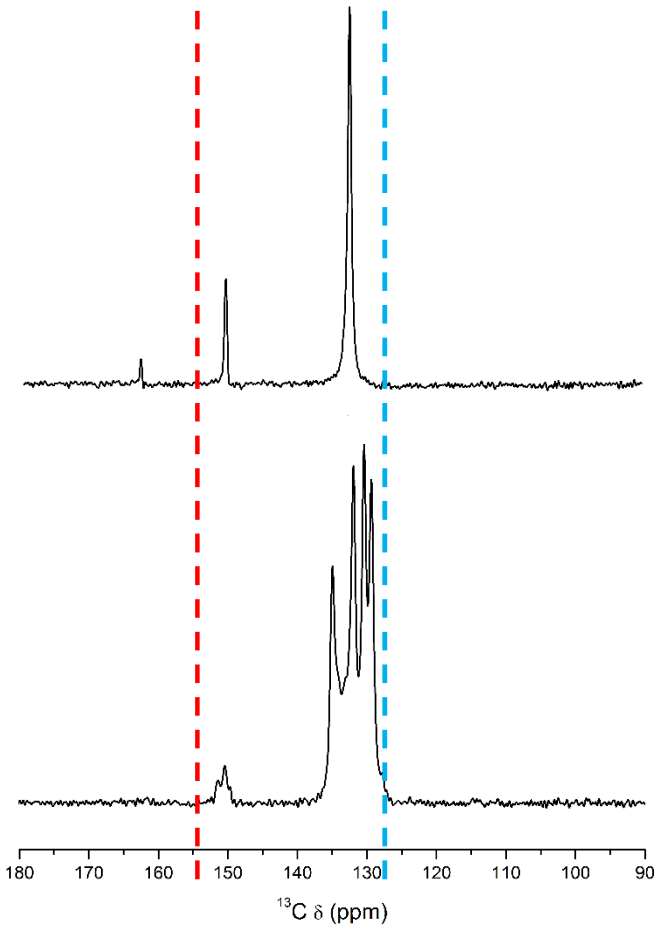

Figure 4.14: *^{13}C solid state MAS NMR specta from (top) as-prepared ZIF-65(Zn) in cubic symmetry and (bottom) MeOH-exchanged and heated ZIF-65(Zn) (mixture of 2 phases). The dashed lines indicate peak region assigned to C1 (red) and C4/C5 (blue) carbon atoms in the NIm linker.*

4.5 A Novel Single Linker Zeolitic Imidazolate Framework

The above investigations demonstrate the sensitive response of cubic ZIF-65(Zn) to the thermal removal of DMF and MeOH. Further experiments were carried out (by David Price, StA, collaboration) to synthesize the cubic sodalite phase directly in methanol to avoid solvent exchange reactions when aiming for the phase transformation. This gave a

different $Zn(NIm)_2$ phase. The highly crystalline material was indexed from PXRD with a = 18.9161 Å, b = 14.5055 Å, c = 8.4496 Å, α = β = γ = 90° (Figure 4.15). CHN analysis gave the elemental composition for $Zn(NIm)_2$. Single crystals amenable to structure solution by SXRD gave a new type of ZIF in *Pccn* (Table 4.3). The full chemical composition was obtained by a combination of TGA and elemental analysis.

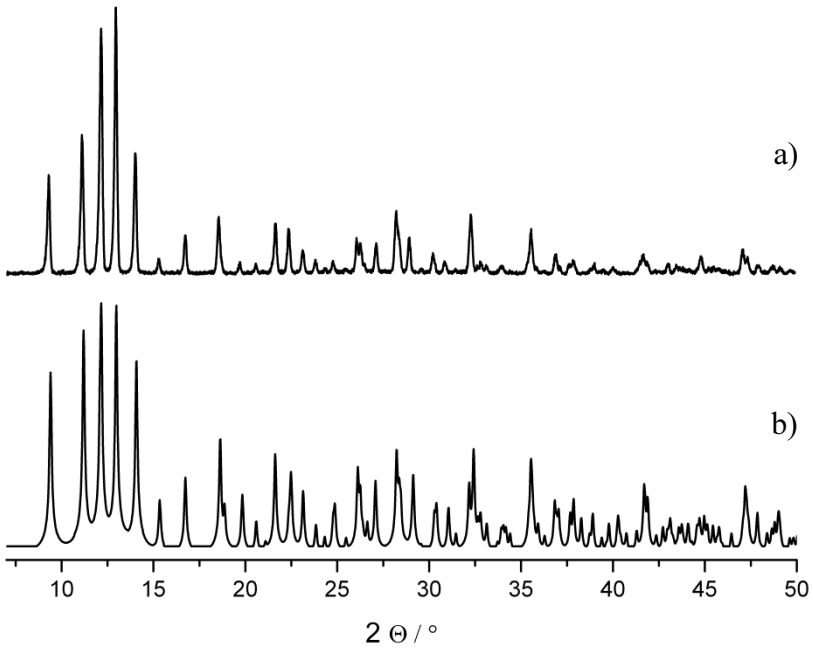

Figure 4.15: *Powder XRD pattern of a) as prepared $Zn(NIm)_2$ compared with b) the simulated pattern of the structure obtained from single crystal XRD.*

Structural analysis revealed a network consisting of distorted 6mrs. These rings fold in 3 different conformations; an envelope and boat conformation, similar to organic molecules seen in cyclohexane and a distorted envelope illustrated in Figure 4.16 with the colour code red, yellow and blue, respectively. This type of structure has to my knowledge not been found as inorganic or metal organic frameworks.

The mode of coordination is similar to known ZIFs where a zinc cation is surrounded by four imidazolate nitrogens building up Zn-N_4 tetrahedra as secondary building unit. The open framework contains empty channels along the *a*-axis (Figure 4.17a). There is a disorder of two ligands per zinc where each of these linkers can be located over two positions, resulting in linkers aligned along the channels. Remaining NIm linkers arrange with higher degree of ordering pointing either with NO_2 or CH moieties into the pore channels creating a crystallographically one dimensional porous material (Figure 4.17d). This results in a ultramicroporous diameter of ~4 Å that shows no porosity to nitrogen at 77 K (Kinetic diameter N_2 = 3.64 Å). Pore windows along *b*- and *c*-axis show free diameters of only 2.2 Å and 1 Å.

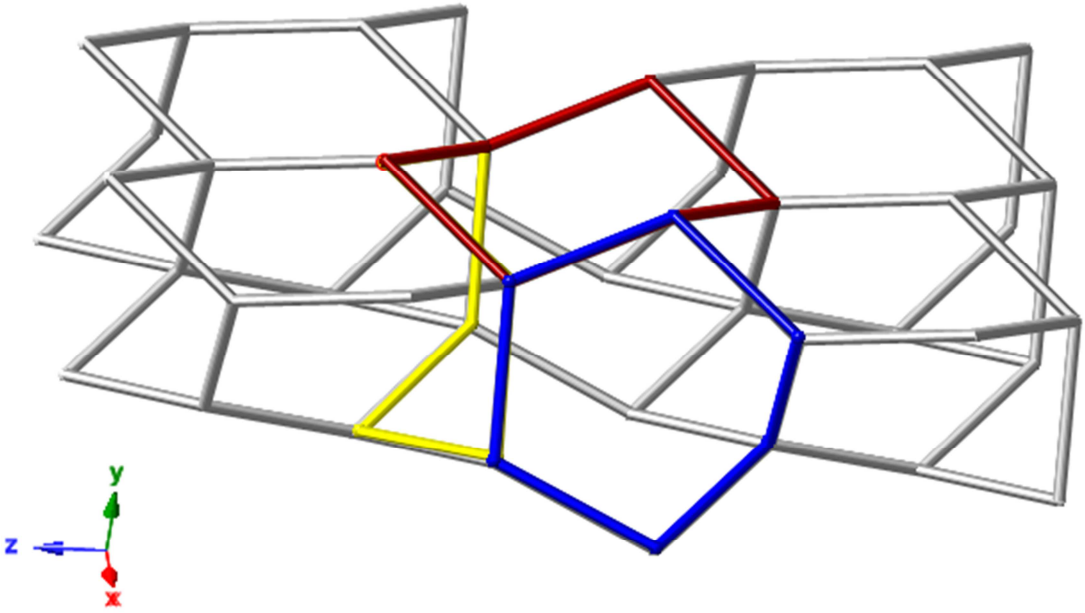

Figure 4.16: *Graph illustrating 6mr rings building up framework of $Zn(NIm)_2$ with different conformations. Envelope (red), boat (yellow) and distorted envelope (blue).*

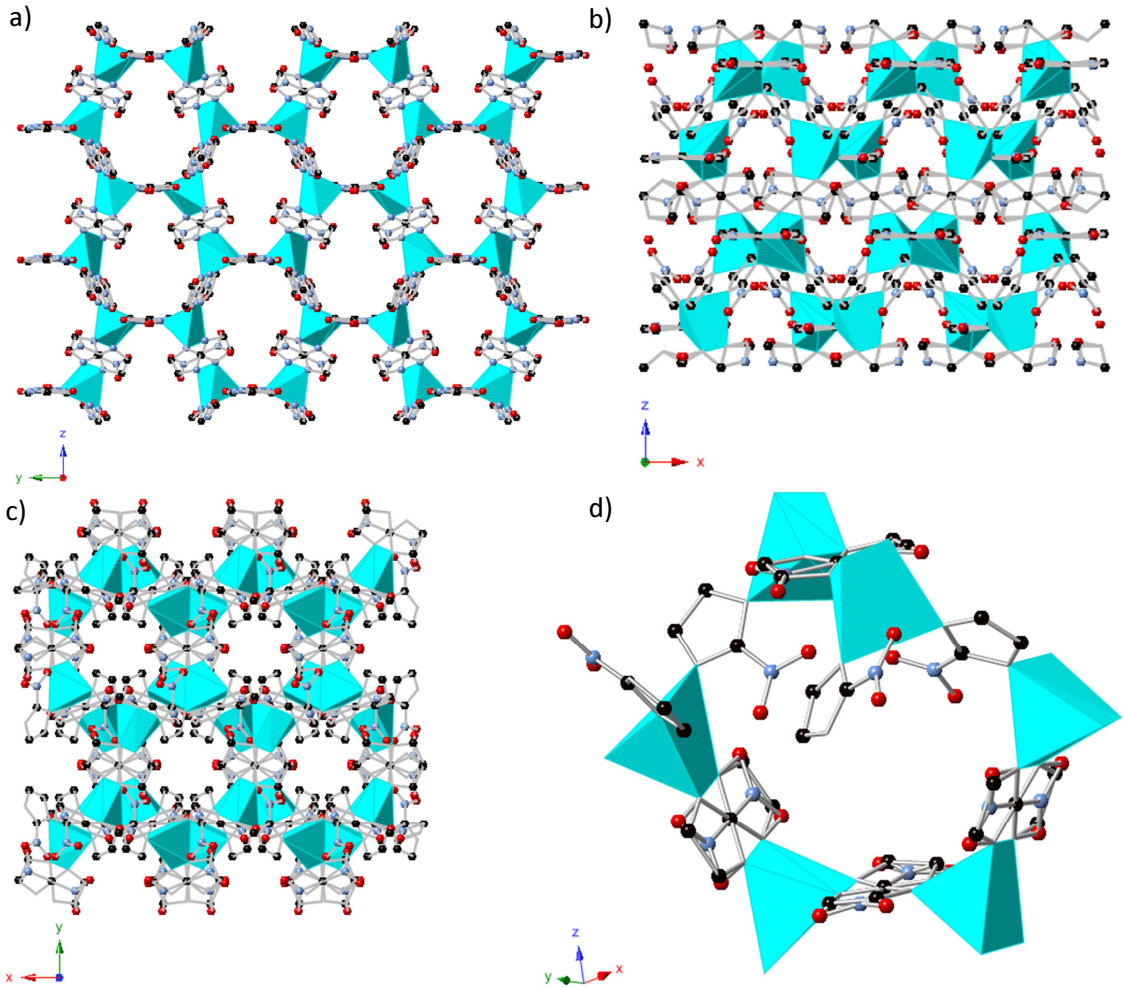

Figure 4.17: *View of orthorhombic Pccn Zn(NIm)$_2$ along a) a-axis showing largest pore channels, b) b-axis, c) c-axis and d) illustrating ordered and disordered ligand arrangement decorating open framework channels. C black, N blue, O red, Zn turquoise, H omitted for clarity.*

Thermogravimetric analysis indicated high thermal stability and shows no mass loss until decomposition at 650 K (Figure 4.18). The material was not found to be porous to nitrogen (77 K) or carbon dioxide (298 K or 198 K). Further studies of H_2 adsorption are planned.

Table 4.3: *Crystallographic data of dense structure, $Zn(NIm)_2$.*

Refined composition	$C_6N_6O_4Zn$
Formula mass [g / mol]	285.48
Calculated Density / g cm^{-1}	1.639
Space group	*P c c n*
Z	4
a [Å]	8.4620(10)
b [Å]	14.5490(10)
c [Å]	18.7990(10)
α [°]	90
β [°]	90
γ [°]	90
V [$Å^3$]	2314.4(3)
λ [Å]	1.54187
Radiation type	Copper
Crystal Morphology	Prism
Temperature / K	173
Unique/Total Reflections	2059/26196
Residual e- density min/max	-0.723/0.787
R_f	0.1089
$R_f[I > 2\sigma(I)]$	0.1022

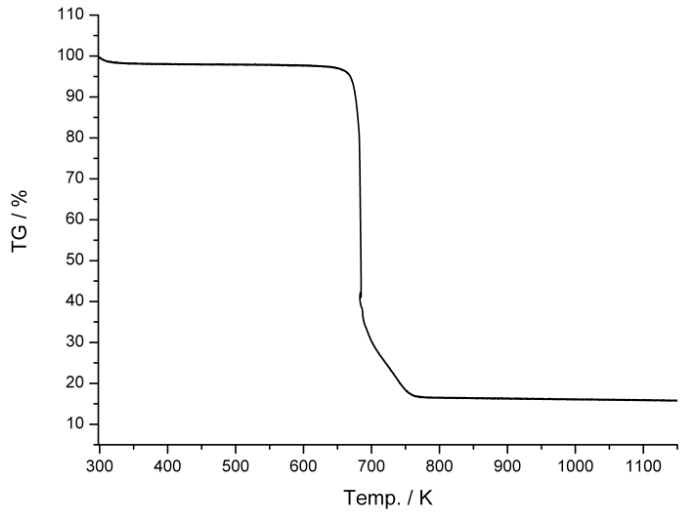

Figure 4.18*: Illustrates the TGA of $Zn(NIm)_2$ indicating high thermal stability and empty pore channels.*

4.6 Conclusion

In summary, the reaction of NIm with zinc cations, using zinc nitrate as a precursor results in two single linker materials. By replacing cobalt by zinc in the reported synthesis procedure of ZIF-65 gives highly crystalline ZIF-65(Zn). Its structure was refined via the Rietveld method matching the topological analogue of ZIF-65(Co). The removal of pore solvent of as-prepared ZIF-65(Zn) via thermal treatment leads to the partial transformation into a novel phase that shows high porosity to nitrogen. This phase change can be driven to high completion by residual DMF with methanol and was shown to be reversible over several cycles. The structure of the obtained phase was not accessible due to its low crystallinity, but will be part of further investigations most likely via simulation. It is likely to be a low symmetry variant of ZIF-65, with the same topology. Using methanol instead of DMF in the solvothermal synthesis gave a ZIF material with NIm linkers coordinating zinc cations as seen to be common in ZIFs. The structure consists of distorted 6mrs only and features one dimensional empty channels running along the a axis with narrow dimensions. The material was not found to be porous to nitrogen or carbon dioxide but shows high thermal stability.

NO_2-Imidazole is therefore a strongly structure-directing linker in ZIF synthesis, and is used together with other functionalised imidazolate linkers in ZIF synthesis of novel adsorbents in the following chapters.

4.7 References

1. X.-C. Huang, Y.-Y. Lin, J.-P. Zhang and X.-M. Chen, *Angew. Chem. Int. Edit.*, 2006, **45**, 1557-1559.

2. K. S. Park, Z. Ni, A. P. Co, J. Y. Choi, R. Huang, F. J. Uribe-Romo, H. K. Chae, M. O'Keeffe and O. M. Yaghi, *Proc. Natl. Acad. Sci. U.S.A.,* 2006 **103**, 10186-10191.

3. B. Assfour, S. Leoni and G. Seifert, *J. Phys. Chem. C*, 2010, **114**, 13381-13384.

4. H. Wu, W. Zhou and T. Yildirim, *J. Phys. Chem. C*, 2009, **113**, 3029-3035.

5. Z. Xiang, X. Peng, X. Cheng, X. Li and D. Cao, *J. Phys. Chem. C*, 2011, **115**, 19864-19871.

6. H.-L. Jiang, B. Liu, T. Akita, M. Haruta, H. Sakurai and Q. Xu, *J. Am. Chem. Soc.*, 2009, **131**, 11302-11303.

7. X. Zhao, X. Fang, B. Wu, L. Zheng and N. Zheng, *Sci. China Chem.*, 2013, 1-6.

8. W. Morris, C. J. Doonan, H. Furukawa, R. Banerjee and O. M. Yaghi, *J. Am. Chem. Soc.*, 2008, **130**, 12626-12627.

9. O. Karagiaridi, M. B. Lalonde, W. Bury, A. A. Sarjeant, O. K. Farha and J. T. Hupp, *J. Am. Chem. Soc.*, 2012, **134**, 18790-18796.

10. S. Bernt, M. Feyand, A. Modrow, J. Wack, J. Senker and N. Stock, *Eur. J. Inorg. Chem.*, 2011, **2011**, 5378-5383.

11. R. Banerjee, A. Phan, B. Wang, C. Knobler, H. Furukawa, M. O'Keeffe and O. M. Yaghi, *Science*, 2008, **319**, 939-943.

12. C. Dey and R. Banerjee, *Chem. Commun.*, 2013, **49**, 6617-6619.

13. B. P. Biswal, T. Panda and R. Banerjee, *Chem. Commun.*, 2012, **48**, 11868-11870.

14. Y.-Q. Tian, S.-Y. Yao, D. Gu, K.-H. Cui, D.-W. Guo, G. Zhang, Z.-X. Chen and D.-Y. Zhao, *Chem. Eur. J.,* 2010, **16**, 1137-1141.

15. S. Aguado, G. Bergeret, M. P. Titus, V. Moizan, C. Nieto-Draghi, N. Bats and D. Farrusseng, *New J. Chem.*, 2011, **35**, 546-550.

16. R. Banerjee, H. Furukawa, D. Britt, C. Knobler, M. O'Keeffe and O. M. Yaghi, *J. Am. Chem. Soc.*, 2009, **131**, 3875-3877.

17. D. Fairen-Jimenez, S. A. Moggach, M. T. Wharmby, P. A. Wright, S. Parsons and T. Düren, *J. Am. Chem. Soc.*, 2011, **133**, 8900-8902.

18. D. Fairen-Jimenez, R. Galvelis, A. Torrisi, A. D. Gellan, M. T. Wharmby, P. A. Wright, C. Mellot-Draznieks and T. Duren, *Dalton Trans.*, 2012, **41**, 10752-10762.

5. Synthesis of Purine-Containing ZIFs and their Structure and Adsorption Properties

5.1 Introduction

The 2-nitroimidazole (NIm) linker was shown to give the zinc form of ZIF-65 by direct synthesis in Chapter 4. Mixed linker MOFs offer tuneable functionality.[1] Previously, Yaghi et al prepared a series of ZIFs with the GME topology type via isoreticular synthesis, based on mixed-linker syntheses with (NIm) and other imidazolate linkers with the aim to create materials with enhanced adsorption sites for carbon dioxide capture from flue gas. ZIF-68 with the GME topology was prepared using a mixture of NIm and benzimidazole, for example. This approach has shown to be an effective route to direct topologies in ZIF materials.[2] Further, introducing ligand functionalities appears as a strategy to direct ZIF structures and was underlined by the theoretical approach of Galvelis et al.[3] This chapter focus on the extension of this approach to introduce functionality through the use of mixtures of imidazolate linkers by including purine as one component (in purine a pyrimidine ring is fused to the imidazolate C4 and C5 positions) (Figure 5.1). Structural similarities between purine and bzIm suggest a ZIF with the GME topology would be obtained, hosting an increased number of nitrogen lone pairs. In related studies performed in the last couple of years, Liao et al presented a structure with bis-triazole linkers in coordinated Zn^{2+} cations leaving unsaturated N-donors that were used for binding CO_2 molecules.[4] A zeolite-like framework incorporating a tetrazole linker with high CO_2 capacity was published by Cui et al.[5]

Further, nitrogen lone pairs are known to act as chelating agents complexing metals in open framework structures (Figure 5.2), which may also act as adsorption sites.[6]

Using purine alone as a component of ZIFs has previously been shown to yield ZIF-20, which has the LTA framework topology,[7] and An et al. have reported the use of the related adenine as a framework constituent in cobalt adeninate bio-MOFs, although in the latter case there are also carboxylate linkers incorporated into the framework structure.[8]

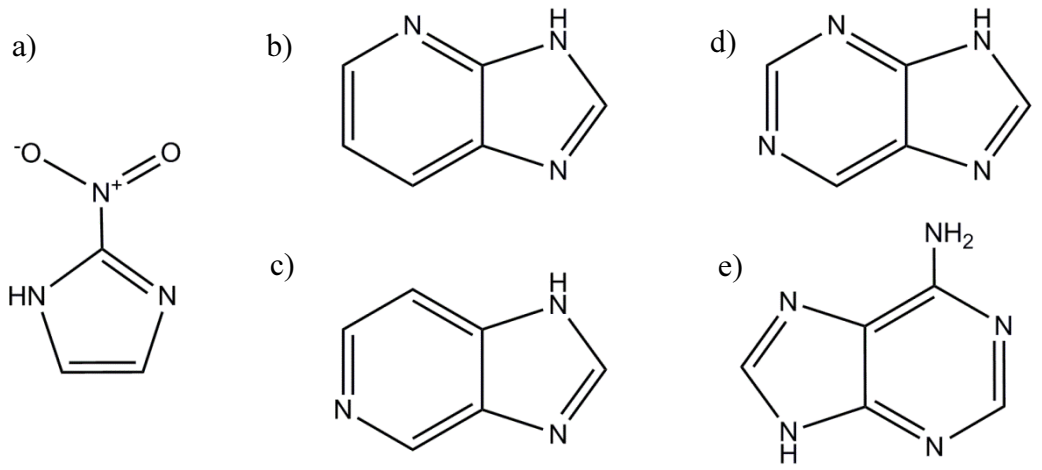

Figure 5.1: *Chemical structures of a) 2-Nitroimidazole, b) 4-Azabenzimidazole, c) 5-Azabenzimidazole, d) Purine and e) Adenine.*

This work aimed at the outset to prepare a purine-containing ZIF with the GME topology via a mixed-linker synthesis including 2-nitro-imidazole and purine, reasoning that this would provide additional Lewis basic sites for interaction with carbon dioxide or coordination with *exo* metal cations, which might find applications in selective adsorption or catalysis. Crystallisation with a mixture of NIm and purine ligands under specific conditions of solvent and metal source gives the desired GME topology. Varying metal source and solvent affects the synthesis, also giving open framework zinc purinates where the purines coordinate via both imidazolate and pyrimidine N atoms

and a large pore version of the RHO (ZIF-11 type) structure in which extra framework (exo) zinc species coordinating to N atoms of pyrimidine rings are bridged by exo NIm ligands.

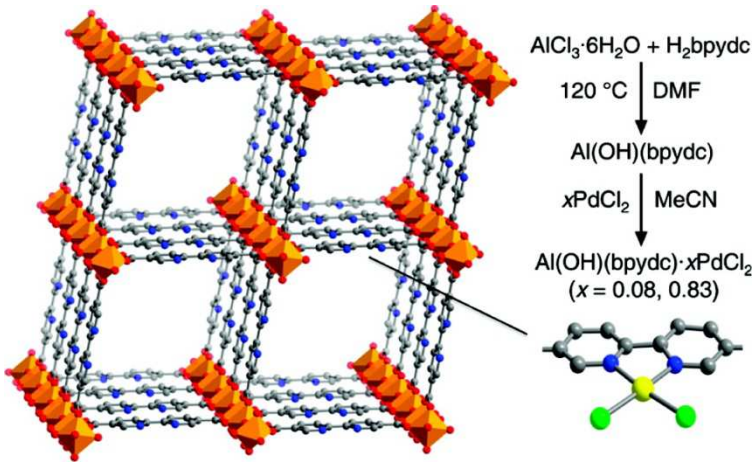

Figure 5.2: *Al(OH)(bpydc)•$PdCl_2$ as an example framework with donor lone pairs accessible for post-synthetic metal insertion. Reprinted with the permission of the American Chemical Society.*[6]

5.2 Experimental section

In a usual synthesis zinc oxide, zinc bromide, zinc acetate or zinc nitrate together with 2-nitroimidazole and purine in a molar ratio of 1:1:1 were placed in a Teflon-lined steel autoclave, combined with DMF and heated to 373 K for 7 days. After cooling the reaction in all four cases a solid was obtained which was then filtered and washed with DMF followed by drying at room temperature. All preparations except the one using zinc nitrate yielded crystals amenable for SXRD. By admixing small amounts of methanol in the DMF solvent the zinc nitrate preparation also gave single crystals suitable for X- ray diffraction experiments (without changing the product phase). For the synthesis using zinc oxide the metal source could be exchanged for zinc acetate and NMP could be used as a solvent instead of DMF resulting in the same material.

Table 5.1: *Crystallographic data of as-prepared structure 1, 2, 3 and 4.*

	Structure **1**	Structure **2**	Structure **3**	Structure **4**
Formula	$C_8 H_5 N_7 O_3 Zn$	$C_{11.5} H_{9.5} N_{8.5} O_{0.5} Zn_2 Br_2$	$C_5 H_3 N_4 O_1 Zn$	$C_{11.50} N_6 O_{4.17} Zn_{1.33}$
Formula Weight of Unit Cell	281.2	537.10	201.4	375.9
Calculated Density / g cm^{-3}	1.049	1.815	1.234	1.224
Space Group	P 6_3 / m m c	P 2_1/n	I -4	I m -3 m
a / Å	26.8840(15)	13.636(7)	15.02(3)	29.044(6)
b /Å	26.8840(15)	10.209(5)	15.02(3)	29.044(6)
c / Å	18.1210(10)	14.124(7)	9.570(19)	29.044(6)
α / °	90	90	90	90
β / °	90	91.568(9)	90	90
γ / °	120	90	90	90
V / $Å^3$	11342.3(11)	1965.5(17)	2158(6)	24500(9)
Z	24	4	8	48
Crystal Morphology	Prism	Prism	Prism	Prism
Temperature / K	173	93(2)	93(2)	173
Radiation type	Cu K_α	Mo K_α	Mo K_α	Cu K_α
Wavelength / Å	1.54178	0.71073	0.71073	1.54178
Unique/Total Reflections	3828/155295	3874/14892	2016/11116	2174/99240
Residual e^- density min/max	-0.898/2.017	-1.132/1.565	-0.899/2.267	-0.918/3.308
R_F	0.2718	0.0640	0.0854	0.1270
R_F [I > 2σ(I)]	0.2362	0.0561	0.0848	0.1253

5.3.1 Synthesis of **1** Zn(pur)(NIm).X Topology type GME

Zinc oxide (1 mmol, 81.4 mg, Aldrich), 2-nitroimidazole (1 mmol, 113.1 mg, Alfa Aesar), purine (1 mmol, 120.1 mg, Aldrich) and 15 ml DMF (Aldrich) in a 40 ml Teflon-lined steel autoclave were heated at 373 K for 7 days and then cooled to room temperature. This gave a bright orange powder of crystallites of structure **1** in a mixture with unreacted ZnO.

Zinc acetate dihydrate (1 mmol, 219.5 mg, Aldrich), 2-nitroimidazole (1 mmol, 113.1 mg, Alfa Aesar), purine (1 mmol, 120.1 mg, Aldrich) and 15 ml N-methylpyrrolidone (NMP) (Aldrich) in a 40 ml Teflon lined steel autoclave were heated at 373 K for 7 days and then cooled to room temperature. A brown powder was obtained, washed with DMF and dried at room temperature, and determined to be pure **1** (289 mg, 81%). Elemental analysis for pure **1** from which solvent had been removed by heating, Zn(pur)(NIm), topology type GME, $C_8H_7N_5ZnO_2$: Found % (Calcd. %); C 32.39 (32.31); H 1.69 (1.60); N 33.06 (32.98).

5.3.2 Synthesis of **2** Zn(pur)Br·xDMF

Zinc bromide (1 mmol, 219.5 mg, Fisons Scientific), 2-nitroimidazole (1 mmol, 113.1 mg, Alfa Aesar), purine (1 mmol, 120.1 mg, Aldrich) and 15 ml DMF (Aldrich) in a 40 ml Teflon-lined steel autoclave were heated at 373 K for 7 days and then cooled to room temperature. White crystals were collected from filtration, washed with DMF and dried at room temperature (83.7 mg, 31%). Elemental analysis for as-prepared Zn(pur)Br·0.125 DMF: $C_{43}H_{31}N_{33}Br_8Zn_8O$. Found % (Calcd %). C 23.64 (23.58); H 1.42 (1.33); N 20.91 (21.11)

5.3.3 Synthesis of **3** Zn(pur)(OAc)·xX

Zinc acetate dihydrate (1 mmol, 219.5 mg, Aldrich), 2-nitroimidazole (1 mmol, 113.1 mg, Alfa Aesar), purine (1 mmol, 120.1 mg, Aldrich) and 15 ml DMF (Aldrich) in a 40 ml Teflon lined steel autoclave were heated at 373 K for 7 days and then cooled to room temperature. Orange single crystals were obtained from filtration, washing with DMF and drying at room temperature (195 mg, 69%). Elemental analysis of pure sample heated under vacuum to 473 K, estimated as Zn(pur)(OAc) ·0.5pur·0.37DMF: $C_{10}H_{8.6}N_{6.2}Zn_1O_{2.2}$ Found % (Calcd %). C 37.52 (38.17); H 2.39 (2.73); N 27.51 (27.38).

5.3.4 Synthesis of **4** $Zn_{1.33}(O,OH)_{0.33}(pur)(NIm)_{1.167}$ .xX (Topology type RHO)

Zinc nitrate hexahydrate (1 mmol, 297.5 mg, Aldrich), 2-nitroimidazole (1.05 mmol, 119 mg, Alfa Aesar), purine (1 mmol, 120.1 mg, Aldrich) were dissolved in 15 ml DMF (Aldrich) in a 40 ml Teflon lined steel autoclave. The solution was heated at 373 K for 7 days and then cooled to room temperature. An orange powder was collected by filtration, washed in DMF and dried at room temperature. Single crystals suitable for SXRD were obtained by adding 0.5 ml methanol (Aldrich) to the reaction mixture (277 mg, 87%). Elemental analysis of **4**, from which the solvent had been removed by heating in vacuum, $Zn_{1.33}(O,OH)_{0.33}(pur)(NIm)_{1.167}$: $C_{51}H_{34}N_{45}Zn_8O_{16}$. Found % (Calcd. %); C 29.84 (29.81); H 1.65 (1.70); N 30.91 (30.68).

The water-treated sample was obtained by placing the as-synthesized material together with 20 ml of distilled water for four weeks in a plastic bottle without refreshing the

liquid, followed by filtration, washing with water and drying at ambient temperature. Chemical compositions were estimated from a combination of TGA, elemental analysis and solution NMR of the solids, dissolved by mixing with DMSO-d_6 and 0.1 M HNO_3 followed by sonication for 5 minutes. In each case the porosity after solvent removal by heating under a vacuum was determined by N_2 adsorption at 77 K and the CO_2 uptake at 298 K was measured up to ca. 1 bar.

5.4 Results and Discussion

A series of solvothermal syntheses was performed (373 K, 7 d) in dimethylformamide (DMF) with a reactant ratio of Zn salt : NIm : pur = 1 : 1 : 1, where the zinc source was varied for each experiment ZnO, $ZnBr_2$, $Zn(AcO)_2$ or $Zn(NO_3)_2$. Four different products depending on the used metal source were obtained, as shown by XRPD (Figure 5.3-5.6).

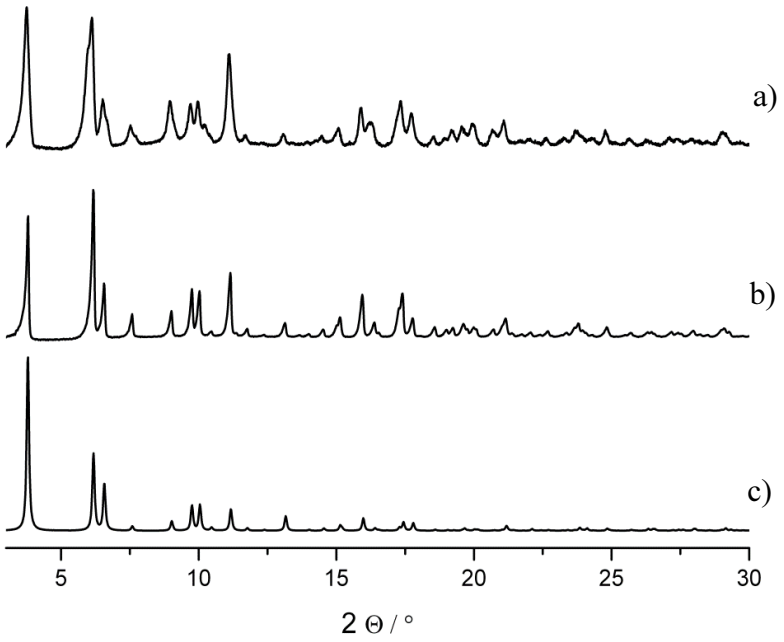

Figure 5.3: *Powder X-Ray diffraction patterns of structure **1** Zn(pur)(NIm) (GME) prepared with a) ZnO, and b) as-prepared with $Zn(OAc)_2$, c) compared with a powder XRD pattern simulated using the structure of **1** determined by SXRD.*

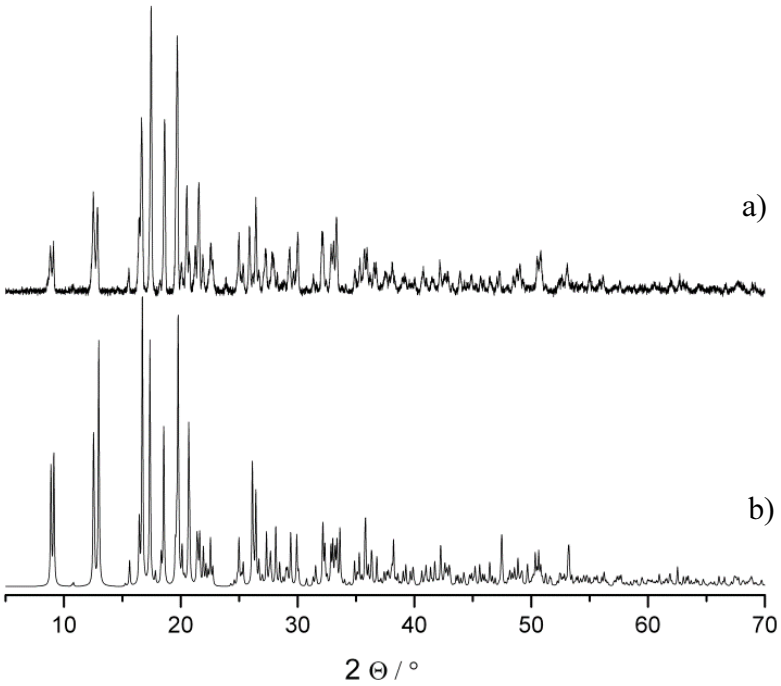

Figure 5.4: *Powder X-Ray diffraction pattern of a) as-prepared Zn(pur)Br, structure **2** (prepared from zinc bromide / DMF method) compared with b) simulated using the structure determined from single crystal diffraction.*

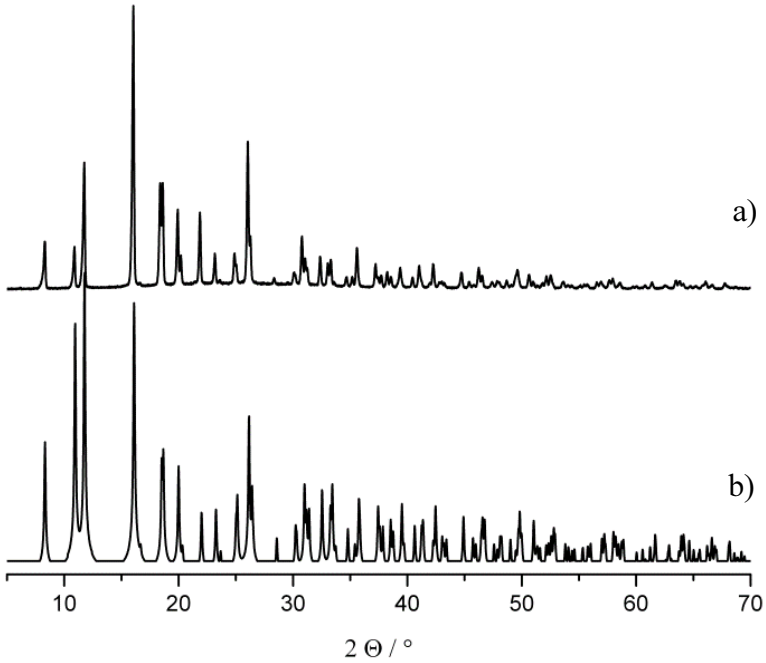

Figure 5.5: *Powder X-Ray diffraction pattern of a) as-prepared Zn(pur)OAc.xX, structure **3** (prepared from zinc acetate / DMF method), compared with b) simulated using the structure determined from SXRD.*

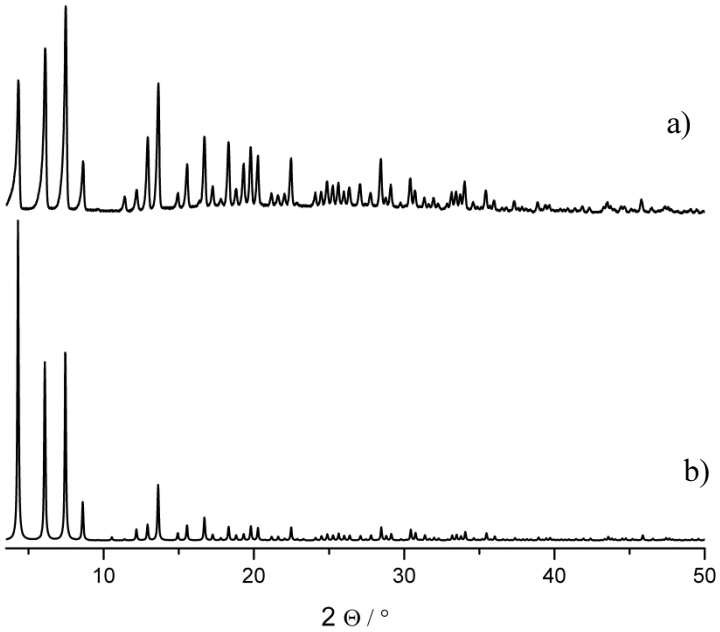

Figure 5.6: *Powder X-Ray diffraction pattern a) as-prepared $Zn_{1.33}(O,OH)_{0.33}(pur)(NIm)_{1.167}$, structure **4**, compared with b) simulated using the structure determined from SXRD on the as-prepared material.*

5.4.1 Mixed Linker ZIF with GME Topology

The ZIF prepared using zinc oxide, structure **1**, was indexed from powder XRD as the target GME phase (*P* $6_3/mmc$, *a* = 26.884 Å, *c* = 18.112 Å). The materials prepared via synthesis with zinc bromide (structure **2**), acetate (**3**) and nitrate (**4**) crystallised as single crystals amenable to structure solution by single crystal diffraction (SXRD). In addition, structure **1** was prepared as crystals amenable to SXRD by reaction in N-methylpyrrolidone and with zinc acetate. Structural details are given below: although not of the highest quality, the data permit confirmation of the framework structure.

Structure **1** is the Zn(pur,NIm) ZIF with the GME topology with the NIm and pur ligands ordered 1:1 in the structure in a very similar way to that observed for ZIF-68 (Zn(NIm,bzim)): the presence of both NIm and pur ligands is confirmed both by X-ray

crystallography (Figure 5.3) and solution state NMR of the dissolved solid (Figure 5.8). The GME topology consists of d6r built up from six 4mrs perpendicular aligned to 6mrs, forming one dimensional channels along the c-axis. These d6r are connected by 4mrs resulting in *gme* cages (Figure 5.7). These 4mrs are alternatively built up from

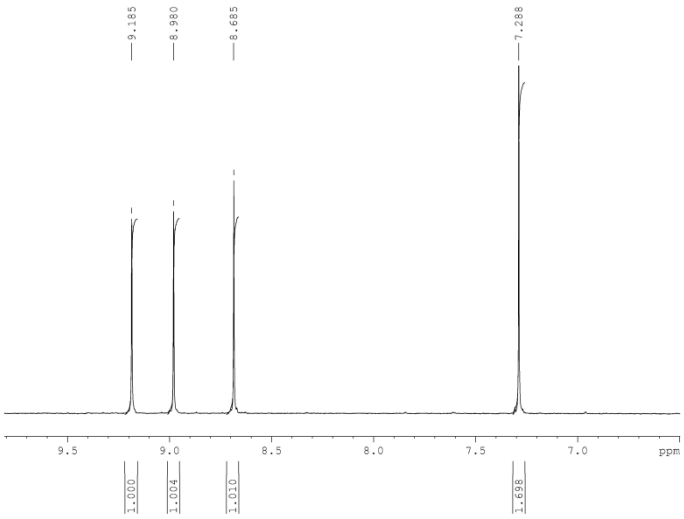

Figure 5.8: *^{1}H NMR of dissolved structure **1** after heating of as-prepared solid under vacuum at 413 K for 4 h showing resonances for purine (9.185 – 8.685 ppm) and NIm (7.288 ppm).*

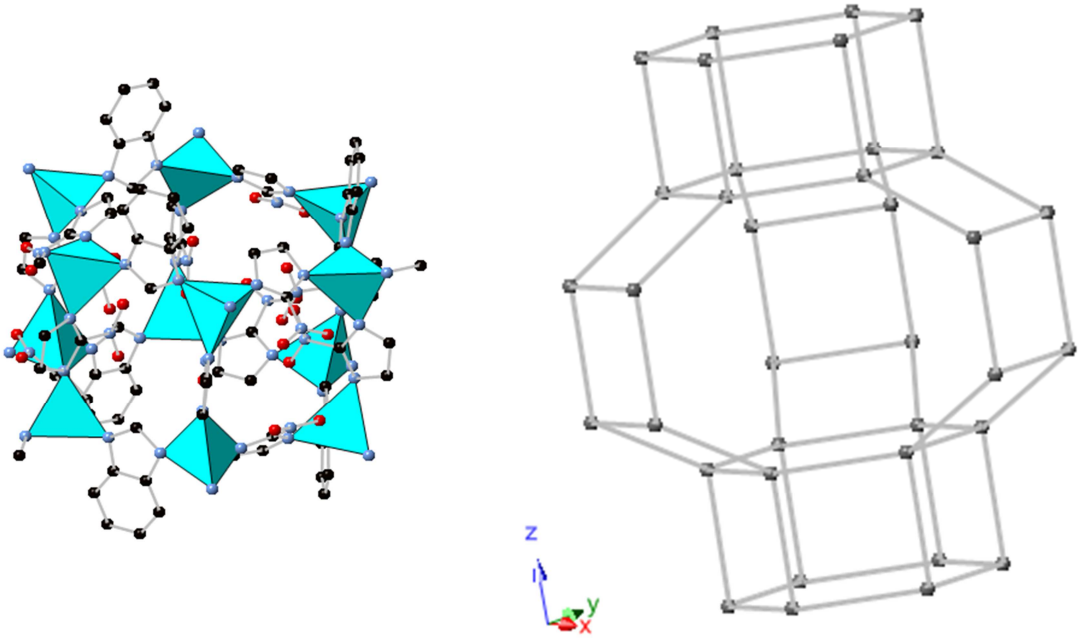

Figure 5.7: *Illustrates the ligand arrangements in a d6r formed by 4mrs (left) and a ball and stick model of the interconnection of two d6rs (right). (Zn, turquoise or grey; N, blue; C, black; H, not shown)*

NIm and purine linkers or only of NIm. Notably, oppositely arranged nitro groups are pointing towards the centre of the 4mr, an arrangement which is found in the earlier discussed ZIF-65(Zn) structure (chapter 4) and in structure **4**, presented later in this chapter. The structural similarities within these pure or mixed linker NIm frameworks might be caused due to structure directing nature of NIm. Six of these d6r/4mr GME cages located in the same level in the unit cell create 12mrs with even larger channels aligned parallel to the d6r (Figure 5.9). Pyrimidine N atoms project into the void space, and present a possible coordination site for extra-framework metal cations, although such cations are not present in the as-prepared ZIF (Figure 5.10).

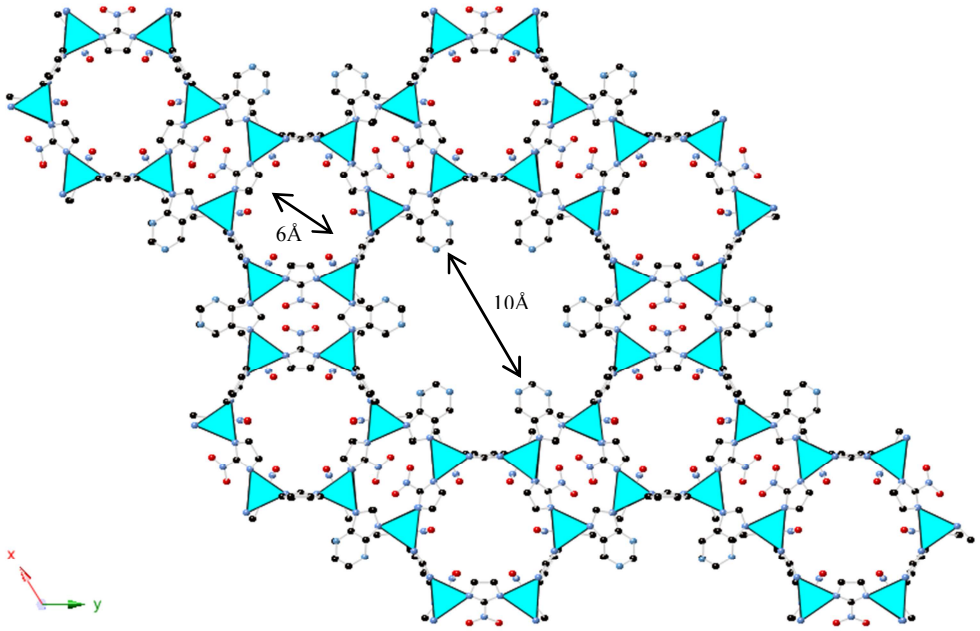

Figure 5.9: *Showing d6rs and 12mr forming channels along the c-axis. (Zn, turquoise; N, blue; C, black; H, omitted for clarity).*

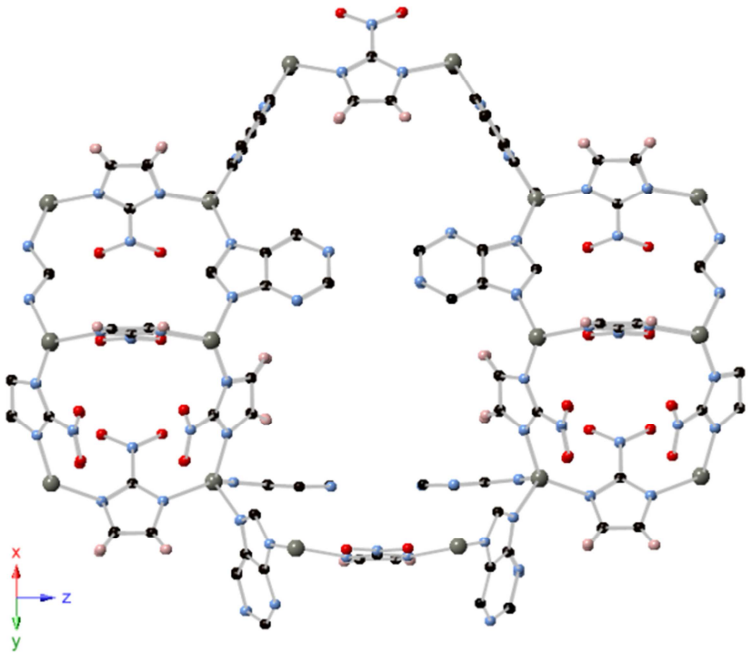

Figure 5.10: *Structure obtained from single crystal analysis of* ***1*** *viewed perpendicular to channels along c-axis. (Zn, grey; N, blue; C, black; H, pink).*

TGA reveals the loss of water and solvent occurs from 293 K and continues up to 333 K (2.5 wt.%) followed by the loss of NMP up to 500 K (17 wt.%). A step at 550 K indicates decomposition. Solvent is therefore lost by heating under vacuum at 473 K (Figure 5.11).

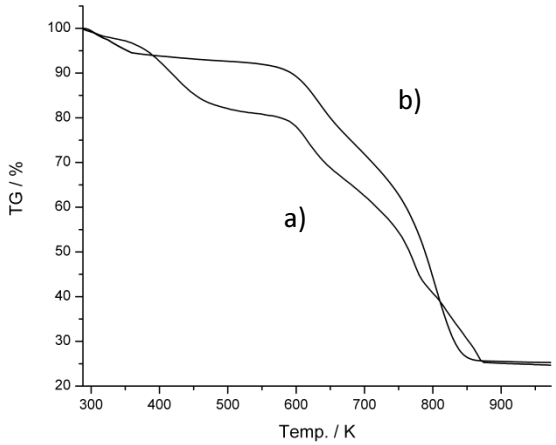

Figure 5.11: *TGA of structure* ***1****, both a) as-prepared and b) after heating under vacuum at 473 K.*

The Zn(NIm,pur) GME material is highly porous, with a maximum N_2 uptake of 9.8 mmol g^{-1} and a pore volume of 0.34 cm^3 g^{-1} (BET 813 m^2 g^{-1}) which is lower than for ZIF-68 with similar linker functionalities (bIm).[2] Simulation of the N_2 adsorption isotherm via Grand Canonical Monte Carlo (GCMC) methods[9] (BET 912 m^2 g^{-1}) matches more closely the uptake measured on the sample prepared with ZnO as a precursor (Figure 5.12). The difference between the sample prepared with zinc acetate (a) and zinc oxide (b) might be related to higher crystallinity of the latter. Carbon dioxide adsorption at 298 K show uptake comparable with ZIF materials of the same topology, of 0.3 mmol g^{-1} at 0.1 bar (Figure 5.12).[2]

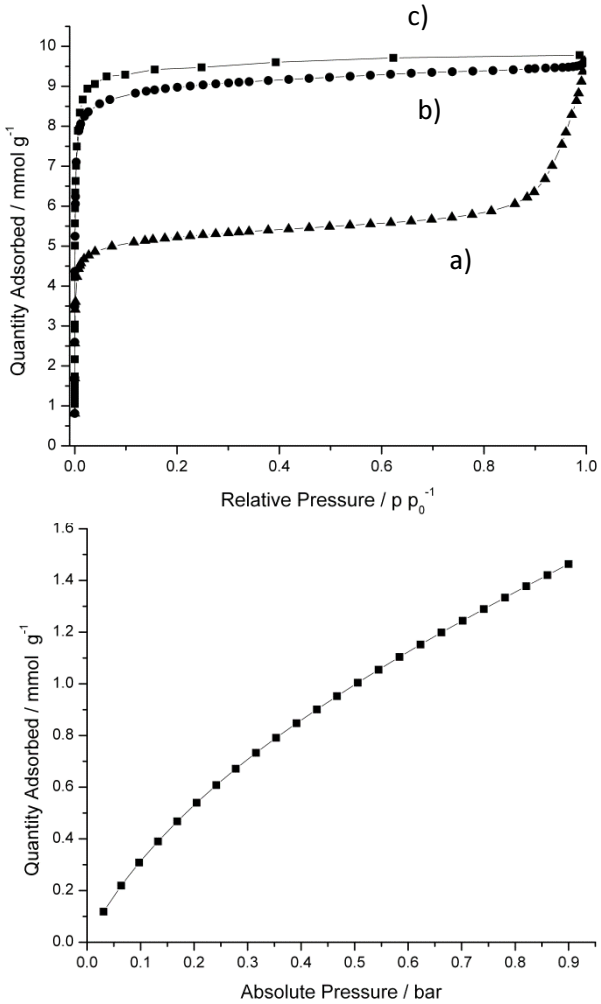

Figure 5.12: *(Top) Nitrogen adsorption isotherm (77 K) for structure **1** , Zn(pur)(NIm) – GME, desolvated at 473 K. Material obtained from a) zinc acetate and b) zinc oxide compared with c) GCMC simulated isotherm. (Bottom) CO_2 isotherm (298 K) of structure **1** prepared with ZnO as precursor.*

5.4.2 Dense Zinc Purinates from Mixed Linker Synthesis

By changing the metal precursor, zinc oxide, in two separate DMF syntheses to the acetate and bromide salts, two novel structures were formed. For structures **2**, Zn(pur)Br.0.125DMF and **3**, Zn(pur)(AcO)xDMF, only the purine ligand is present in the framework, as indicated by SXRD and also confirmed by solution phase NMR of as-prepared samples (Figure 5.13 and Figure 5.14). Its mode of coordination is via both imidazole N atoms and the N in the 1 position of the pyrimidine ring. In the framework of structure **2** each zinc atom is coordinated to two pur linkers via N atoms from two different imidazole groups and a third pur linker via the pyrimidine N. The fourth coordination to the tetrahedral Zn^{2+} ion is from a Br^- ion from the original zinc bromide (Figure 5.15 top).

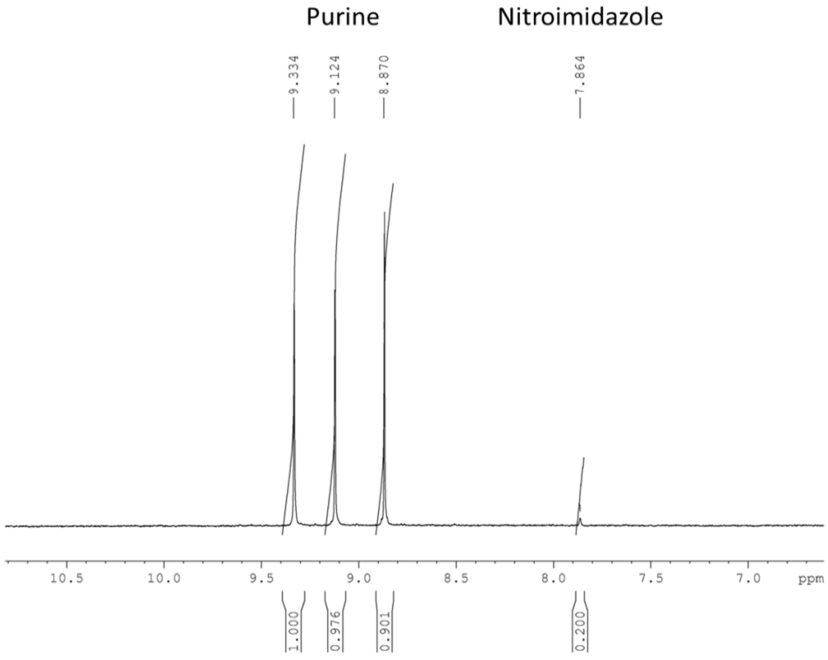

Figure 5.13: *^{1}H NMR of digested structure **2**, Zn(pur)Br.0.125DMF, obtained via zinc bromide preparation showing resonances for purine (9.334– 8.870ppm) and residual NIm (7.864 ppm) from the mixed linker synthesis.*

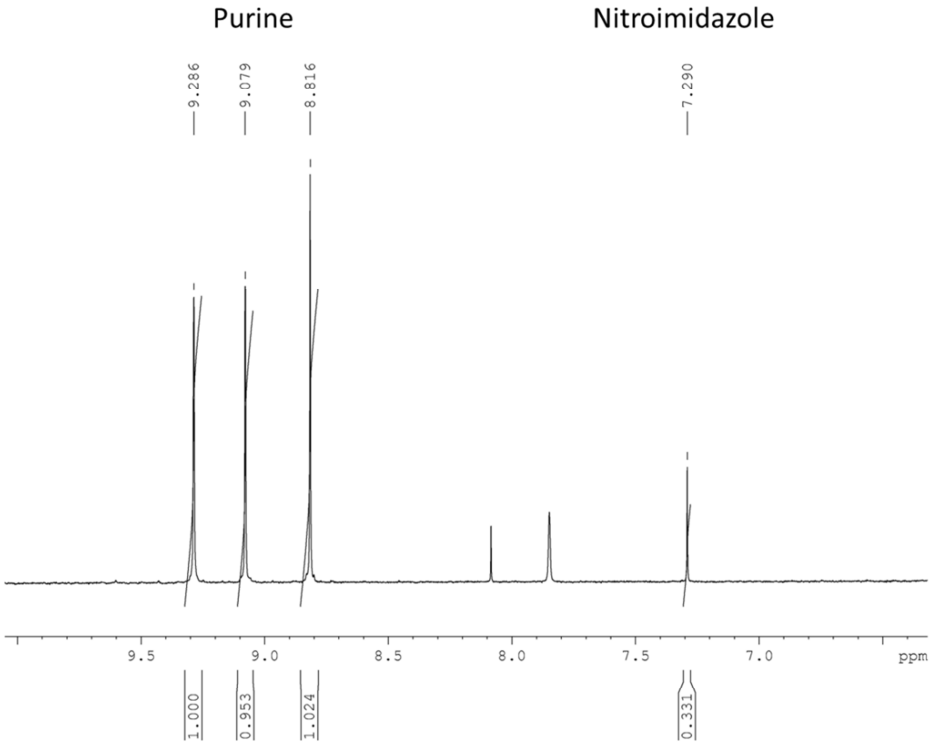

Figure 5.14: *^{1}H NMR of dissolved, as-prepared structure 3, Zn(pur)(AcO)xDMF, showing resonances of purine (9.286 – 8.816 ppm) and residual 2-nitroimidazole (7.290 ppm). The two additional peaks were assigned to DMF and its hydrolysis product formic acid, respectively.*

The open framework has channels that contain DMF molecules: the walls of these channels are made up by both pur linkers and Br^- ions (Figure 5.16, top). In structure **3** (Figure 5.16, bottom) the zinc is similarly coordinated to three different pur ligands, with the fourth coordination position taken up by disordered acetate ions, again giving an open framework. The TGA trace of structure **2** shows continuous weight loss from 300 to 550 K which indicates the loss of DMF (10.5 wt.%) with the final decomposition above 750 K (Figure 5.17 left). Structure **3** shows an initial loss of solvent up to 350 K (3.5 wt.%) followed by loss of weight attributed to included DMF and 2-nitroimidazolate above 450 K. A sharp step at 600 K indicates the decomposition of the structure (Figure 5.17 right). It was not possible to render either **2** or **3** porous to N_2 or

CO_2 by thermal removal of included solvent. The reason why only purine was incorporated in the structures is not clear, but one explanation could be the higher solubility of NIm over purine in DMF leading later to increased integration into the solids of the latter.

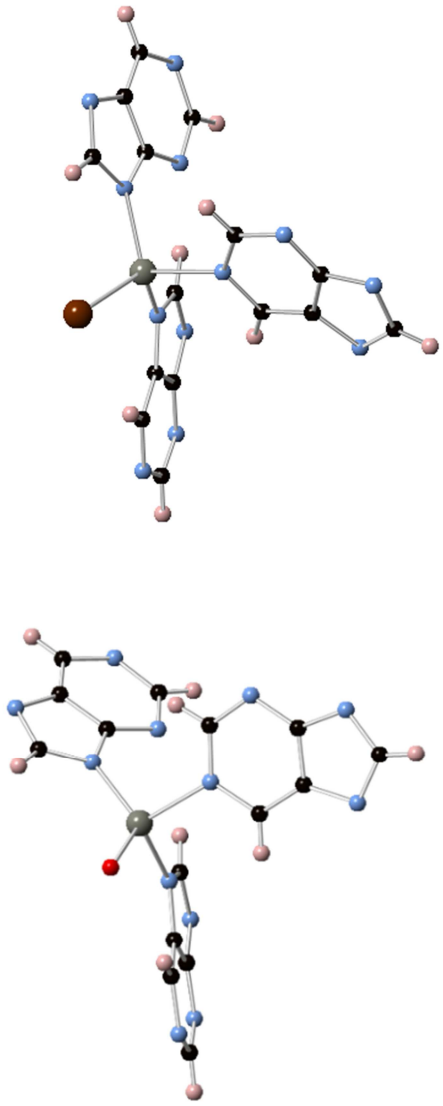

Figure 5.15: *(Top) Tetrahedral ZnN_3Br environment of structure **2**, showing coordination to two imidazolate N atoms, one pyrimidine N of purine and a bromide ion. (Zn, grey; N, blue; C, black; H, pink, Br brown). (Bottom) Tetrahedral ZnN_3O environment of structure **3**, showing coordination of Zn to two imidazolate N, one pyrimidine N of purine, and an O atom, thought to be part of a disordered acetate ligand. (Zn, grey; N, blue; C, black; O, red; H, pink)*

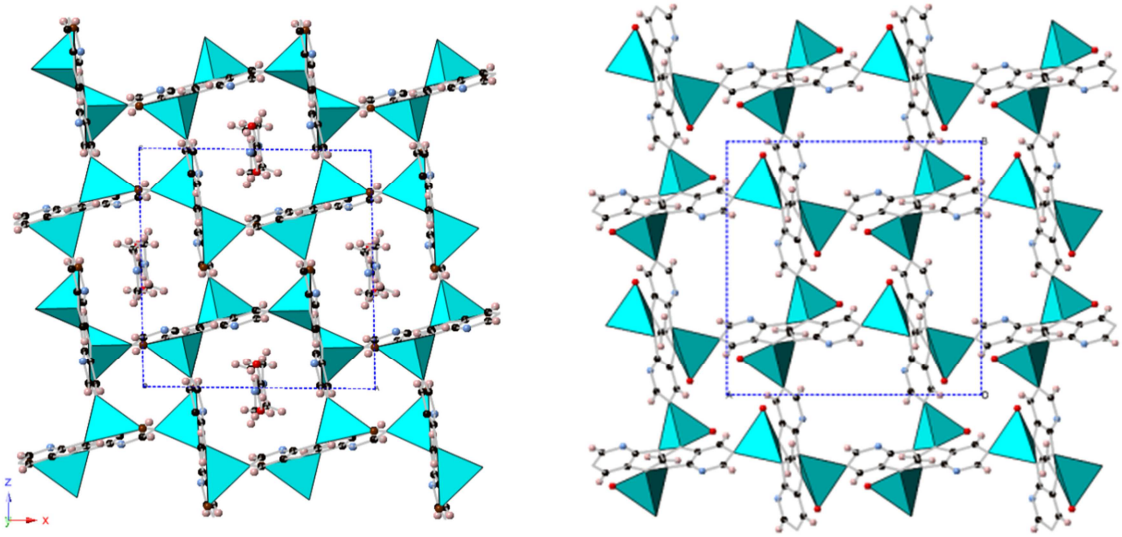

Figure 5.16: *(Left) The structure of Zn(pur)Br•0.5DMF, including occluded DMF molecules (**2**) and (right) the framework structure of Zn(pur).(OAc) (**3**), each viewed down their largest channel axes. The Zn coordination tetrahedra are depicted in blue. Structure 3 also contains disordered extra framework species, not shown. (Zn, cyan; N, blue; C, black; O, red; H, pink; Br brown).*

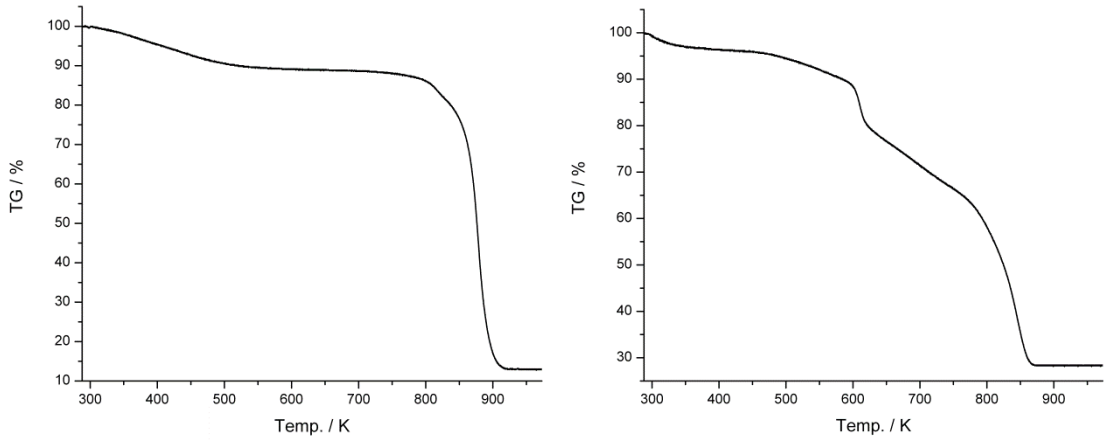

Figure 5.17: *TGA of as-prepared structures **2** (left) and **3** (right).*

5.4.3 NIm-Purinate RHO: A ZIF with Zinc / NIm Decorated Cavities

The fourth material synthesised with purine and NIm, using zinc nitrate as metal precursor, structure **4**, was shown by solution phase NMR to contain both NIM and purine linkers, in the approximate ratio of 1 : 1 (Figure 5.18). SXRD of the crystals indicated that structure **4** has the RHO topology type, as possessed by ZIF-11 ($Zn(bzim)_2$) and ZIFs prepared with other imidazolates functionalised in both 4- and 5-

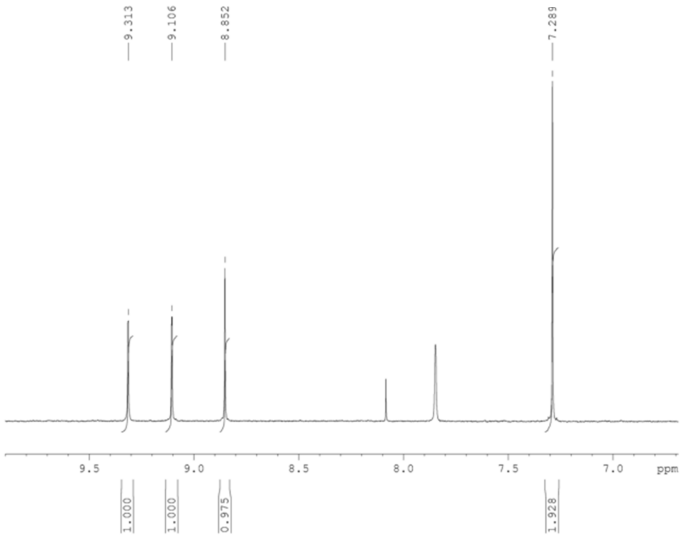

Figure 5.18: *^{1}H NMR of as-prepared structure **4**, heated at 463 K and activated under vacuum at 423 K showing resonances for purine (9.313 – 8.852 ppm) and NIm (7.289 ppm). The two additional peaks were assigned to DMF and its hydrolysis product formic acid, respectively.*

positions (Figure 5.19). Structure **4** has symmetry *Im-3m*, different from that of ZIF-11 (RHO), which has *Pm-3m* symmetry. There is a number of ZIFs in RHO topology and body centred unit cell.[10-12] It is notably that all such structures which were obtained in appreciable quantities comprise of C2 functionalised imidazolate linkers with nitro groups and cobalt or cadmium metal nodes. This observation suggests the structure directing nature of NIm towards I centring in mixed linker structure **4**.

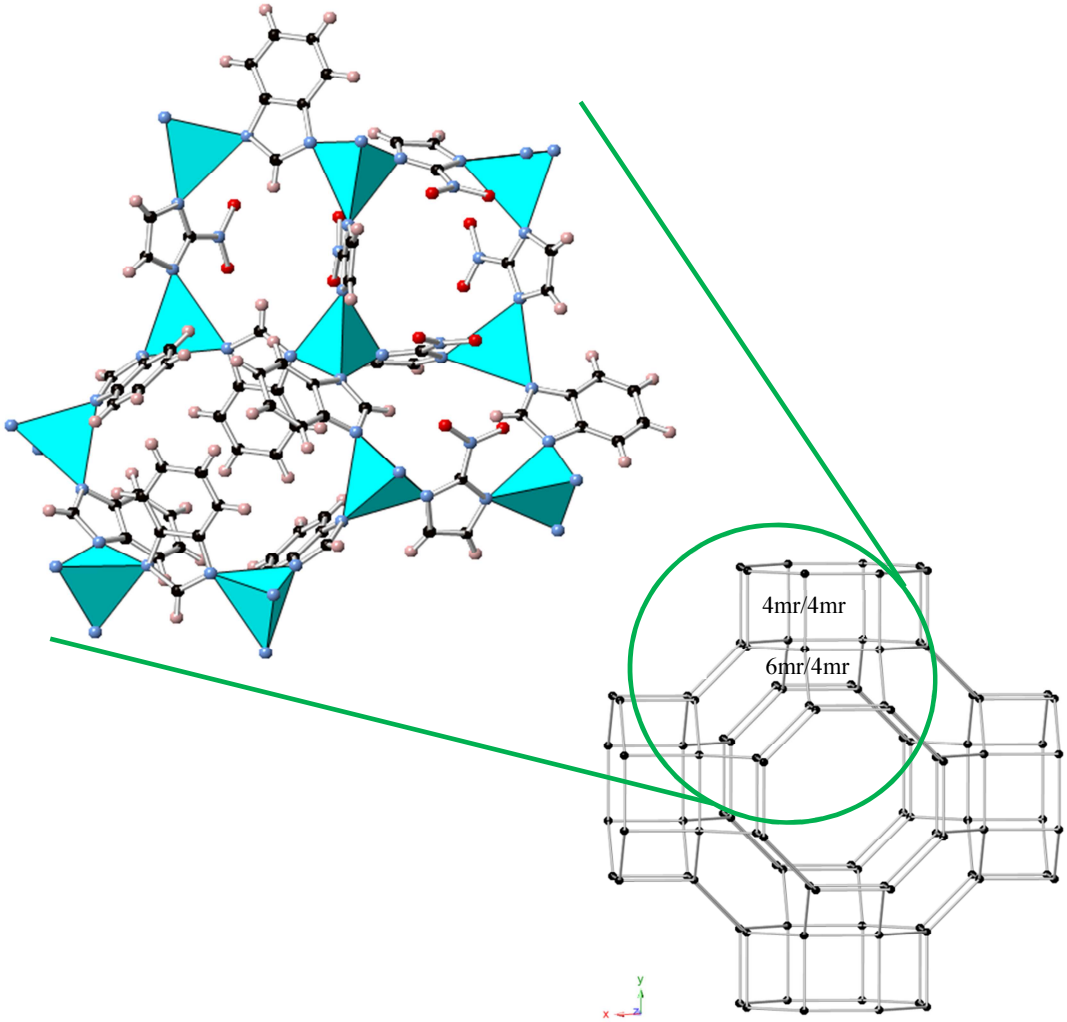

Figure 5.19: *Illustration of the RHO topology (bottom) with black balls indicating zinc positions. The location of different ligand arrangements in 4mrs between two 4mr and one pair of 6mr/4mr sharing edges is presented on top (green circle). Zn (turquoise), O (red), C (black), N (blue) and H (pink).*

Structural analysis reveals that the different symmetries of ZIFs with the RHO topology result from the different orientations of the imidazole groups linking the zinc centres. Both structures can be discussed in terms of ZnN_4 tetrahedra linked into the RHO topology, where the N atoms belong to bridging imidazole groups. These tetrahedra form two different types of secondary building units in the structure; rho4mrs, and double eight membered rings, d8rs, comprising 16 ZnN_4 tetrahedra (Figure 5.19). In the

RHO framework type each supercage is attached to six others via the d8rs, and there are two interpenetrating but unconnected arrays of supercages and windows. In this framework type there are two distinct linker positions in a 1:1 ratio, the first between two edge-sharing 4mrs and the second between 4mrs and 6mrs that share edges (Figure 5.19).

In ZIF-11, bzim linkers occupy both linker positions. For linkers in the position between the two 4mrs, the phenyl groups project into the d8mr windows closing them to molecules the size of N_2 or larger (Figure 5.20 left). The phenyl groups of the second crystallographic bzim group project into the rho supercages, but in two different ways, so that there are two different supercage environments.

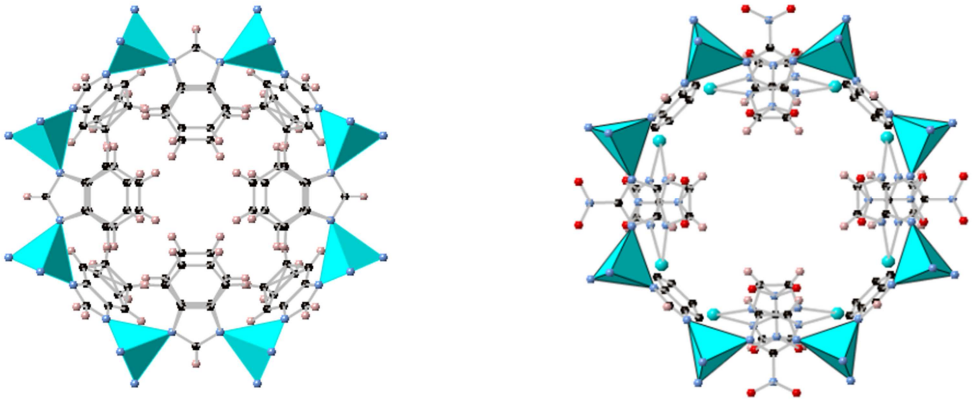

Figure 5.20: *Figures illustrate the ligand alignment in an 8mrs in (left) ZIF-11 is compared with the ligand arrangement in (right) structure **4**. Zn (turquoise), O (red), N (blue), C (black), H (pink).*

This results in the I-centred symmetry of the framework topology being reduced to P-centred. In the framework of the new ZIF (structure **4**) the NIm and pur linkers order into the two topologically different sites (4mr/4mr and 4mr/6mr). The NIm groups are arranged around the d8r openings so that the window is much larger, since only either nitro- groups or the CH groups of NIm reduce the opening (Figure 5.20 right). As a

result, this new RHO ZIF readily takes up N_2 and has a 9 Å pore size, much larger than those ZIF-11 analogues reported by Morris et al.[13] The pyrimidine groups of the purine linkers project into the supercage, capping the 6mrs. All supercages are identical.

Structure **4** also possesses a structural feature not found in ZIF-11 or its analogues - the presence of additional zinc 2-nitroimidazolate groups coordinated to the ZIF framework. These 'decorating' species are described here as exo zinc cations and exo NIm ligands. The coordination of zinc cations to the framework shown in Figure 5.21 is made possible by the presence of pyrimidine N atoms in close proximity on different pur pyrimidine rings that are situated above the 6mrs in the supercage, around the triad axis.

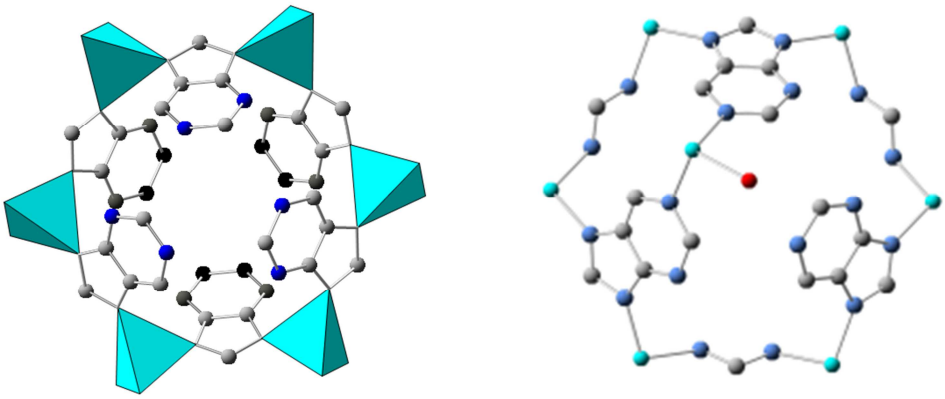

Figure 5.21: *Diagrams show (left) pyrimidine rings capping 6mrs within the supercages, giving coordination sites for exo Zn cations (right), themselves linked by exo NIm linkers. Zn (turquoise), O (red), C (black), N (blue) and H (pink).*

The disordered orientation of the pyrimidine groups results in two N lone pairs of adjacent rings being in a suitable configuration to bind to zinc. There are three equally likely positions for this exo zinc in each of these '6mr' positions, one of which is shown in the figure, corresponding to 8 per supercage. These exo zinc cations are bridged by 4 exo NIm linkers, which show statistical occupancy. As well as being disordered over 12

symmetrically equivalent pairs of exo Zn^{2+} cation positions, the ligands are able to occupy two different configurations between each pair of two Zn^{2+} cations, one example of which is shown in Figure 5.22. The final coordination site on each Zn^{2+} cation is assumed to be taken by an anion (such as NO_3^-) leaving one positive charge per pair of Zn^{2+} cations, assumed to be balanced by disordered anions in the cages (Figure 5.22 top right). One explanation why RHO crystallises in preference to GME could be that NO_3^- anions have a stabilising effect on the formation of the *exo*-moieties.

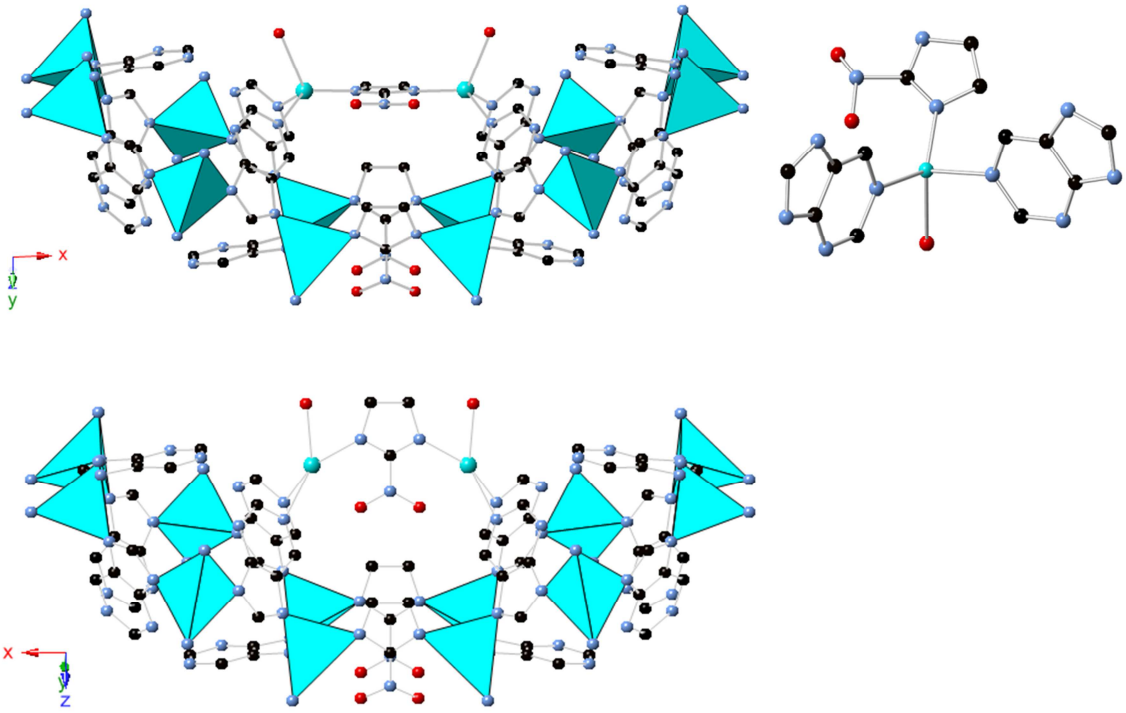

Figure 5.22: *The as-prepared structure **4** with (top left) one possible arrangement of exo-NIm and (top right) exo-zinc environment balancing charge by coordination to disordered anions. The flipped NIm linker in the as-prepared material after heating to 458 K in vacuum (bottom). Zn (turquoise), O (red), C (black), N (blue) and H (pink).*

Rietveld refinement of the structure obtained from SXRD was carried out against synchrotron X-ray powder data of an as-prepared material heated in vacuum to 458 K and examined at I11 at the Diamond Light Source. The refinement was carried out using the EXPGUI[14]/GSAS[15] software package. Solvent molecules were removed from cavities. Bond length and planar constraints were applied to purine and NIm linkers. *Exo* moieties turned out to have high thermal parameters which are consistent with refinement of low occupancies from powder XRD data. Final agreement factors are sufficiently good to indicate agreement between the single crystal structure and bulk material (Table 5.2 and Figure 5.23). Although the structure is partially misbehaving (there are chemically unreasonable angles to the *exo*-oxygen). This revealed a tilting of the *exo*-NIm linker upon solvent removal and underlines the framework flexibility in ZIF materials (Figure 5.22).

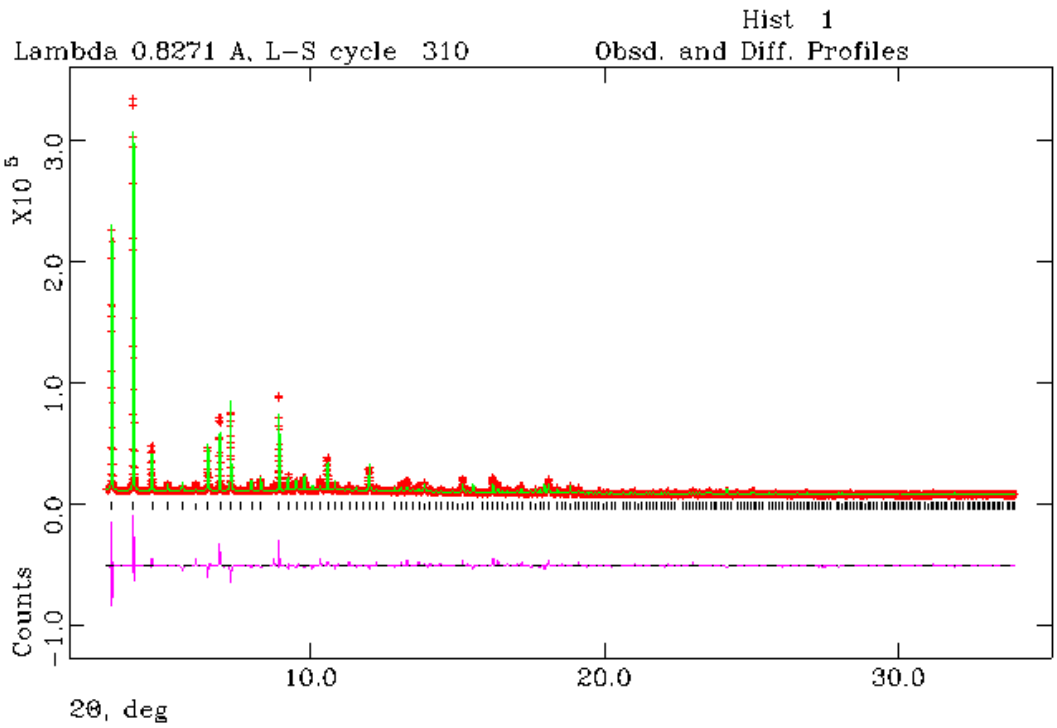

Figure 5.23: *Rietveld plot of the refinement of the structure of $Zn_{1.33}(OH)_{0.33}(NIm)_{1.167}(pur)$ against synchrotron X-ray powder diffraction data of as-prepared material after heating to 458 K in vacuum (λ = 0.827055 Å, Rwp = 0.0673) Observed pattern, red crosses, fitted profile in green, difference curve between observed and calculated pattern in pink.*

Table 5.2: *Crystallographic data for the Rietveld refinement of as-prepared structure **4** after heating to 458 K in vacuum, $Zn_{1.33}(O,OH)_{0.33}(NIm)_{1.167}(pur)$.*

Refined composition	$C_{31.00}N_{15.77}O_{7.51}Zn_{3.99}$
Formula mass [g / mol]	974.24
Space group	*Im-3m*
Z	16
a [Å]	29.0145(5)
b [Å]	29.0145(5)
c [Å]	29.0145(5)
V [$Å^3$]	24425.7(13)
λ [Å]	0.827055
2Θ range [°]	3 - 35.0
No. of reflections	9249
Rp	0.0407
Rwp	0.0671
$R(F^2)$	0.3274

Table 5.3: *Atomic position and occupancies obtained from Rietveld refined of desolvated structure **4**, $Zn_{1.33}(O,OH)_{0.33}(NIm)_{1.167}(pur)$.*

Atom	x	y	z	Occ	Uiso	Multiplicity
C1	0.2563(4)	0.3951(4)	0	1	0.017(5)	48
C2	0.2021(5)	0.3529(4)	0.02324(19)	1	0.017(5)	96
C3	0.3275(5)	0.3275(5)	0.1059(5)	1	0.017(5)	48
C4	0.31936(23)	0.35287(24)	0.1759(4)	1	0.017(5)	96
C7	0.1641(14)	0.1641(14)	0	0.33	0.017(5)	24
C8	0.1159(14)	0.1158(14)	0.02396(20)	0.17	0.017(5)	48
CN5	0.3051(5)	0.3790(5)	0.2168(5)	1	0.017(5)	96
CN6	0.3272(4)	0.3625(4)	0.2578(4)	1	0.017(5)	96
N1	0.2426(4)	0.37309(33)	0.03786(16)	1	0.017(5)	96
N2	0.2975(5)	0.4183(5)	0	1	0.017(5)	48
N3	0.30372(33)	0.36093(33)	0.1272(5)	1	0.017(5)	96
N4	0.1982(14)	0.1983(14)	0	0.17	0.017(5)	24
N5	0.1495(14)	0.1494(14)	0.03857(15)	0.17	0.017(5)	48
O11	0.39814(34)	0.39814(34)	0.39814(34)	1	0.017(5)	16
O1	0.3207(4)	0.4187(4)	0.03707(19)	1	0.017(5)	96
O2	0.2135(14)	0.2135(14)	0.03746(19)	0.17	0.017(5)	48
Zn1	0.25	0.40040(18)	0.09960(18)	1	0.0393(27)	48
Zn2	0.34171(32)	0.3868(6)	0.34171(32)	0.33	0.0943(27)	48

The TGA trace of a sample of **4** derived from synthesis in the presence of methanol is shown in Figure 5.24a. The initial loss results from removed methanol or water between 300 K and 330 K and is followed by loss of DMF up to 550 K. Decomposition starts at around 600 K. Samples heated at 500 K (Figure 5.24b), or water-treated and heated at 413 K (Figure 5.24c), show complete removal of DMF.

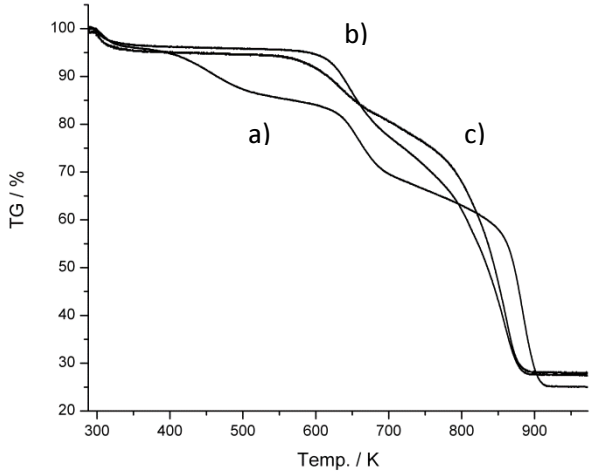

Figure 5.24: *TGA of a) as-prepared structure **4** and b) the same structure previously heated under vacuum at 500 K showing all the solvent molecules are removed by that heating. c) Plot shows the TGA on structure **4**, water-treated and heated (463 K, 4 h / 413 K, 3 h in vacuum).*

Adsorption of N_2 on structure **4** after heating under vacuum at 423 K ($Zn_{1.33}(O,OH)_{0.33}(NIm)_{1.167}(pur)$) gives a Type I isotherm with a maximum uptake of 6.5 mmol g^{-1} (0.23 cm^3 g^{-1}, BET 578 m^2 g^{-1}), whereas GCMC simulation for a structure without *exo*-moieties indicate an uptake of 10 mmol g^{-1} should be possible (Figure 5.25 full circles and open squares). In order to activate the solid, it was soaked in water over several weeks and the wash removed. This resulted in some loss of mass of the material, and NMR indicated loss of both pur and NIm linkers, with integrated ligand ratios of 1 : 1.4 / pur : NIm (Figure 5.26), but the remaining solid was crystalline as shown by the comparison of powder XRD of as-prepared and water-treated materials (Figure 5.27).

Furthermore, the crystal morphology remained unchanged (Figure 5.28).

Subsequent N_2 adsorption measurements showed a much higher uptake on the water-washed material, with a total uptake of around 12.5 mmol g^{-1} (BET 897 m^2 g^{-1}), including a small step at around p/p_0= 0.65 (Figure 5.25). This uptake corresponds

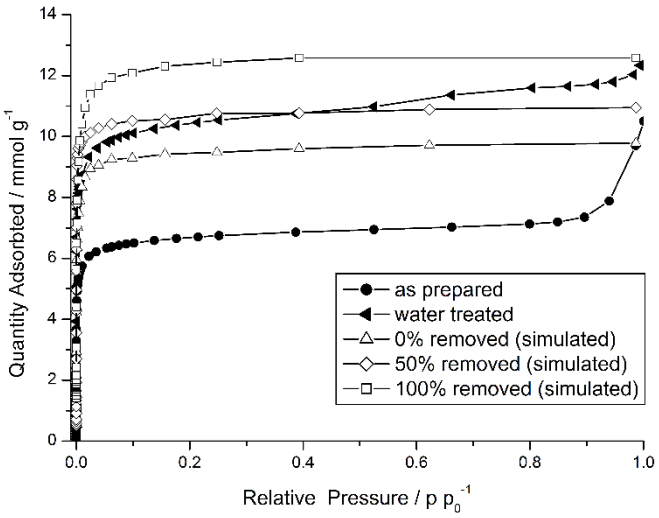

Figure 5.25: *Nitrogen adsorption (77 K) for structure **4** $Zn_{1.33}(OH)_{0.33}(pur)(NIm)_{1.167}$. Experimental data of as-prepared material heated at 463 K and activated under vacuum at 423 K (full circles) and a sample treated in water and heated under vacuum to 393 K (full triangles) compared to simulated as-prepared (open triangle), half of the exo species removed (open diamond) and all exo species removed (open squares).*

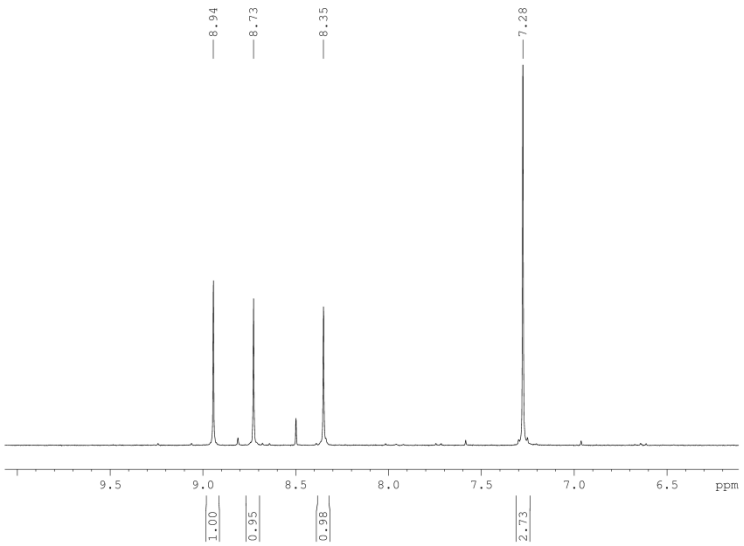

Figure 5.26*: ^1H NMR of mother liquor after water treatment of structure **4** showing resonances for purine (9.94 – 8.35 ppm) and NIm (7.28 ppm).*

approximately to that predicted by GCMC simulation on a material from which around one half the exo species had been removed (Figure 5.25). Similar values of surface area were found for ZIF-93 (BET 864 m^2 g^{-1}) and ZIF-96 (BET 960 m^2 g^{-1}) materials with the RHO topology which contain single linker functionalised at C4 and C5.[13] Washing with water therefore increases the uptake by making more of the expected pore volume of the bare framework available by removing exo Zn^{2+} cations and linkers. This is illustrated schematically below, where Figure 5.29 (left) corresponds to as-prepared structure **4** and Figure 5.29 (right) to the framework where all *exo*-zinc and -linker species are removed. The spheres (radii 13.8 Å and 18.2 Å) represent the open pore volume for the as-prepared and water-treated material, respectively.

Additionally, CO_2 isotherms at 298 K were collected and show some porosity for the as-prepared structure **4** (0.38 mmol g^{-1} at 0.1 bar), where the water-treated material

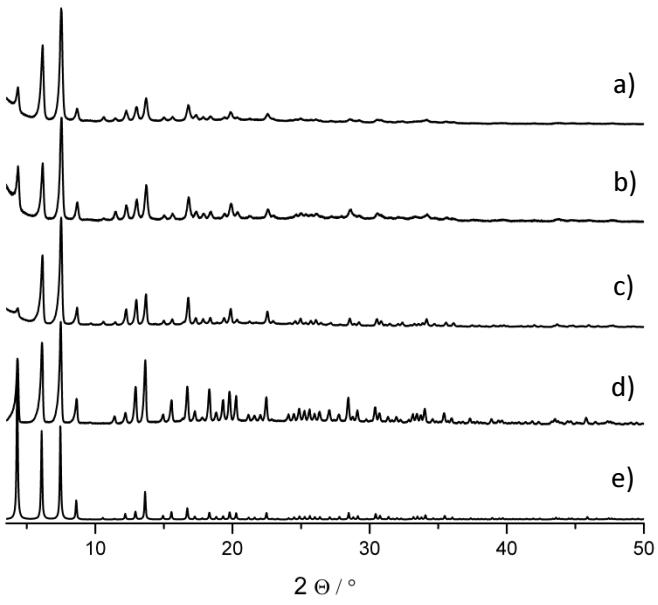

Figure 5.27: *Powder X-Ray diffraction pattern of a) as-prepared and treated with water followed by desolvating, b) as-prepared and treated with water, c) as-prepared desolvated, d) as-prepared* $Zn_{1.33}(O,OH)_{0.33}(pur)(NIm)_{1.167}$*, structure **4**, compared with that e) simulated using the structure determined from SXRD on the as-prepared material.*

takes up less carbon dioxide with 0.25 mmol g^{-1} at 0.1 bar (Figure 5.30). The observed values are comparable with uptakes presented for ZIF with the same topology.[13] One explanation for the lower uptake could be the loss of adsorption sites by removing some of the *exo* species.

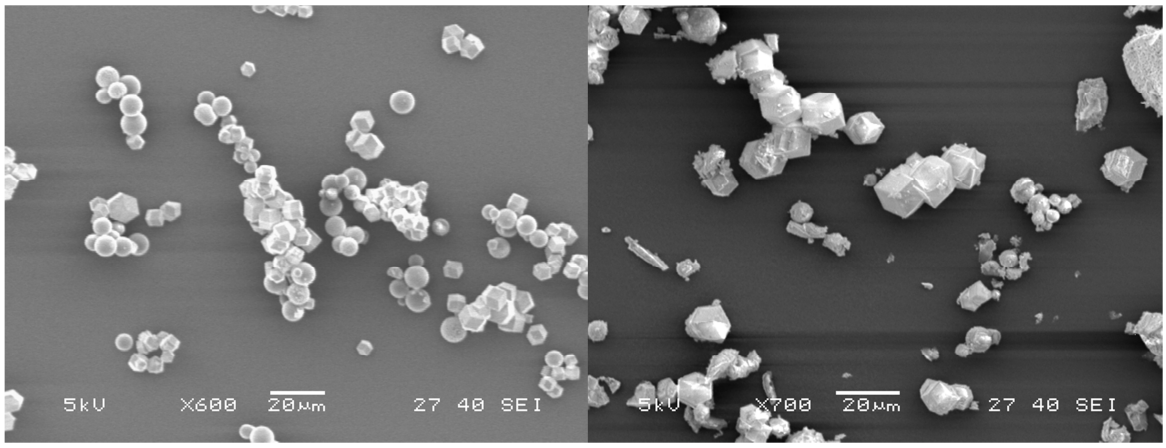

Figure 5.28: *SEM images of as-prepared structure 4 (left) and a similar sample after soaking in water (right)*

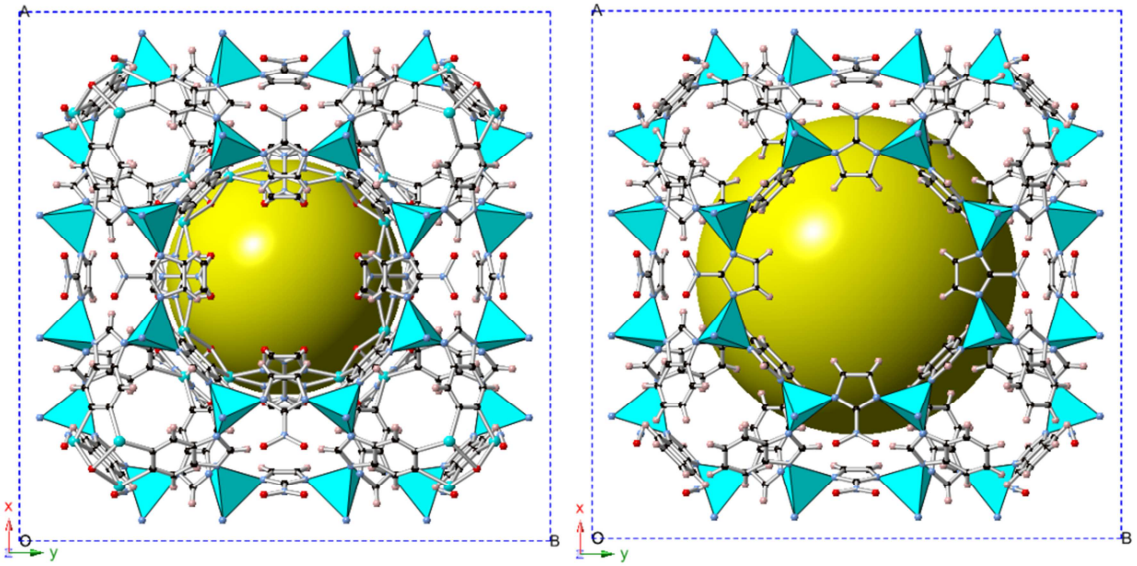

Figure 5.29: *Represents RHO cages with space filling spheres indicating the additional volume of a material without any exo species coating the cavities (right) compared with an as-prepared structure **4** with decorating exo species (left).*

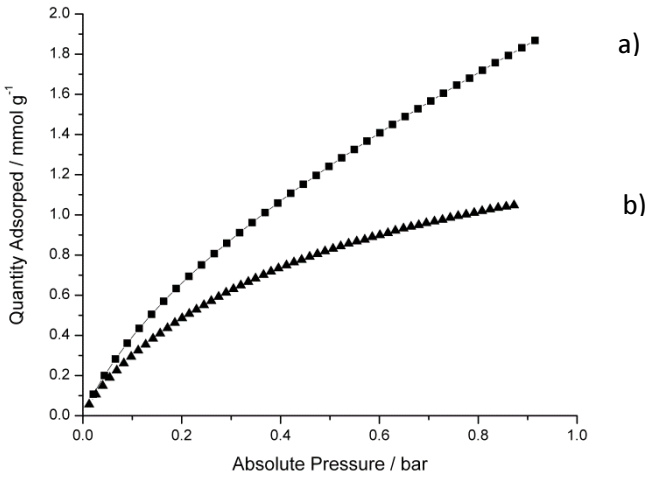

Figure 5.30: *Carbon dioxide adsorption (298 K) for structure **4** of a) as-prepared sample heated under vacuum to 473 K compared to b) water treated and heated under vacuum to 413 K.*

These experiments show architectural stability of the rho supercage upon water treatment, with the *exo* moieties partially removed. This raises the question of whether removable Zn can be exchanged for other metals and so create catalytically active sites. Therefore metal cation exchange reactions of as-prepared structure **4** were attempted with acetonitrile solution of $CuCl_2$, $PdCl_2$ and $CoCl_2$ at 338 K without stirring. Visual observation of the resultant powder showed the additives were deposited only as a layer on top of unreacted solids, the colour of which remained unchanged. EDX analysis revealed unreacted metal chlorides as the main component, suggesting the metal cation exchange reactions were unsuccessful in all cases.

Table 4: *Results from EDX measurement of Structure **4** treated with $CuCl_2$, $PdCl_2$ and $CoCl_2$.*

	Zn Atomic%	Cu Atomic%	Pd Atomic%	Co Atomic%	Cl Atomic%
$CuCl_2$	33.3	18.3	--	--	48.3
$PdCl_2$	61.6	--	11.8	--	26.4
$CoCl_2$	8.11	--	--	30.5	61.4

Further, catalytic reaction conducted by Laura Mitchell (St. Andrews) with as prepared and $PdCl_2$ treated structure **4** as catalyst in the Lewis acid catalyst conversions of (1) α-methyl styrene and (2) ethyl-3,3,3-trifluoropyruvate into (3) ethyl-2-hydroxy-4-phenyl-2-trifluoromethyl)pent-4-enoate did not show any significant activity (Scheme 5.1 and Table 5.5).

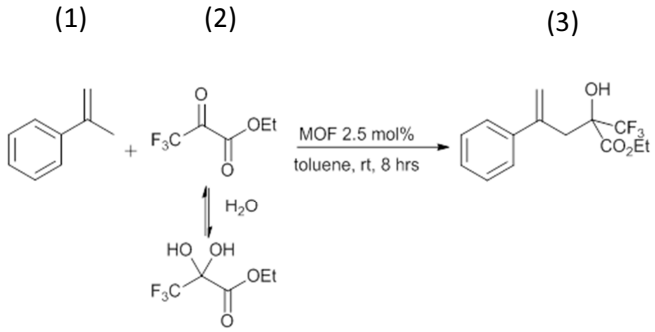

Scheme 5.1: *Illustrates reaction of the catalytic conversion of (1) α-methyl styrene and (2) ethyl-3,3,3-trifluoropyruvate to (3) ethyl-2-hydroxy-4-phenyl-2-trifluoromethyl)pent-4-enoate with a Pd treated structure **4** as catalyst.*

Table 5.5: *Catalytic results obtained from the as prepared and Pd^{2+}-treated structure **4** as catalysts compared to a reaction without catalyst.*

Catalyst	Reactant (%)	Product (%)	Hydrate (%)	Other (%)
no catalyst	85	12	2	1
Structure **4** as prepared	74	14	12	0
Structure **4** - Pd	79	14	5	2

Additional synthesis with different ligand ratios or cobalt salts as the metal cation source in place of Zn^{2+} did not give crystalline materials.

In situ synchrotron powder XRD measurements taken during CO_2 adsorption at 200 K at I11 (at the Diamond Light source) of as-prepared and water-treated structure **4** revealed only minor changes in the powder pattern, indicating weak interactions between the framework and the adsorbed gas (Figure 5.31 and Figure *5.32*).

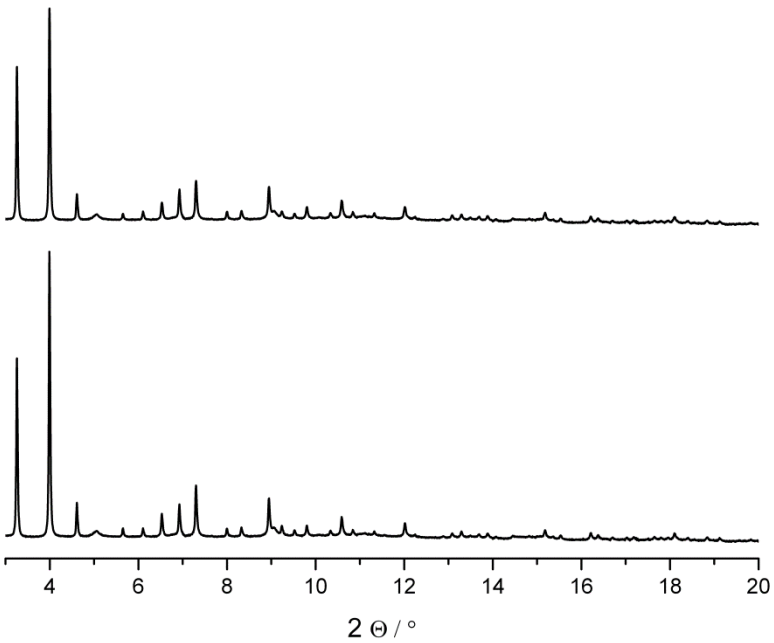

***Figure 5.31**: Synchrotron PXRD data of a water treated structure **4** activated at 403 K for 2 h under vacuum and measured at 0 bar (bottom) compared at 1.38 bar CO_2 pressure at 200 K (top). The incident beam radiation wavelength was λ = 0.827055 Å.*

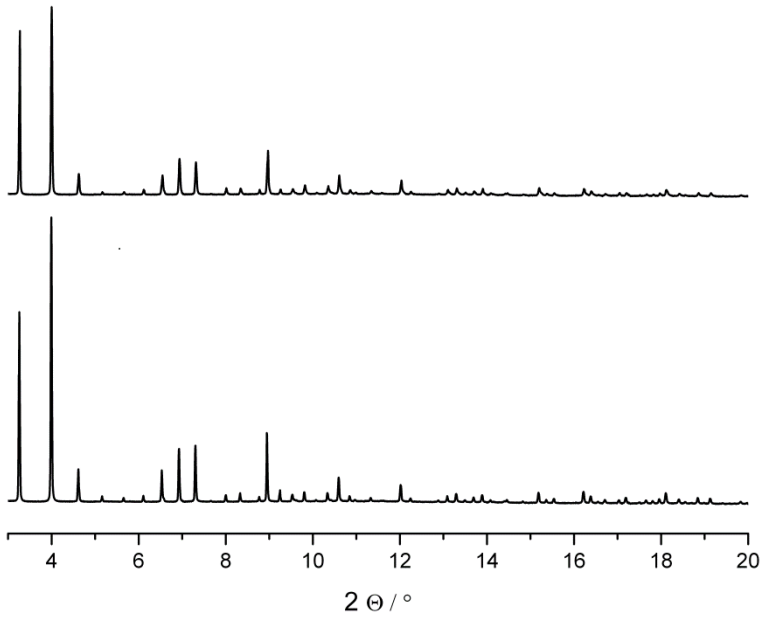

***Figure 5.32:** Synchrotron PXRD data of as-prepared structure **4** activated at 403 K for 2 h under vacuum and measured at 0 bar (bottom) compared at 1.423 bar CO_2 pressure at 200 K (top). The incident beam radiation wavelength was λ = 0.827055 Å.*

5.5 Conclusion

In summary, syntheses including mixtures of NIm and pur ligands give rise to four novel solids via variation of the metal source. Two of these include only the purine ligand, whereas the two resulting novel ZIF materials include ordered mixtures of imidazolate ligands in their frameworks (and the ZIF-20 (LTA) prepared in the absence of the NIm ligand does not crystallise). The phase selectivity under these crystallisations is influenced by the anions. In the absence of strongly coordinating anions ZIFs, with the GME and RHO topologies result, whereas with bromide and acetate the anion ends up coordinated to the zinc and only purine is included, coordinating via imidazolate and pyrimidine nitrogen atoms. Crystallisation in the presence of the nitrate anion results in a new ZIF with the RHO framework topology. The ordered inclusion of NIm and pur ligands results in a change of symmetry compared to ZIF-11, so that in the new material there is only one type of supercage (into which the pyrimidine groups of purine project). The presence of the smaller NIm ligands around the d8r windows results in a 9 Å window. Pyrimidine N atoms from adjacent purine groups coordinate exo zinc cations that are in turn bridged by exo NIm ligands. The porosity of the as-prepared solid, heated and evacuated, is 6.5 mmol g^{-1}, but can be increased to 12.5 mmol g^{-1} by removal of the exo cations and ligands.

This work underlines the versatility of purine as a framework component of MOFs, and the role that additional non-imidazolate N atoms can play in metal coordination in and outside of the frameworks. It is likely that use can be made of this in optical, catalytic and selective adsorption applications.

5.6 References

1. A. D. Burrows, *CrystEngComm*, 2011, **13**, 3623-3642.

2. R. Banerjee, H. Furukawa, D. Britt, C. Knobler, M. O'Keeffe and O. M. Yaghi, *J. Am. Chem. Soc.*, 2009, **131**, 3875-3877.

3. R. Galvelis, B. Slater, R. Chaudret, B. Creton, C. Nieto-Draghi and C. Mellot-Draznieks, *CrystEngComm*, 2013, **15**, 9603-9612.

4. P.-Q. Liao, D.-D. Zhou, A.-X. Zhu, L. Jiang, R.-B. Lin, J.-P. Zhang and X.-M. Chen, *J. Am. Chem. Soc.*, 2012, **134**, 17380-17383.

5. P. Cui, Y.-G. Ma, H.-H. Li, B. Zhao, J.-R. Li, P. Cheng, P. B. Balbuena and H.-C. Zhou, *J. Am. Chem. Soc.*, 2012, **134**, 18892-18895.

6. E. D. Bloch, D. Britt, C. Lee, C. J. Doonan, F. J. Uribe-Romo, H. Furukawa, J. R. Long and O. M. Yaghi, *J. Am. Chem. Soc.*, 2010, **132**, 14382-14384.

7. H. Hayashi, A. P. Cote, H. Furukawa, M. O/'Keeffe and O. M. Yaghi, *Nat. Mater.*, 2007, **6**, 501-506.

8. J. An, S. J. Geib and N. L. Rosi, *J. Am. Chem. Soc.*, 2009, **132**, 38-39.

9. D. Frenkel and B. Smit, *Academic Press, San Diego*, 2002, **2nd Ed**.

10. Y.-Q. Tian, S.-Y. Yao, D. Gu, K.-H. Cui, D.-W. Guo, G. Zhang, Z.-X. Chen and D.-Y. Zhao, *Chem. Eur. J.,* 2010, **16**, 1137-1141.

11. X.-C. Huang, Y.-Y. Lin, J.-P. Zhang and X.-M. Chen, *Angew. Chem. Int. Edit.*, 2006, **45**, 1557-1559.

12. B. P. Biswal, T. Panda and R. Banerjee, *Chem. Commun.*, 2012, **48**, 11868-11870.

13. W. Morris, B. Leung, H. Furukawa, O. K. Yaghi, N. He, H. Hayashi, Y. Houndonougbo, M. Asta, B. B. Laird and O. M. Yaghi, *J. Am. Chem. Soc.*, 2010, **132**, 11006-11008.

14. B. H. Toby, *J. Appl. Crystallogr.*, 2001, 210-213.

15. C. Larson and R. B. von Dreele, *Los Alamos National Labaratory: Los Alamos, NM*, 2001.

6. A Novel Diamino-Functionalised Open Framework ZIF

6.1 Introduction

The current state of technology for removing CO_2 on a large scale from flue gas streams involves the use of aqueous amines as adsorbents through chemisorption processes.[1-3] However, the large volume of water makes the regeneration processes energy intensive and necessary replacement of amines causes environmental issues arising from volatilisation and material degradation when the process is operated at high temperatures. These issues taken together with the corrosive nature of the solution, makes aqueous amine adsorption an energetic and expensive approach to carbon capture from flue gas on an industrial scale. Therefore, solid sorbents are under investigation as alternatives for use in pressure swing adsorption / desorption processes that are theoretically less energy intensive and have the potential to be free from corrosion and solvent loss described above.[4] In particular materials like zeolites,[5, 6] polymers (as membranes)[7-9] and metal-organic frameworks (MOFs)[10-12] are under investigation. MOFs such as CPO-27 and HKUST-1 exhibit Lewis acidic open metal sites (cus – coordinatively unsaturated sites) as adsorption sites with strong attraction to various gases which makes them favourable for gas separation processes,[13-15] but a potential pitfall arises with water being adsorbed preferentially at cus over all other components in wet gas streams under flue gas conditions, with the result of decreased performance and stability issues.[16]

In aqueous amine solutions, CO_2 capture by primary amines is based on two reactions:

(R1) $2(R\text{-}NH_2) + CO_2 \leftrightarrow R\text{-}NH_3^+ + R\text{-}NH\text{-}COO^-$

(R2) $R\text{-}NH_2 + H_2O + CO_2 \leftrightarrow R\text{-}NH_3^+ + HCO_3^-$

CO_2 adsorption processes in solids may follow a similar process, with the reaction including water in the stoichiometry making them suitable for applications as adsorbents under wet flue gas conditions. Therefore, amine-functionalised adsorbents are suitable materials for separation processes in wet CO_2-containing gas mixtures.[17-21]

This work discusses the introduction of amino functionalities, albeit using amines on aromatic rings into a porous open framework material through a mixed linker synthesis approach that includes the diamino-functionalised purine derivative, 2,6-diaminopurine, together with 2-nitroimidazole (Figure 6.1). The unsubstituted purine linker was shown earlier in this work to act as a suitable precursor in mixed linker syntheses yielding mixed linker ZIFs with the GME and RHO topologies.[22] Furthermore, adenine is a purine base with mono-amino functionalization in position 2 and is found in many MOFs as a bidentate ligand. Open framework materials from mixed linker syntheses were obtained by Rosseinsky et al. yielding 1D-porous structures.[23] Wang et al reported a cadmium-adeninate paddlewheel structure.[24] Zinc-adeninate secondary building units (ZABUs) were presented by Rosi et al. in studies where 1D zinc-adeninate columns form the basis of highly porous bio-MOFs via interconnecting dicarboxylate linkers.[25, 26] Zhang et al. reported a structure where adenine coordinates only through its imidazolate moiety as monodentate linker and the amino group hydrogen bonds to neighbouring carboxylate oxygen atoms and so stabilizes the host framework. Free NH_2-groups pointing into open pore space contribute to its CO_2 uptake of 1.12 mmol g^{-1} at 0.1 bar and 298 K.[27]

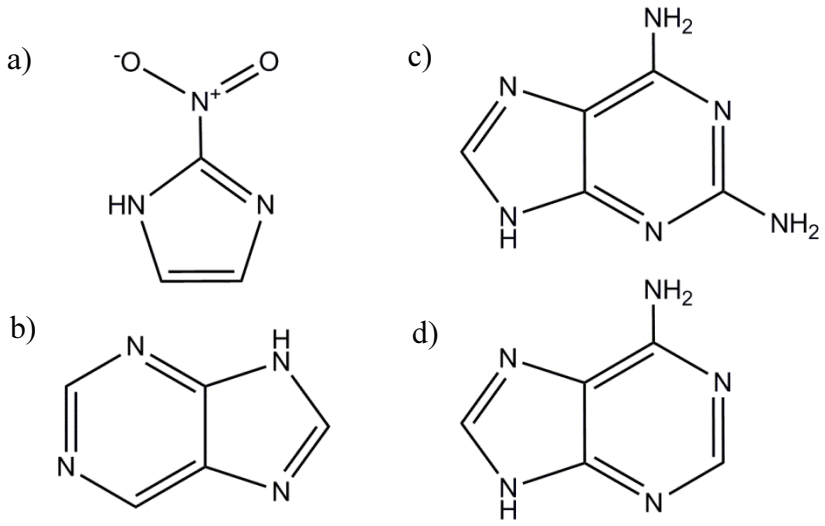

Figure 6.1: *Showing the structure of a) 2-nitroimidazole (NIm), b) purine, c) 2,6 diaminopurine (DAP) and d) adenine.*

Further investigations with the aims of enhancing adsorption and overcoming performance issues of open metal sites facing wet flue gas conditions were made by using 2,6-diaminopurine (DAP) (with two amines) within a mixed linker approach. NIm was chosen to serve as an additional linker that has been shown by us and others to be suitable as a directing agent in the synthesis of mixed ligand ZIFs.[22, 28] Inclusion of DAP as a component of MOFs has to our knowledge not been reported. A novel DAP-bearing ZIF has been prepared here, indicating that additional functionalization of purine can result in materials with novel framework topologies and potential properties in carbon capture.

6.2 Experimental

A typical synthesis was carried out by combining a mixture of zinc nitrate, NIm and DAP in the ratio 1 : 1 : 1 in a Teflon-lined steel autoclave with DMF. The resultant gel was heated at 373 K for 7 days. After the reaction was allowed to cool to room temperature the solid product was filtered and washed with DMF before drying at room temperature. In order to increase the crystal size of the novel product, numerous experiments were conducted in which ligand ratios, temperatures, solvents and gel concentrations were varied. Additional experiments using zinc acetate, cobalt nitrate and cobalt acetate as metal salt precursors were also carried out.

6.2.1 Synthesis of STA-17 $Zn(NIm)_{1.33}(DAP)_{0.66}$ xDMF

Zinc nitrate hexahydrate (1mmol, 297.5 mg, Aldrich), 2-nitroimidazole (1 mmol, 113.1 mg, Alfa Aesar), 2,6-diaminopurine (1 mmol, 150.1 mg, Alfa Aesar) and 15 ml DMF (Aldrich) in a 40 ml Teflon lined steel autoclave were heated at 373 K for 7 days and then cooled to room temperature. The yellow product was filtered and washed three times with DMF followed by drying at room temperature.

The reaction gave a yellow solid comprising small needle-shaped crystals. Experiments to increase the crystal size were carried out increasing the concentration of the precursors (3 times) or using a 1 : 1 solvent mixture of DMF and MeOH. The novel material was characterized by laboratory and synchrotron powder X-ray diffraction, IR,

electron microscopy and adsorption measurements. Its composition was determined using elemental analysis, TGA, EDX, solution phase and solid state NMR.

6.3 Results and Discussion

A new phase was identified on the basis of PXRD (Figure 6.2). Later confirmation of porosity (see below) led to it being labelled STA-17 (St. Andrews microporous material No. 17) The pure single crystalline phase obtained was not amenable for laboratory single crystal X-ray diffraction studies, even for the largest crystals obtained, because of the acicular nature of the crystals (even though the length reached 25 μm, the thickness was less than 5 μm) (Figure 6.3). Attempts were made via the single crystal diffraction rapid access route at the Diamond synchrotron (station I19) but scattering was only observed out to 2 Å and no unit cell could be obtained.

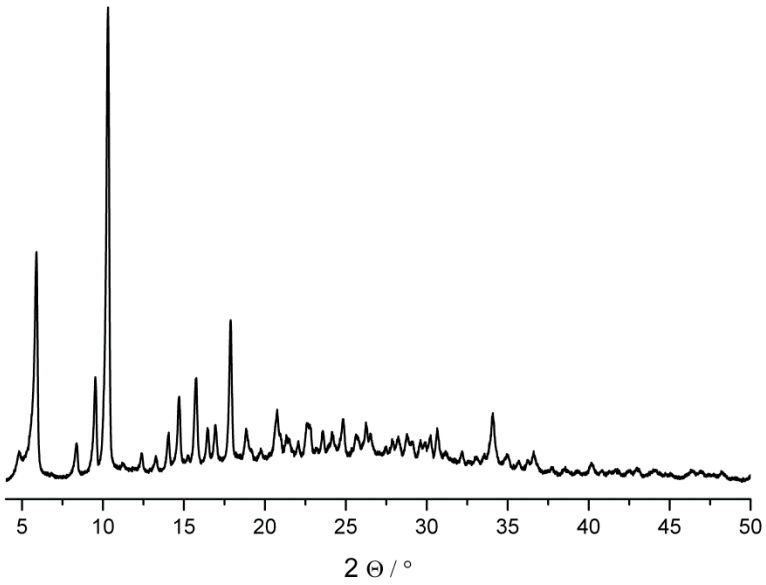

Figure 6.2: *PXRD pattern of as prepared STA-17 (λ = 1.54051 Å).*

In order to investigate the impact of different ligand ratios in synthesis, experiments with varying linker concentration were carried out with the objective of understanding the role of the two imidazolate linkers in the crystallisation process (Figure 6.4).

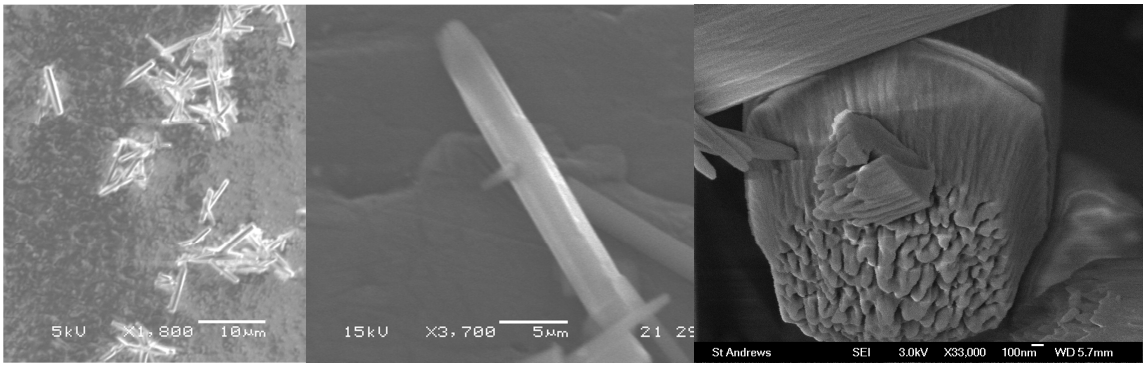

Figure 6.3: *High resolution FEGSEM images of as prepared STA-17. Courtesy of Heather Greer.*

Doubling the NIm concentration and using a NIm : DAP ratio of 2 : 0.1, a powder pattern of the cubic ZIF-65(Zn) in SOD topology, discussed earlier in this thesis, was obtained as the only phase (Figure 6.5 a). Using a 2:1 ratio of NIm to DAP yielded mainly ZIF-65 with the SOD topology, with some additional reflections not matching

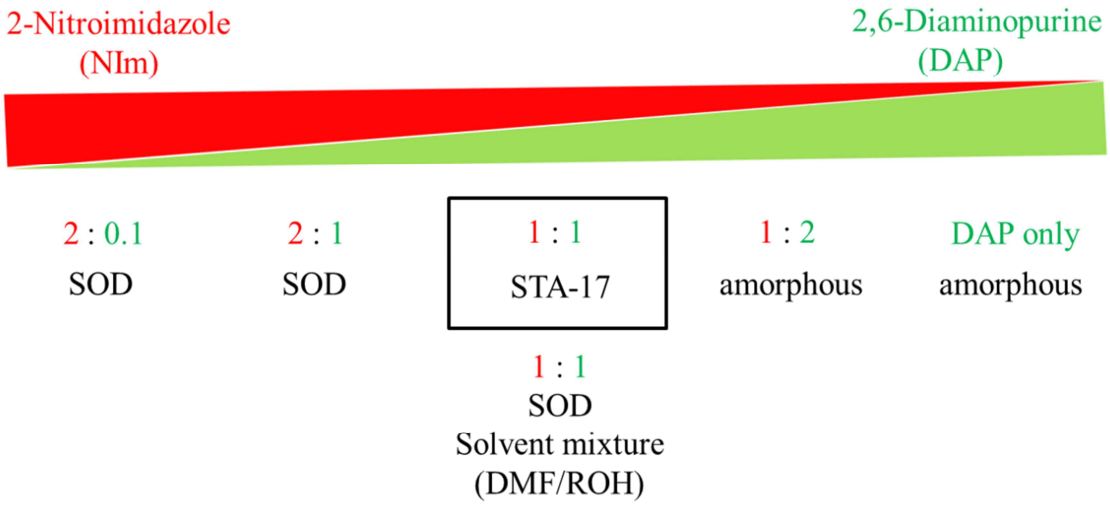

Figure 6.4: *Summary of ligand ratios (NIm-red, DAP-green) and obtained phases (black) in the mixed linker synthesis with increasing DAP concentration from left to right. The reactions were carried in DMF unless stated different.*

with STA-17 (Figure 6.5 b). Exploring ligand ratios towards increased DAP concentration (beyond 1 : 1) resulted in amorphous solids. Applying the mixed solvent approach reported earlier in this thesis where a mixture of DMF and MeOH was used in synthesis to increase crystal size (chapter 5), again resulted in the formation of the ZIF-65 (SOD) material with noticeable reflections from impurities (Figure 6.5 c shows a XRD pattern obtained from synthesis of a 1:1 DMF to MeOH ratio). STA-17 could therefore only be obtained within a narrow range of experimental parameters and its crystallisation turned out to be highly sensitive to precursor and solvent compositions.

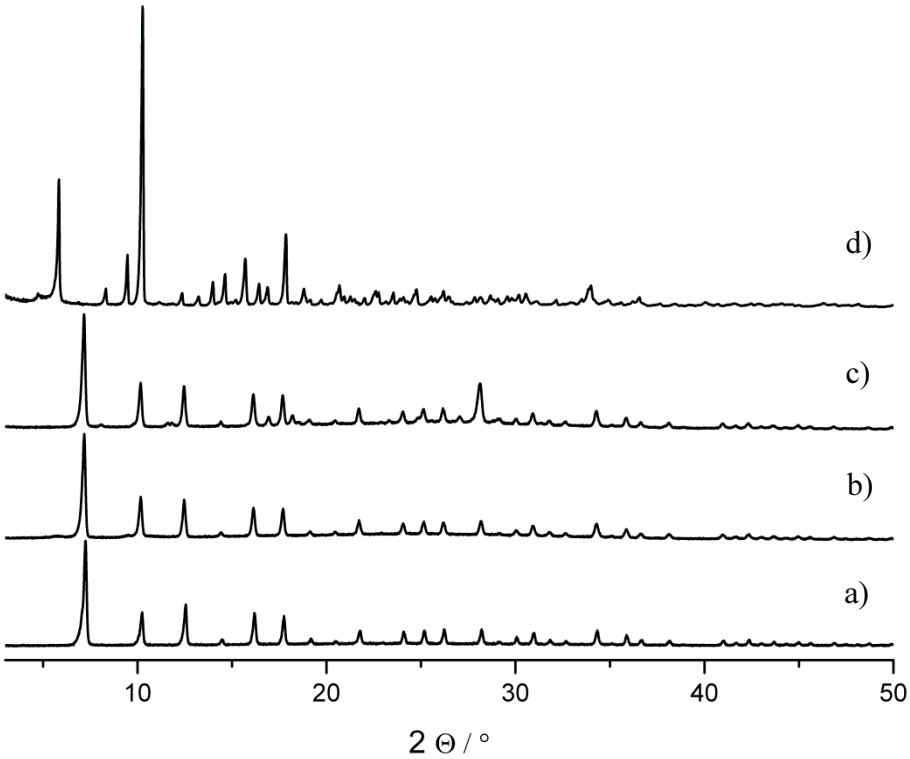

Figure 6.5: *Powder XRD pattern of products of crystallisation using different NIm : DAP ratios. a) 2 : 0.1, b) 2 : 1 and c) 1:1 in a DMF : MeOH mixture of 1 : 1 compared to d) STA-17 prepared using NIm : DAP ratios of 1 : 1.*

The synchrotron X-ray powder diffraction pattern measured at I11, Diamond Light Source, on as-prepared STA-17 was indexed to give a hexagonal unit cell with $a = b =$ 29.725 Å and c = 18.606 Å (Figure 6.6). This was consistent with the hexagonal prismatic morphology observed by SEM (Figure 6.3). It remained crystalline upon solvent exchange reactions in MeOH and after solvent removal via heating to 383 K. The framework was stable up to 493 K (Figure 6.7).

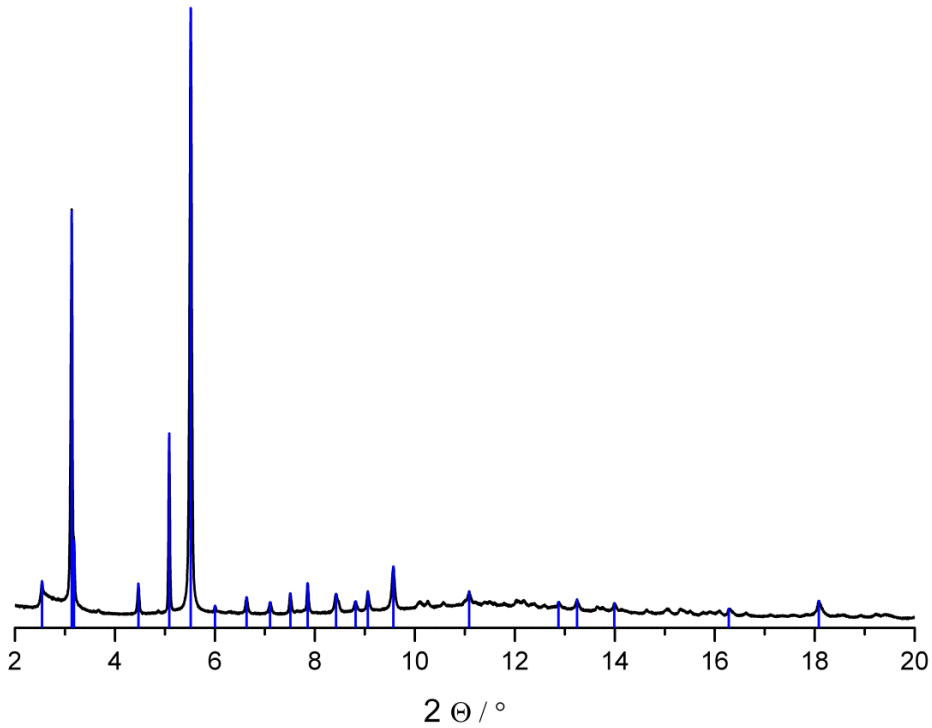

Figure 6.6: *Powder XRD pattern of as-prepared STA-17 measured at I11 with synchrotron radiation of λ = 0.827055 Å which was used for indexing. Blue tick marks indicate peaks used for indexing.*

The presence of both linkers in the structure was shown by solution phase ^{1}H and solid state ^{13}C NMR (Figure 6.8 and also see Figures 7.4 and 7.5 in solid state MAS NMR note chapter 7). Integrated peaks from solution phase NMR suggest a NIm : DAP ratio of 2:1 with assigned resonances at 7.31 ppm (2H,s) for C_4H and C_5H in NIm and 8.05

ppm (0.4H,s) for the C_8H proton of DAP. There are two additional peaks 7.68 ppm (0.7H,s) and at 8.10 ppm (0.2H,s) assigned to DMF and formic acid, respectively, the latter occurring as a hydrolysis product of DMF.[29] These peaks show lower intensity for a material heated to 493 K where most of the DMF is removed (Figure 6.8 bottom). A similar ligand ratio (2 : 1) was also found by integration of ^{13}C peaks in solid state NMR.

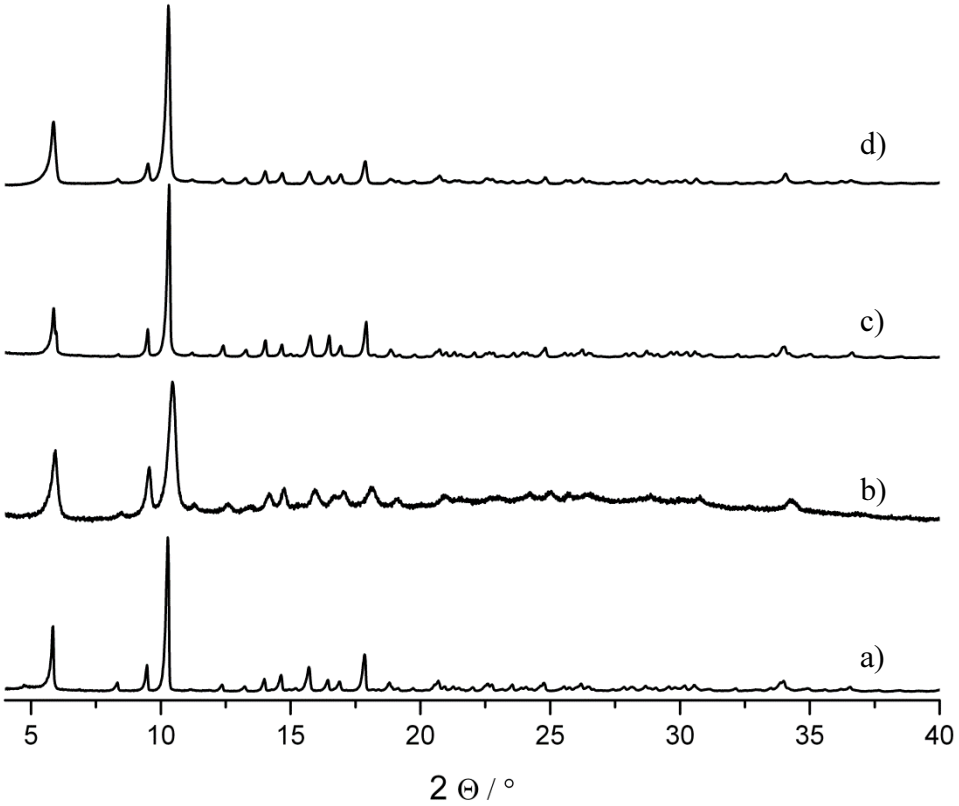

Figure 6.7: *Powder XRD pattern of a) as-prepared STA-17, b) STA-17 heated to 493 K, c) MeOH exchanged STA-17 and d) STA-17 after MeOH exchange and subsequent heating to 383 K under vacuum (measured in a sealed capillary). Patterns were collected with a Cu $K_{\alpha 1}$ X-ray radiation (λ = 1.54051 Å).*

Additionally, IR measurements indicate the presence of both linkers in the structure with NH_2 between 3500-3300 cm^{-1} for the DAP linker and the NO_2 asymmetric stretch band at 1375 cm^{-1} for NIm (Figure 6.9).

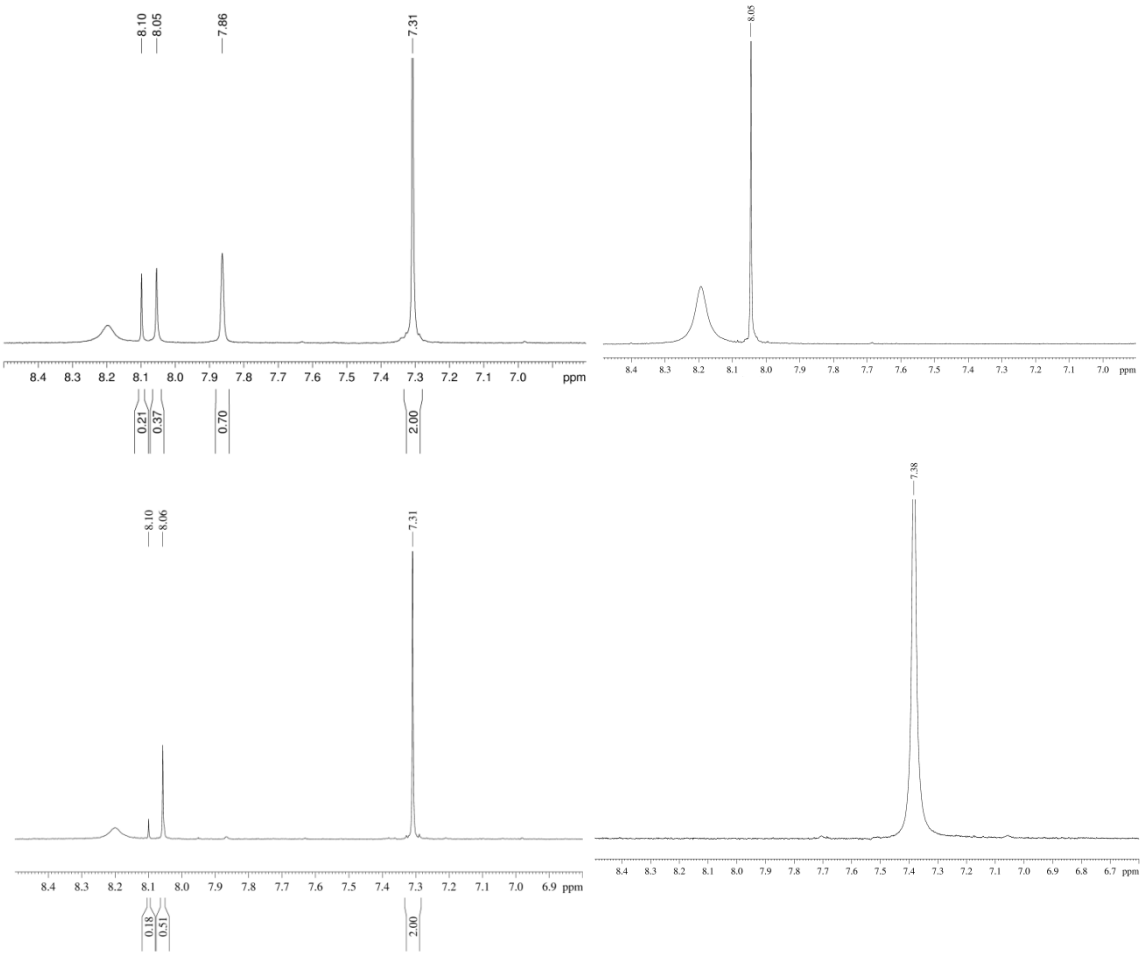

Figure 6.8: *^{1}H-NMR spectra of as prepared STA-17 (top left) compared to STA-17 heated to 493 K (bottom left), digested in 0.2 M nitric acid and DMSO-d_6. The spectra shows protons from NIm at DAP at 8.05 ppm and 7.31 ppm. Spectra of pure DAP (top right) and NIm (bottom right) giving resonances at 8.04 ppm and 7.38 ppm, respectively. The peaks at 7.86 ppm and 8.10 ppm were assigned as the formaldehyde proton in DMF and formic acid that result from hydrolysis of DMF.*

TG analysis of as-prepared and MeOH-exchanged STA-17 confirmed the finding and further shows the almost-complete exchange of DMF by MeOH. (Figure 6.10). Further, careful observation of a MeOH-treated sample shows the loss of solvent (13.7 %) below

373 K. Additional mass loss of 5.1 % between 400 K and 540 K was assigned to small amounts of residual DMF. The final framework degradation is initiated by the decomposition of NIm at 555 K. Directly heating the material to 493 K results in the complete removal of solvent before decomposition, but causes some loss of crystallinity. (Figure 6.7 and Figure 6.10).

Taken together, NMR and TGA analysis suggest an empirical formula of $Zn(NIm)_{1.33}(DAP)_{0.67}$ •1.3DMF for the as-prepared material. For the TGA in air, a sample with composition $Zn(NIm)_2$ (such as ZIF-65(Zn)) would have a ratio of ligand weight lost (2 NIm) to ZnO remaining (as confirmed by XRD) of 2.8. For the ZIF-65(Zn) of chapter 4, a value of 2.6 was measured. For a material of composition $Zn(NIm)_{1.33}(DAP)_{0.67}$, the calculated value for the same ratio is 3.1. The measured value for STA-17 is 3.0, which supports a model of DAP inclusion in the ZIF. CHN analysis could not match the composition due to the mixed linker system and unresolved composition of hydrolysis products of DMF and residual solvent.

STA-17 was demonstrated to have permanent porosity by measurement of N_2 uptake at 77 K after heating at 463 K under vacuum. The N_2 isotherm is of type I, typical of activated microporous materials (Figure 6.11) with a maximum nitrogen uptake (at 77 K) of 6.5 mmol g^{-1} (pore volume 0.23 cm^3 g^{-1}). The BET was calculated as 428 m^2 g^{-1}. Additionally, CO_2 adsorption measurements at 298 K and 198 K were found to be 0.5 mmol g^{-1} at 0.1 bar and 4.75 mmol g^{-1} at 0.89 bar, respectively, (Figure 6.12) which is comparable to values found in the literature for mixed linker ZIFs.[28]

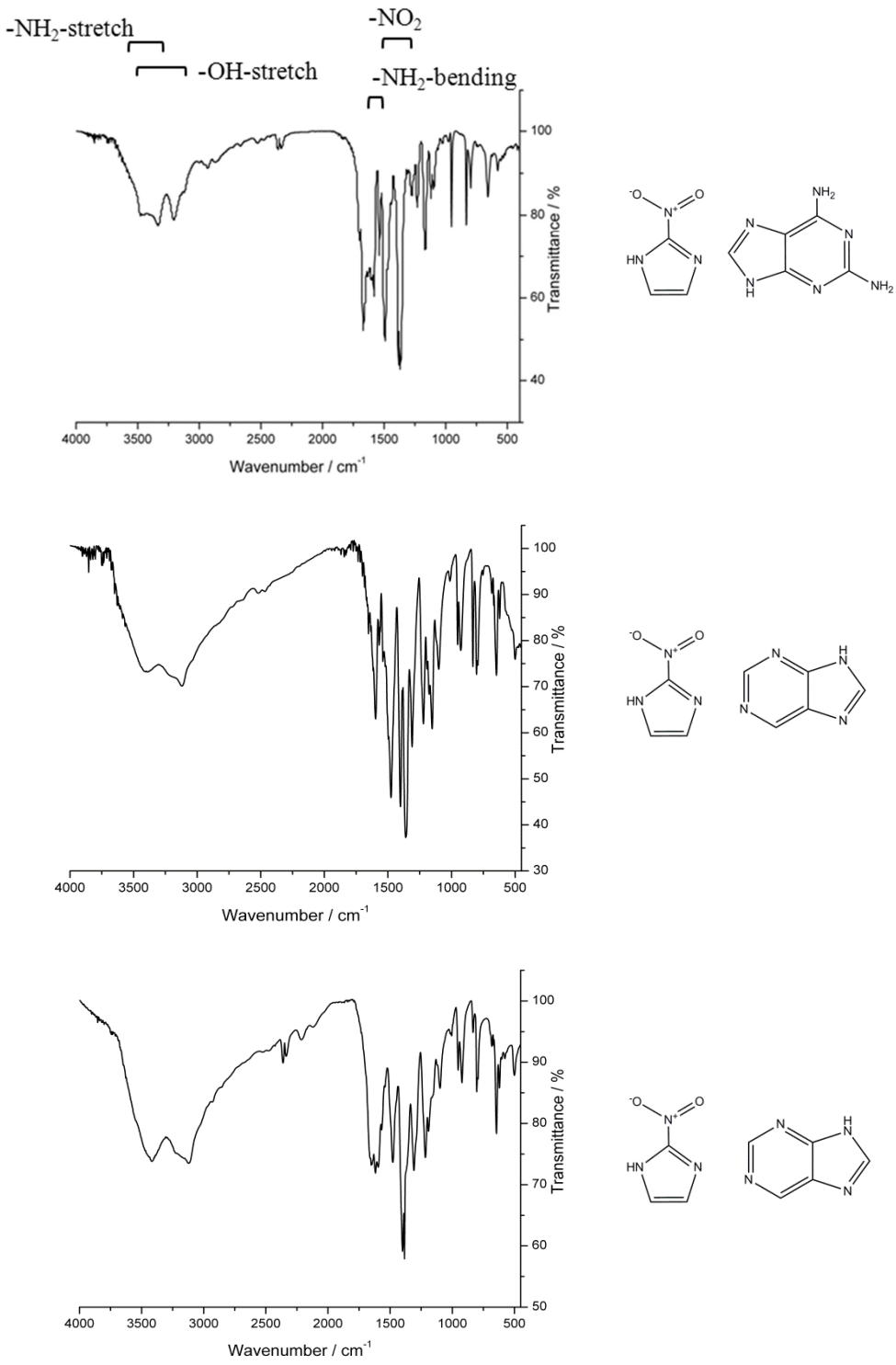

Figure 6.9: *IR plots of as prepared STA-17 (top) showing the presence of -NH_2 and -NO_2 functionalities compared to as-prepared structure **1**, GME, (middle) and structure **4**, RHO (bottom) (both comprising of NIm and purine). Structures of the linkers found in each framework are presented on the right.*

In situ powder XRD measurements of CO_2 adsorption (200 K) collected at the Diamond Light Source (I11) for a methanol-exchanged STA-17 heated at 423 K for 3 h under vacuum prior to in situ measurements showed only small changes, suggesting weak interactions between the framework and carbon dioxide (Figure 6.13).

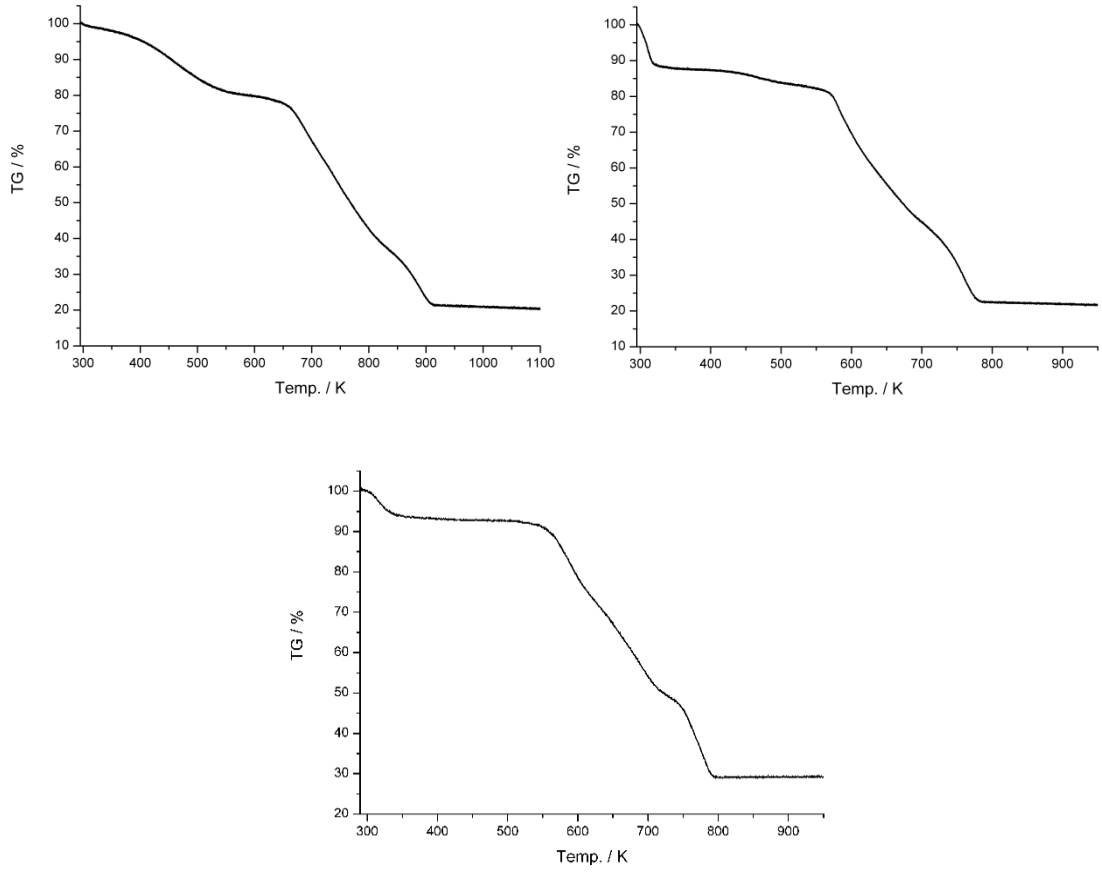

Figure 6.10: *TGA plots of STA-17 (top left) as prepared, (top right) MeOH exchanged and (bottom) heated in flowing air at 5 K / min to 493K.*

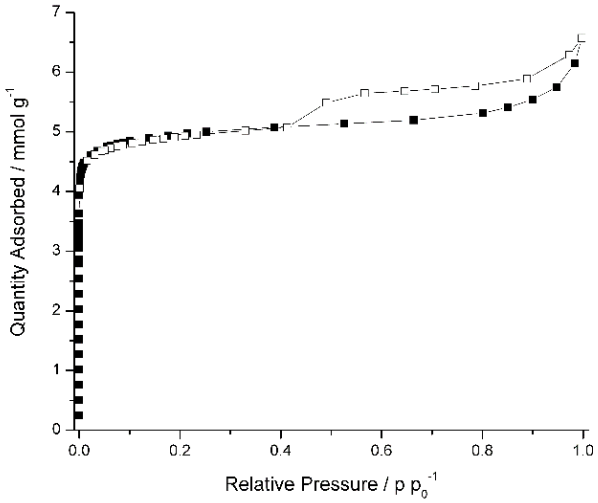

Figure 6.11: *Illustration of nitrogen isotherm collected at 77 K of as prepared STA-17 heated under vacuum at 463 K prior measurement. (Adsorption – full symbols, desorption – empty symbols).*

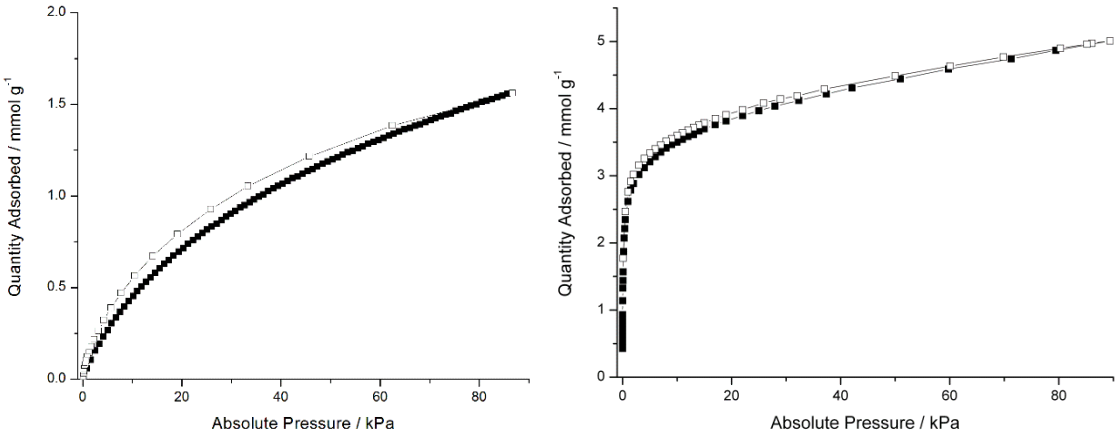

Figure 6.12: *CO_2 adsorption at 298 K (left) and 198 K (right) of as prepared STA-17 activated under vacuum at 463 K. (Adsorption – full symbols, desorption – empty symbols)*

Phase impurities in synthesis with lower DAP concentration indicate that STA-17 crystallisation is in competition with other reactions and suggest a multistep reaction path leading to the final product. In order to investigate the crystallisation sequence, experiments with reaction times of 3 h, 12 h and 18 h were conducted with the results

presented in Figure 6.14. ZIF-65 (SOD topology) forms initially and over time STA-17 becomes the major product. The initial ZIF-65 phase shows reflections of small intensities of a second phase different from the final STA-17. After 12 h weak reflections of STA-17 next to the cubic SOD phase start to appear which suggests a process where SOD dissolves and STA-17 crystallizes at the cost of the cubic ZIF-65 structure, including DAP from solution into the crystallising material. Subsequent solution phase NMR analysis showed small amounts of DAP as well as NIm in samples

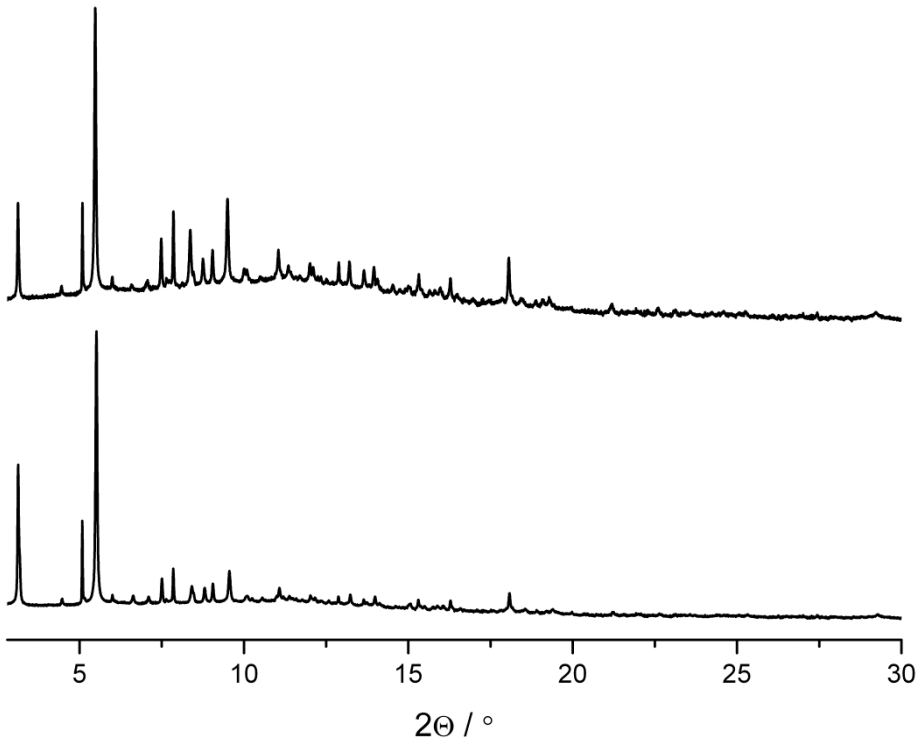

Figure 6.13: *Synchrotron powder XRD pattern of MeOH exchanged and heated to 423 K under vacuum STA-17 measured in situ during CO_2 adsorption at 200 K. Pattern were collected at 0 bar (bottom) and 1.344 bar (top) CO_2 pressure. The incident beam radiation wavelength was λ = 0.827055 Å.*

crystallised after 3 h and 12 h reaction times, despite PXRD patterns showing the SOD phase as the only or main component (Figure 6.15). This observation can be explained by the low solubility of DAP in DMF. The starting reaction is a white gel rather than a clear solution that indicates the presence of undissolved DAP since reactions of zinc nitrate and NIm (compare ZIF-65(Zn) in chapter 4) show clear solutions.

The incorporation of DAP and formation of STA-17 was shown to appear after elapsed reaction time and it is most likely that extended reaction times at elevated temperature increases the DAP solubility and therefore allows the crystallisation of the mixed linker material.

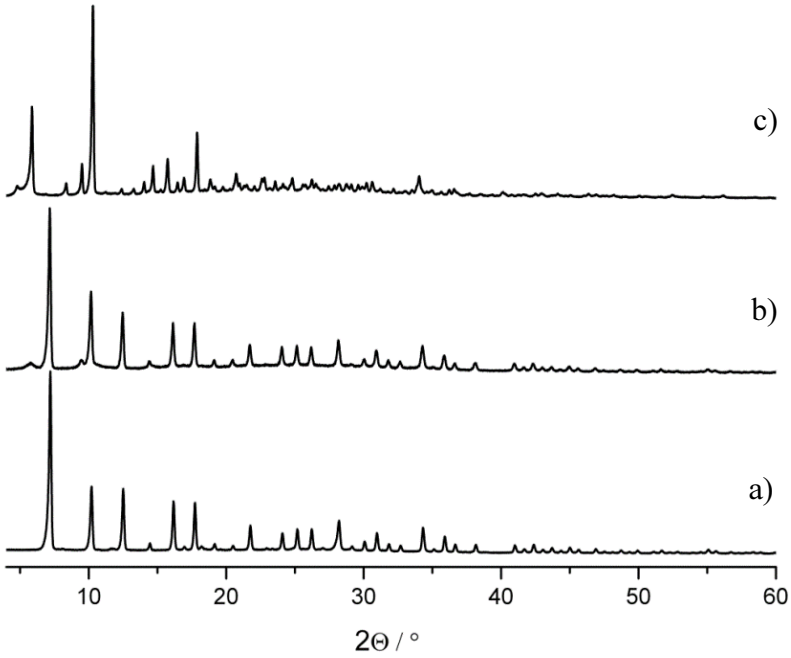

Figure 6.14: *Illustrating powder XRD pattern after conducting experiments with zinc : NIm : DAP in the ratio of 1 : 1 : 1 with reaction times of a) 3h, b) 12h and c)18h.*

Additional experiments were conducted with the aim of increasing STA-17 particle size to obtain single crystals amenable for SXRD. As well as varying the ratio of zinc : NIm : DAP as described previously, a synthetic approach with cobalt and cadmium metal sources, prone to yield ZIFs using large crystals, was also investigated. Keeping the reaction conditions and ligand-to-metal ratios unchanged, $Co(NO_3)_2$, $Co(OAc)_2$, $CdCl_2$, $CdBr_2$, $Cd(NO_3)_2$ and $Cd(OAc)_2$ appeared suitable for crystallisation processes. Only

cadmium bromide and cadmium nitrate salts yielded in crystalline materials, identified as the cubic CdIF-8 (SOD)[30] and a physical mixture of the latter and an unknown phase, as shown in Figure 6.16. Single crystal data of the unknown phase gave unit cell parameters of a = 23.432 Å, b = 24.20 Å, c = 46.43 Å, β = 98.426 ° (monoclinic), but the quality of the data did not allow any structure solution. In no cases was STA-17(Cd) prepared.

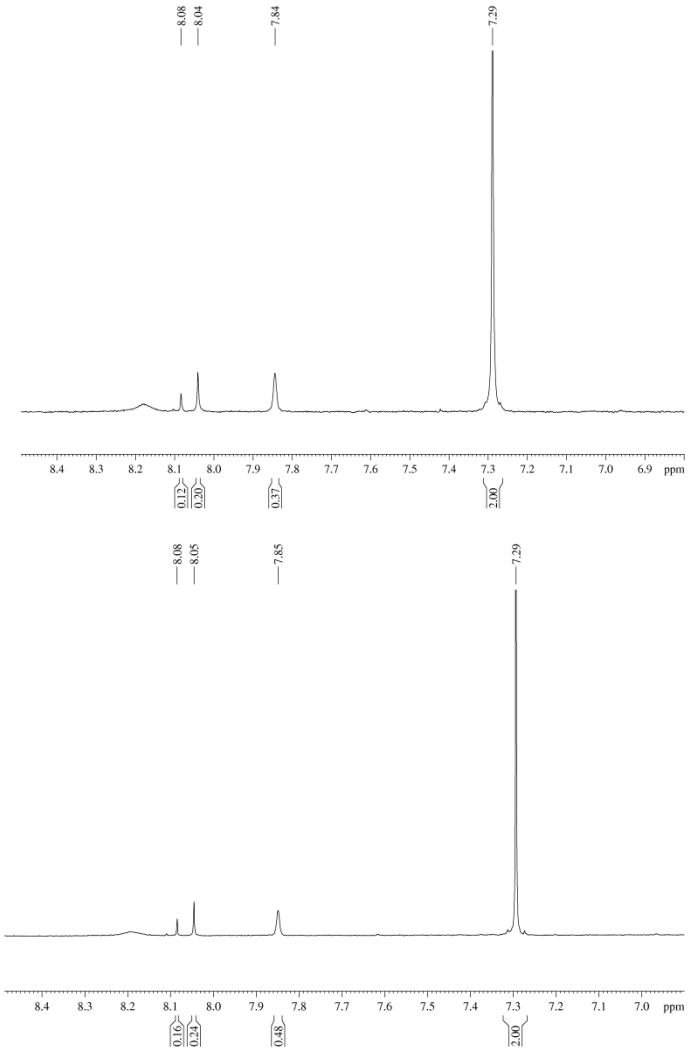

Figure 6.15: *^{1}H NMR spectra of STA-17 products of synthesis stopped after 3 h (top) and 12 h (bottom) reaction time. The solids were digested in 0.2 M nitric acid and DMSO-d_6. Resonances at 7.29 ppm and DAP at ~8.05 ppm indicate the presence of both linkers, NIm and DAP, in the solid. The peaks at ~7.85 ppm and 8.08 ppm were assigned as the formaldehyde proton in DMF and formic acid that result from hydrolysis of DMF.*

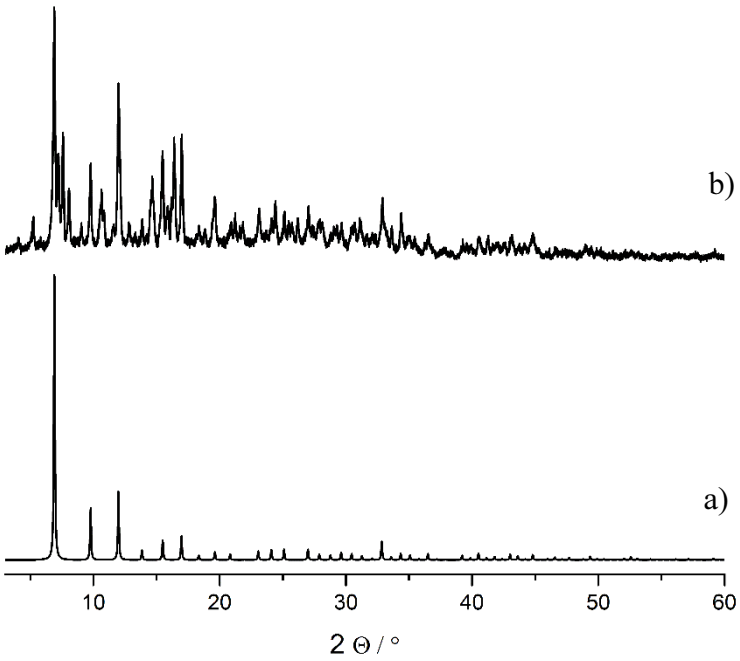

Figure 6.16: *Powder XRD pattern of a) simulated CdIF-8 and a physical mixture of CdIF-8 and the monoclinic phase obtained from the solvothermal reaction of zinc nitrate with NIm and DAP. The pattern was recorded using copper X-ray radiation (λ = 1.5405 Å)*

6.4 Towards the Structure Solution of STA-17

Studies indicate a novel, mixed linker ZIF has been prepared and characterized by PXRD with a hexagonal cell ($a = b = 29.725$ Å, $c = 18.606$ Å). To understand and explain the adsorption behaviour, it is necessary to determine the structure. This is usually achieved for ZIFs by SXRD.

For STA-17, however, it was not possible to obtain data from such experiments, even though crystals up to 25 μm long were examined at I19. Therefore use must be made of PXRD. Direct, *ab initio* methods were attempted extensively to solve the structure from

PXRD, but no convincing structure solutions were obtained. As an alternative approach, use was made of the structural analogues between ZIFs and zeolites (aluminosilicates) (Figure 6.17).

Many ZIFs have zeolite topologies (e.g. ZIF-8 (SOD), ZIF-68 (GME), ZIF-20 (LTA) etc.) Direct correlation between Zn-Zn distance in ZIFs and Si-Si distance in Zeolites yielded a factor of 1.9 which was then used to reduce the indexed unit cell of STA-17 giving new axis lengths for a 'theoretical zeolite' of a = 15.6 Å and c = 9.8 Å. This does

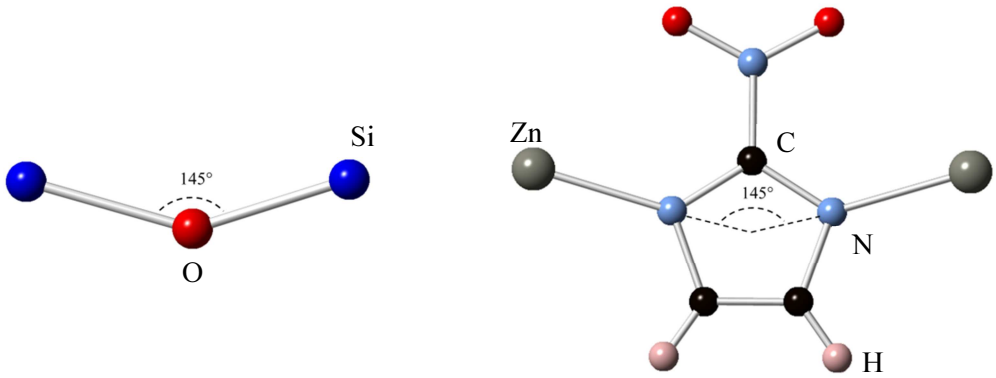

Figure 6.17: *Model illustrates the geometric similarity of Zeolites and Zeolitic Imidazolate Frameworks (ZIFs). The angle between Si-O-Si and Zn-Im-Zn is ~145°.*

not match any known zeolite structures, but because of the great importance of these materials great efforts have been made to enumerate hypothetical zeolite structures *in silico*, and to rank them in terms of energy, to act as tool for zeolite structure discovery. The online available "Atlas of Prospective Zeolite Structures" is one such example, initiated by Martin D. Foster and Michael M. J. Treacy.[31] It contains a vast number of possible inorganic framework work based on optimized structure with composition SiO_2. For STA-17, this database was searched for zeolite topologies, assuming it belongs to a zeolitic imidazole framework structure type. First the lattice parameters were scaled to those expected if the topology had a silicate composition, and then this was searched in the database, excluding structures containing 3mrs as those are assumed

to be unlikely in a ZIF. Results of hypothetical frameworks with the lowest energies are presented in Table 6.1.

Table 6.1: *Results obtained from search in "Atlas of Prospective Zeolite Structures". The structures 5 and 6 were chosen in initial investigations.*

No.	Code	Space-group	Energy (eV/TO_2)	FD (T/1000 $Å^3$)	Lat_par A	Lat_par B	Lat_par C
1	176_3_2657048	P 6_3 m	0.0734	21.622	15.2331	15.2331	8.2849
2	189_3_1603	P -6 2 m	0.1244	21.058	15.457	15.457	8.2625
3	176_3_2090342	P 6_3 m	0.1254	20.628	15.441	15.441	8.4521
4	176_3_2599805	P 6_3 m	0.1494	20.621	15.5643	15.5643	8.3215
5	194_3_3911	P 6_3 / mmc	0.1594	19.822	15.6106	15.6106	8.6059
6	186_3_1617	P -6 2 m	0.1654	19.022	15.54	15.54	9.0492
7	189_4_238498	P -6 2 m	0.1854	20.665	15.4213	15.4213	8.4585
8	189_3_1796	P -6 2 m	0.2254	17.323	15.9742	15.9742	9.4042
9	189_4_238499	P -6 2 m	0.2274	20.396	15.4739	15.4739	8.5117
10	189_4_226355	P -6 2 m	0.2274	19.379	15.3458	15.3458	8.3499

The most reasonable structures with acceptable SiO_4 tetrahedra geometry and lowest energies were found in structures No. 5 and No. 6 with *P 6₃/m m c* and *P -6 2 m* symmetry, presented in Figure 6.18**.** Comparing the expected reflections for each space group with the observed powder pattern yields *P -6 2 m* as the better fit matching all observed peaks (Figure 6.19).

After choosing a plausible zeolite structure the unit cell parameter was rescaled to experimentally-indexed values and silicon atoms were exchanged by zinc positions. Relative coordinates of imidazolate linkers were extracted from existing SOD and GME structures using the CrystalMaker® software package. The model grid of Zn positions exhibits d6rs as seen in the GME topology, interconnected via 4mrs (Chapter 5 structure **1**). These structural similarities were extracted and used as a starting point to introduce sensible NIm and DAP linker alignments into the initial STA-17 structure. Zn-N_4

tetrahedra were built up with zinc nitrogen distances of ~ 2.0 Å, typically found in ZIFs. In a similar manner DAP linkers were added to the structure where close attention was paid to reduce steric hindrance between amino functionalities and adjacent groups (Figure 6.20).

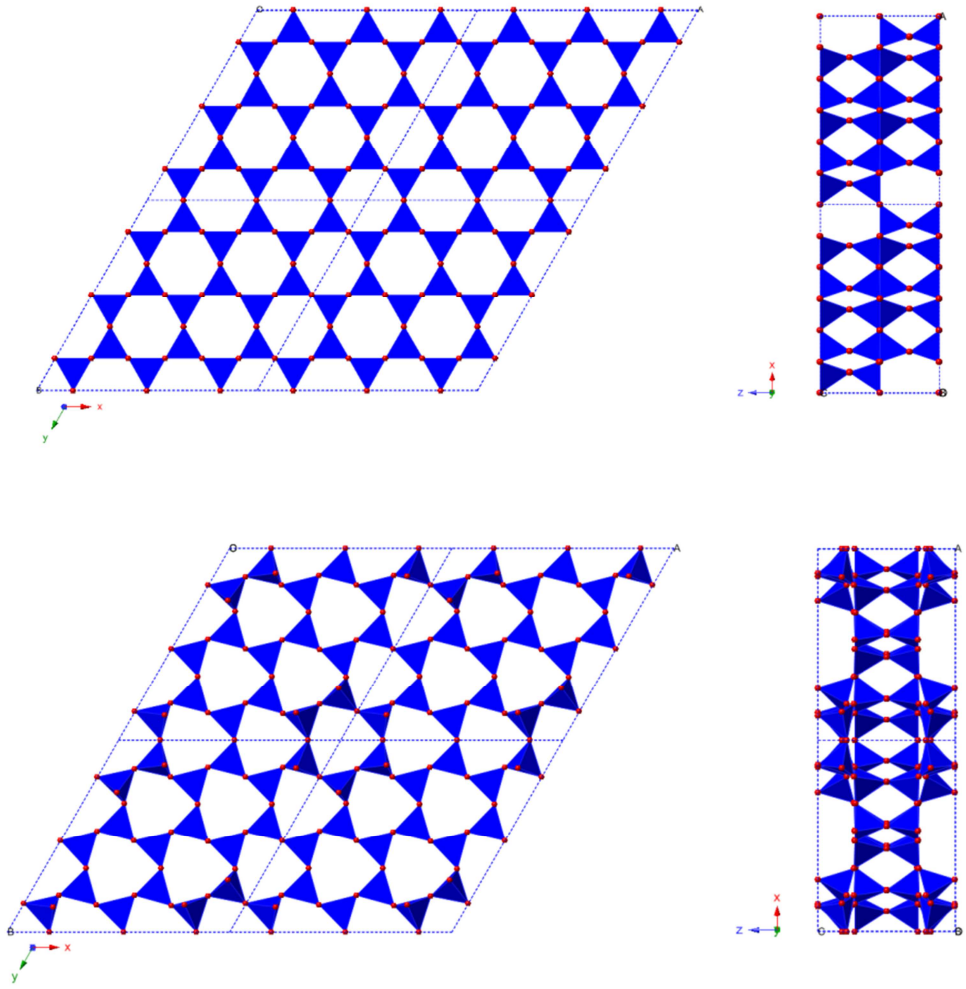

Figure 6.18: *Showing hypothetical two Zeolite structures obtained from search in "Atlas of Prospective Zeolite Structures".*[31] *The presented structures are generated by applying P 6_3 / m m c (top) and P -6 2 m (bottom) viewing along b-axis (right) and c-axis (left).*

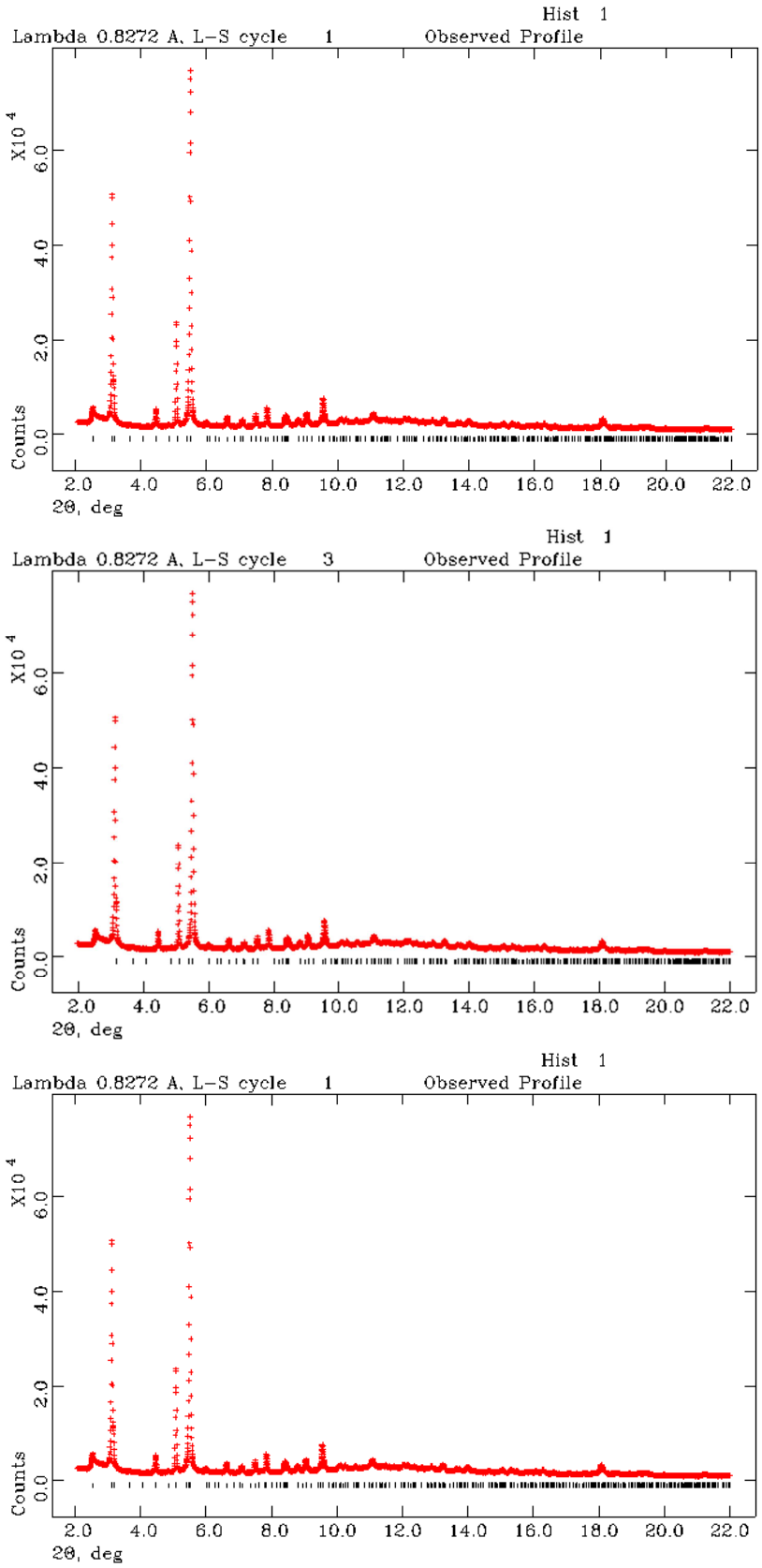

Figure 6.19: *Synchrotron powder XRD pattern of as prepared STA-17 collected at I11 (red) compared to different hexagonal space groups (black tick marks). (Top) P6, (middle) $P6_3/mmc$ and (bottom) P-62m.*

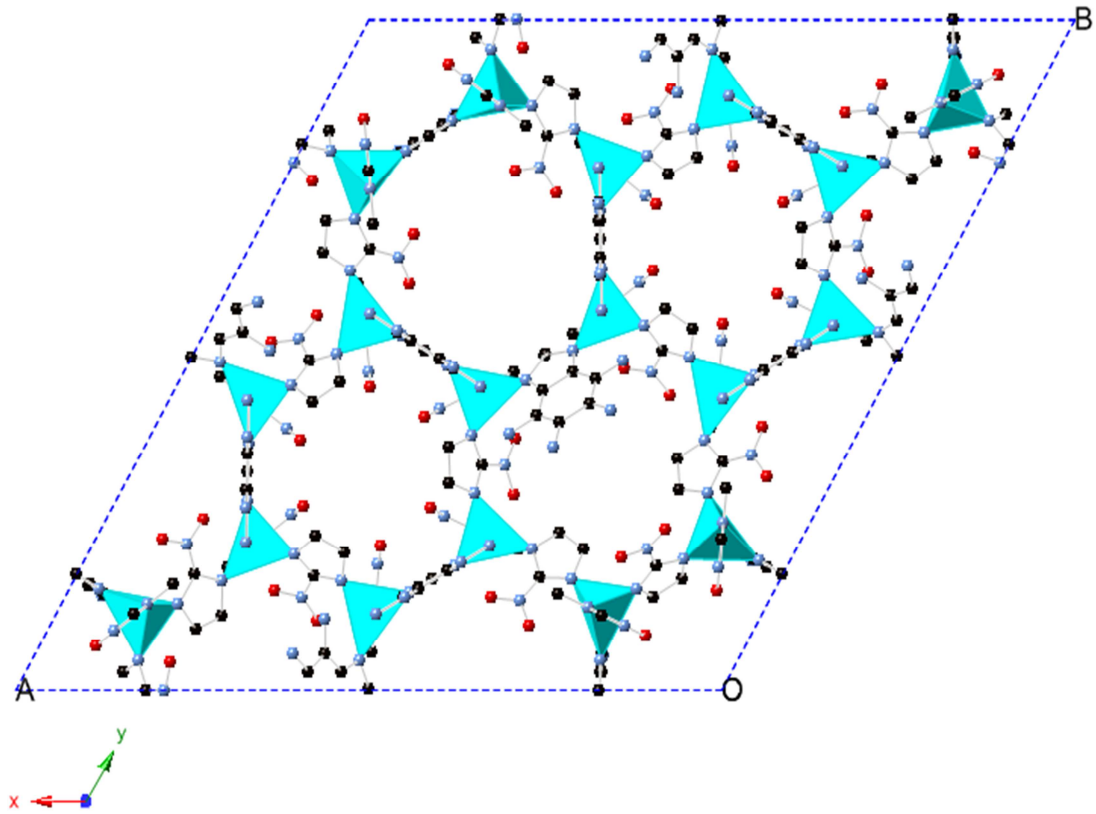

Figure 6.20: *Structure of a STA-17 model in P -6 2 m viewing along c-axis. Zinc positions are derived from a hypothetical Zeolite structure. C black, N blue, O red, Zn turquoise, H omitted for clarity.*

The chosen model exhibits a novel ZIF topology consisting only of 4mr and 6mr rings. Their arrangement is divided into 4mrs parallel to the *c*-axis and 6mrs parallel to the *xy*-plane. There are two different six membered ring topologies which can be further discussed as three crystallographic distinguishable ligand arrangements. The first type is a d6r that was initially extracted from the GME topology and consists of two parallel single six membered rings (6mr) interconnected via 4mrs, resulting in windows of 6.1 Å diameter along the *c*-axis. This 4mr/6mr topology was chosen as the structural starting point for the construction of the framework (Figure 6.21a). Two d6rs show half open arrangements connected only via three 4mr on one half and with the opposite side flipping up and down, making space for DAP linkers parallel to the main axis and pointing to each other (Figure 6.21b, c) leading to pore apertures between 5.1 and 6 Å.

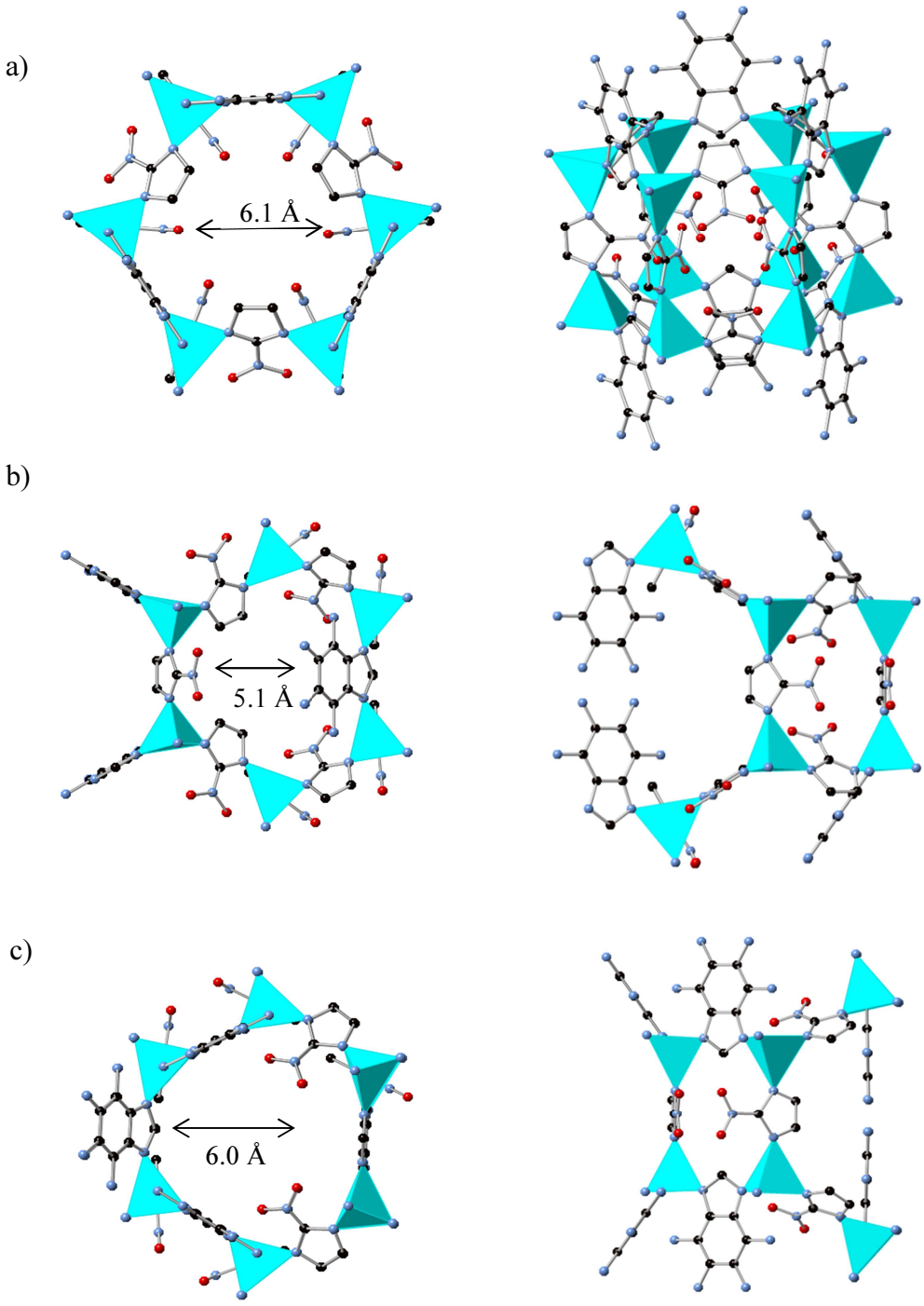

Figure 6.21: *Plots of three crystallographic different 6mrs from the model obtained in P -6 2m. a) Parallel arranged d6mr with DAP linker pointing into the open space forming top and bottom of a discoid cavity. Plots b) and c) illustrating distorted 6mr building the edge of the open cavity. View on the left shows perspective along the c-axis and on the right perpendicular to it. C black, N blue, O red, Zn turquoise, H are not shown. Amino functionalities have 0.5 occupancy and positions of C in benzene moieties binding to amino groups are half N occupied.*

The parallel d6rs are formed from alternating NIm and DAP linkers with the latter pointing towards each other and therefore no interconnection to levels above or below is established creating a cavity with the shape of an oblate sphere (Figure 6.22).

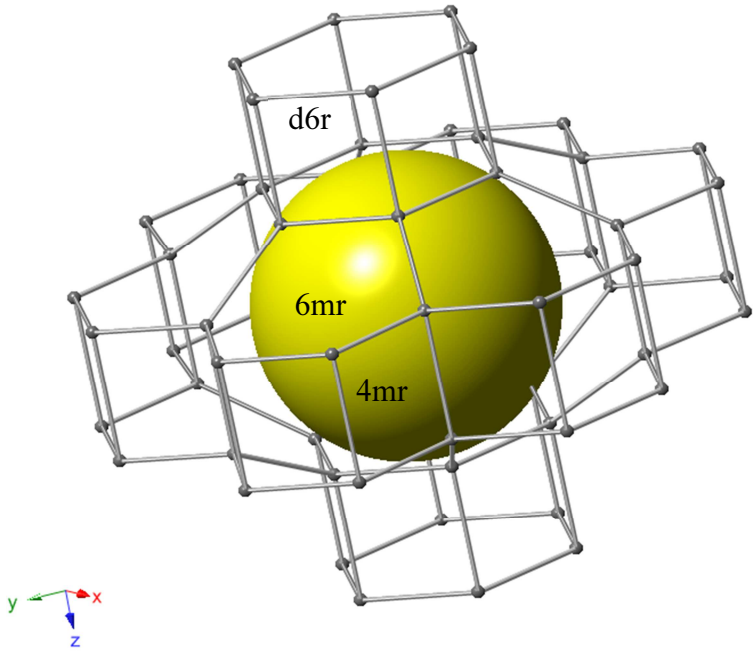

Figure 6.22: *Illustrating proposed topology for STA-17 with zinc positions (black balls) obtained from a hypothetical zeolite structure. The framework shows two different forms of 6mrs. The location of the oblate cavity is indicated by the yellow sphere.*

Structural refinement using the Rietveld method was carried out against synchrotron powder X-ray data collected at the Diamond light source on a sample which was activated at 427 K under 10^{-5} mbar vacuum. Rigid body constraints were applied on organic linkers with fractional occupancies of 0.5 for amino functionalities. At this stage carbons in the pyrimidine moiety were left with occupancy 1.0. The structural refinement did not converge. Refining only instrumental, profile and lattice parameters gives R_{wp} values of 5.38 % (Table 6.2, Figure 6.23). The fit suggests that the presented topology may be correct, but the ligand ordering scheme is not yet established. In

summary, a model has been obtained for the topology of the STA-17 framework, but the absence of SXRD data precludes full structure solution.

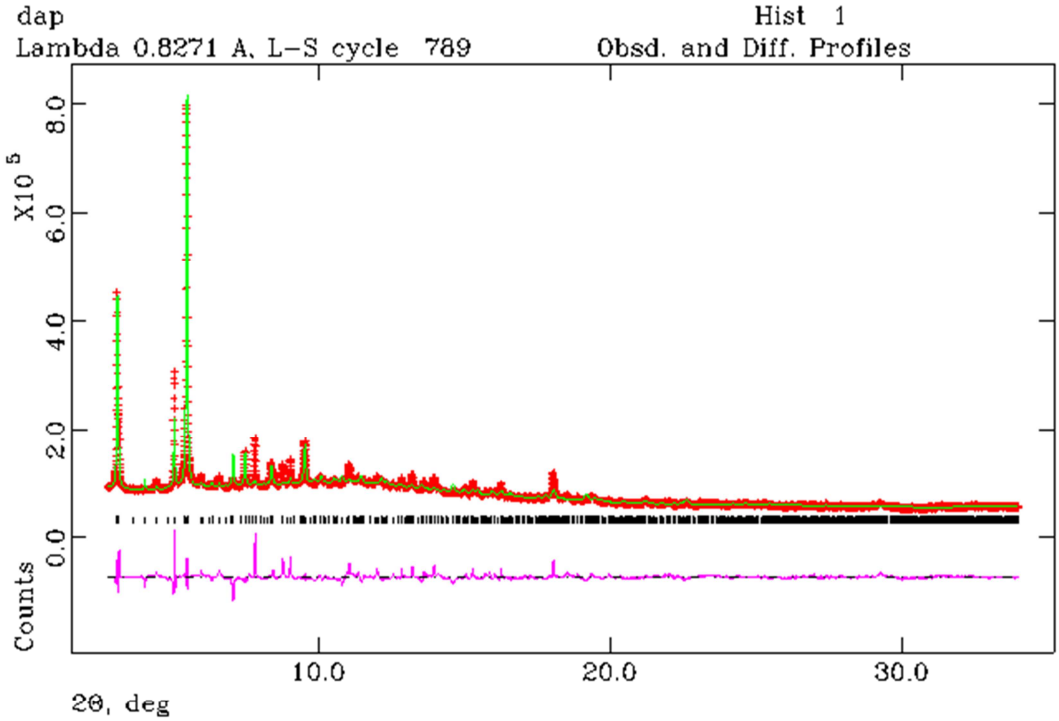

Figure 6.23: *Rietveld plot of the refinement from powder data of the proposed STA-17 structure collected with synchrotron radiation (λ = 0.827055 Å, R_{wp} = 0.0538). The sample was activated at 427 K under 10^{-5} mbar vacuum. Observed pattern, red crosses, fitted profile in green, difference curve between observed and calculated pattern in pink.*

Table 6.2: *Crystallographic data from Rietveld refinement of STA-17, $Zn(NIm)_{1.33}(DAP)_{0.66}$.*

Refined composition	$C_{26}N_{22}O_8Zn_3$
Formula mass [g / mol]	944.57
Space group	*P -6 2 m*
Z	12
a [Å]	29.7594(27)
b [Å]	29.7594(27)
c [Å]	18.6289(26)
β [°]	120
V [Å^3]	14288(4)
λ [Å]	0.827055
2Θ range [°]	2.75 - 35.0
Rp	0.0332
Rwp	0.0537
R(F^2)	0.32559

6.5 Conclusion

To conclude, the introduction of the diamino functionalised purine, DAP, via a mixed linker solvothermal synthesis also containing nitroimiazole results in the crystallisation of a novel zeolitic imidazolate framework or ZIF. It was found to have a hexagonal unit cell with a = 29.7594 Å and c = 18.6289 Å. The material was found to be stable to methanol and temperatures up to 493 K. Gas adsorption measurement show high porosity to nitrogen with a calculated BET of 428 $m^2 g^{-1}$ and some uptake of CO_2 at 298 K. The mixed linker STA-17 is the second product of a sequential crystallisation reaction. After 3 h reaction time the cubic single linker ZIF-65(Zn) was found as a pure phase product. At longer crystallisation times small amounts of the hexagonal phase appear suggesting a mechanism where the mixed linker material grows at the expense of the cubic single linker framework (SOD) in a recrystallization. Crystallisation of the pure mixed linker phase occurred after 18 h. The outcome of the solvothermal synthesis is strongly dependent on precursor ratios and solvent. Deviation from a 1 : 1 : 1 ratio of zinc : NIm : DAP or the use of methanol as solvent led to the cubic ZIF-65(Zn) (SOD) phase. Crystallisation attempts with metal salts other than zinc nitrate yielded in either amorphous or undesired phases. Since the synthesis of a material amenable for SXRD was unsuccessful, a model in *P -6 2 m* was chosen for Rietveld refinement from powder XRD data, derived from the database of hypothetical zeolite structures. The structural refinement process against synchrotron data was not found to give a final structure, but yielded a profile fit with R_{wp} of 5.38 %. The suggested model topology is constructed from 4mrs and d6mrs aligned parallel to the *c*-axis or the *xy*-plane, respectively, forming an oblate sphere shaped cavity. Further investigations are required to solve the detailed structure.

6.6 References

1. M. C. Duke, B. Ladewig, S. Smart, V. Rudolph and J. C. D. da Costa, *Front. Chem. Eng. China*, 2010, **4**, 184-195.

2. J. D. Figueroa, T. Fout, S. Plasynski, H. McIlvried and R. D. Srivastava, *Int. J. Greenh. Gas Con.*, 2008, **2**, 9-20.

3. H. Yang, Z. Xu, M. Fan, R. Gupta, R. B. Slimane, A. E. Bland and I. Wright, *J. Environ. Sci.*, 2008, **20**, 14-27.

4. B. Dutcher, M. Fan, B. Leonard, M. D. Dyar, J. Tang, E. A. Speicher, P. Liu and Y. Zhang, *J. Phys. Chem. C*, 2011, **115**, 15532-15544.

5. A. Samanta, A. Zhao, G. K. H. Shimizu, P. Sarkar and R. Gupta, *Ind. Eng. Chem. Res.*, 2011, **51**, 1438-1463.

6. F. Chang, J. Zhou, P. Chen, Y. Chen, H. Jia, S. M. I. Saad, Y. Gao, X. Cao and T. Zheng, *Asia-Pac. J. Chem. Eng.*, 2013, **8**, 618-626.

7. L. Zhang, N. Xu, X. Li, S. Wang, K. Huang, W. H. Harris and W. K. S. Chiu, *Energ. Environ. Sci.*, 2012, **5**, 8310-8317.

8. X. He and M.-B. Hägg, *Membranes*, 2012, **2**, 706-726.

9. K. Ramasubramanian and W. S. W. Ho, *Curr. Op. Chem. Eng.*, 2011, **1**, 47-54.

10. Z. Zhang, Y. Zhao, Q. Gong, Z. Li and J. Li, *Chem. Commun.*, 2013, **49**, 653-661.

11. J. Liu, P. K. Thallapally, B. P. McGrail, D. R. Brown and J. Liu, *Chem. Soc. Rev.*, 2012, **41**, 2308-2322.

12. Y.-S. Bae and R. Q. Snurr, *Angew. Chem. Int. Edit.*, 2011, **50**, 11586-11596.

13. H. Wu, J. M. Simmons, G. Srinivas, W. Zhou and T. Yildirim, *J. Phys. Chem. Let.*, 2010, **1**, 1946-1951.

14. S. R. Caskey, A. G. Wong-Foy and A. J. Matzger, *J. Am. Chem. Soc.*, 2008, **130**, 10870-10871.

15. J. Liu, Y. Wang, A. I. Benin, P. Jakubczak, R. R. Willis and M. D. LeVan, *Langmuir*, 2010, **26**, 14301-14307.

16. A. C. Kizzie, A. G. Wong-Foy and A. J. Matzger, *Langmuir*, 2011, **27**, 6368-6373.

17. J. C. Hicks, J. H. Drese, D. J. Fauth, M. L. Gray, G. Qi and C. W. Jones, *J. Am. Chem. Soc.*, 2008, **130**, 2902-2903.

18. X. Xu, X. Zhao, L. Sun and X. Liu, *J. Nat. Gas Chem.*, 2009, **18**, 167-172.

19. J. R. Long, T. M. McDonald and D. M. d'Alessandro, *PCT Int. Appl.*, 2013.

20. X. Wang, H. Li and X.-J. Hou, *J. Phys. Chem. C*, 2012, **116**, 19814-19821.

21. B. Yuan, D. Ma, X. Wang, Z. Li, Y. Li, H. Liu and D. He, *Chem. Commun.*, 2012, **48**, 1135-1137.

22. J. Kahr, J. P. S. Mowat, A. M. Z. Slawin, R. E. Morris, D. Fairen-Jimenez and P. A. Wright, *Chem. Commun.*, 2012, **48**, 6690-6692.

23. K. C. Stylianou, J. E. Warren, S. Y. Chong, J. Rabone, J. Bacsa, D. Bradshaw and M. J. Rosseinsky, *Chem. Commun.*, 2011, **47**, 3389-3391.

24. F. Wang and Y. Kang, *Inorg. Chem. Commun.*, 2012, **20**, 266-268.

25. J. An, O. K. Farha, J. T. Hupp, E. Pohl, J. I. Yeh and N. L. Rosi, *Nat Commun*, 2012, **3**, 604.

26. J. An, S. J. Geib and N. L. Rosi, *J. Am. Chem. Soc.*, 2009, **132**, 38-39.

27. E. Yang, H.-Y. Li, F. Wang, H. Yang and J. Zhang, *CrystEngComm*, 2013, **15**, 658-661.

28. R. Banerjee, H. Furukawa, D. Britt, C. Knobler, M. O'Keeffe and O. M. Yaghi, *J. Am. Chem. Soc.*, 2009, **131**, 3875-3877.

29. A. D. Burrows, K. Cassar, R. M. W. Friend, M. F. Mahon, S. P. Rigby and J. E. Warren, *CrystEngComm*, 2005, **7**, 548-550.

30. Y.-Q. Tian, S.-Y. Yao, D. Gu, K.-H. Cui, D.-W. Guo, G. Zhang, Z.-X. Chen and D.-Y. Zhao, *Chem. Eur. J.,* 2010, **16**, 1137-1141.

31. M. D. Foster and M. M. J. Treacy, *A Database of Hypothetical Zeolite Structures: http://www.hypotheticalzeolites.net*.

7. *A Note on Solid State NMR of ZIF Materials*

7.1 Aim

A program of solid state MAS NMR was conducted to elucidate the information that technique yields on zinc imidazolates. Initially, the aim was to confirm the presence of different imidazolate linkers in zinc zeolitic imidazolate framework, ZIF, materials that were prepared in mixed linker syntheses where 2-nitroimidazole (NIm) was part of all reactions. The ^{13}C and ^{15}N chemical shifts of materials synthesised in this thesis were compared with selected examples of mixed linker ZIFs found in the literature[1] and one single linker NIm ZIF, ZIF-65(Zn), discussed previously in this thesis. In addition, it was hoped that solid state NMR could yield structural information on ZIF materials from the number and broadening of the observed peaks.

ZIF materials containing nitro-groups on at least one linker were prepared (ZIF-68, ZIF-70 and ZIF-78)[1] (see Table 7.1) and compared with those presented in this thesis. ^{13}C and ^{15}N MAS NMR spectra were collected with in-house solid state NMR operated by Scott Sneddon (Group of Sharon Ashbrook, St. Andrews) under the conditions reported in chapter 2 (MAS NMR spectroscopy). The chemical shift of ^{13}C and ^{15}N of the imidazolate sub-unit depend on the presence of substituents, which themselves give rise to ^{13}C (-$\underline{C}$HN$\underline{C}$HN- [purine], -$\underline{C_2}H_2\underline{C_2}H_2$- [benzimidazole], -$\underline{C_2}H_2\underline{C_2}(NO_2)H_2$- [6-nitrobenzimidazole], -$\underline{C_2}(NH_2)N\underline{C}(NH_2)N$- [2,6-diaminopurine]) and ^{15}N (-$\underline{N}O_2$ [2-nitroimidazole], -CH$\underline{N}$CH$\underline{N}$- [purine], -$C_2H_2C_2(\underline{N}O_2)H_2$- [6-nitrobenzimidazole], -$C_2(\underline{N}H_2)\underline{N}C(\underline{N}H_2)\underline{N}$- [2,6-diaminopurine]) signals.

Table 7.1: *Summary of materials, their topologies (if known) and linkers present in the framework of ZIFs measured with solid state MAS NMR.*

ZIF	Topology	Imidazolate groups present
ZIF-65 as prepared	SOD	NIm
ZIF-65 desolvated	unknown	NIm
ZIF-68	GME	NIm, benzimidazole
ZIF-70	GME	NIm, imidazole
ZIF-78	GME	NIm, 6-nitrobenzimidazole
Zn(NIm)(Pur), structure **1**	GME	NIm, purine
$Zn_{1.33}(O,OH)_{0.33}(NIm)_{1.167}(Pur)$, structure **4**	RHO	NIm, purine
$Zn(NIm)_{1.33}(diaminopurine)_{0.66}$, STA-17	unknown	NIm, 2,6-diaminopurine

7.2 Experimental

All samples were measured as prepared without any pre-treatment except ZIF-70 which was methanol exchanged and heated at 343 K. One sample of ZIF-65(Zn) was methanol exchanged and heated to 343 K prior measurement. The structure of each linker is presented in Figure 7.1 and a summary of linkers present in the ZIF is given in Table 7.1. The presented spectra are shown with chemical shift ranges focused on the functional groups between 90 - 180 ppm for ^{13}C and 5 - (-250) ppm for ^{15}N. Solvent peaks for DMF (~30 ppm and ~165 ppm, ^{13}C) were observed in as-prepared samples

and as small residual solvent peaks in those which were methanol-exchanged and heated. No resonances were assigned to methanol.

For experimental details of materials described in this thesis the reader is referred to the respective chapters: otherwise synthesis procedure were taken from the literature.[1]

7.2.1 Synthesis of ZIF-68, ZIF-70 and ZIF-78[1]

A typical synthesis (the preparation of ZIF-68 is exemplified) was carried out by David Price, Univ. St. Andrews, via mixing zinc nitrate hexahydrate (1 mmol, 297.5 mg, Aldrich), 2-nitroimidazole (1 mmol, 113 mg, Alfa Aesar) and benzimidazole (1 mmol, 118 mg, Aldrich) in a Teflon-lined autoclave and dissolving in 15 ml DMF. The solution was heated to 373 K for 4 days before cooling to room temperature. The reaction was filtered and washed with DMF before drying at room temperature. ZIF-70 and ZIF-78 were obtained by using imidazole and 6-nitrobenzimidazole, respectively, purchased from Sigma Aldrich. The phase and purity of each sample was confirmed by PXRD (Figure 7.2).

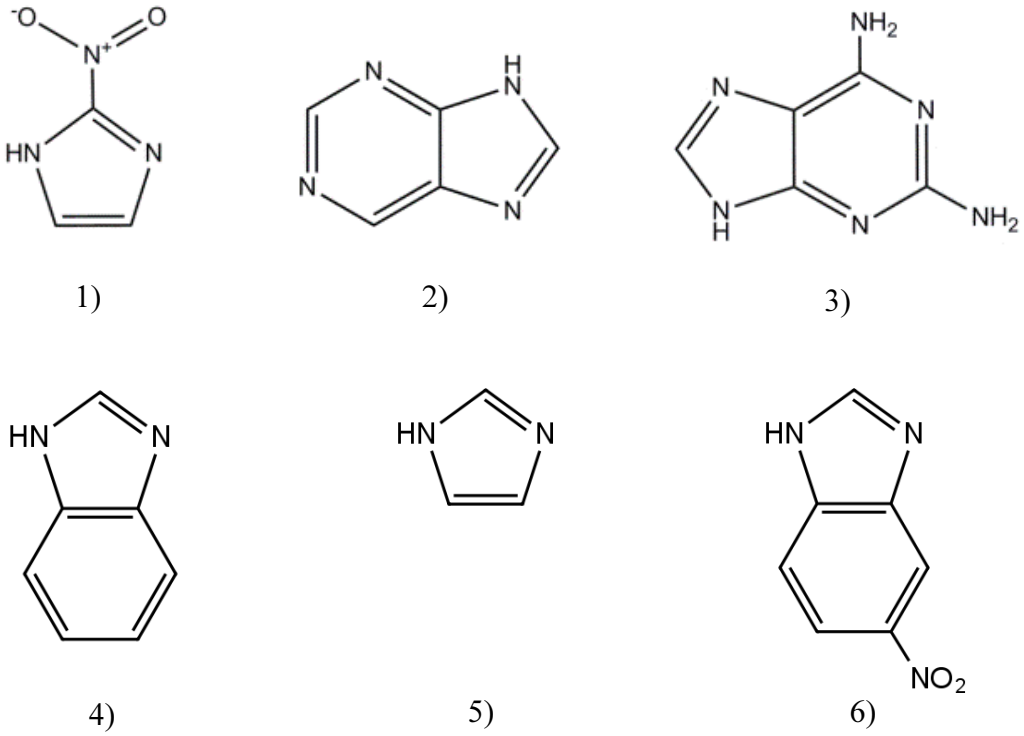

Figure 7.1: *Structures of imidazole linkers used to synthesise ZIFs. 1) 2-Nitroimidazole (NIm), 2) Purine (Pur), 3) 2,6-Diaminopurine, 4) Benzimidazole, 5) Imidazole and 6) 6-Nitroimidazole.*

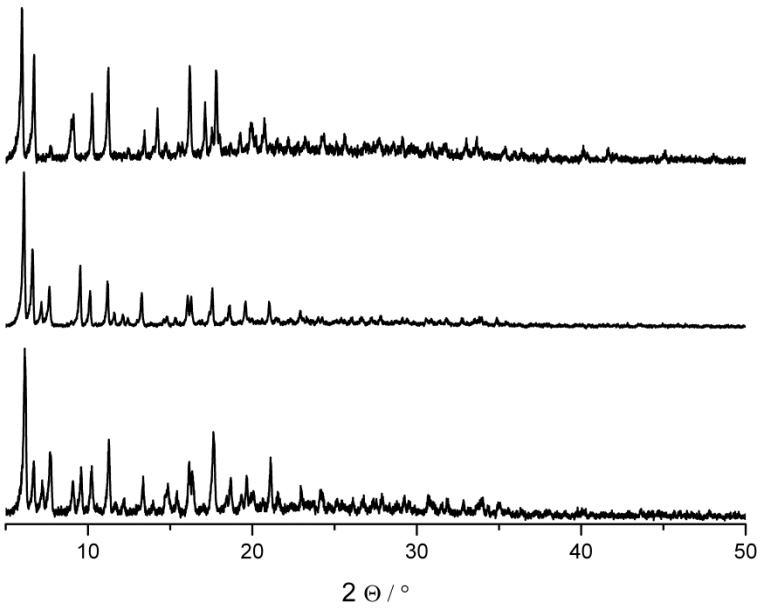

Figure 7.2: *Powder XRD pattern of as prepared ZIF-68 (bottom), MeOH exchanged and heated to 343 K ZIF-70 (middle) and as prepared ZIF-78 (top).*

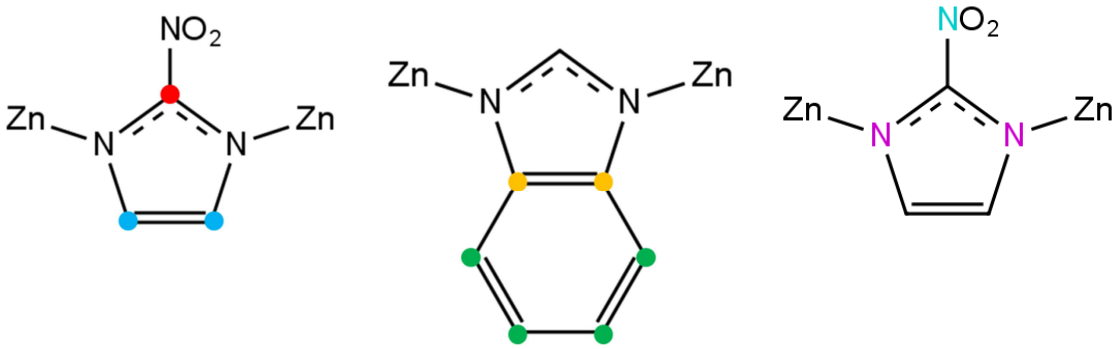

Figure 7.3: *Structural description and colour code marking the positions of nuclei measured in MAS NMR of imidazolate linkers used in single and mixed linker synthesis.*

7.3 Results and Discussion

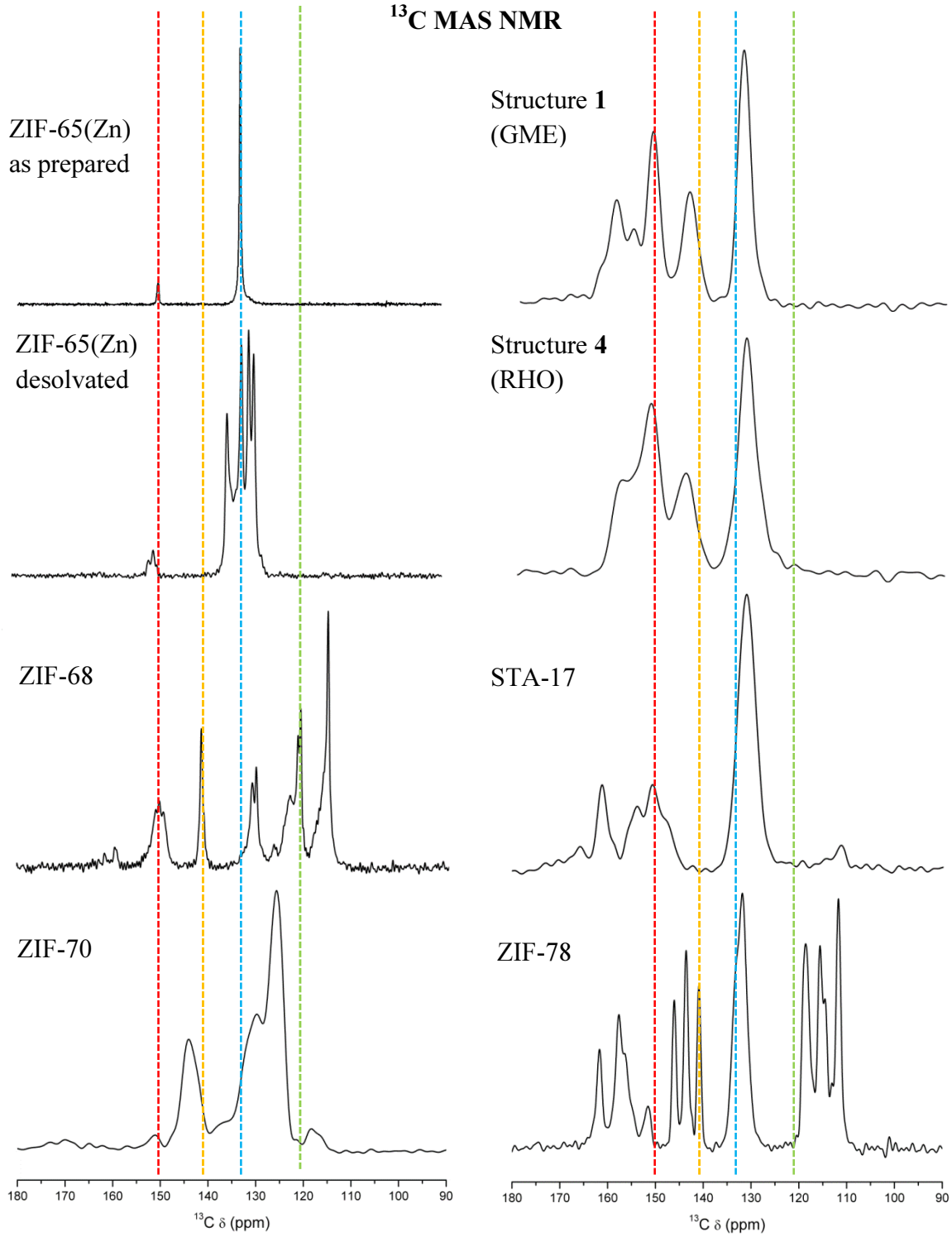

Figure 7.4: *^{13}C (14.1 T, 12.5 kHz MAS) CP MAS spectra. The spectra were the result of signal averaging [454 (ZIF-65(Zn) as-prepared), 1024 (ZIF-65(Zn) desolvated), 128 (ZIF-68), 1024 (ZIF-70), 512 (ZIF-78), (structure 1), 1024 (structure 4), 1024 (STA-17)] transients using a 1 ms contact time (ramped for ^{1}H) and a recycle interval of 3 seconds. ^{1}H SPINAL-64 decoupling[2] was employed during signal acquisition at a radiofrequency field strength ($\gamma B1/2\pi$) of ~100 kHz.*

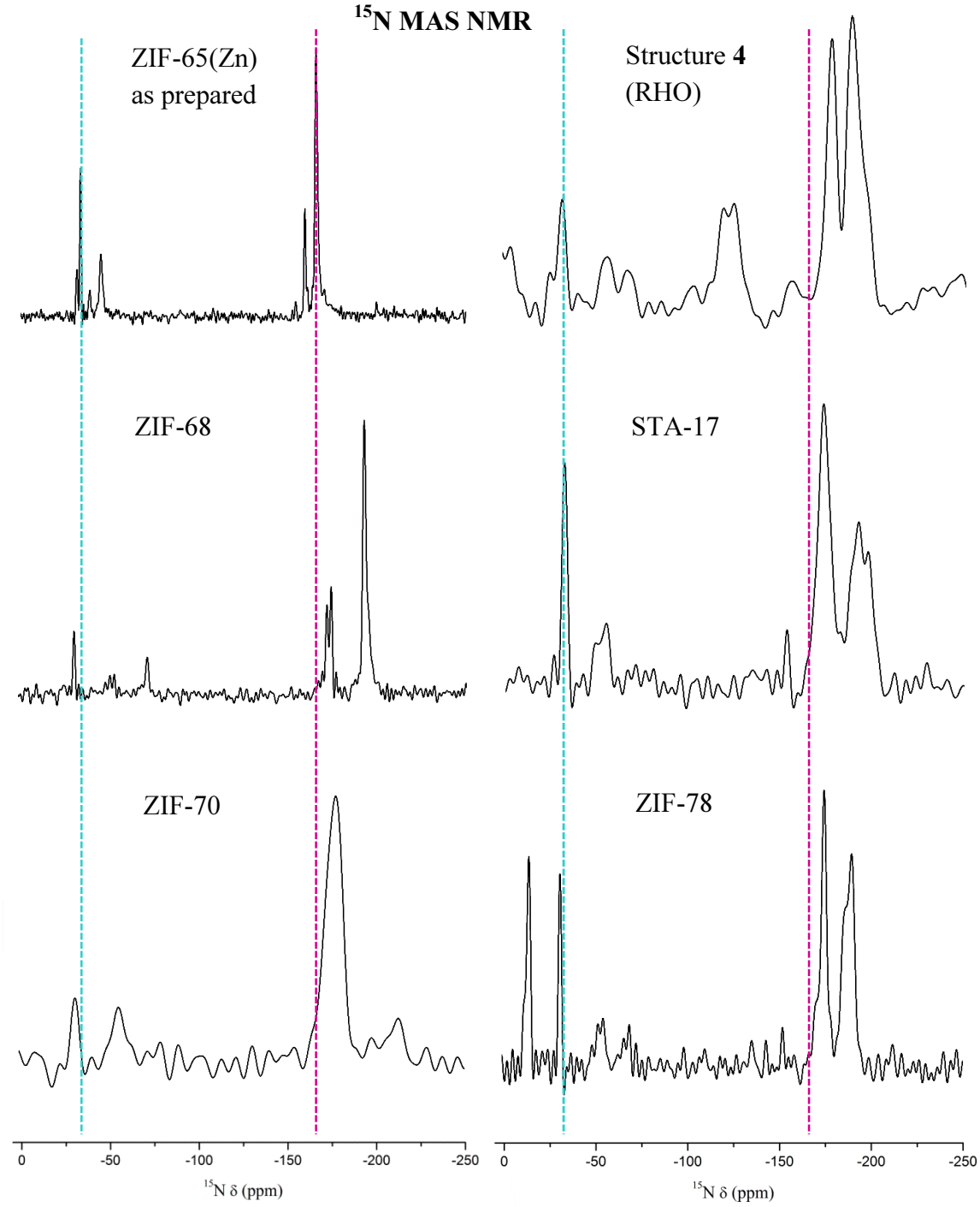

Figure 7.5: *^{15}N (9.4 T, 5.0 kHz MAS) CP MAS spectra. The spectra were the result of signal averaging [2120 (ZIF-65(Zn) as-prepared), 12416 (ZIF-68), 16464 (ZIF-70), 33578 (ZIF-78), 20480 (structure **4**), 33088 (STA-17)] transients using a 10 ms contact time (ramped for ^{1}H) and a recycle interval of 5 seconds. ^{1}H continuous wave decoupling was employed during signal acquisition at a radiofrequency field strength ($\gamma B1/2\pi$) of ~100 kHz.*

Comparing the results of the ^{13}C measurements of the single NIm linker ZIF-65(Zn) with mixed linker ZIFs (in all of them NIm was part of the reaction mixture) confirms the presence of NIm in all structures. A single narrow resonance at around 130 ppm for C4/C5 atoms is observed in the as prepared ZIF-65(Zn) together with one peak at around 150 ppm for C2 attached to the nitro functionality indicating high symmetry and a single crystallographic site that is also found from SXRD. By removing the solvent from this structure peak splitting occurs suggesting a change of symmetry, which is also observed in PXRD data (cubic to hexagonal) and might be due to an increase of crystallographically distinguishable sites. Notably, the peak width changes little which can be explained by retention of high local ordering. All mixed linker materials show peaks in the same regions at around 150 ppm indicating (i) the presence of NIm and (ii) similar local environment around C2 and C4/C5. Additional peaks suggest the existence of a second linker in the framework. Broad peak shapes in all mixed linker ZIF, except ZIF-68, indicates some local disorder originated from linker movement (up / down flipping over the Zn-N – N-Zn axis) that was also found in structure **1** (GME), expressed through elevated thermal parameters derived from SXRD of C4/C5 atoms and carbon atoms in benzene moieties.

Analysing the ^{15}N spectra underlines these inferences. The spectrum of as-prepared ZIF-65(Zn) shows more peaks than expected, which might be due to partial solvent loss before or during measurement that caused a partial transformation of the cubic SOD to the distorted form, but still gives information for quantifying functional groups. The chemical shift of N in the nitro group was assigned to around -27 ppm and for those coordinating to zinc at around -170 ppm. The interpretation of the peak shape indicating a high local ordering agrees with the ^{13}C spectra. The ^{15}N spectra of the mixed linker ZIFs show results broadly consistent with those gained from the carbon MAS NMR.

Two peaks around -170 ppm are assigned to the coordination of two different linkers to the zinc atom, particularly when the linkers have two rings (benzene, purine, diaminopurine, nitrobenzimidazole). Notably, the spectrum for ZIF-68 shows sharp peaks with splitting in this region (~-175 ppm) which can be explained by two crystallographically different sites for each linker in the ZIF series with GME topology. The peak splitting indicates a high degree of ordering for this site, which is probably masked in the other GME structures due to peak broadening. The chemical shift at around -27 ppm arising from the nitro group shows little variation between spectra indicating the presence of NIm with similar environments. The presence of the second nitro group in ZIF-78 is represented through an additional resonance at higher field of around -10 ppm.

7.4 Conclusion

MAS NMR can become a valuable tool in the structural characterisation of ZIF materials as solids. The incorporation of 2-nitroimidazole was proven successfully by ^{13}C and ^{15}N MAS NMR, as was the presence of a second linker used in the mixed linker syntheses. This gave additional confidence in the presence of both NIm and DAP linkers in the structure of STA-17. The peak broadening observed in ^{13}C and ^{15}N spectra of STA-17 was found for most other mixed linker ZIFs indicating similarly high local disorder. High short range and low long range order was concluded from single peaks with narrow peak width for C2 and C4/C5 in as-prepared ZIF-65(Zn). Peak splitting in the ^{13}C spectrum after solvent removal supports the change to lower symmetry observed in PXRD studies, while the narrow peak shapes indicate a high degree of local ordering.

7.5 References

1. R. Banerjee, H. Furukawa, D. Britt, C. Knobler, M. O'Keeffe and O. M. Yaghi, *J. Am. Chem. Soc.,* 2009, 131, 3875-3877.

2. B. M. Fung, A. K. Khitrin and K. Ermolaev, *J. Mag. Res.*, 2000, 142, 97-101.

8. *General Conclusions and Future Work*

8.1 General Conclusions

The main aim of this thesis was to investigate porous metal organic frameworks (MOFs) as adsorbents for the removal of CO_2 from flue gas streams at ambient temperature and pressure.

Initially the microporous CPO-27(Mg) was examined. It was chosen due to the high concentration of open metal sites which act as positions of strong adsorption for carbon dioxide when activated. Research in literature gave a wide range of activation procedures, most of them not applicable on industrial scale. Early experiments following simple thermal activation gave materials with low porosity to nitrogen at 77 K which did not reproduce values found by other groups for more complex activation processses. It was reasoned that possible surface effects cause pores to block, possibly due to rearrangement of unsaturated metal sides or linkers as a result of the activation process. Adsorption measurements on the nickel form showed appreciable nitrogen uptake, so efforts were made to enrich the surface of CPO-27(Mg) crystals with 'epitaxial' CPO-27(Ni) to enhance the surface stability. A post-synthetic step was introduced where nickel salts were added in combination with weak acids. As a result the porosity of nickel-modified CPO-27(Mg) to nitrogen at 77 K was increased to values of up to 17 mmol g^{-1} obtained by simple thermal treatment under vacuum as activation procedures. Additionally, it was possible to increase the adsorption of carbon dioxide of unmodified CPO-27(Mg) at 0.1 bar and 298 K to up to 6.7 mmol g^{-1} through the modification step. Further, it was found that a sample modified with 10% nickel

acetate / H_3PO_3 can be cycled several times in an activation / CO_2 adsorption process retaining an uptake of 6.1 mmol g^{-1}. This observation indicates the stabilizing effect of modifying CPO-27(Mg) with nickel when dehydrating during the activation process. One explanation of this behaviour could be that CPO-27(Mg) is less stable to solvent removal and the surface of CPO-27(Ni) is more stable due to the better tolerance of Ni^{2+} cations to the lower coordination numbers. The subsequent exchange of magnesium by nickel cations during the modification on the external surface would therefore improve the stability of CPO-27(Mg) against dehydration. The CO_2 adsorption data rules out crystallographic defects blocking the pores of N_2 at 77 K while leaving them permeable to CO_2 at ambient temperature. This suggests that interaction strength between surface and gas rather than size as key to the pores' accessibility. The modification procedure was also applied to other species of CPO-27 materials. The modification of CPO-27(Ni) with 10% Mg^{2+} / H_3PO_3 and CPO-27(Co) with 10% Ni^{2+} / H_3PO_3 yielded in improved porosity to nitrogen of 12.5 mmol g^{-1} and 12 mmol g^{-1}, respectively.

The introduction of nickel into CPO-27(Mg) is facilitated through the addition of nickel salts and weak acids, including carboxylic acids and also phosphorous acid leading to a material with a Ni^{2+}-enriched surface but also with Ni^{2+} distributed throughout the crystal. Bulk measurements obtained from EDX on modified CPO-27(Mg) revealed nickel contents of up to 66.5 % by adding 90 mol% of metal additive when XPS analysis shows at the same time 100% nickel at the surface which indicates some zonation. The bulk measurement was underlined by synchrotron PXRD data giving refined occupancies for Mg and Ni of 64.6% and 35.4%, respectively. SEM analysis shows acicular crystals retaining their morphology during the modification process suggesting isomorphous replacement of Mg^{2+} by Ni^{2+}. Experiments preclude dissolution and recrystallization of the crystals, but show a small increase in crystal size during

modification. EDX mapping identifies this growth as a nickel rim-enriched coating the whole crystal. The increase of the nickel concentration in the crystals leads to a decrease in thermal stability, agreeing with TGA measurements of unmodified CPO-27(Mg) with the pure CPO-27(Ni) where the latter decomposes at lower temperature. This demonstration of post-synthetic framework cation exchange suggests this method can be used more widely to prepare compositions of MOFs that cannot be synthesised directly.

Zeolitic imidazolate frameworks were also examined as part of this thesis. The single linker ZIF, $Zn(NIm)_2$, isostructural to the cobalt ZIF-65 with the SOD topology, was prepared and examined. The structure was refined and was shown to match its cobalt analogue. The removal of solvent via thermal activation led to a partial phase transformation which was shown to be reversible upon exposure to the solvent. It was possible to obtain an almost pure phase of the transformed material by exchanging DMF by methanol and then to return it to its initial structure. This phenomenon was shown to be reversible over several cycles. The low crystallinity precluded solution of the desolvated structure and the broad peak shape in the powder XRD data allowed only a rough estimation of the unit cell parameter, hexagonal with $a = b \approx 27.00$ Å, $c \approx 9.00$Å. Nitrogen adsorption at 77 K shows an isotherm with several steps up to 13 mmol g^{-1}. A similar phenomenon was observed for CO_2 at 198 K with a total uptake of 7 mmol g^{-1}. There is a pronounced hysteresis in the desorption branches for both isotherms. This indicates a highly flexible framework. The broad peak shapes in the PXRD pattern indicate the loss of long range order when transforming into the unknown phase. In contrast, solid state NMR studies of as-prepared and desolvated materials show sharp peaks which indicate a highly ordered local environment around carbon and nitrogen atoms. The lower symmetry suggested from PXRD data is supported by the increased

number of peaks found in the spectrum of the desolvated sample. A dense $Zn(NIm)_2$ novel ZIF structure was obtained by changing the solvent from DMF to methanol indicating the high sensitivity to the final product in synthesis using zinc salts and the NIm linker.

A series of novel mixed linker ZIFs was obtained from employing NIm together with purine in a mixed linker synthesis. The variation of the zinc metal source gave four novel ZIFs in high crystallinity. Structure **1** crystallised as an isoreticular product to ZIF-68 in GME topology composed of NIm and DAP with the ratio 1 : 1 giving a composition of Zn(NIm)(pur). The material was found to be porous to nitrogen with a total uptake of 9.8 mmol g^{-1}. Structures **2** and **3** were shown to host purine as the only linker. Both materials show no porosity to nitrogen or carbon dioxide. The connectivity of the purine linker to zinc is in both structures similar and follows the coordination through imidazole N atoms, as seen in ZIFs and via a nitrogen atom in the pyrimidine moiety. Anions from the metal salt balance the framework charge by forming bonds to zinc in the fourth coordination position. Crystallisation in the presence of zinc nitrate yields a novel mixed linker ZIF with RHO framework topology. Structure **4** has the same framework topology as ZIF-11, but incorporates NIm and purine linkers in an ordered way with the latter pointing towards the centre of 6mrs opening up the d8r. This results in only one type of supercage. NIm linkers project into 4mr and give 8mr windows with 9 Å free diameter. A novel feature of in this structure is the presence of *exo*-NIm linkers bridging between *exo*-zinc cations coordinating to pyrimidine N atoms of the purine linker in 6mrs. These decorating species protrude into supercages. They can be removed by soaking in water, increasing the pore volume from 6.5 mmol g^{-1} to 12.5 mmol g^{-1}.

Introducing diaminopurine (DAP) as a second imidazolate linker into the mixed linker synthesis, together with NIm, gave a novel porous zeolitic imidazolate framework denoted STA-17. The unit cell was found to be hexagonal with cell dimensions of a = 29.7594 Å and c = 18.6289 Å. STA-17 shows good thermal stability and was shown to be stable to soaking in MeOH. Investigation of the crystallisation sequence revealed ZIF-65(SOD) as the initial product observed after only 1 h reaction time which then recrystallizes to the final product STA-17 after 18 h. The exposure to methanol has no noticeable impact on the structure of STA-17. Despite the fact that the material is only obtained when using a 1 : 1 : 1 ratio of Zn : NIm : DAP the final composition of as-prepared STA-17 was estimated as $Zn(NIm)_{1.33}(DAP)_{0.67}$•1.3DMF. Solid state NMR studies confirm both linkers to be present. The observation of broad ^{13}C and ^{15}N peak shapes indicates low ordering in the local environment which was also found in mixed linker structures (**1** and **4**) containing NIm suggesting similar local environments. Attempts were made to solve the structure from powder XRD data which involved the extraction of starting models from the database of hypothetical zeolite structures. This yielded in a possible topology that hosts an oblate sphere shaped cavity composed from 4mr and d6r, but a detailed structure solution awaits the preparation of crystals of suitable quality for SXRD.

The nickel form of CPO-27 remains the most promising material for carbon capture from flue gas due its higher stability to wet gas streams compared to CPO-27(Mg). The generally low CO_2 uptake of ZIFs at low partial pressure and ambient temperature makes them more likely to be useful as adsorbents in pre-combustion processes or as components in mixed membrane composites.

8.2 Future Work

Future work should include further investigations on linker systems capable of chelating metal cations and creating possible open metal sites with the ultimate aim of making a robust host framework stable upon the exposure of their active sites to chemically reactive gases. Additionally, post-synthetic metal cation exchange reaction would open up the materials as adsorbents or catalytically active species.

Further, framework cation exchange reaction in MOFs via post-synthetic modification should be considered to give materials with compositions that are not accessible by direct synthesis methods.

More work should be done on the structure elucidation of the desolvated and poorly crystalline version of ZIF-65(Zn) by applying modelling methods (e.g. Ab initio molecular dynamics).

A model of the structure of STA-17 has been presented and was obtained from a hypothetical zeolite approach. Structure solution methods based on direct and indirect methods from high resolution synchrotron powder data should be investigated further and different crystallisation methods should be applied to obtain single crystals suitable to obtain structural information from SXRD data.